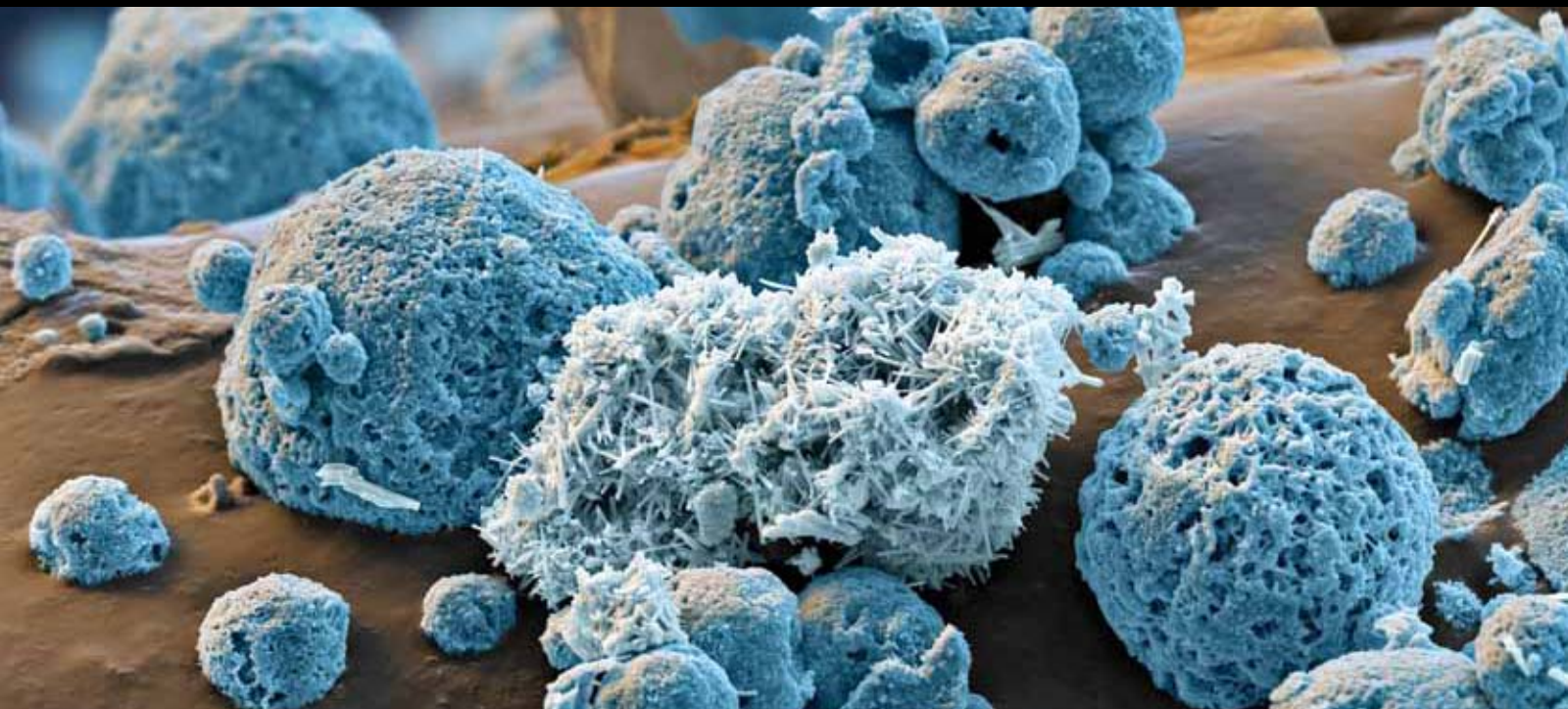


New Trends on the Boron-Doped Diamond Electrode: From Fundamental Studies to Applications

Guest Editors: Giancarlo Richard Salazar Banda, Yasuaki Einaga,
and Carlos Alberto Martinez-Huitle





**New Trends on the Boron-Doped Diamond
Electrode: From Fundamental Studies to
Applications**

International Journal of Electrochemistry

**New Trends on the Boron-Doped Diamond
Electrode: From Fundamental Studies to
Applications**

Guest Editors: Giancarlo Richard Salazar Banda, Yasuaki Einaga,
and Carlos Alberto Martinez-Huitle



Copyright © 2012 Hindawi Publishing Corporation. All rights reserved.

This is a special issue published in volume 2012 of “International Journal of Electrochemistry.” All articles are open access articles distributed under the Creative Commons Attribution License, which permits unrestricted use, distribution, and reproduction in any medium, provided the original work is properly cited.

Editorial Board

Maria Carmen Arévalo, Spain
Shen-Ming Chen, Taiwan
Abel César Chialvo, Argentina
Jean-Paul Chopart, France
A. Rodrigues de Andrade, Brazil
Sergio Ferro, Italy
Gerd-Uwe Flechsig, Germany
Rubin Gulaboski, Germany
Shengshui Hu, China
Mehran Javanbakht, Iran
Jiye Jin, Japan

Emilia Kirowa-Eisner, Israel
Boniface Kokoh, France
Emmanuel Maisonhaute, France
Grzegorz Milczarek, Poland
Valentin Mirceski, Macedonia
Mohamed Mohamedi, Canada
Angela Molina, Spain
Davood Nematollahi, Iran
K. I. Ozoemena, South Africa
María Isabel Pividori, Spain
Miloslav Pravda, Ireland

Manfred Rudolph, Germany
Benjamín R. Scharifker, Venezuela
Auro Atsushi Tanaka, Brazil
Germano Tremiliosi-Filho, Brazil
Hamilton Varela, Brazil
Jay D. Wadhawan, UK
Jose H. Zagal, Chile
Sheng S. Zhang, USA
Jiujun Zhang, Canada
Xueji Zhang, USA

Contents

New Trends on the Boron-Doped Diamond Electrode: From Fundamental Studies to Applications, Giancarlo Richard Salazar Banda, Yasuaki Einaga, and Carlos Alberto Martinez-Huitle
Volume 2012, Article ID 548504, 2 pages

Investigation of a Cu/Pd Bimetallic System Electrodeposited on Boron-Doped Diamond Films for Application in Electrocatalytic Reduction of Nitrate, Jorge T. Matsushima, Valéria C. Fernandes, Andrea B. Couto, Maurício R. Baldan, and Neidenêi G. Ferreira
Volume 2012, Article ID 213420, 10 pages

Sensitive Electrochemical Detection of Glucose at Glucose Oxidase-Cobalt Phthalocyanine-Modified Boron-Doped Diamond Electrode, Takeshi Kondo, Masaru Horitani, and Makoto Yuasa
Volume 2012, Article ID 943957, 6 pages

Controllable Electrochemical Activities by Oxidative Treatment toward Inner-Sphere Redox Systems at N-Doped Hydrogenated Amorphous Carbon Films, Yoriko Tanaka, Hiroshi Naragino, Kohsuke Yoshinaga, Akira Nakahara, Takeshi Kondo, Akira Fujishima, and Kensuke Honda
Volume 2012, Article ID 369130, 14 pages

Electrocatalytic Properties of BDD Anodes: Its Loosely Adsorbed Hydroxyl Radicals, Nicolaos Vatisas
Volume 2012, Article ID 507516, 7 pages

Benzene Oxidation on Boron-Doped Diamond Electrode: Electrochemical-Impedance Study of Adsorption Effects, Yuri Pleskov, Marina Krotova, Valerii Elkin, Valentin Varnin, and Irina Teremetskaya
Volume 2012, Article ID 437063, 9 pages

Nanodiamond Films for Applications in Electrochemical Systems, A. F. Azevedo, M. R. Baldan, and N. G. Ferreira
Volume 2012, Article ID 508453, 16 pages

The Use of Diamond for Energy Conversion System Applications: A Review, K. I. B. Eguiluz, J. M. Peralta-Hernández, A. Hernández-Ramírez, J. L. Guzmán-Mar, L. Hinojosa-Reyes, C. A. Martínez-Huitle, and G. R. Salazar-Banda
Volume 2012, Article ID 675124, 20 pages

Automated Online Solid-Phase Extraction Coupled with Sequential Injection-HPLC-EC System for the Determination of Sulfonamides in Shrimp, Pimkwan Chantarateepa, Weena Siangproh, Shoji Motomizu, and Orawon Chaillapakul
Volume 2012, Article ID 862823, 9 pages

A Brief Review on Environmental Application of Boron Doped Diamond Electrodes as a New Way for Electrochemical Incineration of Synthetic Dyes, J. M. Peralta-Hernández, M. Méndez-Tovar, R. Guerra-Sánchez, C. A. Martínez-Huitle, and J. L. Nava
Volume 2012, Article ID 154316, 18 pages



Anodic Stripping Voltammetry of Se^{4+} on Gold-Modified Boron-Doped Diamond Electrodes,

Stéphane Fierro, Takeshi Watanabe, Kazumi Akai, Mikito Yamanuki, and Yasuaki Einaga

Volume 2012, Article ID 758708, 5 pages

A Brief Review on the *In Situ* Synthesis of Boron-Doped Diamond Thin Films, Vadali V. S. Srikanth,

P. Sampath Kumar, and Vijay Bhooshan Kumar

Volume 2012, Article ID 218393, 7 pages

Electrochemical Biosensor Based on Boron-Doped Diamond Electrodes with Modified Surfaces,

Yuan Yu, Yanli Zhou, Liangzhuan Wu, and Jinfang Zhi

Volume 2012, Article ID 567171, 10 pages

Editorial

New Trends on the Boron-Doped Diamond Electrode: From Fundamental Studies to Applications

Giancarlo Richard Salazar Banda,¹ Yasuaki Einaga,²
and Carlos Alberto Martinez-Huitle³

¹*Instituto de Tecnologia e Pesquisa/Programa de Pós-Graduação em Engenharia de Processos, Universidade Tiradentes, 49032-490, Aracaju, SE, Brazil*

²*Department of Chemistry, Faculty of Science and Technology, Keio University, 3-14-1 Hiyoshi, Yokohama 223-8522, Japan*

³*Universidade Federal do Rio Grande do Norte, Centro de Ciências Exatas e da Terra. Departamento de Química, 59078-970 Natal, RN, Brazil*

Correspondence should be addressed to Giancarlo Richard Salazar Banda, gianrsb@gmail.com

Received 29 September 2011; Accepted 29 September 2011

Copyright © 2012 Giancarlo Richard Salazar Banda et al. This is an open access article distributed under the Creative Commons Attribution License, which permits unrestricted use, distribution, and reproduction in any medium, provided the original work is properly cited.

Boron-doped diamond (BDD) is presently the subject of considerable interest as an electrode material. This is a consequence of its very wide potential window in aqueous solution (*ca.* ~ 3 V), low background currents, resistance to thermal shock, extreme electrochemical stability, and corrosion stability in aggressive media. Diamond electrodes have indeed the largest potential window so far measured in aqueous electrolytes. This makes them also totally different to common electrode materials such as gold, platinum, or mixed metal oxide DSA-type electrodes.

Because of their unique electrochemical properties, doped diamond electrodes can be used for a plethora of applications. Since their properties largely differ from those of conventional electrode materials, in most cases, they will not replace these materials but will make electrochemical processes that were impossible before possible. Because of their wide range of applications, studies to contribute to the advance of the fundamental knowledge of this material are strongly important for their further technological application.

The electrochemistry of diamond has developed rapidly in recent years and is growing with the development of many practical applications of diamond electrodes, which impact almost every aspect of electrochemistry, from electroanalysis to industrial applications.

Several analytes can be oxidized or reduced by conducting diamond compared to other carbon-based materials

before the breakdown of water in aqueous electrolytes. This is important for detecting and/or identifying species in solution since oxygen and hydrogen evolution do not interfere with the analysis. Thus, conductive diamond electrodes take electrochemical detection into new areas and extend their usefulness to analytes which are not feasible with conventional electrode materials.

This special issue initially contains four papers concerning the use of BDD electrode surfaces in the electrochemical detection of analytes using different techniques. Initially, bare BDD surfaces were used for the separation and determination of sulfonamides using a fully automated online solid phase extraction coupled with sequential injection analysis and high-performance liquid chromatography. The use of modified BDD surfaces with Cu/Pd or Au for the detection of nitrate or Se⁴⁺, respectively, is also reported, as well as the use of glucose-oxidase-cobalt phthalocyanine-modified BDD electrode, without any additional electron mediator in the electrolyte solution, for the electrochemical detection of glucose.

The use of BDD surfaces for the electrochemical oxidation or combustion of pollutants from water is summarized and discussed in three papers. The first of these is a review article on the environmental application of BDD electrodes for electrochemical incineration of azo dyes in synthetic and real wastewaters. The other two papers deal with experimental results on the benzene oxidation in 0.5 M K₂SO₄ aqueous

solution studied by cyclic voltammetry and electrochemical impedance spectroscopy and with the study of the BDD capacity to generate hydroxyl radicals that are not consumed in the adsorption layer and are available to oxidize other organic or inorganic species.

Four other review articles related to (i) the several important advances in the synthesis of boron-doped diamond thin films, especially those synthesized via gas-phase manipulation, (ii) the uses of BDD for energy conversion systems like fuel cells and rechargeable batteries, (iii) the current development status of nanocrystalline diamond electrodes for electrochemical applications, and (iv) recent advances in the use of BDD electrodes with different surfaces including nanostructured surface and chemically modified surface for the construction of various electrochemical biosensors are also reviewed in this special issue. Thus, several subjects from the synthesis to the application of BDD materials in electroanalysis, wastewater treatment, oxidants production, energy conversion systems, and nanodiamond electrochemistry are covered in the special issue.

In addition the synthesis of N-doped hydrogenated amorphous carbon (DLC) thin films, oxygen plasma treated, with high electrochemical reactivity and stability is reported in one paper. The N-doped DLC thin films exhibited a wide working potential range over 3 V, low double-layer capacitance, and reversible electron transfer kinetics for inorganic redox analytes, $[\text{Fe}(\text{CN})_6]^{3-/4-}$, $\text{Ru}(\text{NH}_3)_6^{2+/3+}$, and $\text{Fe}^{2+/3+}$, which were on the same level as those of BDD.

Finally, we thank the authors for their contributions to this special issue and also commend the reviewers for their constructive and timely reviews. It is our hope that this issue will stimulate new ideas and expand further the growing area of BDD electrochemistry, for the benefit of electrochemists, engineers, and the broader scientific community.

Giancarlo Richard Salazar Banda

Yasuaki Einaga

Carlos Alberto Martinez-Huitle

Research Article

Investigation of a Cu/Pd Bimetallic System Electrodeposited on Boron-Doped Diamond Films for Application in Electrocatalytic Reduction of Nitrate

Jorge T. Matsushima,¹ Valéria C. Fernandes,² Andrea B. Couto,¹
Maurício R. Baldan,¹ and Neidenêi G. Ferreira¹

¹Laboratório Associado de Sensores e Materiais (LAS), Instituto Nacional de Pesquisas Espaciais—INPE, 12.245-970
São José dos Campos, SP, Brazil

²Instituto de Pesquisa Energéticas e Nucleares—IPEN, Centro de Células a Combustível e Hidrogênio (CCCH), 05508-000
São Paulo, SP, Brazil

Correspondence should be addressed to Jorge T. Matsushima, jtmatsushima@yahoo.com.br

Received 31 March 2011; Revised 7 June 2011; Accepted 5 July 2011

Academic Editor: Giancarlo R. Salazar-Banda

Copyright © 2012 Jorge T. Matsushima et al. This is an open access article distributed under the Creative Commons Attribution License, which permits unrestricted use, distribution, and reproduction in any medium, provided the original work is properly cited.

The Cu/Pd bimetallic system electrodeposited on boron-doped diamond (BDD) films for application, as electrode material in the electrochemical reduction of nitrate was studied. The electrochemical behavior of Cu, Pd, and Cu/Pd bimetallic system was evaluated by cyclic voltammetry. From these results, the formation of the Cu/Pd composite was verified. In addition, Cu with different phases and a Cu/Pd phase in the composite were obtained. Morphological analysis by scanning electron microscopy (SEM) revealed a homogeneous distribution of Cu/Pd bimetallic particles with intermediary dimensions compared to those observed in Cu or Pd electrodeposits separately. These composites were tested as electrocatalysts for nitrate reduction in Britton-Robinson buffer solution (pH 9). Electrochemical measurements showed that composites with higher Cu content displayed the best electrocatalytic activity for nitrate reduction, and the Cu/Pd phase in the bimetallic system served to improve the Cu adherence on BDD electrode.

1. Introduction

The contamination of ground and surface waters by nitrate ions has been considered a common environmental problem, especially because of the large use of nitrogen-based compounds in agriculture and industrial wastes. The necessary control and removal of nitrate ions has stimulated intensive research, because nitrate causes detrimental effects not only on human health but also on aquatic ecosystems [1, 2]. The methods which are often used for the reduction of nitrate are biological denitrification and ion exchange. However, these methods have some drawbacks such as continuous monitoring, slow kinetics, and the generation of byproduct. On the other hand, electrochemical methods have received a great deal of attention because of their advantages such as the use of clean reagents (electrons) and their low cost.

The majority of papers which deal with the electrochemical reduction of nitrate demonstrate the reaction efficiency of the single metal electrode [3–6], while some papers show the viability of the boron-doped diamond (BDD) films as an electrode material, for the electrochemical reduction of nitrate [7–10]. Particularly, BDD films are excellent electrode materials for this purpose, because of their singular physicochemical properties such as low background currents, wide potential window which analyzes the chemical species without involving water decomposition reaction, high corrosion resistance, and mechanical stability [11, 12]. In spite of the thermodynamic feasibility of the nitrate reduction, the charge transfer kinetics on BDD electrode is slow and direct reduction of nitrate has been characterized by poor sensitivity and selectivity of these electrodes. In this sense, the surface modification with a

specific electrocatalysts has been an important strategy to improve their electrocatalytic properties. In general, binary metal electrodes in the form of alloys [13, 14], codeposited films [15], or electrodes modified with foreign adatoms on their surface [16–21] have been some of the strategies used to enhance the electrode properties concerning to the electrochemical reduction of nitrate.

It is important to emphasize that BDD electrodes, due to the inert nature of their surface, are a natural substrate to make the surface modification without any major interference. Moreover, their mechanical and chemical stability permit the surface modification in the extreme conditions of preparation (e.g., high temperature) without any significant modification of the surface properties. The surface modification of BDD electrodes with Au [22–24] and Pt [25–27] nanoparticles were carried out, and interesting results were obtained. Such modifications increased the electrocatalytic activity for oxygen reduction and methanol oxidation. Recent studies also showed that the surface modification of the BDD electrodes with Cu nanoparticles obtained by simple electrochemical deposition was used to detect nitrate electrochemically using an *in situ* method [28, 29]. Besides, Cu exhibits the best electrocatalytic activity for electrochemical reduction of nitrate when compared to other materials like Ni, graphite, and Pt [30]. However, the modified BDD electrode is limited by the poor surface adherence, by the formation of toxic subproducts (nitrite and ammonia), and by the cumulative passivation effect. Up to now, bimetallic Cu/Pd electrocatalyst is considered one of the most promising materials with maximum selectivity for N_2 of 60%–70%, which is justified by its bifunctional character, in which nitrate is reduced on Cu sites into NO_2^-/NO , and subsequently reduced into N_2 on Pd sites [31, 32]. Moreover, the Cu poor adherence, previously mentioned, could also be improved when prepared in the alloy form or composite. In order to obtain such conditions, the choice of preparation method is of fundamental importance. Among the several methods used for production of alloys and composites, the electrodeposition is an interesting method due to their simplicity, their compatibility of the processing at room temperature, and their controllability of thin film properties.

To the best of our knowledge, the production of Cu/Pd bimetallic system on BDD electrodes by electrodeposition has not been studied. Nevertheless, some papers present the advantages of a Cu/Pd system electrodeposited as alloys or composite [31–35]. Vinogradov et al. succeeded in the deposition Cu/Pd alloys coating with good physicochemical properties [33]. Recently, Milhano and Pletcher produced Cu/Pd alloys coating Pt by coelectrodeposition [34]. Cu/Pd composites (without reaction between Cu and Pd) were also prepared by electrodeposition [31, 32]. Thus, this work associates the singular properties of BDD films, as electrode material, with the best conditions for the production of the Cu/Pd bimetallic system on BDD electrode. In addition, it is used as a possible composite material to be applied to the electrochemical reduction of nitrate.

2. Experimental

The BDD films were grown on silicon by hot filament-assisted vapor deposition (HFCVD) technique. The filament temperature was kept constant at 780°C. The deposition was performed for 7 h, and a gaseous mixture of 99% vol. H_2 and 1% vol. CH_4 and a total pressure of 50 Torr were used. The boron doping was obtained from H_2 forced to pass through a bubbler containing B_2O_3 dissolved in methanol. From the Mott Schottky plot, the doping level was estimated to approximately 10^{20} boron atoms· cm^{-3} [36]. The morphology of the BDD films was analyzed by scanning electronic microscopy (SEM) using a Jeol equipment JSM-5310, while that the quality was evaluated by micro-Raman scattering spectroscopy (Renishaw microscope system 2000) in backscattering configuration at room temperature employing 514 nm argon-ion laser.

All electrolytic solutions were prepared using ultrapure water from a Millipore water purifier system and analytical grade reagents were used. Prior to the experiments, the electrolytic solutions were deaerated with N_2 gas during 10 min.

Electrochemical measurements were performed using Autolab PGSTAT 302 equipment with a three-electrode cell. The BDD films were used as working electrode. The geometric area in contact with the electrolyte was 0.27 cm^2 . A platinum coil wire served as a counter electrode and Ag/AgCl electrode was chosen as the reference electrode.

Electrochemical behavior of the Cu and Pd on BDD electrodes was studied by cyclic voltammetry from solutions containing 5 mM Cu(II) + 0.5 M $HClO_4$ and 1 mM Pd(II) + 0.5 M $HClO_4$. The solutions containing Cu(II) and Pd(II) were prepared using $CuSO_4$ and $PdCl_2$ salts, respectively. With respect to the Cu/Pd composite, electrochemical studies were also realized by cyclic voltammetry using solutions containing different Cu(II) concentrations (1, 5 and 10 mM $CuSO_4$), where in these solutions, 1 mM Pd(II) and 0.5 M $HClO_4$ were maintained constant. So, (1:1), (5:1), and (10:1) Cu(II):Pd(II) ratio were used. Prior each electrochemical measurement, a mixture (3:1) HCl/HNO_3 ratio was used to clean the BDD surface. After this, BDD films maintained the same physicochemical characteristics verified in the SEM and Raman analysis.

Cu/Pd-modified BDD electrodes were produced under constant potential. Morphological analysis of the Cu/Pd composite and their composition were examined by a scanning electron microscopy (Jeol equipment JSM-5310) incorporating an energy dispersive X-ray (EDX) unit with a software for elemental analysis. In order to evaluate the composition uniformity (Cu and Pd content), multiple EDX spectra were recorded at different points over the BDD surface. Electrochemical reduction of nitrate was investigated by linear sweep voltammetry (LSV) as a function of time and deposition potential and also the Cu(II):Pd(II) ratio used for electrodeposition of the Cu/Pd composite on BDD electrode. A Britton-Robinson (BR) buffer solution (pH 9.0) without and with 0.1 M KNO_3 were used in our studies.

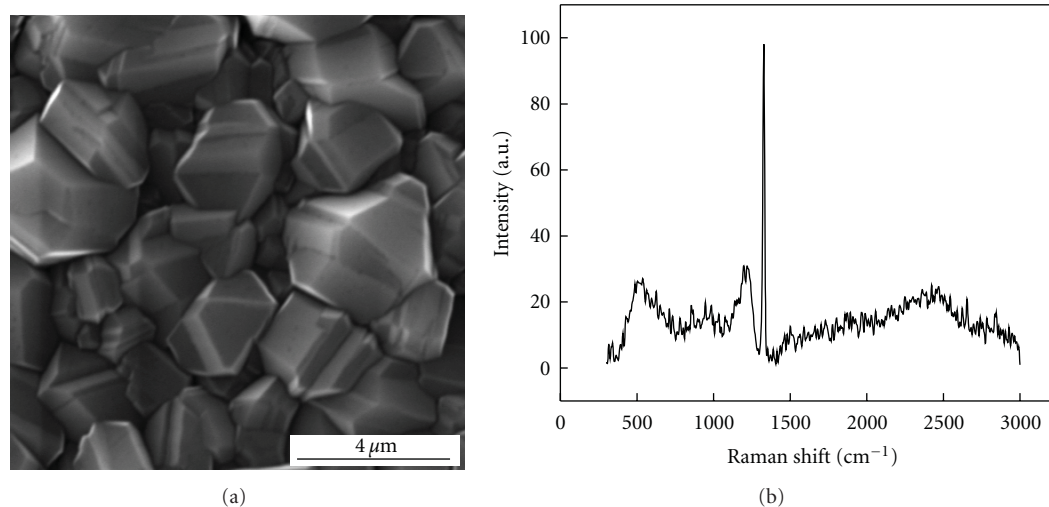


FIGURE 1: (a) SEM image and (b) Raman spectrum of the BDD film.

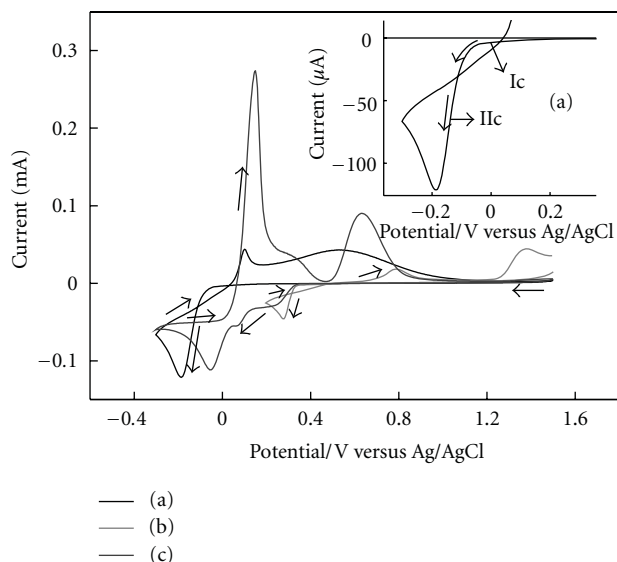


FIGURE 2: Cyclic voltammograms of the BDD electrode in solutions containing (a) 5 mM Cu(II), (b) 1 mM Pd(II), and (c) 5 mM Cu(II) + 1 mM Pd(II). All solutions containing 0.5 M HClO₄ as supporting electrolyte. Scan rate of 10 mVs⁻¹.

3. Results and Discussion

Morphological and structural characterization of BDD films was carried out prior to electrochemical experiments. Figure 1(a) shows the SEM image of the BDD film. The morphological aspect shows a film formed by symmetric and faceted grains with a uniform texture. The Raman spectra presented in Figure 1(b) confirms the quality of BDD films even after the chemical treatment with (3:1) (HCl:HNO₃) ratio. From the Raman spectroscopy is observed a peak at ~1320 cm⁻¹ that is characteristic of the diamond. This peak presented a shift to lower energies due to tensions caused by boron incorporation in the diamond films. In addition, the

spectrum presented two bands located at 500 cm⁻¹ and at 1230 cm⁻¹ that are associated to boron incorporation in the diamond films [37, 38].

In order to investigate the possible formation of a Cu/Pd alloy or composite on the BDD electrode, cyclic voltammetry measurements were carried out. Three different solutions were used in these experiments: one solution containing only Cu(II), the other one containing only Pd(II), and last one containing the mixture of the two metal ions. Figure 2 illustrates the cyclic voltammograms of the BDD electrode recorded at these three solutions. The curve (a) was studied in the solution containing only Cu(II), the curve (b) only Pd(II) and curve (c) a mixture of the two metal ions. The curve (a) represents the electrochemical behavior of the Cu in 5 mM Cu(II) + 0.5 M HClO₄ solution. The inset of the Figure 2(a) evidence the two regions of Cu cathodic current, labeled as (Ic) and (Iic). The first region (Ic) that begins at a more positive potential may be associated to underpotential deposition (UPD) (or intercalation) of Cu. The second region (Iic) is related to the region of bulk Cu deposition. According to Bouamrane et al., the occurrence of the UPD of Cu is related to the BDD surface condition, where it was verified to happen only in the crystalline defects, probably in the graphitic inclusions (sp² carbon sites) [39]. Besides, the UPD has been observed in other forms of carbon such as pyrolytic graphite, where it is believed to occur at sp² carbon sites which cannot be completely avoided [40]. The reverse sweep shows significant hysteresis that is consistent with the Cu deposition reaction involving nucleation as well as growth of the Cu layer. The Cu deposition continues to 0.0 V, and immediately after that, the Cu stripping is accompanied by two anodic current regions. A well-defined anodic peak at 0.05 V is associated to the maximum current of bulk Cu stripping followed by a large potential region, involving the anodic current due to the stripping of other deposited Cu phase. The overall charge balance, $Q_{\text{anodic}}/Q_{\text{cathodic}}$ ratio close to 1.0, shows that all deposited Cu was dissolved after the end of the reverse sweep. The

curve (b) represents the electrochemical behavior of the Pd in 1 mM Pd(II) + 0.5 M HClO₄ solution. The Pd deposition occurred at 0.35 V where a well-formed reduction wave was observed. The negative potential sweep was limited at 0.2 V, because from this potential, high current is observed due to hydrogen absorption into the Pd surface/lattice. Again, the reverse sweep shows substantial hysteresis with deposition continuing to 0.47 V. In this case, the $Q_{\text{anodic}}/Q_{\text{cathodic}}$ ratio was 0.47, indicating an incomplete redissolution of the Pd. The Q_{anodic} fraction indicates the residual Pd on the BDD surface, where an anodic process with a current maximum at 1.4 V is associated to the formation of the palladium oxide. The curve (c) represents the cyclic voltammogram of the Cu/Pd system obtained in 5 mM Cu(II) + 1 mM Pd(II) + 0.5 M HClO₄ solution. The deposition of the Cu/Pd system occurred in the same region of Pd deposition. The deposition process is characterized by three cathodic waves with the current maximum localized at 0.23 V, 0.07 V, and -0.05 V. This behavior may be associated with the electrodeposition of a Cu/Pd composite on BDD electrode. In this case, no alloy formation was verified (simultaneous coelectrodeposition). The more positive cathodic wave may be attributed to the reduction of Pd(II) to metallic Pd. This process was confirmed from the voltammetric study (not shown in this work). In this study, the potential sweep was reverted at -0.35 V near to the maximum current involved in the Pd deposition and revealed only the presence of the Pd deposition. As response, the resulting anodic process presented the same behavior of Pd dissolution as seen in the curve (b). The cathodic wave located at 0.07 V may be associated with the onset of the Cu deposition with different phases. One of phases may be attributed to the UPD of Cu, since it is observed at a potential region near to occurrence of the Cu UPD process, as it was discussed earlier during the electrochemical studies of Cu. On the other hand, the more negative cathodic wave at -0.05 V is confirmed to be the bulk Cu phase deposition. In spite of the more positive potential about 100 mV compared to bulk Cu deposition, the occurrence of this process is confirmed from the analysis of the reversing potential sweep, since the more positive anodic process, associated to the bulk Cu phase dissolution, begins at the same dissolution potential of the bulk Cu. Continuing the sweep to a more positive potential, an anodic current shoulder at 0.3 V is attributed to oxidation of a Cu phase followed by an anodic current wave at 0.63 V. The shifted potential to a more negative value and a high anodic charge compared to Pd dissolution process show the dissolution of a Cu/Pd phase initially electrodeposited during the negative potential sweep.

The investigation of the Cu/Pd composite on BDD electrode was carried out for three other solutions, where the Pd(II) concentration was maintained constant and Cu(II) concentration was varied. In this study, this condition was defined considering the best composition of Cu/Pd bimetallic system. As reported by Milhano and Pletcher [34], nitrate is not reduced at the Pd surface but occurs at the CuPd surface, so it is necessary to have greater Cu amount due to their high electrocatalytic activity for electrochemical reduction of nitrate. In this case, the choice of Pd for the

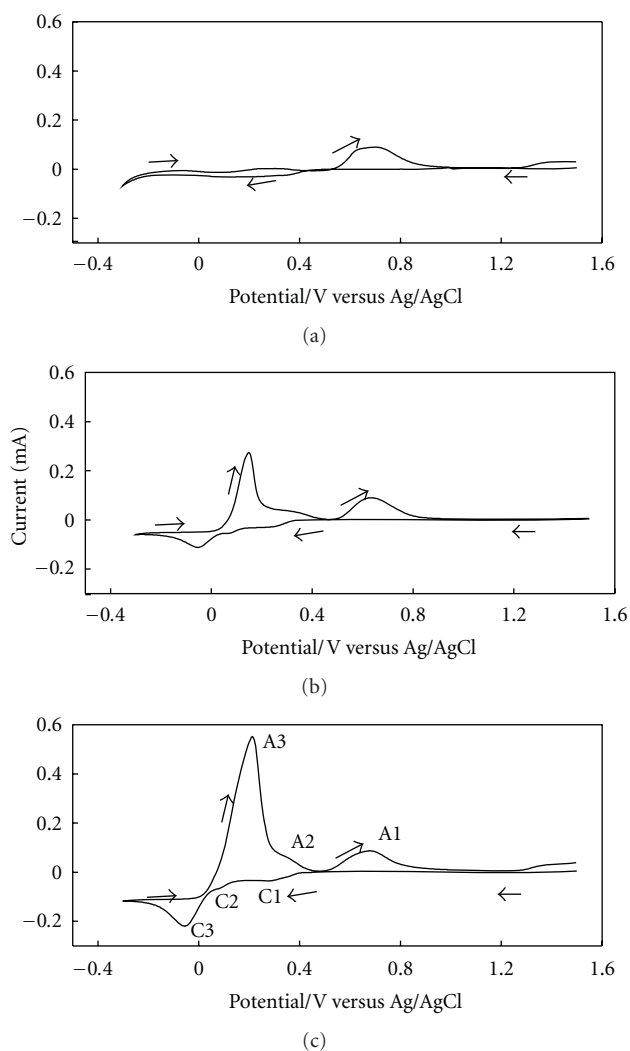


FIGURE 3: Cyclic voltammograms of BDD electrode in solutions with (a) (1 : 1), (b) (5 : 1), and (c) (10 : 1) Cu(II) : Pd(II) ratio. Scan rate of 10 mV s⁻¹.

production of a composite with Cu on BDD electrodes was made in an attempt to enhance the physical chemical properties of the Cu/Pd composite due to binding energy between Pd and Cu and also to provide active sites for obtaining nontoxic subproducts during the electrochemical reduction of nitrate.

Figure 3 presents the cyclic voltammograms of the Cu/Pd composite on BDD electrode in solutions with different Cu(II) : Pd(II) ratio. From voltammetric profiles is observed that the deposition of the Cu/Pd composite begins practically in the same potential region independently of the Cu(II) : Pd(II) ratio. In all the profiles presented, the occurrence of the two cathodic processes (C1 and C2) was observed. These processes are associated with the bulk Pd deposition and the Cu phase deposition, respectively. However, the C3 process was not evidenced for the (1 : 1) Cu(II) : Pd(II) ratio. Although an increase of the cathodic peak current intensity at -0.05 V was observed with the

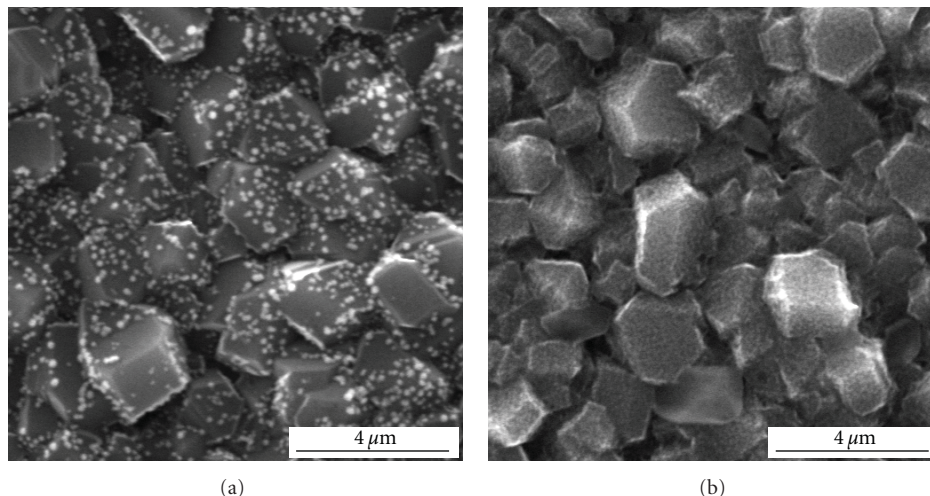


FIGURE 4: SEM images of (a) Cu and (b) Pd electrodeposited on BDD electrode. Both were deposited by 120 s, and -0.3 V and 0.2 V were applied to deposit Cu and Pd, respectively.

increase of the Cu(II):Pd(II) ratio in the solution. This result shows that increasing the Cu(II):Pd(II) ratio, thermodynamically, the simultaneous codeposition of Cu and Pd was not favored. Then, no alloying between Cu and Pd occurred. In this case, it may be only due to bulk Cu deposition with high Cu content in the Cu/Pd composite formed. In particular, hydrogen evolution reaction in the solution with (1 : 1) Cu(II) : Pd(II) ratio was observed, due to high density of catalytic Pd sites that favored the reaction. The anodic processes (A1, A2, and A3) were observed in solutions with (5 : 1) and (10 : 1) Cu(II) : Pd(II) ratio, and it may be associated to dissolution of Cu with different phases (A3 and A2 processes) and a Cu/Pd phase (A1 process) as reported earlier. The absence of A3 process in solution with (1 : 1) Cu(II) : Pd(II) ratio shows that the bulk Cu deposition did not occur. The highest anodic current intensity (A3 process) observed in solution with (10 : 1) Cu(II) : Pd(II) ratio indicates a more bulk Cu dissolution. In this process, the same current plateau commencing at 0.07 V represents a diffusion-controlled dissolution process. On the other hand, a current shoulder at -0.08 V (A2 process) and an anodic wave with current maximum at 0.63 V (A1 process) were observed in all Cu(II) : Pd(II) ratio. Independently of the Cu(II) : Pd(II) ratio, the anodic charge (~ 2.1 mC) corresponding to the A1 process presented the same value, indicating the dissolution of an identical Cu/Pd phase. The onset of the Cu/Pd phase dissolution at a more negative potential confirms the dissolution of a less noble phase compared to bulk Pd phase, as can be seen in Figure 1.

The electrochemical characterization of the Cu, Pd, and Cu/Pd composite on BDD electrode was accompanied by morphological and elemental composition analysis. Figure 4, shows the SEM images of the (a) Cu electrodeposited at -0.3 V for 120 s from a solution containing 5 mM Cu(II) + 0.5 M HClO₄ and (b) Pd electrodeposited at 0.2 V for 120 s from a 1 mM Pd(II) + 0.5 M HClO₄. The deposition

potential was defined from a region controlled by diffusion. In Figure 4(a), the SEM image reveals that Cu submicron (~ 100 nm) particles are uniformly distributed all over the BDD surface. In the case of the Pd, nanoparticles homogeneously distributed on BDD surface were produced, as shows the Figure 4(b). On the basis of these results, the morphology of the Cu/Pd composite on BDD electrodes became easier to be analyzed. The composites were produced at -0.3 V during 120 s from the solutions containing different Cu(II) : Pd(II) ratio. The SEM images are shown in Figure 5. As can be seen, all electrodeposited films were uniformly distributed on BDD electrodes. However, the size and distribution of the film particles are dependent of the solution composition. In Cu/Pd composite produced at (1 : 1) Cu(II) : Pd(II) ratio, the morphology of this particles presented intermediary dimensions compared to those of Cu and Pd electrodeposited separately. Probably, this coating refers to the deposition of a Cu/Pd phase (Figure 5(a)). This affirmation is consistent with the electrochemical results, since the bulk Cu deposition in this solution composition was not observed, as can be seen in Figure 3(a). By increasing the Cu(II) concentration, a coating of a bulk Cu phase (Figures 5(b) and 5(c)) at Cu/Pd composite was produced, since particles distribution over BDD electrode with similar dimensions to that of the Cu electrodeposit was verified. By analyzing the electrochemical behavior of the Cu/Pd composites produced at (5 : 1) and (10 : 1) Cu(II) : Pd(II) ratio, as discussed earlier in Figures 3(b) and 3(c), the morphological aspect involving particles of larger dimensions compared to Cu/Pd composite produced at (1 : 1) Cu(II) : Pd(II) ratio is associated to effect of bulk Cu deposition.

In order to obtain the Cu and Pd content in these composites, EDX analysis was carried out considering several local points ($1 \times 1 \mu\text{m}$) on BDD surface as function of the Cu(II)/Pd(II) ratio. Table 1 illustrates the elemental composition for each Cu/Pd composite. As expected, higher C content is associated with the diamond composition. On

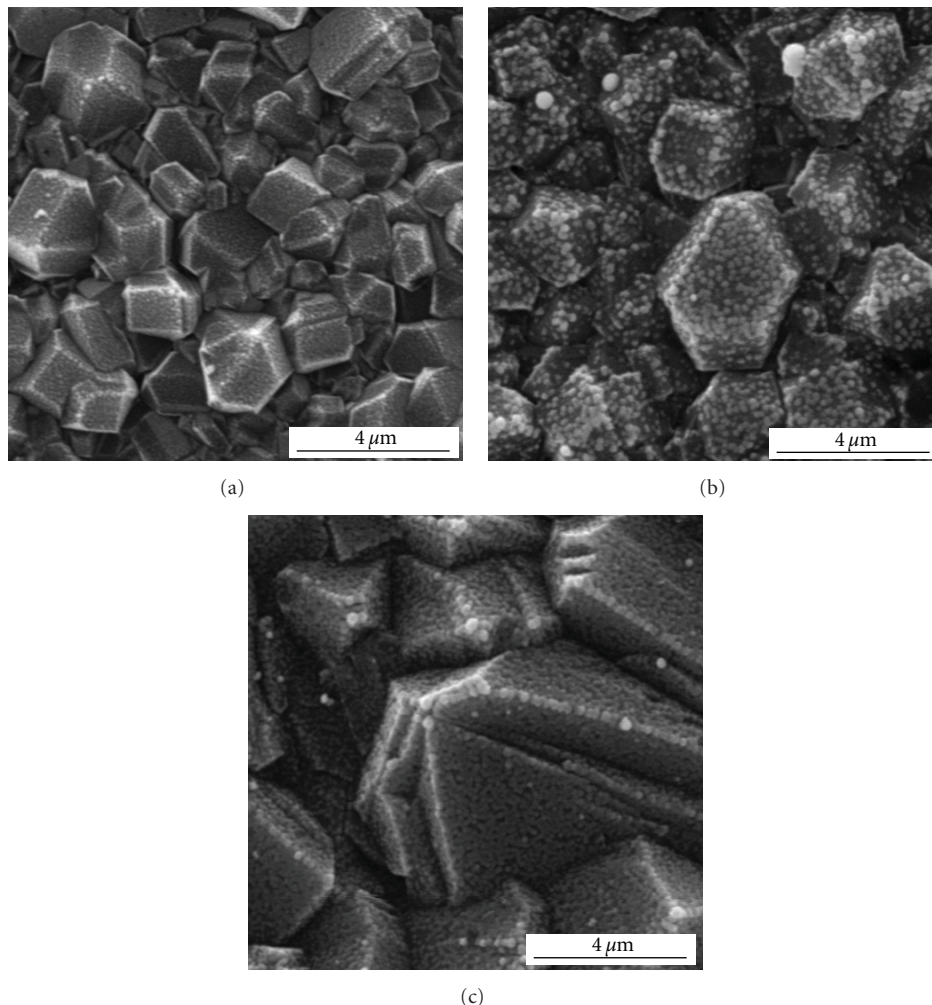


FIGURE 5: SEM images of the Cu/Pd composite electrodeposited on BDD electrode in solutions with different Cu(II) : Pd(II) ratio: (a) (1 : 1), (b) (5 : 1), and (c) 10 : 1. All were deposited applying -0.3 V by 120 s.

TABLE 1: Elemental composition (C, O, Cu, and Pd) determined by EDX analysis of the Cu/Pd composites electrodeposited on BDD electrode in solutions with different Cu(II) : Pd(II) ratio. All were deposited applying -0.3 V by 120 s.

Cu(II) : Pd(II) ratio	Composition/% at.			
	C	O	Cu	Pd
(1 : 1)	89.13	0.99	1.17	8.71
(5 : 1)	81.04	3.71	6.85	8.40
(10 : 1)	49.22	12.95	28.21	9.62

the other hand, the C content decreases, as function of the Cu(II) : Pd(II) ratio increase was verified. This result can be better visualized from the SEM image illustrated in Figure 5(c), where the BDD surface was completely covered by Cu/Pd coating. The increase of the O content in these composites may be associated to the copper oxide formation, since the O content was not found in the pure Pd electrodeposit. About 8.5% at. of Pd was found in all the Cu/Pd composites. As expected, an increase of the

atomic ratio between Cu and Pd as function of the Cu(II) concentration increase was verified.

After the electrochemical, morphological, and composition analyses, the Cu/Pd-modified BDD electrodes were used in the electrochemical reduction of nitrate. This investigation was carried out using $0.1\text{ M KNO}_3 + \text{BR}$ buffer solutions at extreme pH values (pH 1.9 and 9.0). In our initial experiments, the best condition for analyzing the nitrate response was obtained using BR buffer solution (pH 9). This condition was also achieved by other authors in their studies on Cu/Pd alloy modified by Pt and Ni electrodes [34, 35]. Figure 6(a) presents the LSV curves of the BDD electrode and Cu/Pd-modified BDD electrode in BR buffer solution pH 9. The BDD electrode shows no significant current ($3.9\text{ }\mu\text{A}$ at -1.3 V) for hydrogen evolution reaction. In contrast, the water reduction was verified to occur at more positive potentials on Cu/Pd modified BDD electrode, where a high current (0.94 mA , at -1.3 V) was involved. At -1.3 V , a current increase of 240 times confirms the high catalytic capacity of modified BDD electrode for water reduction.

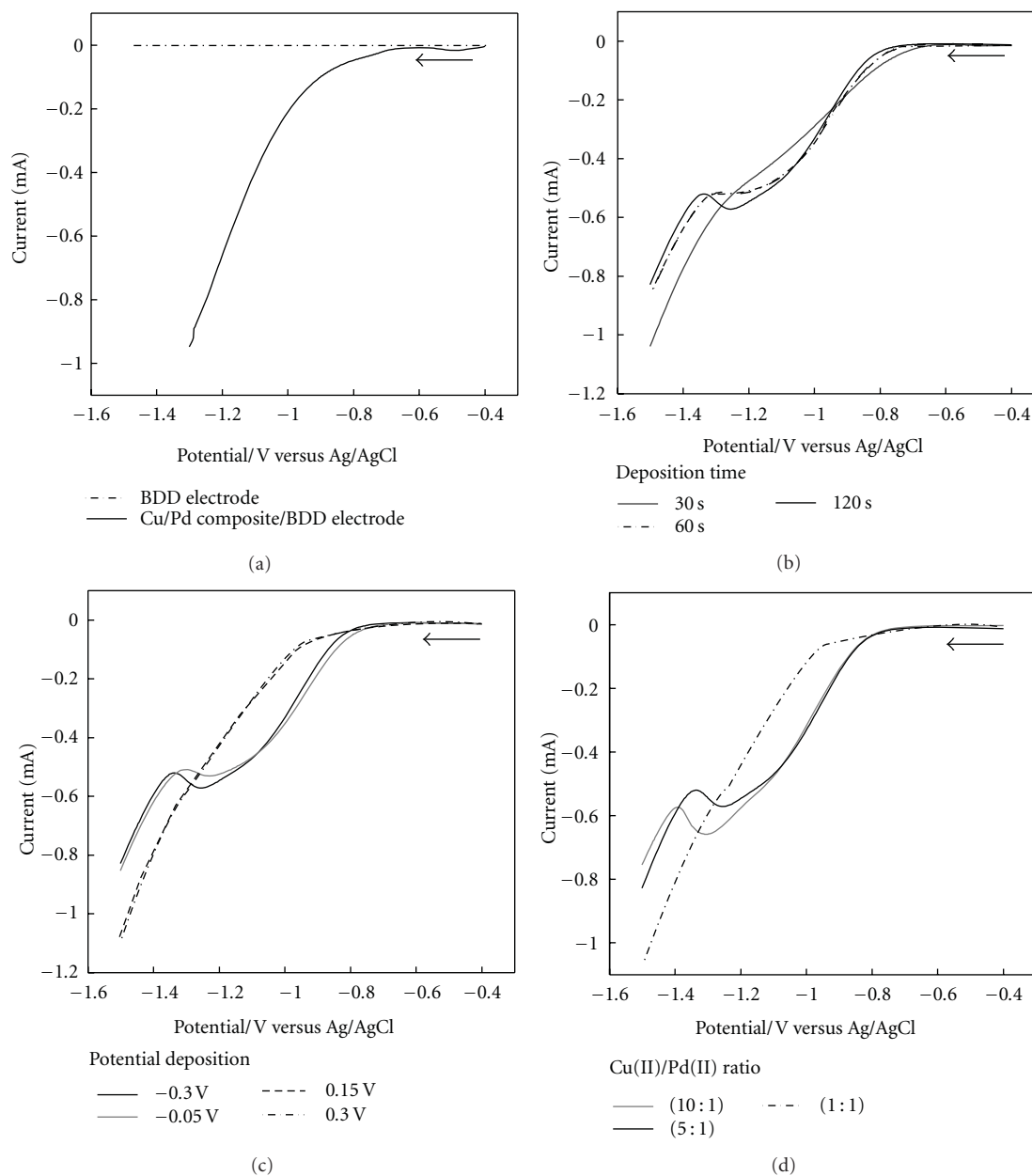


FIGURE 6: (a) LSV curves of the BDD and Cu/Pd-modified BDD electrodes in BR buffer solution (pH 9). Nitrate response of the Cu/Pd composite electrode deposited on BDD electrode at different (b) deposition time, (c) deposition potential, and (d) Cu(II):Pd(II) ratio. The nitrate response in (b) (c), and (d) was investigated in 0.1 M KNO_3 + BR buffer solution (pH 9). The Cu/Pd composite used in (a), (b), and (c) was electrodeposited using 5 mM Cu(II) + 1 mM Pd(II) + 0.5 M HClO_4 . Scan rate of 10 mV s^{-1} .

From these results, nitrate response on Cu/Pd modified BDD electrode was investigated using different electrodeposition conditions of the Cu/Pd composite such as deposition time (Figure 6(b)), deposition potential (Figure 6(c)), and Cu(II) concentration (Figure 6(d)). Such conditions were focused to obtain Cu/Pd composites with different ranges and then evaluate the nitrate reduction. The definition of scan onset from -0.4 V to -1.5 V was performed in the region where no reactions involving the Cu/Pd occur. Figure 6(b) shows the LSV curves from the Cu/Pd composite electrode deposited at different deposition time in 0.1 M KNO_3

+ BR buffer solution (pH 9). A peak current about -1.25 V is observed for the Cu/Pd composite electrode deposited by 120 s and may be attributed to nitrate reduction, which was not observed in the blank solution, as can be seen in Figure 6(a). Nitrate analysis was also carried out using Cu and Pd electrodeposits on BDD electrode for the same experimental conditions. The nitrate response on Cu-modified BDD electrode was not possible to analyze due to poor adherence of Cu, while the nitrate reduction on Pd electrodeposit was not observed due to more electrocatalytic efficiency with respect to hydrogen evolution reaction. The best nitrate

response was verified to depend on the deposition time of Cu/Pd composite, where the reduction peak current cannot be seen at short deposition time. It was also studied the nitrate response at long time of Cu/Pd composite deposition (not shown), but a negligible variation of the current peak intensity was verified. From these results, the existence of a limited time condition to produce a composite with well-defined characteristics to increase the sensitivity for the nitrate reduction is evident. A cathodic peak of nitrate reduction close to -1.25 V was also observed by Reyter et al. in their electrocatalytic tests realized in alkaline medium using Cu-Pd alloys produced on Ni electrode. In this study, maximum currents of nitrate reduction at different potentials were observed over a wide range of elemental composition [35]. Milhano and Pletcher studying Cu-Pd alloys electrodeposited on Pt microdisc electrode observed that nitrate reductions commencing close to -1.2 V in alkaline medium, but two nitrate reduction processes were noted [34].

In an attempt to enhance the efficiency of nitrate reduction, the Cu-Pd system electrodeposited at several deposition potentials, covering a wide range of elemental composition was investigated. The LSV curves are illustrated in Figure 6(c). In a potential region close to bulk Cu deposition (-0.05 V to -0.3 V), the nitrate reduction was observed. On the other hand, nitrate reduction wave at potential corresponding to the Cu/Pd phase formation ($+0.15$ V and $+0.30$ V, resp.) was not observed. Such behavior makes us believe that higher Cu content is necessary to improve the catalytic activity of nitrate reduction. In this case, the Cu/Pd phase coating may improve the adherence of Cu particles. However, electrocatalytic activity, with this coating to reduce nitrate, was not evidenced. The latter investigation involved the nitrate response using Cu/Pd-modified BDD electrode electrodeposited in solutions with different Cu(II) : Pd(II) ratio. The LSV curves are presented in Figure 6(d). From these results, it was possible to confirm all discussion previously made, where a higher cathodic current associated to nitrate reduction and commencing at the same potential was verified for the composite with higher Cu content. Besides, the peak potential shift of nitrate reduction to a more negative was verified at Cu/Pd composite electrodeposited in solution with (10 : 1) Cu(II) : Pd(II) ratio, showing a more required energy to reduce nitrate.

4. Conclusions

In this work, the electrochemical characterization in the solution containing only Cu(II) ions, Pd(II), ions and a mixture of the two metal ions performed by cyclic voltammetry was fundamental to evaluate the formation of a Cu/Pd bimetallic system on BDD electrode. From the voltammetric curves, Cu with different phases and a Cu/Pd phase were verified to be formed in Cu/Pd composite. The deposition of Cu different phases depended upon the Cu(II) : Pd(II) ratio, where the bulk Cu phase in solution with (1 : 1) Cu(II) : Pd(II) ratio was not observed. The formed Cu/Pd phase was characterized from the potential shift to more

negative values and an increase of anodic current to compare the A1 process (Cu/Pd stripping) and the bulk Pd stripping. From the morphological analysis it was possible to verify the different particles sizes deposited and also their composition. As expected, a higher Cu content was verified at the Cu/Pd composite electrodeposited in solution with highest Cu(II) concentration. On the other hand, the Cu and Pd content at Cu/Pd phase remained constant, independently of the (Cu(II) : Pd(II)) ratio used in solution. The Cu/Pd-modified BDD electrodes, tested as electrocatalysts for nitrate reduction, showed the best electrocatalytic activity for composites with higher Cu content, and formed Cu/Pd phase, was fundamental to improve the Cu adherence on BDD electrode.

Acknowledgments

The authors are so grateful to Brazilian Agencies CAPES (Process no. 02491/09-5), CNPq (processes 471356/2006- and 9305009/2006-0), and FAPESP (Processes nos. 05/51387-6, 07/00013-4, and 2009/10661-9) by the financial support. Special thanks to Maria Lucia Brison by SEM and EDX analyses.

References

- [1] K. H. Gelberg, L. Church, G. Casey et al., "Nitrate levels in drinking water in rural New York State," *Environmental Research*, vol. 80, no. 1, pp. 34–40, 1999.
- [2] H. Borchering, S. Leikefeld, C. Frey, S. Diekmann, and P. Steinrücke, "Enzymatic microtiter plate-based nitrate detection in environmental and medical analysis," *Analytical Biochemistry*, vol. 282, no. 1, pp. 1–9, 2000.
- [3] K. Bouzek, M. Paidar, A. Sadílková, and H. Bergmann, "Electrochemical reduction of nitrate in weakly alkaline solutions," *Journal of Applied Electrochemistry*, vol. 31, no. 11, pp. 1185–1193, 2001.
- [4] G. E. Dima, A. C. A. De Vooy, and M. T. M. Koper, "Electrocatalytic reduction of nitrate at low concentration on coinage and transition-metal electrodes in acid solutions," *Journal of Electroanalytical Chemistry*, vol. 554–555, no. 1, pp. 15–23, 2003.
- [5] H. L. Li, J. Q. Chambers, and D. T. Hobbs, "Electroreduction of nitrate ions in concentrated sodium hydroxide solutions at lead, zinc, nickel and phthalocyanine-modified electrodes," *Journal of Applied Electrochemistry*, vol. 18, no. 3, pp. 454–458, 1988.
- [6] M. C. P. M. Da Cunha, M. Weber, and F. C. Nart, "On the adsorption and reduction of NO_3^- ions at Au and Pt electrodes studied by in situ FTIR spectroscopy," *Journal of Electroanalytical Chemistry*, vol. 414, no. 2, pp. 163–170, 1996.
- [7] C. Lévy-Clément, N. A. Ndao, A. Katty et al., "Boron doped diamond electrodes for nitrate elimination in concentrated wastewater," *Diamond and Related Materials*, vol. 12, no. 3–7, pp. 606–612, 2003.
- [8] F. Bouamrane, A. Tadjeddine, J. E. Butler, R. Tenne, and C. Lévy-Clément, "Electrochemical study of diamond thin films in neutral and basic solutions of nitrate," *Journal of Electroanalytical Chemistry*, vol. 405, no. 1–2, pp. 95–99, 1996.
- [9] C. Reuben, E. Galun, H. Cohen et al., "Efficient reduction of nitrite and nitrate to ammonia using thin-film B-doped

- diamond electrodes,” *Journal of Electroanalytical Chemistry*, vol. 396, no. 1-2, pp. 233–239, 1995.
- [10] R. Tenne, K. Patel, K. Hashimoto, and A. Fujishima, “Efficient electrochemical reduction of nitrate to ammonia using conductive diamond film electrodes,” *Journal of Electroanalytical Chemistry*, vol. 347, no. 1-2, pp. 409–415, 1993.
- [11] M. C. Granger, M. Witek, J. Xu et al., “Standard electrochemical behavior of high-quality, boron-doped polycrystalline diamond thin-film electrodes,” *Analytical Chemistry*, vol. 72, no. 16, pp. 3793–3804, 2000.
- [12] J. A. Bennett, J. Wang, Y. Show, and G. M. Swain, “Effect of sp²-bonded nondiamond carbon impurity on the response of boron-doped polycrystalline diamond thin-film electrodes,” *Journal of the Electrochemical Society*, vol. 151, no. 9, pp. E306–E313, 2004.
- [13] M. C. P. M. da Cunha, J. P. I. De Souza, and F. C. Nart, “Reaction pathways for reduction of nitrate ions on platinum, rhodium, and platinum-rhodium alloy electrodes,” *Langmuir*, vol. 16, no. 2, pp. 771–777, 2000.
- [14] C. Lu, S. Lu, W. Qiu, and Q. Liu, “Electroreduction of nitrate to ammonia in alkaline solutions using hydrogen storage alloy cathodes,” *Electrochimica Acta*, vol. 44, no. 13, pp. 2193–2197, 1999.
- [15] J. F. E. Gootzen, L. Lefferts, and J. A. R. Van Veen, “Electrocatalytic nitrate reduction on palladium based catalysts activated with germanium,” *Applied Catalysis A: General*, vol. 188, no. 1-2, pp. 127–136, 1999.
- [16] J. F. E. Gootzen, P. G. J. M. Peeters, J. M. B. Dukers, L. Lefferts, W. Visscher, and J. A. R. Van Veen, “The electrocatalytic reduction of NO₃ on Pt, Pd and Pt + Pd electrodes activated with Ge,” *Journal of Electroanalytical Chemistry*, vol. 434, no. 1-2, pp. 171–183, 1997.
- [17] F. J. G. de Dios, R. Gómez, and J. M. Feliu, “Preparation and electrocatalytic activity of Rh adlayers on Pt(1 0 0) electrodes: reduction of nitrous oxide,” *Electrochemistry Communications*, vol. 3, no. 11, pp. 659–664, 2001.
- [18] O. A. Petrii and T. Y. Safonova, “Electroreduction of nitrate and nitrite anions on platinum metals: A model process for elucidating the nature of the passivation by hydrogen adsorption,” *Journal of Electroanalytical Chemistry*, vol. 331, no. 1-2, pp. 897–912, 1992.
- [19] T. Y. Safonova and O. A. Petrii, “Effect of inorganic cations on the electroreduction of nitrate anions on Pt—Pt electrodes in sulfuric acid solutions,” *Journal of Electroanalytical Chemistry*, vol. 448, no. 2, pp. 211–216, 1998.
- [20] K. Shimazu, T. Kawaguchi, and K. Tada, “Preparation of binary metal electrocatalysts by self-assembly of precursor ionic species on gold and reduction of nitrate ions,” *Journal of Electroanalytical Chemistry*, vol. 529, no. 1, pp. 20–27, 2002.
- [21] K. Shimazu, R. Goto, and K. Tada, “Electrochemical reduction of nitrate ions on tin-modified platinum and palladium electrodes,” *Chemistry Letters*, no. 2, pp. 204–205, 2002.
- [22] B. E. Roustom, G. Fóti, and C. Comninellis, “Preparation of gold nanoparticles by heat treatment of sputter deposited gold on boron-doped diamond film electrode,” *Electrochemistry Communications*, vol. 7, no. 4, pp. 398–405, 2005.
- [23] Y. Zhang, S. Asahina, S. Yoshihara, and T. Shirakashi, “Oxygen reduction on Au nanoparticle deposited boron-doped diamond films,” *Electrochimica Acta*, vol. 48, no. 6, pp. 741–747, 2003.
- [24] Y. Zhang, V. Suryanarayanan, I. Nakazawa, S. Yoshihara, and T. Shirakashi, “Electrochemical behavior of Au nanoparticle deposited on as-grown and O-terminated diamond electrodes for oxygen reduction in alkaline solution,” *Electrochimica Acta*, vol. 49, no. 28, pp. 5235–5240, 2004.
- [25] F. Montilla, E. Morallón, I. Duo, C. Comninellis, and J. L. Vázquez, “Platinum particles deposited on synthetic boron-doped diamond surfaces. Application to methanol oxidation,” *Electrochimica Acta*, vol. 48, no. 25-26, pp. 3891–3897, 2003.
- [26] G. Siné and C. Comninellis, “Nafion-assisted deposition of microemulsion-synthesized platinum nanoparticles on BDD: activation by electrogenerated OH radicals,” *Electrochimica Acta*, vol. 50, no. 11, pp. 2249–2254, 2005.
- [27] K. Tsujimoto, S. Mitani, T. Teraji, and T. Ito, “Fabrication of nano-sized platinum particles self-assembled on and in CVD diamond films,” *Applied Surface Science*, vol. 237, no. 1–4, pp. 488–493, 2004.
- [28] C. M. Welch, M. E. Hyde, C. E. Banks, and R. G. Compton, “The detection of nitrate using in-situ copper nanoparticle deposition at a boron doped diamond electrode,” *Analytical Sciences*, vol. 21, no. 12, pp. 1421–1430, 2005.
- [29] S. Ward-Jones, C. E. Banks, A. O. Simm, L. Jiang, and R. G. Compton, “An in situ copper plated boron-doped diamond microelectrode array for the sensitive electrochemical detection of nitrate,” *Electroanalysis*, vol. 17, no. 20, pp. 1806–1815, 2005.
- [30] K. Bouzek, M. Paidar, A. Sadílková, and H. Bergmann, “Electrochemical reduction of nitrate in weakly alkaline solutions,” *Journal of Applied Electrochemistry*, vol. 31, no. 11, pp. 1185–1193, 2001.
- [31] A. C. A. de Vooy, R. A. van Santen, and J. A. R. Van Veen, “Electrocatalytic reduction of NO₃ on palladium/copper electrodes,” *Journal of Molecular Catalysis A*, vol. 154, no. 1-2, pp. 203–215, 2000.
- [32] O. Ghodbane, M. Sarrazin, L. Roué, and D. Bélanger, “Electrochemical reduction of nitrate on pyrolytic graphite-supported Cu and Pd-Cu electrocatalysts,” *Journal of the Electrochemical Society*, vol. 155, no. 6, pp. F117–F123, 2008.
- [33] S. N. Vinogradov, G. N. Mal'tseva, and N. A. Gulyaeva, “Electrodeposition of a palladium-copper alloy in non-steady-state electrolysis,” *Russian Journal of Electrochemistry*, vol. 37, no. 7, pp. 715–717, 2001.
- [34] C. Milhano and D. Pletcher, “The electrodeposition and electrocatalytic properties of copper-palladium alloys,” *Journal of Electroanalytical Chemistry*, vol. 614, no. 1-2, pp. 24–30, 2008.
- [35] D. Reyter, D. Bélanger, and L. Roué, “Elaboration of Cu-Pd films by coelectrodeposition: application to nitrate electroreduction,” *Journal of Physical Chemistry C*, vol. 113, no. 1, pp. 290–297, 2009.
- [36] N. G. Ferreira, L. L. G. Silva, E. J. Corat, V. J. Trava-Airoldi, and K. Iha, “Electrochemical characterization on semiconductors p-type CVD diamond electrodes,” *Brazilian Journal of Physics*, vol. 29, no. 4, pp. 760–763, 1999.
- [37] P. W. May, W. J. Ludlow, M. Hannaway, P. J. Heard, J. A. Smith, and K. N. Rosser, “Raman and conductivity studies of boron-doped microcrystalline diamond, faceted nanocrystalline diamond and cauliflower diamond films,” *Diamond and Related Materials*, vol. 15, no. 2, pp. 105–117, 2008.
- [38] R. J. Zhang, S. T. Lee, and Y. W. Lam, “Characterization of heavily boron-doped diamond films,” *Diamond and Related Materials*, vol. 5, no. 11, pp. 1288–1294, 1996.
- [39] F. Bouamrane, A. Tadjeddine, R. Tenne, J. E. Butler, R. Kalish, and C. Lévy-Clément, “Underpotential deposition of Cu on boron-doped diamond thin films,” *Journal of Physical Chemistry B*, vol. 102, no. 1, pp. 134–140, 1998.

- [40] B. H. Vassos and H. B. Mark, "The anodic dissolution of thin films of copper metal from pyrolytic graphite: a study of the multiple dissolution current peaks," *Journal of Electroanalytical Chemistry*, vol. 13, no. 1-2, pp. 1-9, 1967.

Research Article

Sensitive Electrochemical Detection of Glucose at Glucose Oxidase-Cobalt Phthalocyanine-Modified Boron-Doped Diamond Electrode

Takeshi Kondo,^{1,2} Masaru Horitani,¹ and Makoto Yuasa^{1,2}

¹ Department of Pure and Applied Chemistry, Faculty of Science and Technology, Tokyo University of Science, 2641 Yamazaki, Noda 278-8510, Japan

² Reaserach Institute for Science and Technology, Tokyo University of Science, 2641 Yamazaki, Noda 278-8510, Japan

Correspondence should be addressed to Takeshi Kondo, t-kondo@rs.noda.tus.ac.jp

Received 7 May 2011; Revised 28 July 2011; Accepted 1 August 2011

Academic Editor: Giancarlo R. Salazar-Banda

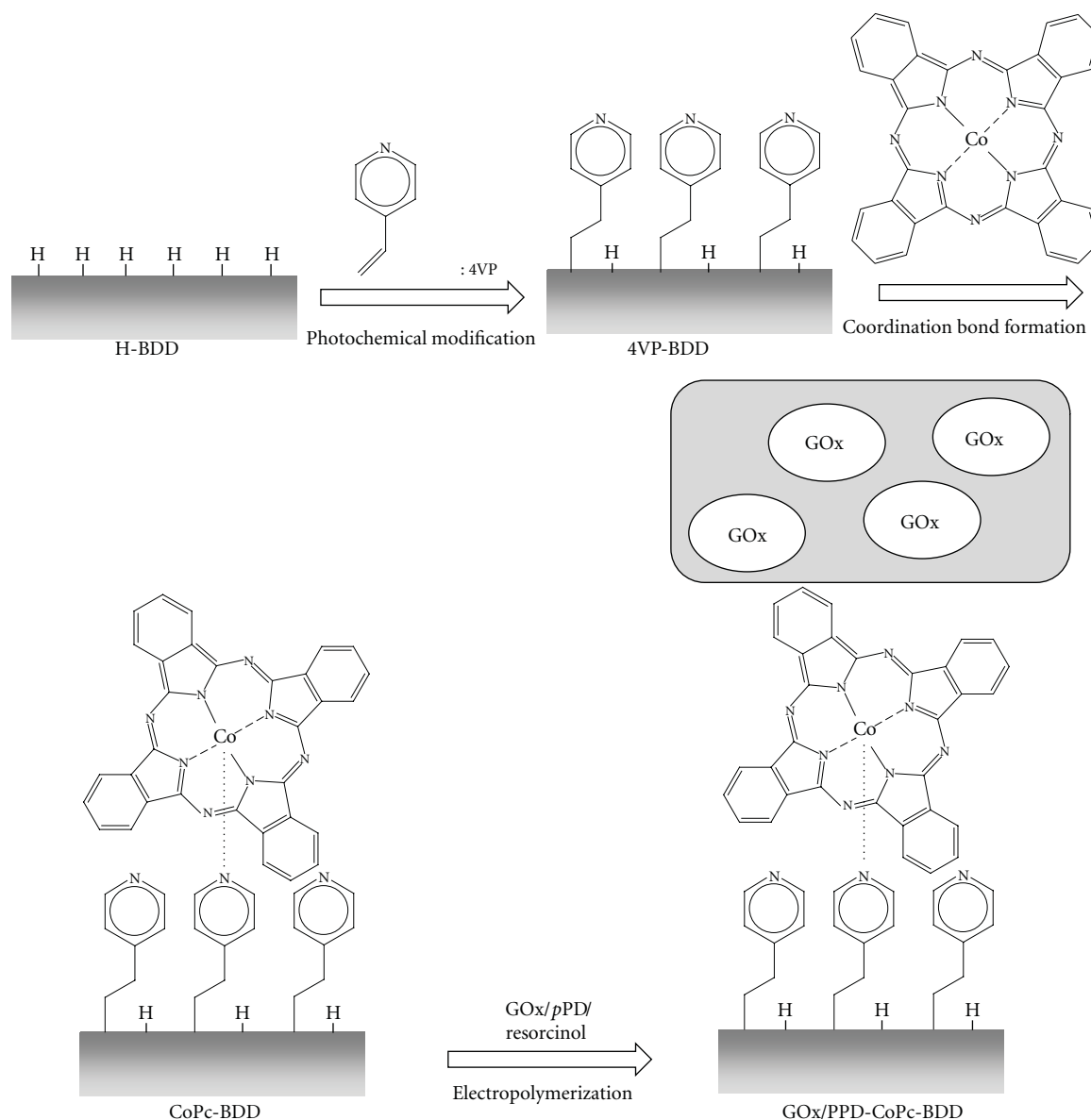
Copyright © 2012 Takeshi Kondo et al. This is an open access article distributed under the Creative Commons Attribution License, which permits unrestricted use, distribution, and reproduction in any medium, provided the original work is properly cited.

Electrochemical detection of glucose was achieved at a glucose oxidase (GOx)-cobalt phthalocyanine (CoPc)-modified boron-doped diamond (BDD) electrode without any additional electron mediator in the electrolyte solution. The surface of the hydrogen-terminated BDD thin film prepared by microwave plasma-assisted CVD was modified with 4-vinylpyridine (4VP) via photochemical modification. The 4VP-BDD was then immersed in a CoPc solution to obtain CoPc-BDD. A poly(*p*-phenylenediamine) (PPD) thin film containing GOx was coated on the CoPc-BDD electrode surface via electropolymerization. At the GOx/PPD-CoPc-BDD electrode, anodic current for glucose oxidation was observed with a sigmoidal voltammetric curve, indicating successful electron mediation of H₂O₂ generated as the result of glucose oxidation at GOx. The signal-to-background ratio for voltammetric current of glucose detection was larger at the GOx/PPD-CoPc-BDD electrode than at the GOx/PPD-modified platinum electrode due to the smaller background current of the modified BDD electrode.

1. Introduction

Highly boron-doped diamond (BDD) electrodes have been known to be a promising electrode material for sensitive electroanalysis based on the wide potential window and low background current as well as physical and chemical stability and biocompatibility [1]. Glucose is a compound, whose concentration is one of the most desired to be determined via electrochemical methods in relation to increasing demands for diabetes care [2]. In order to use BDD electrode for glucose detection, one should modify the surface with catalysts or enzymes due to the large overpotential for direct glucose oxidation at unmodified BDD electrodes. For glucose detection at BDD electrodes using electrocatalysts, Cu [3–5] and Ni [6–9] have been used for modification of the surfaces. Immobilization of particles or line patterns of these metals with micrometer or nanometer scale onto BDD surface enables sensitive glucose detection with low background current. On the other hand, BDD electrodes modified with glucose oxidase (GOx) [10–13] are advantageous because

of their selectivity and sensitivity of the glucose molecule. In some cases, additional mediators, such as ferrocene carboxylic acid [11], were employed for glucose detection at GOx-modified BDD electrodes. Glucose detection without any additional reagents to samples is possible for simple analysis systems, and especially for monitoring concentration. Hydrogen peroxide is a product of glucose oxidation at GOx and thus can act as an electroactive mediator for electrochemical detection of glucose. We have reported that sensitive electrochemical detection of hydrogen peroxide can be achieved at BDD electrodes modified with cobalt(II) phthalocyanine (CoPc) [14]. The limit of detection of hydrogen peroxide at CoPc-BDD electrode using a flow-injection system was found to be in the range of 1–10 nM and that was rather low comparing to Pt-modified BDD electrodes (30 nM) [15]. Thus the use of CoPc-BDD should be effective for fabrication of a GOx-modified BDD electrodes for sensitive glucose detection. In the present study, we prepared a GOx containing poly(*p*-phenylenediamine) (PPD) film on a CoPc-BDD electrode surface to fabricate an



SCHEME 1: Fabrication of GOx/PPD-CoPc-BDD electrode.

electrode material for reagentless sensitive glucose detection (Scheme 1). The signal-to-background ratio of glucose was found to be larger at GOx/PPD-CoPc-BDD electrode than at GOx/PPD-Pt electrode.

2. Experimental

BDD electrodes were prepared by microwave plasma-assisted chemical vapor deposition (MPCVD). The deposition condition was identical to what can be found in our previous report [16]. A conductive polycrystalline BDD thin film with a grain size of 1–5 μm was first grown on a conductive silicon wafer substrate. Surface modification of BDD with CoPc was carried out with a procedure described in the previous report [14]. A hydrogen-terminated BDD (H-BDD) sample was immersed in a 100 mM 4-vinylpyridine (4VP)/acetonitrile

solution. The sample surface was then irradiated with UV light (254 nm) from a low pressure mercury lamp (SUV-40, Sen Lights Corp.) in Ar atmosphere through a quartz window for 3 h. The 4VP-modified BDD sample was then immersed in a 0.1 mM CoPc/chloroform solution for one day to obtain CoPc-BDD. Surface modification with 4VP was confirmed with X-ray photoelectron spectroscopy (XPS) with a XP spectrometer (AXIS-NOVA, Kratos). GOx/PPD film was prepared using an electropolymerization method. Potential cycling, repeated 10 times, between 0 to +0.6 V versus Ag/AgCl was performed in 0.1 M phosphate buffer solution (PBS, pH 7) containing 0.15 mM *p*-phenylenediamine, 0.15 mM resorcinol, and 500 U/mL glucose oxidase (Type VII, from aspergillus niger, Sigma-Aldrich) at a CoPc-BDD electrode at a potential sweep rate of 20 mVs⁻¹. For all electrochemical experiments, an

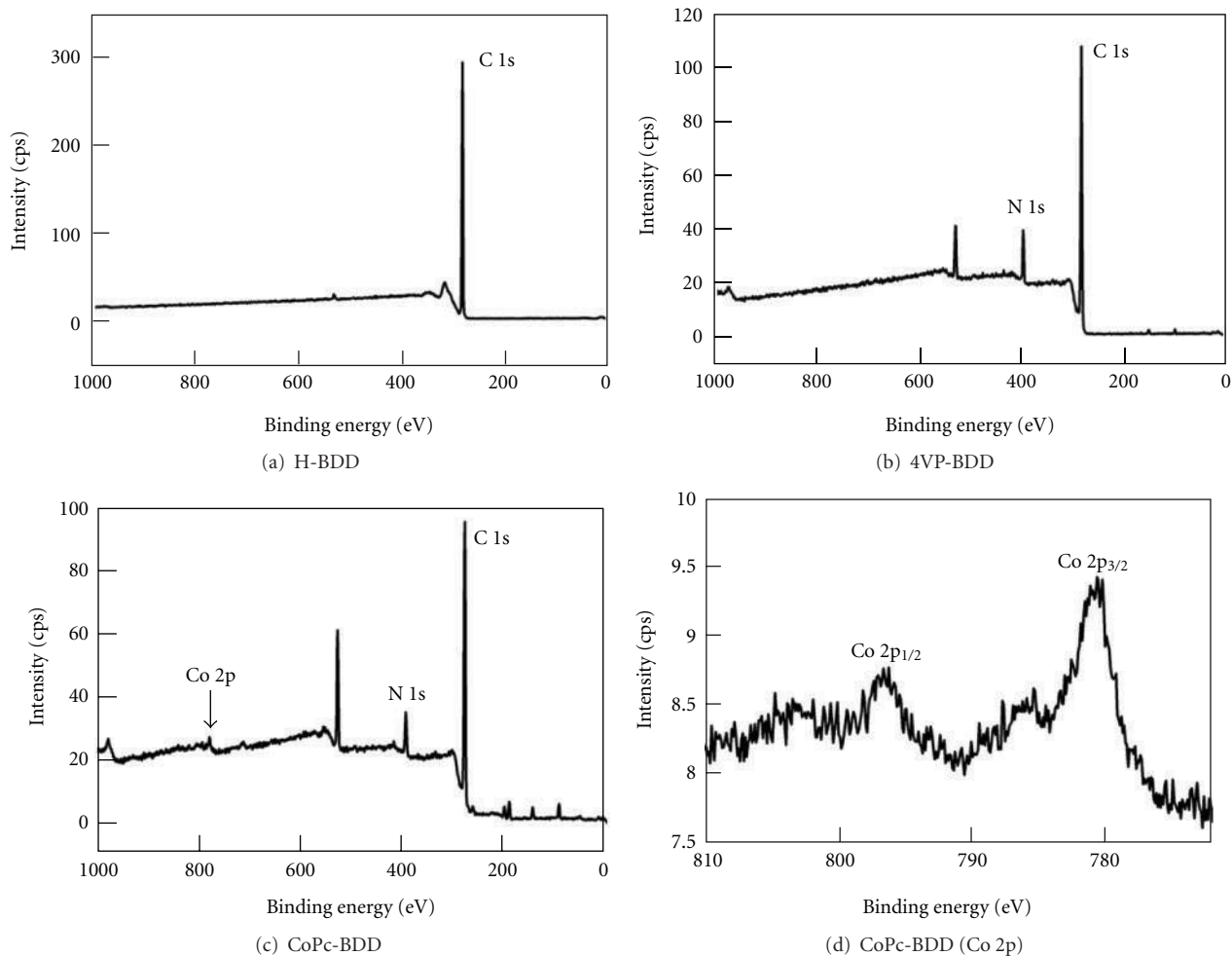


FIGURE 1: XPS of (a) H-, (b) 4VP-, and (c) CoPc-BDD surfaces. (d) Co 2p spectrum of CoPc-BDD surface.

Ag/AgCl electrode with saturated KCl and a platinum spiral wire were used for a reference and a counter electrode, respectively, connecting to a digital potentiostat (HZ-5000, Hokuto Denko).

3. Results and Discussion

3.1. Preparation of CoPc-BDD Electrode. Surface modification of BDD with 4VP was confirmed with XPS. After surface modification with 4VP, an N 1s peak was shown in the XP spectra at 397 eV (Figure 1(b)), which was absent in the spectrum of H-BDD (Figure 1(a)). This should be based on the pyridine moiety on the 4VP-BDD surface. The N/C atomic concentration ratio determined from XPS quantitative analysis was found to saturate with between 2 and 3 h UV irradiation. Thus, we decided the UV irradiation time for the 4VP modification to be 3 h. Immobilization of CoPc on 4VP-BDD surface was also confirmed with Co 2p_{3/2} and (781 eV) Co 2p_{1/2} (797 eV) peaks (Figure 1(c)). The Co/C atomic concentration ratio saturated within 24 h of immersion of a 4VP-BDD in a CoPc solution. Figure 2 shows cyclic voltammograms (CVs) in 0.1 M phosphate

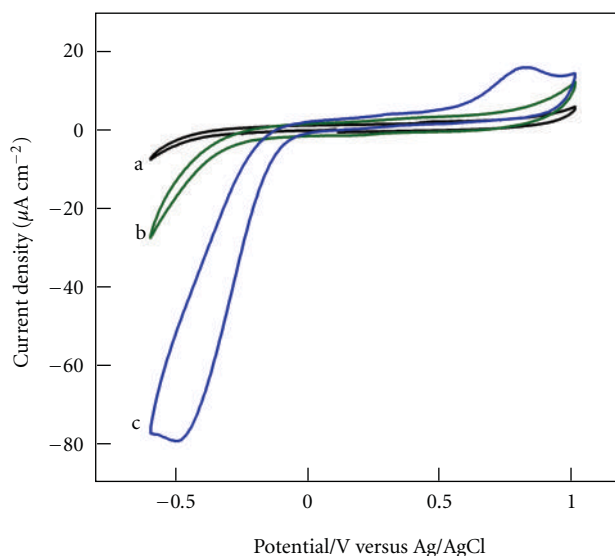


FIGURE 2: CVs in 0.1 M PBS at (a) H-, (b) 4VP-, and (c) CoPc-BDD electrodes. Potential sweep rate was 100 mVs⁻¹.

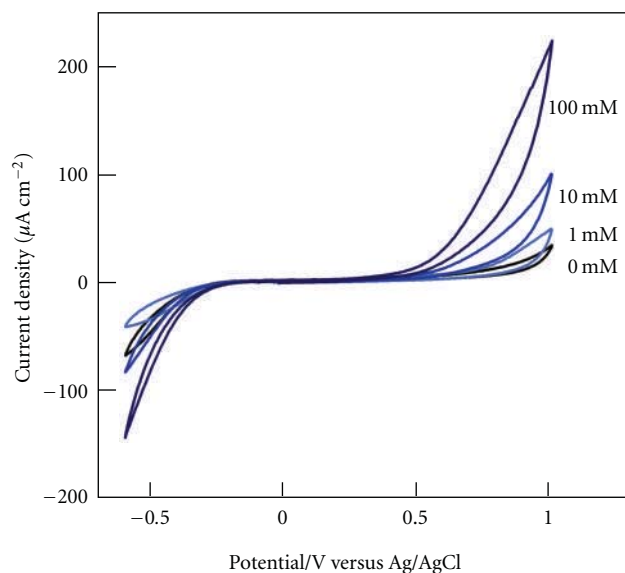


FIGURE 3: CVs in 0.1 M PBS containing 0, 1, 10, and 100 mM H_2O_2 at CoPc-BDD electrode. Potential sweep rate was 100 mVs^{-1} .

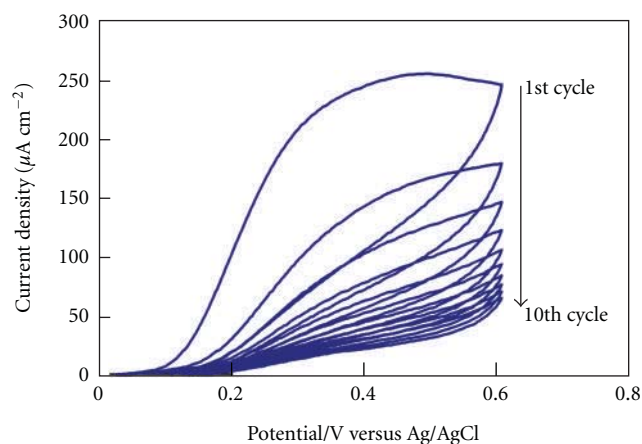


FIGURE 4: CVs in 0.1 M PBS containing 0.15 mM *p*-phenylenediamine, 0.15 mM resorcinol and 500 U/mL GOx at CoPc-BDD electrode for electropolymerization of a GOx/PPD film. Ten successive cycles are indicated. Potential sweep rate was 20 mVs^{-1} .

buffer solution (PBS, pH 7) at modified BDD electrodes. Although no redox peak was found in the CVs at H- and 4VP-BDD electrode, an anodic and a cathodic peak was found at the CoPc-BDD electrode. This result indicates that the immobilized CoPc was redox-active on the modified electrode [14]. Figure 3 shows CVs at CoPc-BDD electrode in 0.1 M PBS containing various concentrations of H_2O_2 . At unmodified (H-terminated) BDD surface, no increase of the faradaic current for H_2O_2 was found. This is due to a large overpotential of the electrode reaction of H_2O_2 at the unmodified BDD electrode. On the other hand, the CV at CoPc-BDD showed an anodic and cathodic faradaic current depending on H_2O_2 concentration, based on the

electrocatalytic activity of CoPc to the electrode reaction of H_2O_2 [17].

3.2. Preparation of GOx/PPD-CoPc-BDD Electrode. In order to immobilize GOx onto the electrode surface, GOx/PPD film was formed via electropolymerization method. Figure 4 shows ten successive CVs for the electropolymerization in 0.1 M PBS containing 0.15 mM *p*-phenylenediamine, 0.15 mM resorcinol and 500 U/mL GOx at CoPc-BDD electrode. The decrease in the anodic current is typical of electropolymerization of similar polymer films and is based on the insulating properties of the film formed at the interface [18]. Figure 5 shows scanning electron microscopy (SEM) images of a BDD and a GOx/PPD-CoPc-BDD electrode surfaces. PPD is known to be a stiff polymer with a ladderlike network structure [19], and it should be responsible for the linear texture of the film observed with SEM. In addition, the PPD film formed with electropolymerization method is known to be a permselective membrane for H_2O_2 [19] and can suppress electrode reaction of electroactive interferences such as ascorbic acid and dopamine [14]. Thus, the use of PPD matrices should be advantageous for selective detection of glucose.

3.3. Glucose Detection. Figure 6(a) shows a CV in 0.1 M PBS containing 5 mM glucose at a GOx/PPD-CoPc-BDD electrode. In the absence of glucose, almost no current was observed. However, in the presence of glucose, anodic current began to flow at +0.15 V versus Ag/AgCl and was almost constant at +0.3 V versus Ag/AgCl or more positive potentials. This sigmoidal curve is typical of enzyme electrode reactions [11], indicating successful electron transfer from glucose to the BDD electrode. In the case of an electrode with a GOx/PPD film formed on the H-BDD surface (GOx/PPD-H-BDD), no current response was observed in the presence of glucose in the electrolyte solution (Figure 6(b)). These results indicate that the current response observed for GOx/PPD-CoPc-BDD was not with direct electron transfer from glucose or GOx and should be based on the mediation of H_2O_2 electrooxidation catalyzed by the CoPc on the BDD surface. Thus, it was shown that electrocatalysts, such as CoPc, are essential for the current response of BDD-based enzyme electrodes using oxidases that can generate H_2O_2 . Similar to the case of GOx/PPD-CoPc-BDD electrode, a sigmoid-shaped voltammetric curve was shown at a Pt electrode covered with a GOx/PPD film via electropolymerization (GOx/PPD-Pt, Figure 6(c)). This result was not surprising because H_2O_2 can be oxidized on a Pt electrode at low potentials without the use of any additional catalyst. The signal current at +0.5 V versus Ag/AgCl was larger at GOx/PPD-Pt electrode ($54 \mu\text{A cm}^{-2}$) than at GOx/PPD-CoPc-BDD electrode ($25 \mu\text{A cm}^{-2}$). On the other hand, however, the background current was much lower at GOx/PPD-CoPc-BDD electrode ($1.8 \mu\text{A cm}^{-2}$) than at GOx/PPD-Pt electrode ($14 \mu\text{A cm}^{-2}$). As a result, the signal-to-background (S/B) ratio at this potential was found to be 12.5 at the GOx/PPD-CoPc-BDD electrode while that was 3.8 at the GOx/PPD-Pt electrode. As seen in previous reports, low background

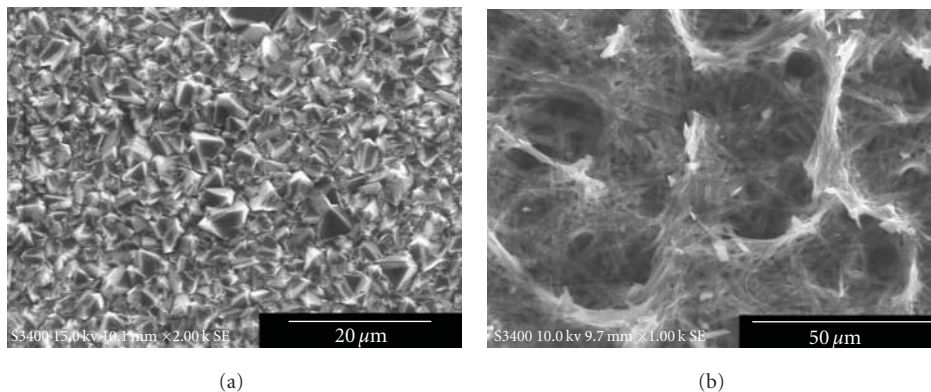


FIGURE 5: SEM image of (a) unmodified BDD and (b) GOx/PPD-CoPc-BDD surface.

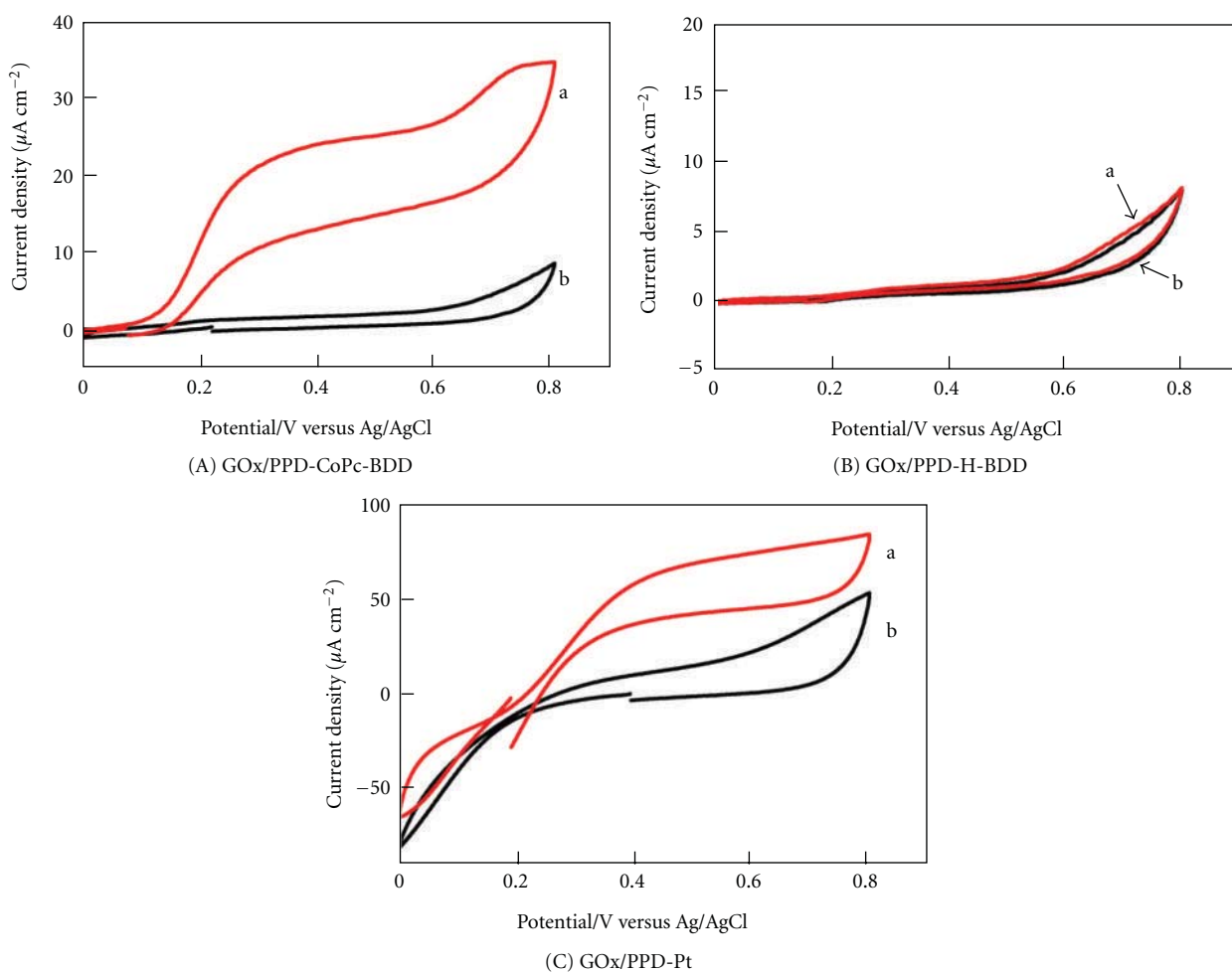


FIGURE 6: CVs for 5 mM glucose in 0.1 M PBS at (A) GOx/PPD-CoPc-BDD, (B) GOx/PPD-H-BDD, and (C) GOx/PPD-Pt electrodes. Curves (a) and (b) indicate CVs for 5 mM glucose and background, respectively. Potential sweep rate was 5 mVs⁻¹.

current at modified BDD electrodes enabled sensitive electrochemical detection of oxalic acid [20] and H₂O₂ [14]. Also in this study, the low background current feature of BDD was maintained even after surface modification with 4VP, CoPc and GOx/PPD film. Therefore, immobilization of enzymes

on CoPc-BDD should be a useful method for fabrication of sensitive enzyme electrodes using other types of oxidase which can generate H₂O₂ (e.g., uricase, cholesterol oxidase, lactate oxidase, alcohol oxidase, bilirubin oxidase, or choline oxidase) based on the low background current.

4. Conclusion

GOx-immobilized PPD polymer film was formed on a CoPc-BDD electrode via electropolymerization. At the GOx/PPD-CoPc-BDD electrode, CV for glucose showed a sigmoidal curve without any additional electron mediator in the electrolyte solution, indicating that the glucose oxidation at the GOx and the electrocatalytic oxidation of H₂O₂, which is a product of glucose oxidation, at the CoPc were successful at the electrolyte/electrode interface. Since the GOx/PPD-CoPc-BDD electrode exhibited significantly small background current, the S/B ratio was found to be larger at the GOx/PPD-CoPc-BDD electrode than at the GOx/PPD-Pt electrode. This result is consistent with our previous result that H₂O₂ can be detected electrochemically on the CoPc-BDD electrode with the lowest limit of detection level based on the small background current [14]. This study showed that this feature of the CoPc-BDD electrode can be maintained even after further modification with GOx. Therefore, sensitive enzyme electrodes, involved with H₂O₂/O₂ redox mediation, having low limit of detection should be able to be fabricated with a similar method using a CoPc-BDD electrode. For application of this electrode to a glucose sensor, amperometric studies using a solution containing glucose and other possible interferents which exist in human blood should be investigated in the future study.

Acknowledgments

This work was supported by Program for Fostering Regional Innovation in Nagano, granted by MEXT, Japan, KAKENHI (21750209), and Iketani Science and Technology Foundation.

References

- [1] *Diamond Electrochemistry*, Elsevier, Tokyo, Japan, 2005.
- [2] K. E. Toghill and R. G. Compton, "Electrochemical non-enzymatic glucose sensors: a perspective and an evaluation," *International Journal of Electrochemical Science*, vol. 5, no. 9, pp. 1246–1301, 2010.
- [3] T. Watanabe, T. A. Ivandini, Y. Makide, A. Fujishima, and Y. Einaga, "Selective detection method derived from a controlled diffusion process at metal-modified diamond electrodes," *Analytical Chemistry*, vol. 78, no. 22, pp. 7857–7860, 2006.
- [4] J. Zhao, R. Tian, and J. Zhi, "Electroless deposition of copper and fabrication of copper micropatterns on CVD diamond film surfaces," *Applied Surface Science*, vol. 254, no. 11, pp. 3282–3287, 2008.
- [5] M. Chiku, T. Watanabe, and Y. Einaga, "Fabrication of Cu-modified boron-doped diamond microband electrodes and their application for selective detection of glucose," *Diamond and Related Materials*, vol. 19, no. 7–9, pp. 673–679, 2010.
- [6] R. Uchikado, T. N. Rao, D. A. Tryk, and A. Fujishima, "Metal-modified diamond electrode as an electrochemical detector for glucose," *Chemistry Letters*, vol. 30, no. 2, pp. 144–145, 2001.
- [7] K. Ohnishi, Y. Einaga, H. Notsu et al., "Electrochemical glucose detection using nickel-implanted boron-doped diamond electrodes," *Electrochemical and Solid-State Letters*, vol. 5, no. 3, pp. D1–D3, 2002.
- [8] T. Watanabe and Y. Einaga, "Design and fabrication of nickel microdisk-arrayed diamond electrodes for a non-enzymatic glucose sensor based on control of diffusion profiles," *Biosensors and Bioelectronics*, vol. 24, no. 8, pp. 2684–2689, 2009.
- [9] K. E. Toghill, L. Xiao, M. A. Phillips, and R. G. Compton, "The non-enzymatic determination of glucose using an electrolytically fabricated nickel microparticle modified boron-doped diamond electrode or nickel foil electrode," *Sensors and Actuators, B*, vol. 147, no. 2, pp. 642–652, 2010.
- [10] C. E. Troupe, I. C. Drummond, C. Graham et al., "Diamond-based glucose sensors," *Diamond and Related Materials*, vol. 7, no. 2–5, pp. 575–580, 1998.
- [11] L. Su, X. Qiu, L. Guo, F. Zhang, and C. Tung, "Amperometric glucose sensor based on enzyme-modified boron-doped diamond electrode by cross-linking method," *Sensors and Actuators, B*, vol. 99, no. 2–3, pp. 499–504, 2004.
- [12] K. B. Male, S. Hrapovic, and J. H. T. Luong, "Electrochemically-assisted deposition of oxidases on platinum nanoparticle/multi-walled carbon nanotube-modified electrodes," *Analyst*, vol. 132, no. 12, pp. 1254–1261, 2007.
- [13] M. J. Song, J. H. Kim, S. K. Lee et al., "Pt-polyaniline nanocomposite on boron-doped diamond electrode for amperometric biosensor with low detection limit," *Microchimica Acta*, vol. 171, no. 3–4, pp. 249–255, 2010.
- [14] T. Kondo, A. Tamura, and T. Kawai, "Cobalt phthalocyanine-modified boron-doped diamond electrode for highly sensitive detection of hydrogen peroxide," *Journal of the Electrochemical Society*, vol. 156, no. 11, pp. F145–F150, 2009.
- [15] T. A. Ivandini, R. Sato, Y. Makide, A. Fujishima, and Y. Einaga, "Pt-implanted boron-doped diamond electrodes and the application for electrochemical detection of hydrogen peroxide," *Diamond and Related Materials*, vol. 14, no. 11–12, pp. 2133–2138, 2005.
- [16] T. Kondo, S. Aoshima, K. Honda, Y. Einaga, A. Fujishima, and T. Kawai, "Fabrication of covalent SAM/Au nanoparticle/boron-doped diamond configurations with a sequential self-assembly method," *Journal of Physical Chemistry C*, vol. 111, no. 34, pp. 12650–12657, 2007.
- [17] P. N. Mashazi, K. I. Ozoemena, and T. Nyokong, "Tetracarboxylic acid cobalt phthalocyanine SAM on gold: potential applications as amperometric sensor for H₂O₂ and fabrication of glucose biosensor," *Electrochimica Acta*, vol. 52, no. 1, pp. 177–186, 2006.
- [18] H. H. Weetall, D. W. Hatchett, and K. R. Rogers, "Electrochemically deposited polymer-coated gold electrodes selective for 2,4-dichlorophenoxyacetic acid," *Electroanalysis*, vol. 17, no. 19, pp. 1789–1794, 2005.
- [19] S. J. Killoran and R. D. O'Neill, "Characterization of permselective coatings electrosynthesized on Pt-Ir from the three phenylenediamine isomers for biosensor applications," *Electrochimica Acta*, vol. 53, no. 24, pp. 7303–7312, 2008.
- [20] T. Kondo, Y. Niwano, A. Tamura et al., "Sensitive electrochemical detection of oxalate at a positively charged boron-doped diamond surface," *Electroanalysis*, vol. 20, no. 14, pp. 1556–1564, 2008.

Research Article

Controllable Electrochemical Activities by Oxidative Treatment toward Inner-Sphere Redox Systems at N-Doped Hydrogenated Amorphous Carbon Films

Yoriko Tanaka,¹ Hiroshi Naragino,¹ Kohsuke Yoshinaga,¹ Akira Nakahara,¹ Takeshi Kondo,² Akira Fujishima,³ and Kensuke Honda¹

¹ Department of Chemistry and Earth Sciences, Faculty of Science, Yamaguchi University, 1677-1 Yoshida, Yamaguchi-shi, Yamaguchi 753-8512, Japan

² Department of Pure and Applied Chemistry, Faculty of Science and Technology, Tokyo University of Science, 2641 Yamazaki, Noda 278-8510, Japan

³ Kanagawa Academy of Science and Technology (KAST), KSP, 3-2-1, Sakado, Takatsu-ku, Kawasaki city, Kanagawa 213-0012, Japan

Correspondence should be addressed to Kensuke Honda, khonda@yamaguchi-u.ac.jp

Received 25 April 2011; Revised 18 July 2011; Accepted 19 July 2011

Academic Editor: Giancarlo R. Salazar-Banda

Copyright © 2012 Yoriko Tanaka et al. This is an open access article distributed under the Creative Commons Attribution License, which permits unrestricted use, distribution, and reproduction in any medium, provided the original work is properly cited.

The electrochemical activity of the surface of Nitrogen-doped hydrogenated amorphous carbon thin films (a-CNH, N-doped DLC) toward the inner sphere redox species is controllable by modifying the surface termination. At the oxygen plasma treated N-doped DLC surface (O-DLC), the surface functional groups containing carbon doubly bonded to oxygen (C=O), which improves adsorption of polar molecules, were generated. By oxidative treatment, the electron-transfer rate for dopamine (DA) positively charged inner-sphere redox analyte could be improved at the N-doped DLC surface. For redox reaction of 2,4-dichlorophenol, which induces an inevitable fouling of the anode surface by forming passivating films, the DLC surfaces exhibited remarkably higher stability and reproducibility of the electrode performance. This is due to the electrochemical decomposition of the passive films without the interference of oxygen evolution by applying higher potential. The N-doped DLC film can offer benefits as the polarizable electrode surface with the higher reactivity and higher stability toward inner-sphere redox species. By making use of these controllable electrochemical reactivity at the O-DLC surface, the selective detection of DA in the mixed solution of DA and uric acid could be achieved.

1. Introduction

Boron-doped diamond (BDD) thin film is an ideal polarizable electrode material because it possesses superior electrochemical properties such as a wide working potential range, low background current, and high stability toward electrochemical reaction. The application of BDD as an electrochemical sensor material has been studied intensely in recent years [1, 2].

Nitrogen-doped amorphous carbon (a-C:N) has recently attracted attention and been investigated as electrode materials. It has been shown that a-C:N has a wide potential window and low back current in aqueous media that are comparable with those observed at the BDD electrode

[3–11]. The methods employed for fabricating a-C:N electrodes were a filtered cathodic vacuum arc (FCVA) [3–8], radio-frequency cathodic sputtering from graphite target [9, 10], and direct ion beam deposition [11].

As a simple method of nitrogen-doped hydrogenated amorphous carbon thin film (N-doped DLC) synthesis, our research group proposed microwave-assisted plasma-enhanced chemical vapor deposition method using the vapor of nitrogen-containing hydrocarbon as carbon and nitrogen sources [12]. This method is widely used for the diamond-like carbon coating. Our research groups have reported that the N-doped DLC films synthesized using this method had a N/C ratio of 0.08 and contain sp^3 -bonded carbons with atomic ratio 25/75 sp^3/sp^2 . The electrical resistivity and

optical gap were 0.695 Ω cm and 0.38 eV, respectively [12]. N-doped DLC thin films exhibited a wide working potential range over 3 V, low double-layer capacitance, high resistance to electrochemically induced corrosion in strong acid media, and reversible electron transfer kinetics for inorganic redox analytes ($\text{Fe}^{2+/3+}$, $[\text{Fe}(\text{CN})_6]^{3-/4-}$, and $\text{Ru}(\text{NH}_3)_6^{2+/3+}$), which were on the same level as those of BDD [12]. Hence, the N-doped DLC films could be an ideal polarizable electrode material with physical stability and chemical inertness, alternative to BDD.

The BDD surface is easily oxidized, and the oxygen-containing functional groups are formed by electrochemical anodization. The charge transfer rates for outer-sphere redox such as ascorbic acid and anthraquinone-2,6-disulfonate (2,6-AQDS) at BDD are significantly altered by the anodic oxidation. Consequently, in the case where BDD is used as the electroanalytical measurements of bio-related compounds (inner-sphere redox species such as dopamine or uric acid), there is a problem that the accuracy of a quantitative analysis might be reduced due to the successive surface oxidation in the long time use.

Since amorphous carbon is composed of a certain amount of sp^2 -bonded carbon atoms, the N-doped DLC electrodes are expected to exhibit the higher reactivity toward inner-sphere redox species same as GC (sp^2 -bonded carbons). The surface ether group and carboxyl group have been reported to act as adsorption sites for inner-sphere redox species at the electrode surface of sp^2 -bonded carbons (such as GC). On the other hand, amorphous carbon is also composed of sp^3 -bonded carbon atoms, and the N-doped DLC electrodes are expected to show the higher stability toward the electrochemical reaction like that at BDD (sp^3 -bonded carbons).

The objective of this study is to realize an ideal polarizable electrode surface that shows the higher reactivity and higher stability toward inner-sphere redox species (as ascorbic acid). The surface of N-doped DLC was modified with O_2 plasma treatment to form ether group and carboxyl group on sp^2 -bonded carbons as a dangling bond and to improve the adsorption properties. Then, the electrochemical reactivity and stability toward inner-sphere redox analyte were investigated.

2. Experimental

2.1. Film Growth. The N-doped a-C:H films were prepared using a SAMCO model BP-10 microwave-assisted plasma chemical vapor deposition (CVD) system (SAMCO Co., Ltd.) (the same procedure described in [12, 13]). Films were deposited on p-Si (111) substrates (5×10^{-3} Ω cm, SUMCO Co., Ltd.) after in situ sputter cleaning with argon ion (150 W for 15 minutes). Vapor at a flow rate of 5 mL/min was introduced into the evacuated reaction chamber from degassed acetonitrile (carbon and nitrogen source) kept at 50°C by heating. The N-doped a-C:H films of 1.5 μm thickness were grown by applying RF power (13.56 MHz) on the cathode which held the Si substrates on a quartz liner. The chamber pressure was adjusted at 10 Pa, and the temperature of the stage was set at 176°C during deposition. It was possible to

fabricate the DLC films with 1.72 (semimetal) Ω cm (values were obtained by four-point probe methods) of resistivity could be synthesized by applying 100 W of RF power. The hardness of resulting N-doped a-C:H films was ca. 9.8 GPa of Martens hardness.

BDD thin films were prepared on a conductive p-Si (111) wafer substrate using a microwave plasma-assisted chemical vapor deposition system (ASTeX, Corp., Woburn, Mass, USA). The typical conditions of deposition have been described in the former reports [14].

The oxygen-terminated surfaces of DLC, BDD, and GC were prepared: as-deposited surface (DLC and BDD) or polished surface of GC was treated with plasma etching apparatus (SAMCO Co., Ltd., BP-1) for 1 minute using O_2 gas as source gas. The operating pressure of chamber was 20 Pa, and the plasma power was 50 W. The resulting oxygen-plasma-treated surface was used for electrochemical measurements after the pretreatment same as DLC.

2.2. Film Characterization. Raman spectra of the samples were obtained at 531.9 nm of excitation wavelength using laser Raman spectrophotometer (JASCO RPM-310).

The nitrogen content of films was measured by secondary ion mass spectroscopy (SIMS). The SIMS analysis was performed using a Cameca IMS 4F instrument. Films were sputtered with 14.5 kV Cs^+ ions, and negative secondary ions were monitored. The SIMS concentration of N in terms of atoms per cubic centimeter was converted to atomic percent by dividing the SIMS concentration values by the overall film atom density.

X-ray photoelectron spectra (XPS) were measured using an XP spectrometer (ESCA Lab MK II, VG Scientific) with a Mg K_{α} X-ray source. Both survey spectra and high-resolution spectra for C 1s were collected. C 1s spectra were deconvoluted with software provided with the instrument. The surface morphology of the films was examined with a scanning electron microscope (SEM, JEOL, Model JSM-820).

2.3. Electrochemical Characterization. N-doped DLC thin film deposited on Si substrate (not removed from Si substrate as free-standing N-doped DLC film) was used as a working electrode. Oxide layer was removed from the back of the highly conductive Si substrates with sand paper, and ohmic contact was formed on it. The DLC electrode was rinsed thoroughly and ultrasonicated in isopropanol for 15 minutes. BDD thin films, which were not removed from Si substrates, were also used as electrodes. The glassy carbon (GC, GC-20; Tokai Co., Ltd.) electrode was polished on a felt pad with alumina powder (α -alumina, 0.5 μm). Then, it was rinsed thoroughly and ultrasonicated in ultrapure water for 5 minutes.

The electrochemical measurements were carried out in a single compartment and three-electrode glass cell with Ag/AgCl as a reference electrode and with a Pt wire as a counter electrode using a digital electrochemical analyzer (Hokuto Denko Co., Ltd., Model HZ-3000). The exposed geometric area of the working electrode was 0.126 cm^2 . AC impedance measurements were carried out with an

amplitude of 10 mV in the frequency range from 100 kHz to 0.1 Hz using a potentiostat/galvanostat and a frequency response analyzer (Solartron, Type 1287 and 1260). Before the measurement, the solutions were bubbled for 15 minutes to remove the dissolved oxygen thoroughly. All the measurements were performed at room temperature (25°C).

All chemicals were used without further purification. 2,4-dichlorophenol (2,4-DCP), 2-propanol, and uric acid were acquired from Wako chemical Co., Ltd. Anthraquinone-2,6-disulfonate (2,6-AQDS) and dopamine hydrochloride were acquired from SIGMA. L(+)-ascorbic acid was acquired from TCI.

3. Results and Discussion

3.1. Film Composition

3.1.1. Raman Spectrum, SIMS Analysis, and Electrical Characterization of N-Doped DLC Thin Films. To clarify the film composition and the physical properties of the resulting nitrogen-doped DLC films, the characterization by the Raman spectroscopy, secondary ion mass spectroscopy and the Hall measurements were carried out. The Raman spectrum for the N-doped DLC surface shows a pronounced G peak at 1564 cm⁻¹ and a shoulder around 1357 cm⁻¹ (D peak) that were usually assigned to zone center phonons of E_{2g} symmetry and K point phonons of A_{1g} symmetry, respectively [15–18]. Both scattering peaks, especially D peak, were broad. These broad peaks indicated the disordered (amorphous) structure of the films and no formation of ordered sp² clusters.

Hydrogen content in amorphous carbon films can be estimated from the Raman spectra. As a result of recombination of electron-hole pairs within sp²-bonded clusters in hydrogenated amorphous carbon (a-C:H) films, the hydrogen content in films gives rise to a strong photoluminescence (PL) peak. The PL emission peak for a-C:H appears between 1.7 and 2.0 eV. When 531.9 nm is used as excitation wavelength, the first-order Raman modes in amorphous carbon films appear in higher part of the tail in the PL spectrum. PL contributes as linear background to the Raman spectrum. The ratio between the slope *m* of the fitted linear background and the intensity of G peak (*I_G*), *m/I_G*, can be used as a measure of the bonded H content in the films. Casiraghi et al. summarized the experimental Raman data of various a-C:H films and have shown that the hydrogen content is related to the normalized PL slope, *m/I_G*, and obtained an empirical relation by means of the fitting of the data points by equation [16]

$$H(\text{atom}\%) = 21.7 + 16.6 \log\left(\frac{m}{I_G(\mu\text{m})}\right). \quad (1)$$

The slope parameter is described in micrometer unit. This method of hydrogen content analysis was carried out for the Raman spectra of N-doped DLC. The slope *m* and the intensity of G peak were found to be 932.5 μm and 1636.5, respectively. The *m/I_G* value (0.5698 μm) indicates that 17.6

atom% of the bonded hydrogen content is included in N-doped DLC films.

Nitrogen contents in the N-doped DLC films were examined using secondary ion mass spectroscopy. The SIMS depth profile showed constant concentration of nitrogen (8.0 × 10²¹ atom cm⁻³) over entire film thickness (1.5 μm). Nitrogen contents of the samples were estimated to be 8.2 atom% using 1.95 g cm⁻³ of the density of the N-doped DLC films.

At the Hall measurements of the N-doped DLC films grown on Si substrate (>30 Ω cm) at 25°C, the Hall coefficient was -3.63 cm³ C⁻¹. This negative value of N-doped DLC implies n-type conduction, suggesting that nitrogen in the DLC films acts as a donor. Carrier concentration, carrier mobility, and resistivity derived from the results of the Hall measurements were 1.625 × 10¹⁸ cm⁻³, 5.38 cm² v⁻¹ s⁻¹, and 0.695 Ω cm, respectively.

From the results, it was clarified that N-doped DLC prepared in this study is the hydrogenated amorphous carbon films in which nitrogen atoms were doped up to 8.2 atom%, and these films exhibit n-type conduction by nitrogen doping.

3.1.2. Confirmation of Dopant Atoms and Surface Functionalities on DLC by XPS Measurement. The surfaces of the as-deposited N-doped DLC (AD-DLC) and the oxygen-plasma-treated DLC (O-DLC) that was fabricated to introduce the oxygen-contained functional groups on the DLC surface were evaluated by X-ray photoelectron spectroscopy analysis. The atomic concentration ratio (O/C) was determined, and the types of surface functional groups were identified. From SEM images of N-doped DLC, BDD, and polished GC surfaces after 1 min oxygen plasma treatment at 50 W of RF power, no significant morphological change was observed (in SEM images of 60000-fold magnification). It indicated that, by O₂ plasma treatment at 50 W for 1 minute, surface termination can be altered without surface etching (no increase in roughness). Actual areas of N-doped DLC, BDD, and GC surfaces were not changed by O₂ plasma treatment.

In the XPS spectra for AD-DLC and O-DLC at a sweep rate of 10 eV min⁻¹, a sharp C 1s peak was observed at 291 eV, and N 1s and O 1s peaks were obtained at 400 eV and 538 eV, respectively.

The atomic concentration ratio was estimated from the peak area and the sensitivity factors of the atomic assigned. For AD-DLC and O-DLC, the O/C ratios from O 1s and C 1s peaks were 0.12 and 0.24, respectively. The density of oxygen-containing functional groups on the AD-DLC surface was doubled by O₂ plasma treatment.

Moreover, to identify the types of oxygen-containing surface functional groups generated on the surfaces of AD-DLC and O-DLC and the ratio of sp³/sp²-bonded carbon, the analysis of waveform separation for C 1s peak obtained at the slow sweep rate of 1 eV min⁻¹ was carried out. The results are shown in Figures 1(c) and 1(d), and the same analysis results of the GC surfaces and the O₂ plasma-treated GC (O-GC) surface are shown in Figures 1(e) and 1(f). For DLC, the main peak at 290.9 eV after the waveform separation analysis was assigned to the carbon with sp² hybrids in the bulk of

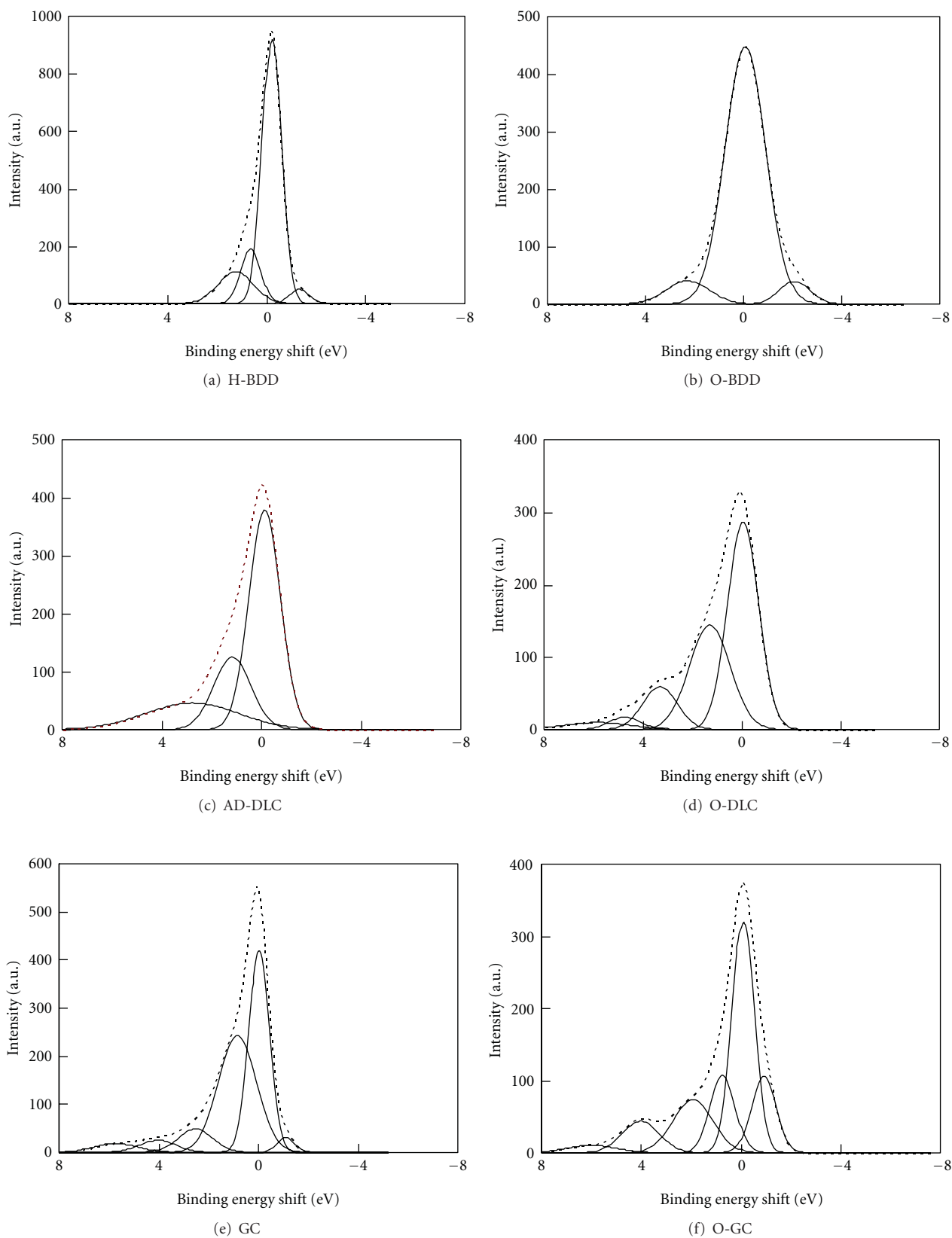


FIGURE 1: XPS C 1s spectrum for (a) H-BDD, (b) O-BDD, (c) AD-DLC, (d) O-DLC, (e) GC, and (f) O-GC, together with the Lorentzian fit line. Sweep rate, 1 eV min^{-1} .

DLC (C1 peak), and it was used as a reference of the binding energy shift (BES).

The other separated peaks for AD-DLC (Figure 1(c)) were the peak of carbon with sp^3 hybrids in the bulk of DLC (C2 peak) at ca. +1.3 eV BES, and the peak (C3 peak) assigned to carbon singly bonded to oxygen (C–O) such as hydroxyl group (C–OH) and ether structure (C–O–C) at ca. +3.1 eV BES [19]. Relative intensity ratios of these two peaks to the main peak were found to be 0.39 and 0.35, respectively.

The C 1s peak of O-DLC could be decomposed into five peaks (C1–C5) as shown in Figure 1(d). In addition to C2 peak at +1.4 eV and C3 peak at +3.4 eV, the peak (C4 peak) assigned to carbon doubly bonded carbon-oxygen (C=O) such as carboxyl group (C–OOH) and carbonyl group (C=O) was observed at +4.7 eV BES (C4 peak), and C5 peak was obtained at +5.9 eV BES. Relative intensity ratios of these 4 peaks to the main peak (C1) were found to be 0.66, 0.23, 0.06, and 0.07, respectively.

The sp^3/sp^2 ratio, which is the ratio of the peak area of C1 and C2 peak, is 0.39. N-DLC is a hydrogenated amorphous carbon film that has 28.1% of the content of sp^3 hybrids (relative to the $sp^3 + sp^2$ carbons) (71.9% of sp^2). By O_2 plasma treatment, the density of C–O functional groups was decreased to approximately half of that of AD-DLC, and the formation of C=O functional groups was clearly confirmed.

Carbon-oxygen functional groups with double (C=O) bonding (C3 peak) were not present on the as-deposited BDD (H-BDD) surface and were not generated by O_2 plasma exposure (O-BDD) as shown in Figures 1(a) and 1(b) (the main peak was sp^3 hybrids in the bulk of BDD; C2 peak).

In the XPS spectra for the polished GC surface (Figure 1(e)), C 1s peak at ca. 289 eV includes the main C1 peak, C–O peak at ca. +2.6 eV BES, and C=O peak at +4.2 eV BES. The relative intensity ratios of C–O and C=O to the main peak were found to be 0.1 and 0.07, respectively. As for the surface of GC treated by O_2 plasma (O-GC), C1s peak also includes the same three peaks (Figure 1(f)). Both relative intensity ratios of C–O (0.2) and C=O (0.14) peaks to C1 peak were increased by two times to the polished GC surface. The types of surface functionalities on GC and the trend of the modification by O_2 plasma treatment are identical to those on DLC. Hence, on the DLC surface, oxygen-containing surface functional groups including carbon doubly bonded to oxygen (C=O), which cannot be formed on BDD, can be introduced by O_2 plasma treatment.

3.2. Fundamental Electrochemical Properties of the Conductive DLC Electrode~Potential Window, Electrochemical Double Layer Capacitance. The fundamental electrochemical properties of the N-doped DLC films that have been reported in a previous publication [12] are summarized as follows. The N-doped DLC films exhibited a wide working potential range over 3 V, which is on the same level as that of BDD. The working potential windows $\Delta E (= E_{ox} - E_{red})$ in 0.1 M Na_2SO_4 for N-doped DLC and BDD were observed to be 2.97 and 2.62, respectively. These results indicate that N-doped DLC exhibits the lower reactivity toward hydrogen and oxygen evolution. It was caused by fewer adsorption sites

than noble metal, which are needed for hydrogen and oxygen evolution (slightly higher than those of BDD), and by the potential drop within the electrode due to the lower carrier density [12]. A wide working potential range in aqueous media indicates that N-doped DLC has ideal polarizable properties, which are close to BDD [20].

The N-doped DLC films exhibited a lower double-layer capacitance, which is also on the same level as that of BDD [12]. In the potential range from -0.5 V to 1 V, double layer capacitance for N-doped DLC estimated from AC impedance measurements were from $8 \mu F cm^{-2}$ to $20 \mu F cm^{-2}$ (obtained from the data at 10 Hz). The values were low and were comparable in magnitude to the values observed for BDD ($8 \sim 17 \mu F cm^{-2}$) and HOPG ($6 \sim 23 \mu F cm^{-2}$) at the same frequency; on the other hand, they were approximately half of those for GC ($24 \sim 37 \mu F cm^{-2}$).

3.3. Electrochemical Activity of N-Doped DLC Electrode Surface. The electrochemical responses of the N-doped DLC surface were evaluated by the electron-transfer kinetics of various inner and outer-sphere redox species. At the BDD electrodes, the electron-transfer rate has been reported to be seriously affected by the substitution of the surface terminated atoms from hydrogen to the oxygen-containing functional groups by anodic oxidation or exposure to O_2 plasma [21]. On the other hand, the surface of as-deposited DLC possesses some of the oxygen-containing functional groups by the reaction with O_2 in the air just after CVD deposition as already shown in XPS results. It is expected that, unlike BDD, the electrochemical response of N-doped DLC is not significantly changed by surface oxidation in the long-term electrochemical use. In this section, the N-doped DLC surface was prepared by the exposure to O_2 plasma, and the electrochemical reactivity at the oxidized surface (O-DLC) was compared with that at the as-deposited N-doped DLC surface (AD-DLC); then, the difference of reactivity between DLC and BDD was verified.

3.3.1. Charge Transfer Kinetics of Outer-Sphere Redox Species. The reactivity toward one-electron outer-sphere redox species, $Ru(NH_3)_6^{3+/2+}$, $Fe^{3+/2+}$, and $Fe(CN)_6^{3-/4-}$, have been examined using cyclic voltammetry in a previous report [12]. The results are roughly summarized as follows.

In cyclic voltammograms (CV) for $Ru(NH_3)_6^{3+/2+}$ at $10 mV s^{-1}$ of sweep rate, the values of peak separation ΔE_p at AD-DLC and O-DLC were 124 mV and 97 mV, respectively, indicating nearly the reversible response. The heterogeneous electron transfer rate constants, k_0 , were $2.66 \times 10^{-3} cm s^{-1}$ and $2.95 \times 10^{-3} cm s^{-1}$ obtained from AC impedance measurements [12]. The values of k_0 for $Ru(NH_3)_6^{3+/2+}$ at N-doped DLC were unaffected by surface oxidation and were insensitive to the surface microstructure. This tendency was same as BDD.

On the other hand, at N-doped DLC, the values of ΔE_p in CVs for $Fe^{3+/2+}$ ($10 mV s^{-1}$) at AD-DLC was 737 mV that was consistent with k_0 , $1.02 \times 10^{-5} cm s^{-1}$ [12]. ΔE_p at O-DLC was 274 mV and decreased by 460 mV after surface oxidation. The value of k_0 increased by a factor of three to $2.72 \times 10^{-5} cm s^{-1}$, and the electron transfer was

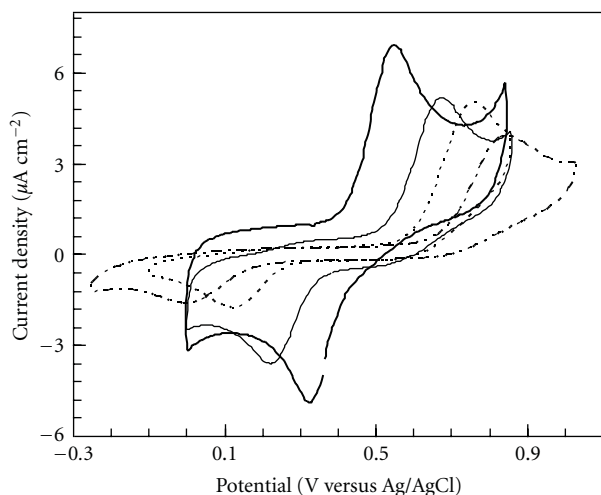


FIGURE 2: Cyclic voltammograms of 20 μM dopamine hydrochloride in 0.1 M HClO_4 at AD-DLC (thin solid line), O-DLC (thick solid line), H-BDD (dotted line), and O-BDD (dashed-dotted line). Sweep rate, 20 mV sec^{-1} .

accelerated by O_2 plasma treatment [12]. This tendency was consistent with BDD. These results indicate that the oxygen-containing functional groups formed on N-doped DLC may mediate the electron transfer of this redox system or that the force of electrostatic attraction for redox ions with positive charges was caused by the surface dipole of the oxygen-containing functional groups.

Consequently, for one-electron outer-sphere redox species with positive charge such as $\text{Fe}^{3+/2+}$ and $\text{Ru}(\text{NH}_3)_3^{3+/2+}$, the electrochemical response and the tendency of the change of the kinetics at N-doped DLC by surface oxidation were very close to those at BDD.

It has been reported that the electron-transfer rate $\text{Fe}(\text{CN})_6^{3-/4-}$ with negative charge at graphite electrodes is not dependent on the amount of surface oxygen but the amount of exposed edge plane on sp^2 -bonded carbon [22, 23], and ΔE_p was decreased by electrochemical (oxidative) pretreatment at GC [21]. On the BDD surface, the electron-transfer kinetics was decreased (ΔE_p was increased) by oxygen plasma treatment due to the electrostatic repulsive force between surface dipole on O-BDD and charges on $\text{Fe}(\text{CN})_6^{3-/4-}$ [21]. At the N-doped DLC electrodes, the value of ΔE_p was approximately constant (ca. 250 mV) before and after surface oxidation. The k_0 values were estimated to be 1.02 and $0.32 \times 10^{-4} \text{ cm} \cdot \text{s}^{-1}$ at AD-DLC and O-DLC, respectively [12].

On the surface of DLC, approximately 3/4 of surface carbons are sp^2 hybrids and 1/4 of surface carbons are sp^3 hybrids. The carbon-oxygen functionalities on sp^3 -bonded carbons introduced by oxygen plasma treatment can exhibit the repulsive force for $\text{Fe}(\text{CN})_6^{3-/4-}$ similar to BDD. O_2 plasma treatment may increase surface roughness and the exposed sp^2 -bonded carbons leading to the enhancement of the reactivity toward $\text{Fe}(\text{CN})_6^{3-/4-}$. Owing to these countervailing effects, it can be supposed that ΔE_p showed the constant values for AD-DLC and O-DLC, and the change of

reactivity toward $\text{Fe}(\text{CN})_6^{3-/4-}$ by surface oxidation may be different from that for BDD.

3.3.2. Evaluation of Electrochemical Response Using Inner-Sphere Redox Species with Positive Charge. N-doped DLC that contains sp^2 -bonded carbons is supposed to have more physical and chemical adsorption sites compared with BDD. The characterization of the N-doped DLC surfaces was studied using the redox systems of which kinetics strongly correlate with the adsorption of the analytes on the electrode surface. First of all, the reactivity toward dopamine (DA) was examined. DA is electrochemically oxidized and changed to 4-(2-amino-ethyl)-[1,2]benzoquinone and exhibit reversible behavior. DA is protonated in acidic media and positively charged in amino group. It has been reported that the kinetics of DA is highly dependent on the surface adsorption [22]. However, at the BDD surface, the kinetics (ΔE_p) is not changed (ΔE_p was slightly increased) by surface oxidation due to a lack of adsorption sites on both as-deposited and oxygen-terminated BDD surfaces [24]. The surface carbon-oxygen functionalities formed on BDD are not influential. Figure 2 shows the cyclic voltammograms of 20 μM DA at the BDD and the N-doped DLC surfaces. The value of ΔE_p at H-BDD was found to be 656 mV; this relatively large ΔE_p indicates that DA exhibits electrochemical irreversibility. As the formal potential of DA is higher than that of $\text{Fe}(\text{CN})_6^{3-/4-}$ (that shows quasireversible behavior as shown in [12]), a low density of electronic state is not a cause of the larger ΔE_p . However, a lack of adsorption on BDD can be one of the causes of slow kinetics. By the oxidative treatment of the BDD surface, ΔE_p was slightly increased to 856 mV, and the potential of oxidation peak was positively shifted by 90 mV.

Interestingly, at the N-doped DLC surface, the ΔE_p value was decreased from 478 mV to 241 mV by oxygen plasma treatment. The potential of the oxidation peak was negatively shifted by 120 mV. The similar behavior of ΔE_p toward oxidative treatment was observed at GC that was composed of sp^2 -bonded carbons (ΔE_p was decreased from 295 mV to 42 mV, and the oxidation peak was negatively shifted by 120 mV). It has been reported that, at GC, ΔE_p is in the range of 125–175 mV [25], and the ΔE_p of DA is dependent on the surface microstructure, the amount of surface oxygen, and the sp^2 bonds carbon on the surface. The π - π interaction between the sp^2 bonds of the surface and polar aromatic DA may play an important role for ΔE_p [22, 26].

Considering that ΔE_p value at AD-DLC was lower by a factor of 0.7 than that at H-BDD (faster electron-transfer kinetics) and the trend of the change in ΔE_p at N-doped DLC and GC by surface oxidation was opposite to that at BDD, it is conceivable that the specific oxygen-containing functionalities which can be generated only at sp^2 -bonded carbons (not generated at BDD) such as carbonyl and carboxyl groups may strongly affect the kinetics of DA. These functional groups are thought to enhance adsorption of inner-sphere redox species. In order to clarify the relation between the rates and the adsorption of DA at N-doped DLC and BDD, the quantitative determination of the surface coverage of dopamine on each electrode surface was examined. The electrolysis charge at N-doped

TABLE 1: Dopamine adsorption data for all six carbon electrodes.

Electrode	Amount of surface coverage (pmol cm^{-2})
O-GC	221
O-DLC	221
AD-DLC	163
GC	130
H-BDD	125
O-BDD	105

DLC was evaluated with the double-step chronocoulometric measurements for $20 \mu\text{M}$ DA in 0.1 M HClO_4 using 5-s potential steps from 740 mV to 170 mV in the presence and absence of DA. The total electrolysis charge is given by the following equation. It contains the double-layer charge Q_{dl} , the charge for adsorbed analyte Q_{ads} , and the faradic charge for the diffusion-controlled electrolysis Q_{faradic}

$$\begin{aligned}
 Q_{\text{total}} &= Q_{\text{faradic}} + Q_{\text{dl}} + Q_{\text{ads}} \\
 &= \frac{2nFAD^{1/2}Ct^{1/2}}{\pi^{1/2}} + Q_{\text{dl}} + nF\Gamma,
 \end{aligned}
 \quad (2)$$

where A represents the electrode area (cm^2), D represents the diffusion coefficient ($\text{cm}^2 \text{ s}^{-1}$), C represents the concentration (pmol cm^{-3}), and Γ represents the surface coverage of adsorbate (pmol cm^{-2}) [24]. The background-corrected charge was plotted against $t^{1/2}$ and, from the charge axis intercept, the surface coverage of adsorbate ($nF\Gamma$) was estimated. In Table 1, the chronocoulometric charge data for dopamine electrolysis at N-doped DLC, BDD, and GC before and after surface oxidation are summarized. The charge data have been converted into units of pmol cm^{-2} using Faraday's law. On the BDD surface, the surface coverage (Γ) of DA was slightly decreased from 125 (H-BDD) to 105 (O-BDD) pmol cm^{-2} by oxygen plasma treatment. On the other hand, Γ at N-doped DLC was increased by a factor of 1.4 after surface oxidation (163 and 221 pmol cm^{-2} at AD-DLC and O-DLC, resp.). The value of Γ at GC was also increased from 130 pmol cm^{-2} to 221 pmol cm^{-2} as in the case of DLC. The trend of Γ for surface oxidation was consistent with the behavior of ΔE_p toward surface oxidation. At the N-doped DLC and GC surfaces which show higher Γ value of DA after surface oxidation, the electron-transfer kinetics was improved. However, at the BDD surface, the rate for dopamine was slightly decreased, and Γ was decreased by surface oxidation.

As shown in Section 3.1.2, at both BDD and N-doped DLC, O/C ratios were increased by oxygen plasma treatment. The Γ value of DA, therefore, is supposed to be related not to the amount of surface oxygen but to the types of oxygen-containing surface groups generated on the oxidized surface. From the result of XPS measurement, only the carbons singly bonded to oxygen (C–O) could be formed on BDD, whereas the carbons doubly bonded to oxygen (C=O) were generated after surface oxidation at N-doped DLC and GC. Hence, it was thought that the C=O functional groups significantly

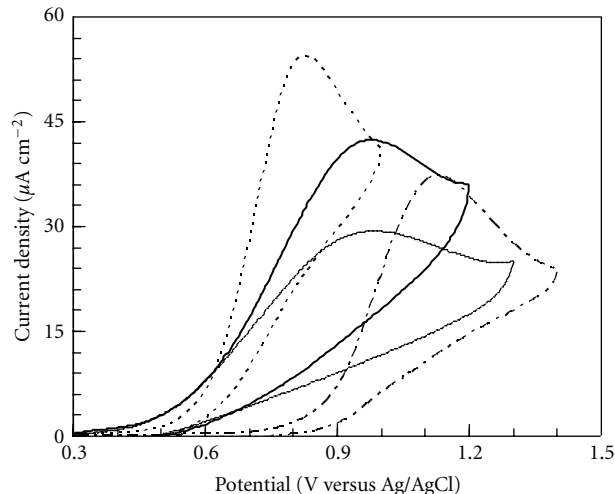


FIGURE 3: Cyclic voltammograms of 0.5 mM ascorbic acid in 0.1 M HClO_4 at AD-DLC (thin solid line), O-DLC (thick solid line), H-BDD (dotted line), and O-BDD (dashed-dotted line). Sweep rate, 20 mV s^{-1} .

contribute to the increase in the amount of adsorption of analytes, which results in the improvement of the electron-transfer kinetics. It is summarized that, for the positively charged inner-sphere redox species like dopamine, at the DLC surface, the electron-transfer rate can be improved by oxidative treatment to a higher value than at H-BDD and O-BDD. This is because the adsorption of redox species can be enhanced in addition to the effect of the electrostatic interaction (attractive force) between the surface dipoles and the charge on the redox analytes.

3.3.3. Evaluation of Electrochemical Response Using Inner-Sphere Redox Species with a Large Dipole or Negative Charge.

Among the inner-sphere redox species, the electrochemical reactivity toward ascorbic acid (AA) was examined at the N-doped DLC surface. The reactivity of AA has been reported to vary significantly after oxidative surface treatment [27]. AA is electrochemically oxidized and changed to dehydroascorbic acid at the electrode surface. (This oxidation is chemically irreversible.) At the BDD surface, the oxidation peak potential (E_p^{ox}) for AA, which is electrically neutral molecule, was positively shifted by 0.27 V in acidic solution by surface oxidation (Figure 3) [27]. This decrease in the rate for AA oxidation is because the most stable distance between AA and the electrode surface extends with the change of the terminated atoms from hydrogen- to oxygen-containing surface groups (from 4.9 \AA to 6.8 \AA) due to the decrease in the interaction energy between AA (6.42 Debyes) and surface dipoles [28]. It results in the lower charge-transfer kinetics. On the other hand, at the GC surface, it has been known that E_p^{ox} for AA exhibits the constant value for the oxidative surface treatment and indicates the stable electrochemical response to surface oxidation [28].

In the cyclic voltammograms of 0.5 mM ascorbic acid (Figure 3), the value of E_p^{ox} at N-doped DLC was observed at 0.98 V and was constant before and after surface oxidation.

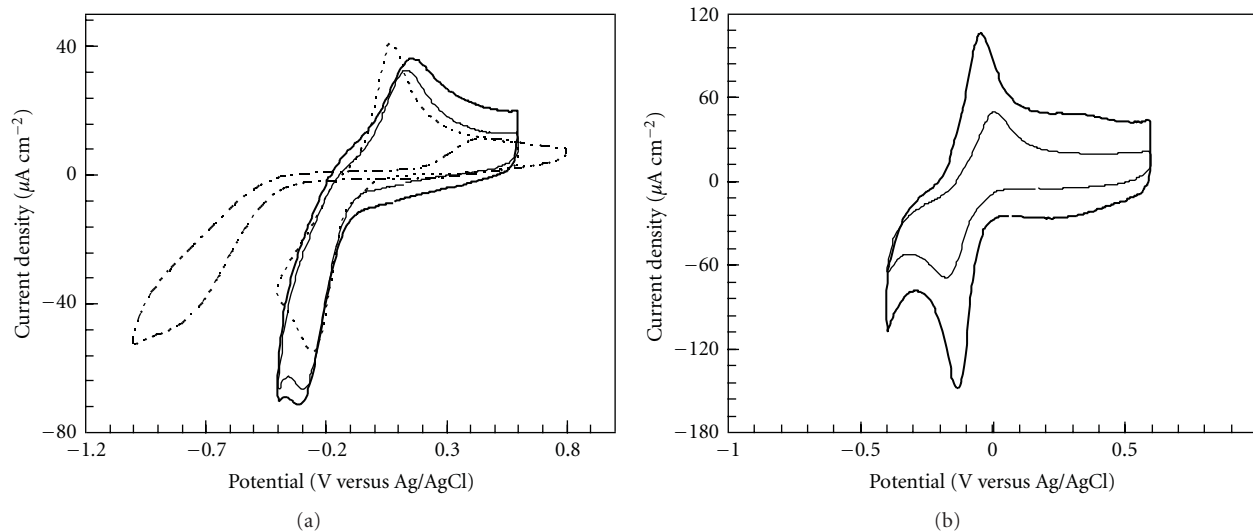


FIGURE 4: Cyclic voltammograms of 100 μM 2,6-AQDS in 0.1 M HClO_4 (a) at AD-DLC (thin solid line), O-DLC (thick solid line), H-BDD (dotted line), and O-BDD (dashed-dotted line), (b) GC (thin solid line) and O-GC (thick solid line). Sweep rate, 20 mV s^{-1} .

Only the current density at the peak potential was increased by 1.3 μA . On the O-DLC surface, the surface dipoles are thought to exhibit the weak interaction energy (repulsive force) for AA, as is the case of the O-BDD surface. On the other hand, the amount of adsorption is considered to be simultaneously improved by the increase of the C=O functional groups (adsorption sites). Owing to these countervailing effects, the stable distance of AA from the DLC surface was not changed even after surface oxidation, and the E_p^{ox} showed the constant values for AD-DLC and O-DLC. In other words, the reactivity of N-doped DLC toward inner-sphere redox species with a large dipole like AA is more stable than that at BDD. It indicates that N-doped DLC is a superior electrode material in electroanalytical assays for electroactive compounds.

The analysis of inner-sphere redox species with negative charge in relation to the electrochemical response and the surface coverage was performed using anthraquinone-2,6-disulfonate (2,6-AQDS), which is polar molecule. 2,6-AQDS undergoes a reversible two-proton and two-electron redox reaction. The oxidized and reduced forms of 2,6-AQDS strongly physisorb on the polar electrode surfaces such as GC by dipole-dipole and ion-dipole interactions although 2,6-AQDS weakly physisorbs on the nonpolar electrode surfaces such as hydrogen-terminated BDD surface [24].

Figure 4 shows cyclic voltammograms of 100 μM 2,6-AQDS at AD-DLC, O-DLC, H-BDD, and O-BDD. Table 2 summarizes the charge data for 2,6-AQDS electrolysis (the values were converted to the surface coverage) that were obtained using the same method employed for the Γ values of dopamine. In Figure 4(a), at BDD, the ΔE_p value was increased from 3542 mV to 1243 mV by oxygen plasma treatment, which indicated that charge-transfer rate was significantly decreased with the increase in the amount of oxygen-containing surface functional groups. The ΔE_p for GC and O-GC were 209 and 120 mV, respectively;

TABLE 2: 2,6-AQDS adsorption data for all six carbon electrodes.

Electrode	Amount of surface coverage (pmol cm^{-2})
O-GC	128
GC	14.0
AD-DLC	10.9
H-BDD	4.72
O-DLC	2.60
O-BDD	2.54

the value was slightly decreased after surface oxidation (Figure 4(b)). The peak current density was increased by a factor of two (from 49 $\mu\text{A cm}^{-2}$ to 100 $\mu\text{A cm}^{-2}$). The values of ΔE_p at AD-DLC and O-DLC were found to be 440 and 478 mV, respectively (Figure 4(a)). The charge-transfer rate for 2,6-AQDS was not varied by oxygen plasma treatment. Therefore, it was clarified that the reactivity toward 2,6-AQDS at N-doped DLC was intermediate between those on the BDD and on the GC surface. At GC, both the decrease of ΔE_p and the increase of peak current density by surface oxidative treatment may be attributable to the increase in the amount of surface coverage of 2,6-AQDS. The Γ value at GC was increased 9-fold from 14.0 pmol cm^{-2} to 128 pmol cm^{-2} as shown in Table 2. On the other hand, at the O-DLC surface, the amount of surface coverage of 2,6-AQDS was 2.6 pmol cm^{-2} , which was close to those at the H-BDD and O-BDD electrodes. This value was relatively lower than that at the as-deposited DLC surface. Hence, at the O-DLC surface, the contribution of the electrostatic repulsive force for the redox species with negative charge (2,6-AQDS) is higher than the increase of the adsorption sites with large surface dipole like C=O groups. As a result, the surface coverage was decreased and the electron-transfer rate

was not improved. At N-doped DLC, it is apparent that the degradation of the electrochemical response for 2,6-AQDS (increase of ΔE_p) in long time use may not occur.

3.3.4. The Durability of the N-Doped DLC Electrodes for Inner-Sphere Redox Species. It is well known that, at the sp^2 -bonded carbon electrodes such as GC, the molecules with larger polarity or charge strongly adsorb and the surface fouling occurs due to the buildup of adsorption reaction products. This surface fouling causes a problem of low stability of the electrode performance in the electroanalytical application. At the DLC surface where the specific inner-sphere species highly adsorb, there is apprehension that the electroanalytical performance is degraded in a prolonged use. Therefore, the stability of the electrochemical performance at the DLC surface before and after oxidative treatment was studied using 2,4-dichlorophenol (2,4-DCP). 2,4-DCP generates passive film by the oxidation at solid electrode, which has strong and continuous adhesion to the electrode surface, resulting in the fouling of the electrode surface [29]. The anodic reaction proceeds through an initial one-electron step to form phenoxy radicals, which subsequently can undergo either polymerization or further oxidation with transfer of oxygen from hydroxyl radicals at the electrode surface to produce *o*-benzoquinone or *p*-benzoquinone. Chlorinated benzoquinone is assumed to be the main oxidation product. The same evaluation was carried out at BDD and GC. First, for low concentration (0.1 mM) of 2,4-DCP in the Britton-Robinson buffer (pH 2), potential cycling tests were carried out in the potential range from -0.7 V to 1.7 V at O-DLC and at O-BDD, from -0.7 V to 1.3 V at H-BDD, and from -0.4 V to 1.1 V at GC, respectively. The CVs for 0.1 mM 2,4-DCP were shown in Figure 5. In CV, the anodic peaks were obtained at approximately 1.1 V versus Ag/AgCl at AD-DLC and O-DLC. The anodic peaks at polished GC and H-BDD were less positive than those of DLC and were found at 0.94 V and 1.05 V, respectively. The shift of the peak potential (from that at GC) was largest at O-BDD (1.44 V). The oxidation peak potential of 2,4-DCP was sensitive to surface microstructure of the electrode. The oxygen-containing functional groups (especially C–O groups formed on sp^3 -bonded carbons) strongly affect the peak potential shift of 2,4-DCP oxidation. The feature of CV was consistent with that at O-BDD reported in the previous publication [29]. The current densities at the oxidation peak during the potential cycling were shown in Figure 6. The peak currents in CV for 0.1 mM 2,4-DCP at AD-DLC and O-DLC were linearly proportional to sweep rate ($v^{1/2}$) in the range of 10 – 500 mV s^{-1} . It indicates that the oxidation current is diffusion controlled. In Figure 6, the peak current densities were decreased to approximately half and 0.7 of the initial value at GC and at H-BDD after 30 cycles, respectively. At GC and H-BDD, the electrode surface was oxidized (or oxygen-terminated) or corroded by applying higher potential in aqueous solution. To prevent surface oxidation, the upper potential limit was set at 1.3 V and 1.1 V, at H-BDD and GC, respectively. The oxidation of phenol derivatives forms passivating polymeric films on the electrode surface, resulting in the inevitable fouling at

GC and H-BDD. In addition, the surface-adsorbed reaction products also have been considered to cause the degradation of electrode performance [29]. After the potential cycling, the surface morphologies of the H-BDD and the GC electrodes were observed by the optical microscope. It was confirmed that small clumps of polymeric films were inhomogeneously distributed on both electrode surfaces.

On the other hand, the peak current at O-DLC at which inner-sphere redox analytes highly adsorb was slightly increased with cycle numbers (by ca. 10% of the initial value at 100 cycles) and reached a constant value at 50 cycles; the trend was same as that at AD-DLC. As a result, it was clarified that the response of 2,4-DCP oxidation at O-DLC was not varied by long-term potential cycling, and the durability of 2,4-DCP oxidation reaction was remarkably high. This higher durability is mainly due to the following: the passive films (the same films formed on GC and H-BDD) could be decomposed by applying higher potential (at over 1.7 V) at O-DLC. Moreover, the adsorption of this decomposed products and phenol derivatives on the O-DLC surface is considered to be very low because of the repulsive force from the negative surface dipolar field formed on the O-DLC surface, as is the case of O-BDD [29]. Therefore, for 2,4-DCP oxidation, the surface fouling did not occur on the DLC surface. These explanations are supported by the fact that the polymeric films cannot be observed by the optical microscope at the O-DLC and O-BDD surfaces after the potential cycling.

The fouling of the electrode is enhanced at higher concentrations (2,4-DCP) [29]. The durability of the performance of the DLC electrodes at high concentration, 5 mM 2,4-DCP, was examined using long-term potential cycling in the range from -0.7 V to 2 V at AD-DLC and from -0.7 V to 2.6 V at O-DLC. The CVs of 5 mM 2,4-DCP at 1st and 5th cycles were shown in Figure 7. At both electrode surfaces, the peak current disappeared by fifth cycles, and the fouling occurred because polymeric films were formed on the electrode surface. However, when the fouled AD-DLC and O-DLC electrodes were treated anodically in the Britton-Robinson buffer solution at 2.64 V versus Ag/AgCl for 4 minutes, the peak current densities could recover to the same levels of the initial values, as shown in Figures 7(c) and 7(d) [29]. The passive layer on DLC was thought to be completely oxidized (decomposed), and the reaction products were thought to be removed from the oxidized DLC surface. The similar recovery by anodic treatment after the potential cycling in higher concentration 2,4-DCP was observed at BDD (Figure 7(b)). The results at BDD were similar to the results in the literature [29]. In the process of the complete oxidation of the passive layer on BDD, hydroxyl radicals generated on the BDD surface at higher potential region (>1.6 V) have been reported to play an important role [29]. The complete recovery of the peak current at DLC suggests the production of hydroxyl radicals at DLC in higher potential range and the decomposition of passive layer by OH radicals. In separate experiment (not shown), OH radicals related to electrogenerated chemiluminescence reaction in the system of $\text{Ru}(\text{bpy})^{3+}$ with ascorbic acid could be observed in the potential over 2.0 V at O-DLC. This

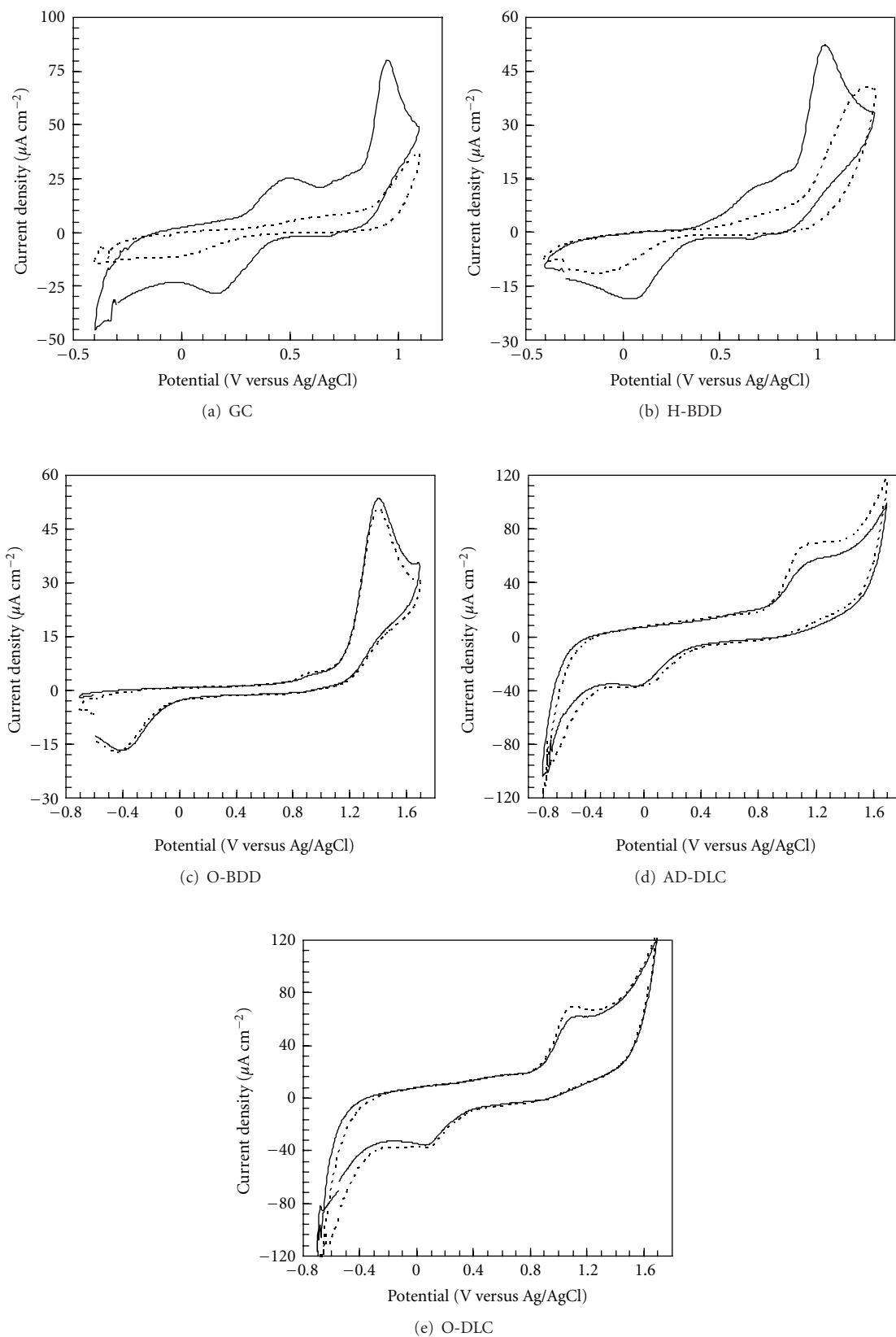


FIGURE 5: Cyclic voltammograms of 0.1 mM 2,4-DCP in the Britton-Robinson buffer (pH 2) at (a) GC, (b) H-BDD, (c) O-BDD, (d) AD-DLC, and (e) O-DLC at initial (solid line) and 30 cycles (dotted line). Sweep rate, 100 mV s⁻¹.

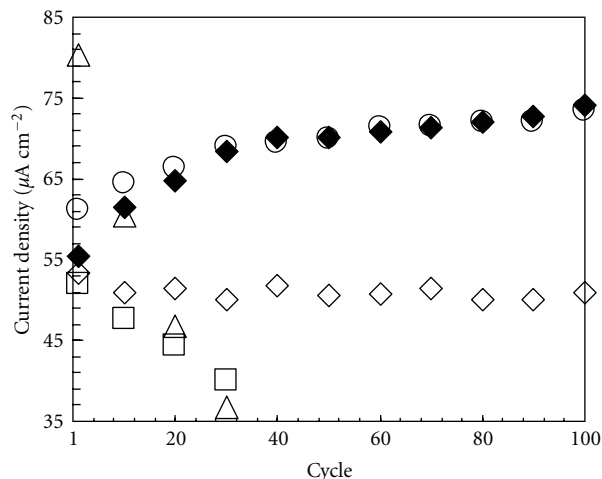


FIGURE 6: Relationship of the number of the potential cycling and the anodic peak current density in cyclic voltammograms of 0.1 mM 2,4-dichlorophenol in the Britton-Robinson buffer (pH 2) at (◆) AD-DLC, (○) O-DLC, (□) H-BDD, (◇) O-BDD, and (△) GC.

observation indicates that OH radicals are available on the DLC surface at higher potential region [30]. At GC, the ratio of the recovered peak current density after anodic treatment to the initial values was relatively lower (0.7) than DLC, and the background current was remarkably increased after surface oxidation (Figure 7(a)).

It can be summarized that DLC exhibits an excellent stability of the electrochemical reaction response for inner-sphere redox species that induce an inevitable fouling of the electrode surface although molecules with polarity are highly adsorbed on the DLC surface. Higher stability at DLC is caused by the production of OH radicals and the negative surface dipolar field on the O-DLC surface. These surface properties were similar to those for BDD.

3.3.5. Selective Electrochemical Detection of Dopamine in the Presence of Uric Acid. While the DLC surface exhibited substantial shift in negative direction of oxidation peak potential for positively charged inner sphere redox species by surface oxidation, the peak potential of the neutral redox compounds at DLC did not vary before and after oxidative treatment. This feature of the oxidized DLC surface makes it possible to discriminate between the dopamine (DA; positively charged) and uric acid (UA; no charge) responses.

In CV of the solution containing single redox analyte at AD-DLC (Figure 8(a)), the peak potential of DA (50 μ M) oxidation was obtained at 0.77 V, and that of UA (50 μ M) was observed at 0.90 V. After oxygen plasma treatment, the peak potential of UA oxidation (in single analyte solution) was observed at 0.88 V with a shift only -20 mV from the peak potential at AD-DLC (Figure 8(b)). In contrast, for DA oxidation at O-DLC, the peak potential was 0.70 V (Figure 8(b)). The value was shifted by approximately

-70 mV from that at the untreated DLC. As a result, by oxidative treatment, the difference between UA and DA peak potentials was increased from 0.13 V to 0.18 V. Cyclic voltammogram of the electrolyte including two-analyte 50 μ M DA and 50 μ M UA at the AD-DLC surface is shown in Figure 8(a). The oxidation peaks for DA and UA were observed at 0.78 V and 0.90 V, respectively. The peak for DA oxidation was not well defined and observed as a shoulder of UA oxidation peak. The peak current densities for DA oxidation showed a linear relation with DA concentration in a range from 5 μ M to 100 μ M in the presence of 50 μ M UA, and the theoretical detection limit of DA detection at AD-DLC was estimated to be 280 nM (S/N = 3).

The cyclic voltammogram obtained at the O-DLC electrode for the solution containing both 50 μ M DA and 50 μ M UA is shown in Figure 8(b). Two well-defined anodic peaks attributable to DA and UA oxidation were observed at 0.70 V and 0.88 V, respectively, and two peaks were clearly separated. The linear relation between the peak current densities and DA concentration was observed in the range from 1 μ M to 250 μ M in the presence of 50 μ M UA at the O-DLC surface. The theoretical detection limit was calculated to be 58 nM (S/N = 3). From these results, it can be concluded that O-DLC allows the selective and highly sensitive (5 times higher) detection of DA compared with AD-DLC from the mixed solution of DA and UA.

At the H-BDD electrode, the oxidation peaks of 50 μ M DA and UA in each solution containing single analyte were observed at 0.77 V and 0.85 V, respectively (Figure 8(c)). On the oxidized BDD surface, the peak potentials of DA and UA oxidation (in single analyte solution) were positively shifted (the peak potential was 0.96 and 0.99 V, resp.). The potential difference was indifferent to the surface condition of BDD. Consequently, voltammograms of a solution containing both 50 μ M DA and 50 μ M UA obtained at both H-BDD and O-BDD (Figures 8(c) and 8(d)) surfaces exhibited a single broad peak. It indicates that BDD could not discriminate DA from the mixed solution of DA and UA.

From these results, by using O-DLC, the kinetics of the positively charged inner-sphere redox species at DLC can be improved by oxidative treatment, the selective detection of the inner-sphere redox species with positive charge such as DA from the mixed media can be realized, which is impossible at BDD. The negative shifts of the oxidation peak potential of inner-sphere redox species (such as DA) at O-DLC can contribute the improvement of the low detection limits by ca. one order of magnitude.

4. Conclusions

Nitrogen-doped hydrogenated amorphous carbon thin films that have a N/C ratio of 0.08 and contain sp^3 -bonded carbons with atomic ratio 22/78 sp^3/sp^2 were synthesized with microwave-assisted plasma-enhanced CVD chemical vapor deposition method. To fabricate the electrode interface with higher electrochemical reactivity and higher stability, the surface were modified by oxygen plasma treatment, and

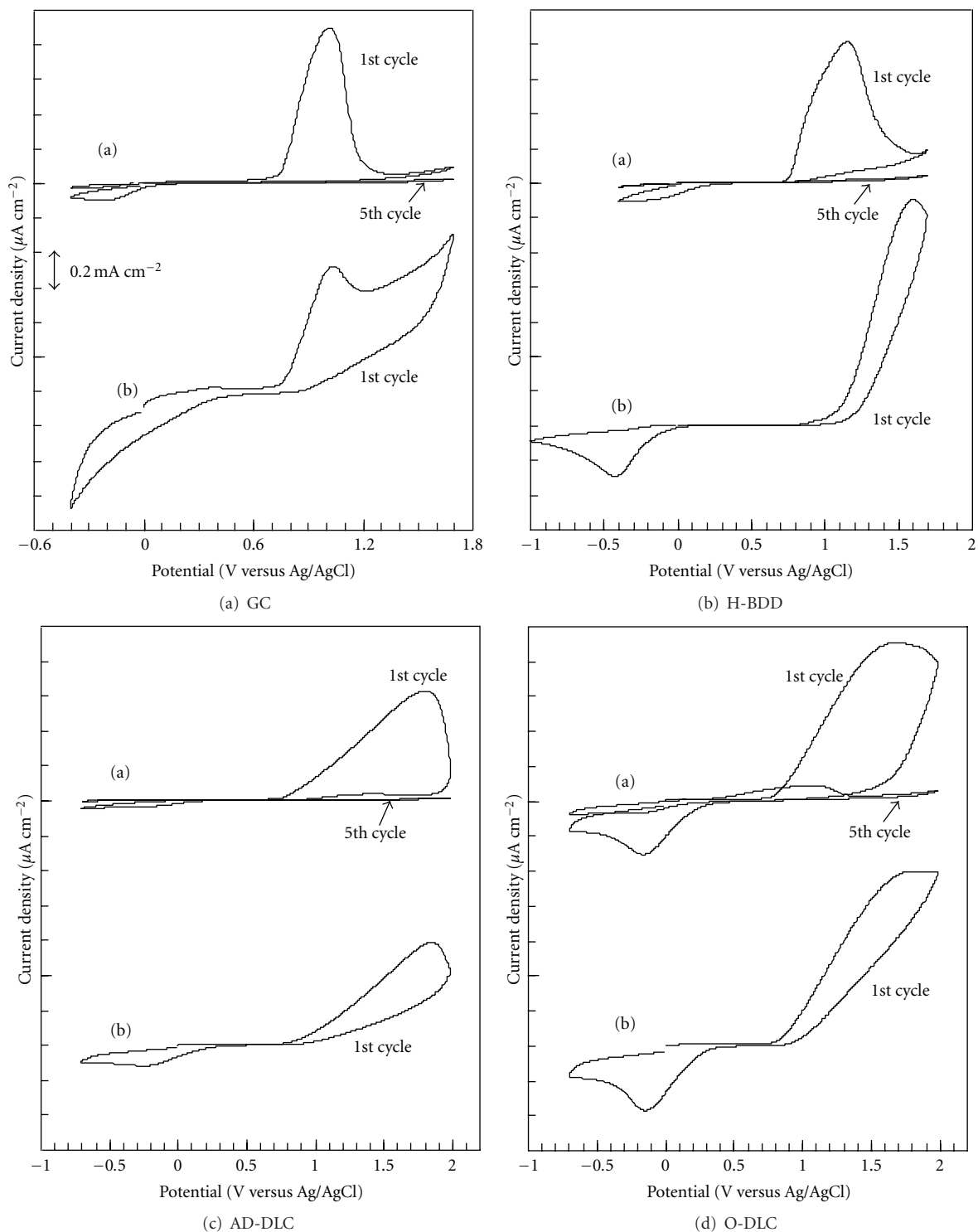


FIGURE 7: Cyclic voltammograms of 5 mM 2,4-DCP in the Britton-Robinson buffer (pH 2) at (a) GC, (b) H-BDD, (c) AD-DLC, and (d) O-DLC at initial (solid line) and 30 cycles (dotted line) (a) before and (b) after the electrochemical treatment at 2.64 V for 4 min. Sweep rate, 100 mV s^{-1} .

the performance and the durability of the oxidized N-doped DLC surface toward electrochemical reaction were evaluated.

The N-doped DLC thin films exhibited a wide working potential range over 3 V, low double-layer capacitance, and reversible electron transfer kinetics for inorganic redox

analytes, $[\text{Fe}(\text{CN})_6]^{3-/4-}$, $\text{Ru}(\text{NH}_3)_6^{2+/3+}$, and $\text{Fe}^{2+/3+}$, which were on the same level as those of BDD.

The electrochemical activity toward the inner-sphere redox species is controllable by modifying the N-DLC surface because N-DLC includes the sp^2 carbons. At the

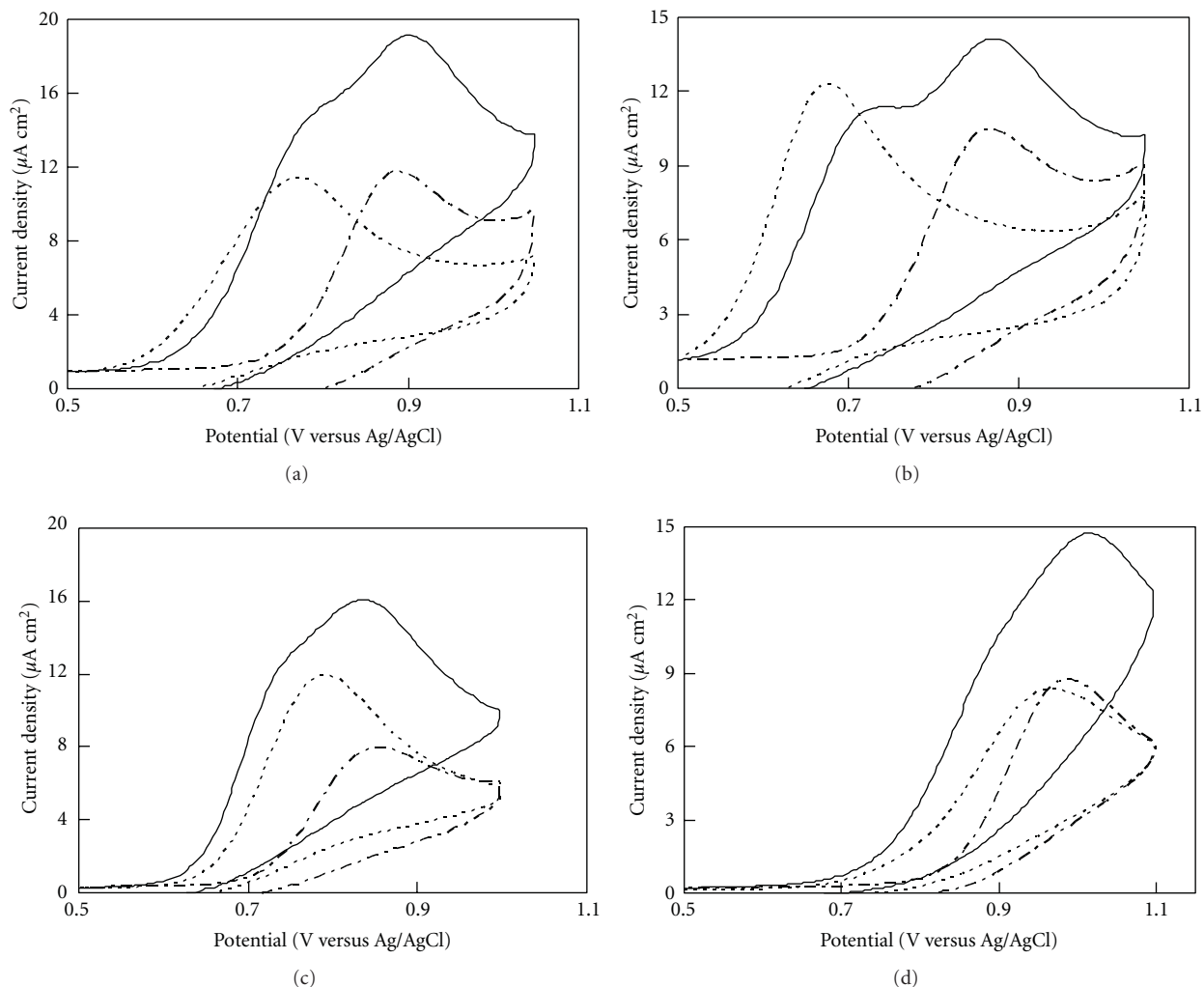


FIGURE 8: Cyclic voltammograms of a solution containing 50 μM dopamine hydrochloride + 50 μM uric acid (solid line), 50 μM dopamine (dotted line) and 50 μM uric acid (dashed-dotted line) at (a) AD-DLC, (b) O-DLC, (c) H-BDD, and (d) O-BDD. Sweep rate, 20 mV s^{-1} .

oxygen-plasma-treated DLC surface, the surface functional groups including carbon doubly bonded to oxygen ($\text{C}=\text{O}$), which improves adsorption of polar molecules, were generated. By this effect, the electron-transfer rate for dopamine, positively charged inner-sphere redox analyte, was improved.

Besides, the AD-DLC and the O-DLC surfaces exhibited remarkably higher stability and reproducibility of the electrode performance, which are close to BDD, for redox reaction of 2,4-DCP which is electrochemically active species and induces the inevitable fouling on the anode surface. These unique electrochemical characteristics of the oxidized surface of DLC make it possible to discriminate between the oxidation peaks of DA and UA in an amperometric measurement for the mixed solution of DA and UA, which was hard at BDD.

Hence, N-doped DLC is a promising ideal polarizable electrode material with higher reactivity and high stability toward inner-sphere redox system and higher physical stability and chemical inertness, alternative to BDD in the future. However, in order to realize the electrochemical applications

using N-doped DLC, there are some problems that should be dealt with. One of them is the higher resistivity of N-doped DLC films.

For example, further functionalities are expected if the comb-like structure can be fabricated using free-standing N-doped DLC thin films. The carrier density of N-doped DLC deposited in this study was not so high. The volume resistivity was approximately three orders of magnitude higher than that of heavily boron-doped diamond. In order to apply the self-standing DLC film in μm order thickness as an electrode with comb-like structures, it is required to reduce the volume resistivity by ca. two orders of magnitude. If the volume resistivity is reduced, N-doped DLC can be applied in a wide range for sure.

References

- [1] J. Xu, M. C. Granger, Q. Chen, J. W. Strojek, T. E. Lister, and G. M. Swain, "Boron-doped diamond thin-film electrodes," *Analytical Chemistry*, vol. 69, no. 19, 1997.

- [2] R. Tenne and C. Lévy-Clément, "Diamond electrodes," *Israel Journal of Chemistry*, vol. 38, no. 1-2, pp. 57–73, 1998.
- [3] K. Yoo, B. Miller, R. Kalish, and X. Shi, "Electrodes of nitrogen-incorporated tetrahedral amorphous carbon. A novel thin-film electrocatalytic material with diamond-like stability," *Electrochemical and Solid-State Letters*, vol. 2, no. 5, pp. 233–235, 1999.
- [4] K. Yoo, B. Miller, X. Shi, and R. Kalish, "Copper electrodeposition and dissolution on tetrahedral amorphous carbon incorporating nitrogen," *Journal of the Electrochemical Society*, vol. 148, no. 2, pp. C95–C101, 2001.
- [5] D. Sopchak, B. Miller, R. Kalish, Y. Avyigal, and X. Shi, "Dopamine and ascorbate analysis at hydrodynamic electrodes of boron doped diamond and nitrogen incorporated tetrahedral amorphous carbon," *Electroanalysis*, vol. 14, no. 7-8, pp. 473–478, 2002.
- [6] N. C. Yee, Q. Shi, W. B. Cai, D. A. Scherson, and B. Miller, "Electrochemical characterization of nitrogen-incorporated tetrahedral carbon films grown by a filtered cathodic vacuum arc," *Electrochemical and Solid-State Letters*, vol. 4, no. 10, pp. E42–E44, 2001.
- [7] A. Zeng, M. M. M. Bilek, D. R. McKenzie, and P. A. Lay, "Correlation of film structure and molecular oxygen reduction at nitrogen doped amorphous carbon thin film electrochemical electrodes," *Diamond and Related Materials*, vol. 18, no. 9, pp. 1102–1108, 2009.
- [8] A. Zeng, M. M. M. Bilek, D. R. McKenzie, and P. A. Lay, "Semiconductor properties and redox responses at a-C:N thin film electrochemical electrodes," *Diamond and Related Materials*, vol. 18, no. 10, pp. 1211–1217, 2009.
- [9] A. Lagrini, C. Deslouis, H. Cachet, M. Benlahsen, and S. Charvet, "Elaboration and electrochemical characterization of nitrogenated amorphous carbon films," *Electrochemistry Communications*, vol. 6, no. 3, pp. 245–248, 2004.
- [10] P. Tamiasso-Martinhon, H. Cachet, C. Debiemme-Chouvy, and C. Deslouis, "Thin films of amorphous nitrogenated carbon a-CN_x: electron transfer and surface reactivity," *Electrochimica Acta*, vol. 53, no. 19, pp. 5752–5759, 2008.
- [11] Y. V. Pleskov, M. D. Krotova, V. I. Polyakov et al., "Electrochemical behaviour of a-C:N:H films," *Journal of Electroanalytical Chemistry*, vol. 519, no. 1-2, pp. 60–64, 2002.
- [12] Y. Tanaka, M. Furuta, K. Kuriyama et al., "Electrochemical properties of N-doped hydrogenated amorphous carbon films fabricated by plasma-enhanced chemical vapor deposition methods," *Electrochimica Acta*, vol. 56, no. 3, pp. 1172–1181, 2011.
- [13] P. Wood, T. Wydeven, and O. Tsuji, "Influence of reactant gas composition on selected properties of N-doped hydrogenated amorphous carbon films," *Thin Solid Films*, vol. 258, no. 1-2, pp. 151–158, 1995.
- [14] L. Boonma, T. Yano, D. A. Tryk, K. Hashimoto, and A. Fujishima, "Observation of photocurrent from band-to-band excitation of semiconducting p-type diamond thin film electrodes," *Journal of the Electrochemical Society*, vol. 144, no. 6, pp. L142–L145, 1997.
- [15] A. C. Ferrari and J. Robertson, "Interpretation of Raman spectra of disordered and amorphous carbon," *Physical Review B*, vol. 61, no. 20, pp. 14095–14107, 2000.
- [16] C. Casiraghi, A. C. Ferrari, and J. Robertson, "Raman spectroscopy of hydrogenated amorphous carbons," *Physical Review B*, vol. 72, no. 8, Article ID 085401, 14 pages, 2005.
- [17] G. Adamopoulos, K. W. R. Gilkes, J. Robertson et al., "Ultraviolet Raman characterisation of diamond-like carbon films," *Diamond and Related Materials*, vol. 8, no. 2–5, pp. 541–544, 1999.
- [18] A. C. Ferrari and J. Robertson, "Raman spectroscopy of amorphous, nanostructured, diamond-like carbon, and nanodiamond," *Philosophical Transactions of the Royal Society A*, vol. 362, no. 1824, pp. 2477–2512, 2004.
- [19] T. Kondo, H. Ito, K. Kusakabe et al., "Plasma etching treatment for surface modification of boron-doped diamond electrodes," *Electrochimica Acta*, vol. 52, no. 11, pp. 3841–3848, 2007.
- [20] H. B. Martin, A. Argoitia, U. Landau, A. B. Anderson, and J. C. Angus, "Hydrogen and oxygen evolution on boron-doped diamond electrodes," *Journal of the Electrochemical Society*, vol. 143, no. 6, pp. L133–L136, 1996.
- [21] I. Yagi, H. Notsu, T. Kondo, D. A. Tryk, and A. Fujishima, "Electrochemical selectivity for redox systems at oxygen-terminated diamond electrodes," *Journal of Electroanalytical Chemistry*, vol. 473, no. 1, pp. 173–178, 1999.
- [22] P. Chen and R. L. McCreery, "Control of electron transfer kinetics at glassy carbon electrodes by specific surface modification," *Analytical Chemistry*, vol. 68, no. 22, pp. 3958–3965, 1996.
- [23] M. C. Granger, M. Witek, J. Xu et al., "Standard electrochemical behavior of high-quality, boron-doped polycrystalline diamond thin-film electrodes," *Analytical Chemistry*, vol. 72, no. 16, pp. 3793–3804, 2000.
- [24] J. Xu, Q. Chen, and G. M. Swain, "Anthraquinonedisulfonate electrochemistry: a comparison of glassy carbon, hydrogenated glassy carbon, highly oriented pyrolytic graphite, and diamond electrodes," *Analytical Chemistry*, vol. 70, no. 15, pp. 3146–3154, 1998.
- [25] Q. Chen and G. M. Swain, "Structural characterization, electrochemical reactivity, and response stability of hydrogenated glassy carbon electrodes," *Langmuir*, vol. 14, no. 24, pp. 7017–7026, 1998.
- [26] Y. Show, M. A. Witek, P. Sonthalia, and G. M. Swain, "Characterization and electrochemical responsiveness of boron-doped nanocrystalline diamond thin-film electrodes," *Chemistry of Materials*, vol. 15, no. 4, pp. 879–888, 2003.
- [27] E. Popa, H. Notsu, T. Miwa, D. A. Tryk, and A. Fujishima, "Selective electrochemical detection of dopamine in the presence of ascorbic acid at anodized diamond thin film electrodes," *Electrochemical and Solid-State Letters*, vol. 2, no. 1, pp. 49–51, 1999.
- [28] D. A. Tryk, H. Tachibana, H. Inoue, and A. Fujishima, "Boron-doped diamond electrodes: the role of surface termination in the oxidation of dopamine and ascorbic acid," *Diamond and Related Materials*, vol. 16, no. 4–7, pp. 881–887, 2007.
- [29] C. Terashima, T. N. Rao, B. V. Sarada, D. A. Tryk, and A. Fujishima, "Electrochemical oxidation of chlorophenols at a boron-doped diamond electrode and their determination by high-performance liquid chromatography with amperometric detection," *Analytical Chemistry*, vol. 74, no. 4, pp. 895–902, 2002.
- [30] K. Honda, Y. Yamaguchi, Y. Yamanaka, M. Yoshimatsu, Y. Fukuda, and A. Fujishima, "Hydroxyl radical-related electrogenerated chemiluminescence reaction for a ruthenium tris(2,2')bipyridyl/co-reactants system at boron-doped diamond electrodes," *Electrochimica Acta*, vol. 51, no. 4, pp. 588–597, 2005.

Research Article

Electrocatalytic Properties of BDD Anodes: Its Loosely Adsorbed Hydroxyl Radicals

Nicolaos Vatistas

DICCISM, University of Pisa, Via Diotisalvi, 2, 6126 Pisa, Italy

Correspondence should be addressed to Nicolaos Vatistas, n.vatistas@diccism.unipi.it

Received 1 May 2011; Accepted 6 July 2011

Academic Editor: Giancarlo R. Salazar-Banda

Copyright © 2012 Nicolaos Vatistas. This is an open access article distributed under the Creative Commons Attribution License, which permits unrestricted use, distribution, and reproduction in any medium, provided the original work is properly cited.

The high oxidative action of boron doped diamond (BDD) anodes on the biorefractory organic compounds has been attributed to the low adsorption of the generated hydroxyl radicals on the BDD surface in respect to other anodic materials. In a previous paper, the effect of low adsorption of BDD has been studied by proposing a continuum approach to represent the adsorption layer. The oxidative action of the hydroxyl radicals is attributed to the values of their diffusivity into the adsorption and adjacent reactive layer as well as to the value of kinetic constant in both layers. In this paper, more details on both layers are reported in order to justify the proposed continuum approach as well as the assumptions concerning diffusivity and kinetic constant in both adsorption and reactive layers, where the oxidative action of hydroxyl radicals occurs.

1. Introduction

The BDD anodes have particular electrocatalytic properties in respect to others, that are, oxygen is generated on its surface, when the anodic overpotential achieves higher values, biorefractory organic species are efficiently eliminated, and peroxide cation are efficiently produced. These specific electrocatalytic properties are attributed to a specific property of the generated hydroxyl radicals HO^\bullet on BDD electrodes in respect to other electrodes [1] that is, these radicals are less adsorbed on the surface of BDD anodes than on the surface of other anodes. In fact, the experimentally detected increase of oxidative action of the anodes $\text{RuO}_2\text{-TiO}_2$, $\text{IrO}_2\text{-Ta}_2\text{O}_5$, Pt, PbO_2 , $\text{SnO}_2\text{-Sb}_2\text{O}_5$, and BDD was attributed to the decreasing electrode-hydroxyl radical interaction resulting in a low electrochemical activity for oxygen evolution reaction and to high chemical reactivity for organics oxidation [2]. The effect of anode-hydroxyl radicals interaction is the formation of a layer of radicals that is defined as *adsorption layer*, so the interactions that form this layer requires further attention.

The term adsorption refers to the process by which species are accumulated on the surface of anode and form a layer adjacent to this surface. In the case of an anode, the adsorbed species of the solution must be transported from

the bulk of the solution in the adsorption layer, while the species that are produced on the anode are immediately available. When such adsorption is due to the universal weak van der Waals interaction, a multilayer of these species is formed, and it is defined *physical adsorption*, while when a stronger and more specific interaction occurs between one species and the electrode, it is assumed that a monolayer is adsorbed and the process is defined as *chemical adsorption*. The interaction which concerns the adsorbed species has been considered by Gibbs [3] by assuming that this layer is two dimensional, that is, a surface. Such treatment, that is characteristic of Gibbs [4] makes easier measurement and studies of energetic aspects of such interfaces. At the same time, this two-dimensional approach is not suitable to study the other aspects that depend on the geometry of this layer.

In the previous paper, it is assumed that the adsorbed species form not a two-dimensional adsorption surface but a three-dimensional thin layer adjacent to the external surface of the anode [5]. In addition, a continuous approach is proposed in this layer that allows to apply the balance equations of the reactive species. Thanks to the use of these tools, the concentrations of reactive species in the adsorption and reactive layer are related to the values of diffusivity and kinetic constants of reactions. The value of the diffusivity

into the adsorption layer was different in respect to the adjacent reactive layer, while similar values of rate constants were adopted. In this paper, more details on the adsorption and reactive layers will be furnished in order to demonstrate both the possibility to apply the continuum approach in the thin adsorption layer and the validity of the proposed different behaviors of diffusivity and kinetic constant into the adsorption and reactive layers.

2. Adsorption Layer

The possibility of the adsorbed species to form a three-dimensional adsorption layer and not an adsorption surface has been demonstrated with the use of high-resolution scanning tunnelling microscopy (STM). Thanks to this technique, the adatoms interaction with each other is quantitatively obtained [6]. Such interaction via mutual perturbation of the surface is known as indirect electronic and elastic weak oscillatory interaction [7, 8]. This is a quantum size effect that induces oscillation in surface charge density near the Fermi level and modulates the adatom surface-binding energies [9]. The effect of the weak and frequent interactions between the adsorbed species have a temporal and spacial smoothing effect on the properties that define this adsorption layer. This smoothing effect is clearly expressed by considering the distribution functions of the various properties that concern this layer. This method is not yet applied in the adsorption field, but such method is not new, and it has been applied in numerous fields [10].

The physical adsorption of species on the various electrodes is due to the universal van der Waals interaction between the electrode and these species. Such interaction between a molecule of this species and the electrode, expressed as potential energy $w_j(z)$, is given by [11]:

$$w_{e,j}z(z) = -\frac{\pi A_{e,j}\rho_e}{6} \frac{1}{z^3}, \quad (1)$$

where $A_{e,j}$ is a specific constant that relate the considered electrode e with species j , ρ_e is the number density of molecules in this anode, and z is the distance between electrode and this molecule. It is interesting to note that the coefficient $A_{e,j}$, of (1), concerns the interaction between the anode e and the species j ; that is, it expresses the specificity of the action between the electrode and adsorbate.

It is considered the case of an electrolyte that shows the following characteristic $A_{e,j} > A_{e,m}$; that is, the previously reported attractive action is higher for the species j than for the other species m . When an electrode is immersed in this electrolyte, the intrinsic chaotic motion of species, due to the temperature, has two opposite effects on the adsorption. The positive effect is that such motion allows the species j to reach the position that optimize the attractive van der Waals interaction. The negative effect is that this motion removes the species j as well as the species m that have just achieved their optimum position. The forward growth rate $r_{f,j}$ of the adsorption concerns the species j , and it is related to the attractive effect, while its backward removal rate $r_{b,j}$ is related to the chaotic motion effect. The stationary state

of adsorption is reached when the whole growth rate ($r = r_{f,j} - r_{b,j}$) becomes zero, and this occurs when a quantity $n_{a,j}$ of molecules has been adsorbed and that adsorbate species form a thin stationary adsorbed layer of constant thickness $\delta_{a,j}$.

3. Transition from the Adsorption to the Adjacent Layer

The main property of the adsorption layer is its higher order in respect to the rest of this solution, and such higher order is attributed to the higher attractive action of the species j of this layer and the electrode e . This order property has a high effect on the quality of the transition of this adsorption layer to the adjacent layer. In order to obtain more details on such transition, the attractive potential concerning the thickness $\delta_j = z_1 - z_0$ of the adsorbed layer is considered [11]

$$W_{e,j}(\delta_j) = -\frac{\pi A_{e,j}\rho_e}{6} \int_{z_0}^{z_0+\delta_j} \frac{\rho_j(z)}{z^3} dz, \quad (2)$$

where z_0 is the minimum distance electrode-adsorbed species j , while $\rho_j(z)$ concerns the number of adsorbed molecules of species j , and z is the distance from the electrode.

As (2) shows, when the distance z reaches a specific value $z_0 + \delta_{a,j}$, the van der Waals interaction that locates the molecules in their optimum positions becomes lower than the chaotic motion due to the temperature that removes these species from the achieved optimum positions. The consequence is a reduction of the density $\rho_j(z_0 + \delta_{a,j})$, and as (2) points out, it introduces an additional reduction of the van der Waals interaction. The synergism of two negative effects (longer distance and lower density) suggests that when the distance reaches this specific value ($\delta_{a,j}$), a rather sharp transition is observed; that is, the layer that is inside this distance is ordered, while outside this layer, the species are subject to a chaotic motion.

Such sharp variation of the properties of adsorption layer assures a good definition of adsorbed layer, and by assuming a constant mean value of density $\rho_j(z)$, that is, $\bar{\rho}_j = \rho_j(z)$, (2) can be integrated, and the attractive potential of the adsorption layer is related to its thickness $\delta_{a,j}$

$$W_{e,j}(\delta_{a,j}) = -\frac{\pi A_{e,j}\rho_e\bar{\rho}_j}{12} \left[\frac{1}{(z_0 + \delta_{a,j})^2} - \frac{1}{z_0^2} \right]. \quad (3)$$

Experimental results show that the adsorbed Cu on the Cu(111) surface can reach a range of over 6 nm, and this interaction decays as a function consistent with the inverse z^2 dependence [12]. It is interesting to note that also the value of the interaction obtained by (3) shows a similar decay.

4. Properties of the Adsorption Layer

As previously reported, the adsorption is represented as a two-dimensional layer, and then, the kinetic theory of particle-on-substrate diffusion is a two-dimensional diffusion; that is, it is assumed that the adsorbate forms a single

layer of adsorbate, and then the diffusion occurs along such adsorbate surface. Such single layer assumption limits the possibility to represent the diffusion process. The proposed two-dimensional diffusion theory along such single layer represents explicitly the molecule surface interaction as well as accounting for intermolecular interaction. More specifically, the molecule-surface interaction has been represented by assuming not a continuum but a discrete adsorption sites approach characterized by the lattice spacing l , the intersite potential barriers V_m , and the frequency of molecular vibration in the sites ν [13].

4.1. Anisotropic Diffusivity into the Adsorption Layer. A preliminary attention is required in order to consider the effect of the morphology of the anode and in particular its external surface on the adsorption. The deviation of such real surface from the geometric plane is commonly defined as roughness. A more exact definition of this surface can be obtained by considering locally its tangent plane, and the deviation of the anodic surface by this tangent plane is defined by the two principal radii of curvature R_1 and R_2 . Low values of these radii indicate high deviation from the plane and then a high local roughness. If the thickness of the previous defined adsorption layer is lower than curvature radii ($\delta_{a,j} \ll R_1$ and $\delta_{a,j} \ll R_2$), the normal and parallel directions of the surface of electrode can be defined locally with respective axes (z, x), and the validity of the previous equations (1)–(3) is assured.

If it is assumed that the adsorption layer has a thickness $\delta_{a,j}$, and the diffusivity of the species j , in the direction that is parallel to the surface of electrode $D_{a,p,j}(z)$, can be defined, and its value depends on z . The mean value of this parallel diffusivity $\bar{D}_{a,p,j}$ is estimated

$$\bar{D}_{a,p,j} = \frac{\int_0^{\delta_{a,j}} D_{a,p,j}(z) dz}{\delta_{a,j}}. \quad (4)$$

The assumption that the adsorption of species j forms a layer of thickness $\delta_{a,j}$ imposes to consider the diffusion of this species in the direction that is normal to the surface of the electrode. Even in this case, the value of the diffusivity is $D_{a,n,j}(z)$; that is, it depends on the distance z , from the anodic surface, and its mean value $\bar{D}_{a,n,j}$ can be estimated as in the case of diffusivity in the direction that is parallel to the electrode of surface.

$$\bar{D}_{a,n,j} = \frac{\int_0^{\delta_{a,j}} D_{a,n,j}(z) dz}{\delta_{a,j}}. \quad (5)$$

If the mean values of normal diffusivity is different from the parallel diffusivity ($\bar{D}_{a,n,j} \neq \bar{D}_{a,p,j}$), the diffusion process of the species j into the adsorption layer is not isotropic.

4.1.1. Relationship between Surface Diffusivity and Parallel Diffusivity. The proposed diffusivity in the parallel direction has not yet been considered in this field, because the adsorption layer has been so far represented as a surface ($\delta_{a,j} \rightarrow 0$). The diffusivity in this last case is defined as

surface diffusivity $D_{s,j}$, and its value must be related to the mean diffusivity in the parallel direction defined in this paper $\bar{D}_{a,p,j}$. In order to obtain this relationship, it is considered the diffusive flow of adsorbate $N_{a,p,j}$ in the adsorption layer according to a direction x that is parallel to the surface of electrode, whose value is

$$N_{a,p,j} = -\bar{D}_{a,p,j} \frac{dC_{a,V,j}}{dx} \delta_{a,j} L. \quad (6)$$

The flow obtained above is equal to the flow $N_{a,s,j}$ that is estimated considering not a layer but a surface absorption, and its value is

$$N_{a,s,j} = -D_{a,s,j} \frac{dC_{a,S,j}}{dx} L, \quad (7)$$

where $C_{a,V,j}$ is the volume concentration used in the case of adsorption layer, $C_{a,S,j}$ is the surface concentration that is used in the case of adsorption surface, and L is the unit length of two- and three-dimensional layers. These concentrations are not independent and their relationship is

$$C_{a,S,j} = \delta_{a,j} C_{a,V,j}. \quad (8)$$

By combining (6), (7), and (8), it is obtained that the mean value of the parallel diffusivity introduced in this paper is equal to the value of the surface diffusivity that has been measured experimentally

$$\bar{D}_{a,p,j} = D_{a,s,j}. \quad (9)$$

Consequently, the available experimental values as well as the estimated values of the surface diffusivity can be used to estimate the introduced in this paper mean parallel diffusivity.

4.1.2. Comparison between Normal and Parallel Diffusivity.

Two different kinds of interactions occurs on the adsorbate j , the substrate-adsorbate and the adsorbate-adsorbate interactions due to induced dipole-induced dipole action. The substrate-adsorbate interaction acts principally at a direction that is normal to the surface of the electrode, while the adsorbate-adsorbate interaction acts principally at a direction that is parallel to the anodic surface. The previous consideration on the specificity of these interactions imposes to assume that the substrate-adsorbate interaction is higher in respect to the adsorbate-adsorbate interaction. In other words, the binding action in the direction that is normal to the electrode surface is higher in respect to the binding action in the direction that is parallel to the same surface.

At a higher binding, action corresponds a higher restriction of motion that concern the adsorbed species j and then a lower value of diffusivity [14]. Consequently, the diffusivity of the species j into the adsorption layer is anisotropic and specifically the value of the diffusivity in the normal direction is lower of its value in the parallel direction respect to the surface of electrode

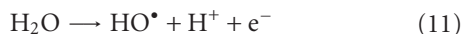
$$\bar{D}_{a,n,j} < \bar{D}_{a,p,j}. \quad (10)$$

The diffusion according to the parallel diffusion is also known as *intralayer* or *across a step* transport, while the diffusion according to the normal direction is known as *interlayer* transport [15]. Experimental observations with field ion microscope (FIM) confirms the above theoretical conclusion, that is, diffusivity according to the normal direction assumes low values [16]; that is, the diffusivity in the adsorption layer is not a scalar but a vector.

The high contribution of surface diffusion in the whole diffusion process into the porous materials [17] points out that the value of surface diffusivity and then the mean value of diffusivity parallel to electrode surface are relatively high. The anisotropy of the diffusivity in the adsorption layer assures that the concentration value of adsorbate species j is practically constant in the direction that is parallel to the anodic surface x , while its value change along the normal direction [$C_{a,j}(z)$].

5. Electrolyte Absent of Hydroxyl Radicals Trappers

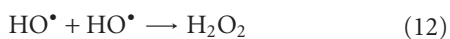
When the anode is operating, the oxidative species j are generated on the anodic surface, and such species enter into the adsorption layer. The escape of these species from the anodic surface is assume instantaneous in this paper. If such species are subjected to attractive action by the anode, its diffusivity $\bar{D}_{a,n,j}$ assumes a low value, and then, the generated species remain for longer time into the adsorption layer. Normally, these oxidative species react between them or oxidise other species, and the consequence of longer permanence in the adsorption layer is the higher consumption of these species. The final effect is that a lower fraction of the generated species escapes from the adsorption layer and achieves the adjacent region. In the case of a BDD anode, the oxidative species are the hydroxyl radicals HO^\bullet that are generated according the following electrochemical reaction [18, 19]:



The flow of the generated hydroxyl radicals is related to the value of the applied anodic current density i_{appl} .

The electrolyte contains other species like biorefractory organic species R in the case of the elimination of this organic species or anions like SO_4^{2-} and CO_3^{2-} in the case of the production of peroxide. The oxidation of these species occurs thanks to the trapping of the freshly generated hydroxyl radicals by these species. In order to point out the principal characteristics of adsorption and adjacent layers, in this paper, the absence of trapped species is assumed.

5.1. Reaction of Hydroxyl Radicals into the Adsorption Layer. If the electrolyte is absent of hydroxyl radicals trappers, the generated hydroxyl radicals that enter in the adsorption layer react with each other to produce hydrogen peroxide according to the following reaction:



when the rate of the reaction (12) follows the second order law

$$-r_{a,\text{HO}^\bullet}(z) = k_{a,\text{HO}^\bullet} C_{a,\text{HO}^\bullet}^2(z), \quad 0 \leq z \leq \delta_{a,\text{HO}^\bullet}, \quad (13)$$

where k_{a,HO^\bullet} is the constant of the reaction rate (13) within the adsorption layer and $C_{a,\text{HO}^\bullet}(z)$ is the concentration of hydroxyl radicals in the same layer.

5.2. Reaction of Hydroxyl Radicals into the Adjacent Reactive Layer. If the generated radicals are not totally consumed into the adsorption layer by the reaction (12), a portion of the generated radicals escapes from the adsorption layer and achieves the adjacent region when this reaction continues to occur. It is assumed that the rate of the reaction (12) in this layer assume a similar expression:

$$-r_{a,\text{HO}^\bullet}(z) = k_{r,\text{HO}^\bullet} C_{a,\text{HO}^\bullet}^2(z), \quad \delta_{a,\text{HO}^\bullet} \leq z \leq \delta_{r,\text{HO}^\bullet}, \quad (14)$$

where k_{r,HO^\bullet} is the constant of the reaction rate (13) into the reactive layer and $C_{a,\text{HO}^\bullet}^2(z)$ is the concentration of hydroxyl radicals into this layer.

5.2.1. Rate Constant into the Adsorption and Reactive Layers. It is interesting to note that despite the occurring same reaction (12), different values of reaction rate constant have been assumed for the adsorption and reactive layers (k_{a,HO^\bullet}) and (k_{r,HO^\bullet}). The different values have been assumed, because the reaction into the adsorption layer concerns hydroxyl radicals that are partially embedded by the attractive action electrode-hydroxyl radicals, while the same reaction into the reactive layer concerns hydroxyl radicals that are freely moved into the electrolyte solution.

Other conditions being equal, an increase in diffusivity follows an increase in the chaotic movement of species that react with an increase in collisions between them, and thus the increase of the reaction rate constant. As previously reported, the diffusivity in the adsorption layer is anisotropic, and then, the principal contribution on the reaction rate is due to the high value of chaotic motion that is parallel to the surface of electrode. In the adjacent reactive layer, the diffusivity is isotropic, and its value is surely higher than the normal diffusivity in the adsorption lower and probably higher than the parallel diffusivity, and then, the comparison of the collisions in the two layers is not an easy task.

6. Adsorption, Reaction, and Diffusion Layers

In the adsorption layer, two events characterize this layer, the interactions in hydroxyl radicals electrode and the reaction (12), while the adjacent layer is characterized by the occurring of the reaction (12), and for this reason, it is defined as *reactive layer*. The events that characterize both adsorption and reaction layer concern the generated hydroxyl radicals on the surface of the anode. Consequently, the existence of the two layers depends on the rate of the generated radicals, and when the anodic surface does not generate hydroxyl radicals, both radicals are absent

$$\delta_{a,\text{HO}^\bullet} = \delta_{r,\text{HO}^\bullet} = 0. \quad (15)$$

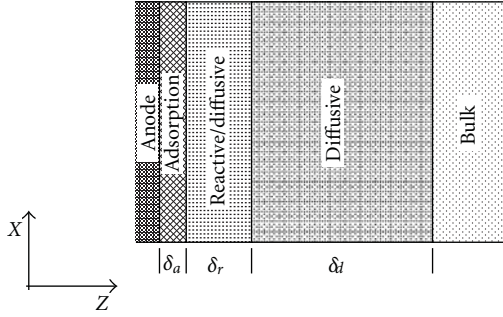


FIGURE 1: Scheme of anode with the adjacent layers of the solution (not in scale).

While when this generation rate is high, both adsorption and reaction layers are present

$$0 \leq \delta_{a,\text{HO}\cdot} \leq \delta_{r,\text{HO}\cdot}. \quad (16)$$

In fact, in the last case, a high number of hydroxyl radicals are generated, and a fraction of these radicals are not transformed to hydrogen peroxide in the adsorption layer according to the reaction (12), and such fraction achieves the adjacent reactive layer, where it reacts and form hydroxyl peroxide.

The two adjacent layers adsorption and reaction are schematically indicated in Figure 1, along with the diffusion layer of thickness δ_d . In this case, through such layer, the generated hydrogen peroxide is transported to the bulk of the electrolyte.

The adopted continuum approach on the adsorption and reactive layers allows to apply the differential balance of hydroxyl radical, and the equation of this balance assumes the following form in the adsorption layer [18]:

$$\bar{D}_{a,n,\text{HO}\cdot} \frac{d^2 C_{a,\text{HO}\cdot}}{dz^2} = k_{a,\text{HO}\cdot} C_{a,\text{HO}\cdot}^2; \quad 0 \leq z \leq \delta_a, \quad (17)$$

while a similar equation is obtained for the subsequent reactive layer

$$D_{r,\text{HO}\cdot} \frac{d^2 C_{r,\text{HO}\cdot}}{dz^2} = k_{r,\text{HO}\cdot} C_{r,\text{HO}\cdot}^2; \quad \delta_a \leq z \leq \delta_r. \quad (18)$$

The balance equation that concerns the adsorption layer assumes the following dimensionless form:

$$\frac{d^2 y_a}{d\xi_a^2} = y_a^2; \quad 0 \leq \xi_a \leq \frac{\delta_a}{\lambda_a}, \quad (19)$$

while a formally similar equation is obtained for the successive reactive layer

$$\frac{d^2 y_r}{d\xi_r^2} = y_r^2; \quad \frac{\delta_a}{\lambda_a} \leq \xi_r \leq \frac{\delta_r}{\lambda_a}, \quad (20)$$

where y_a and y_r are the dimensionless concentrations of hydroxyl radicals into the adsorption and reactive layers

$$y_a = \frac{C_{\text{HO}\cdot,a}}{C_{\text{HO}\cdot}(0)}, \quad y_r = \frac{C_{\text{HO}\cdot,r}}{C_{\text{HO}\cdot}(0)}, \quad (21)$$

where $C_{\text{HO}\cdot}(0)$ is the concentration of hydroxyl radical in the region of the adsorption layer that is adjacent to the electrode. Two characteristic parameters were introduced having the dimension of length, the first concerning the adsorption layer λ_a , and the second concerning the reactive layer λ_r . Such parameters are obtained by combining the various parameters of (17) and (18)

$$\lambda_a = \sqrt{\frac{\bar{D}_{a,n,\text{HO}\cdot}}{k_{a,\text{HO}\cdot} C_{\text{HO}\cdot}(0)}}; \quad \lambda_r = \sqrt{\frac{D_{r,\text{HO}\cdot}}{k_{\text{HO}\cdot} C_{\text{HO}\cdot}(0)}}. \quad (22)$$

The above parameters are defined as *characteristic lengths* of the adsorption λ_a , and reactive layer λ_r and these lengths are used to define the two dimensionless distances: $\xi_a = z/\lambda_a$ and $\xi_r = z/\lambda_r$. The characteristic length of reactive layer λ_r is related to parameters that are usually available, and by considering a diffusion coefficient $D_{r,\text{HO}\cdot} = 2.2 \cdot 10^{-9} \text{ m}^2 \text{ s}^{-1}$, a rate constant $k_{\text{HO}\cdot} = 5.5 \cdot 10^6 \text{ mol}^{-1} \text{ s}^{-1}$, and a concentration $C_{\text{HO}\cdot}(0) = 0.1 \text{ mol dm}^{-3}$, the value of the characteristic length of reactive layer is 32 nm [5], while the estimation of characteristic length λ_a that concerns the adsorption layer is more complicate. In this paper, it is assumed that all the generated hydroxyl radicals on the anodic surface achieve immediately the adjacent region of adsorption layer. The value of λ_a is a measure of survival distance of hydroxyl radicals while they moved into the adsorption layer, while the value of λ_r is a measure of survival distance in the reactive layer.

6.1. Adsorption Layer and Adsorption Parameter. The thickness of the adsorption layer δ_a is a parameter that define the geometry of this layer, but this value is not enough to relate adsorption state of hydroxyl radicals with the reaction and diffusion. An ulterior parameter is required that is obtained by considering the ratio of the previously introduced characteristic adsorption and reactive layers

$$\beta = \frac{\lambda_a}{\lambda_r} = \sqrt{\frac{\bar{D}_{a,n,\text{HO}\cdot} k_{r,\text{HO}\cdot}}{D_{r,\text{HO}\cdot} k_{a,\text{HO}\cdot}}}. \quad (23)$$

This ratio is also a dimensionless number that compares the known constants of the two mechanisms in the reactive layer to the responding unknown constants into the adsorption layer.

In this paper, it is assumed that the values of rate constants in the two layers are approximately equal ($k_{a,\text{HO}\cdot} \approx k_{r,\text{HO}\cdot}$), while the value of the normal diffusivity in the adsorption layer is smaller than the diffusivity value in the reactive layer ($\bar{D}_{a,n,\text{HO}\cdot} < D_{r,\text{HO}\cdot}$). The values of β is, therefore, between zero and one ($0 < \beta < 1$), and when $\beta \rightarrow 1$, the effect of the adsorption is very weak, while this effect becomes strong when $\beta \rightarrow 0$.

The analytic solution of (19) has been obtained in the previous paper [5], and such solution in the adsorption layer assumes the following form:

$$y_a = \frac{1}{(\sqrt{8/3}\xi_a + 1)^2}; \quad 0 \leq \xi_a \leq \frac{\delta_a}{\lambda_a}. \quad (24)$$

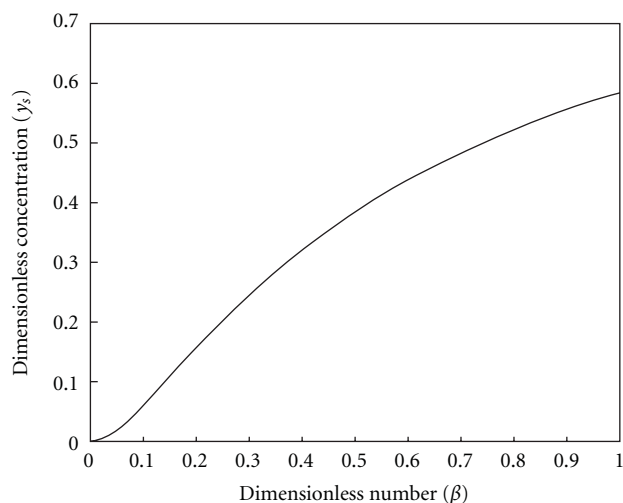


FIGURE 2: Dimensionless concentration y_a versus dimensionless number β ($\delta = 6$ nm and $\lambda_r = 32$ nm).

Equation (24), that represents the dimensionless concentration of hydroxyl radical, is calculated at the outside of the adsorption layer when $\delta_a = 6$ nm and $\lambda_r = 32$ nm and various values of β .

Figure 2 reports the obtained concentration outside the adsorption layer ($\xi_a = \delta_a/\lambda_a$). These results indicate that when the adsorbing property of this layer becomes strong ($\beta \rightarrow 0$), all the generated hydrogen radicals on the anodic surface are eliminated on the adsorption layer, and the hydroxyl radical cannot be detected. In the opposite condition, that is, when the value of $\beta \rightarrow 1$, as in the case of BDD anodes, the adsorbing property is very weak, a high portion of the generated radicals escape from the adsorption layer, and these radicals can be detected by using suitable trappers of these radicals, as N,N-dimethyl-p-nitrosoaniline [20]. It is evident that also the organic compounds as well as anions like sulfate and carbonate trap the hydroxyl radicals.

7. Conclusions

The high oxidative action of BDD anodes has been attributed to its property to adsorb loosely the generated hydroxyl radicals on its surface. This paper contains more elements of the continuum approach theory of hydroxyl radicals adsorption proposed in a previous paper. Such continuum approach allows to obtain many details on the occurring mechanisms into the adsorption layer unobtainable by other approaches. The critical point of such continuum approach is its apparent contradiction with the continuity condition of the properties of this thin layer.

Recent scanning tunnelling microscopy results allow to determine the thickness of this adsorption layer as well as its dynamic state that has quantum size properties (weak oscillating interactions). For an absorbing film, with a such dynamic state, the perturbation theory suggests to represent its particles and its properties in terms of distribution functions. These distribution functions are continuous, and

then, the previously reported contradiction has been avoided thanks to the use of such functions.

In the previous paper, it is assumed that the diffusivity in the adsorption layer is lower than in the adjacent reactive layer. The attractive interaction electrode-hydroxyl radical and mobility of these radicals has been considered in this paper, and such interaction between attraction and mobility points out the validity of the previous assumption on the diffusivity. Moreover, this interaction suggests that the diffusivity in the adsorption layer has an anisotropic property, and more precisely, it is a vector.

In this paper, the adsorption layer has been characterized by its thickness and parameters of diffusivity and rate constants in respect to the adjacent reactive layer.

The fraction of generated hydroxyl radicals that escapes from the adsorption layer and achieves the adjacent reactive layer has been estimated at different values of adsorbing parameter. The obtained results point clearly out the capacity of BDD to generate hydroxyl radicals that are not consumed in the adsorption layer, and then, they are available to oxidize other organic or inorganic species.

References

- [1] J. Iniesta, P. A. Michaud, M. Panizza, G. Cerisola, A. Aldaz, and C. Comninellis, "Electrochemical oxidation of phenol at boron-doped diamond electrode," *Electrochimica Acta*, vol. 46, no. 23, pp. 3573–3578, 2001.
- [2] A. Kapalka, G. Fóti, and C. Comninellis, "Basic principles of the electrochemical mineralization of organic pollutants for wastewater treatment," in *Electrochemistry for the Environment*, C. Comninellis and G. Chen, Eds., Springer, New York, NY, USA, 2010.
- [3] J. W. Gibbs, *Collected Works*, vol. 1, Longmans, London, UK, 1928.
- [4] E. Schrödinger, *Statistical Thermodynamics*, CUP, London, UK, 1946.
- [5] N. Vatisas, "Adsorption layer and its characteristic to modulate the electro-oxidation runaway of organic species," *Journal of Applied Electrochemistry*, vol. 40, no. 10, pp. 1743–1750, 2010.
- [6] L. Österlund, M. Ø. Pedersen, I. Stensgaard, E. Lægsgaard, and F. Besenbacher, "Quantitative determination of adsorbate-adsorbate interactions," *Physical Review Letters*, vol. 83, no. 23, pp. 4812–4815, 1999.
- [7] T. T. Tsong, C. S. Chang, I. S. Hwang et al., "Electron and atom dynamics at solid surfaces and relation to epitaxy," *Journal of Physics and Chemistry of Solids*, vol. 62, no. 9-10, pp. 1689–1730, 2001.
- [8] N. Knorr, H. Brune, M. Epple, A. Hirstein, M. A. Schneider, and K. Kern, "Long-range adsorbate interactions mediated by a two-dimensional electron gas," *Physical Review B*, vol. 65, no. 11, article 115420, 2002.
- [9] L.-Y. Ma, L. Tang, Z.-L. Guan et al., "Quantum size effect on adatom surface diffusion," *Physical Review Letters*, vol. 97, no. 26, article 266102, 2006.
- [10] J. Awrejcewicz, I. V. Andrianov, and L. I. Manevitch, *Asymptotic Approaches in Nonlinear Dynamics*, Springer, Berlin, Germany, 1998.
- [11] J. N. Israelachvili, *Intermolecular and Surface Forces*, Academic Press, London, UK, 1992.

- [12] J. Repp, F. Moresco, G. Meyer, and K. H. Rieder, "Substrate mediated long-range oscillatory interaction between adatoms: Cu/Cu(111)," *Physical Review Letters*, vol. 85, no. 14, pp. 2981–2984, 2000.
- [13] S. Y. Krylov, J. J. M. Beenakker, and M. C. Tringides, "On the theory of surface diffusion: kinetic versus lattice gas approach," *Surface Science*, vol. 420, no. 2-3, pp. 233–249, 1999.
- [14] S. Miret-Artés and E. Pollak, "The dynamics of activated surface diffusion," *Journal of Physics—Condensed Matter*, vol. 17, no. 49, p. S4133, 2005.
- [15] H. Ibach, *Physics of Surfaces and Interfaces*, Springer, Berlin, Germany, 2006.
- [16] G. Ehrlich and F. G. Hudda, "Atomic view of surface self-diffusion: tungsten on tungsten," *The Journal of Chemical Physics*, vol. 44, no. 3, pp. 1039–1049, 1966.
- [17] K. Miyabe and G. Guiochon, "Measurement of the parameters of the mass transfer kinetics in high performance liquid chromatography," *Journal of Separation Science*, vol. 26, no. 3-4, pp. 155–173, 2003.
- [18] A. Kapalka, G. Fóti, and C. Comninellis, "The importance of electrode material in environmental electrochemistry: formation and reactivity of free hydroxyl radicals on boron-doped diamond electrodes," *Electrochimica Acta*, vol. 54, no. 7, pp. 2018–2023, 2009.
- [19] T. A. Enache, A. M. Chiorcea-Paquim, O. Fatibello-Filho, and A. M. Oliveira-Brett, "Hydroxyl radicals electrochemically generated in situ on a boron-doped diamond electrode," *Electrochemistry Communications*, vol. 11, no. 7, pp. 1342–1345, 2009.
- [20] C. Comninellis, "Electrocatalysis in the electrochemical conversion/combustion of organic pollutants for waste water treatment," *Electrochimica Acta*, vol. 39, no. 11-12, pp. 1857–1862, 1994.

Research Article

Benzene Oxidation on Boron-Doped Diamond Electrode: Electrochemical-Impedance Study of Adsorption Effects

Yuri Pleskov, Marina Krotova, Valerii Elkin, Valentin Varnin, and Irina Teremetskaya

Frumkin Institute of Physical Chemistry and Electrochemistry, Russian Academy of Sciences, Leninskii pr. 31, 119991 Moscow, Russia

Correspondence should be addressed to Yuri Pleskov, pleskov@electrochem.msk.ru

Received 29 March 2011; Revised 24 May 2011; Accepted 25 May 2011

Academic Editor: Carlos Alberto Martinez-Huitle

Copyright © 2012 Yuri Pleskov et al. This is an open access article distributed under the Creative Commons Attribution License, which permits unrestricted use, distribution, and reproduction in any medium, provided the original work is properly cited.

Benzene oxidation at a boron-doped diamond anode in 0.5 M K_2SO_4 aqueous solution is studied by cyclic voltammetry and electrochemical impedance spectroscopy. It is shown by measurements of differential capacitance and anodic current that in the ideal-polarizability potential region benzene either is not adsorbed at the diamond electrode or the benzene adsorption does not affect its capacitance. At more positive potentials, the adsorption of some intermediate of the benzene oxidation occurs at the electrode. The intermediate partially blocks the electrode surface and lowers the anodic current. The very fact of the electrode surface blocking is reflected in the complex-plane presentation of the impedance-potential plots.

1. Introduction

Boron-doped diamond (BDD) proved being a corrosion-stable electrode material, particularly suitable for deep anodic oxidation [1]. Indeed, the diamond electrode makes it possible reaching high anodic potentials at which hydroxyl radicals (OH^\bullet) are formed at the anode surface (the oxygen evolution overpotential for diamond is sufficiently large, so this electrochemical reaction occurs with high current efficiency). The radicals oxidize organic and inorganic solutes (carboxylic acids, alcohols, phenols, aromatics) in the course of homogeneous chemical reaction. For this process, a kinetic model was suggested [2], according to which one of the two oxidation mechanisms is realized. In the potential region, where water is electrochemically stable, direct electron transfer occurs, whereas at high anodic potentials, indirect oxidation involving the above-mentioned hydroxyl radicals as mediator takes place (with concurrent oxygen evolution). The anodic oxidation at boron-doped diamond is an effective method of the nature and waste water purification from organic and inorganic pollutants [3, 4].

Benzene and its derivatives are typical water pollutants. The benzene oxidation at boron-doped diamond in 0.5 M H_2SO_4 solution was studied in [5]. It was shown by using high-performance liquid chromatography that a mixture of

the benzene oxidation intermediates (hydroquinone, resorcinol, *p*-benzoquinone, catechol, and phenol) was formed in solution at the anode potential of 2.5 V (versus Ag/AgCl-electrode). The benzene complete incineration yielding CO_2 occurs at potentials more positive than 2.5 V. In our preceding paper [6], the benzene oxidation at boron-doped diamond anode was studied in 1 M HCl solution by electrochemical impedance spectroscopy, with special emphasis on the revealing of the role of adsorption in the process.

In this work, the benzene oxidation at boron-doped diamond anode was studied by electrochemical impedance spectroscopy with the purpose of having deeper insight in the oxidation process, in particular, in some delicate effects caused by the adsorption of benzene-oxidation intermediates at the electrode.

2. Experimental

2.1. Growth of Boron-Doped Diamond Films. Boron-doped diamond films were grown using hot-filament technique, by the depositing of diamond onto conducting silicon wafers from activated reaction gas phase. The gas phase activation was accomplished using a row of tungsten filaments arranged horizontally over the substrate surface at a distance of 5–10 mm. The filaments were heated up to $\sim 2000^\circ C$. The

activator temperature was measured by monochromatic optical pyrometer through quartz window in the upper part of the reactor cap. The purpose of the activation is the formation, in the reaction gas, of large concentration of atomic hydrogen that ensures the selectivity of carbon deposition in the form of diamond.

A mixture of pure methane (ca. 1.2 vol%) with hydrogen (ultra-high purity grade, mark A, the Nauka Company production) was subjected to the activation. The gas mixture composition was controlled by automated gas flow regulators; the full pressure in the reaction gas mixture was 30–36 Torr.

The substrates were KDB-10 silicon plates sized 12 by 12 by 1 mm; the silicon resistivity was 10 Ohm cm. The substrates were arranged on water-cooled substrate holder, in particular, a copper table provided with heater that maintained a preset temperature 850–890°C. The substrate temperature was measured at the substrates' rear side by another optical pyrometer through a special channel in the sample holder.

To impart sufficiently large conductivity to the diamond films, they were doped, during their deposition, with boron. To this purpose, the reaction gas mixture was added by acetone-methanol-trimethylborate solution vapors. The B/C concentration ratio in the reaction mixture was estimated as 2500–3500 ppm.

To shorten the crystallization incubation time and set up high diamond crystallization-center density, the substrate surface was polished by superdispersed diamond polishing paste. The film average thickness was determined by sample weighing prior to and after the film growth; it came to $\sim 18 \mu\text{m}$.

The as-grown films were subjected to heating in air at 520–530°C for 20 min, to free the diamond surface from traces of nondiamond carbon. The nondiamond carbon has been deposited from the reaction gas phase after its activation has been ceased, that is, at the poorly controlled final deposition stage, during the samples cooling in the reactor.

2.2. Electrochemical Measurements. Electrochemical cell-comprised diamond working electrode and platinum auxiliary electrode; the interelectrode distance was 5–7 mm. The anodic and cathodic compartments were not separated. The substrate with diamond film was pressed up to polished flange of round opening in the glass cell wall; a Teflon ring served as gasket. The working electrode active surface area was $\sim 0.3 \text{ cm}^2$. All values of current, differential capacitance, and impedance components are given per 1 cm^2 of geometrical surface.

The impedance spectra were taken using a SOLARTRON SI 1280B spectra analyzer (Great Britain) in two modes: “*f*-sweep” (over 1 Hz to 20 kHz frequency range) and “*E*-sweep”. At special cases, the impedance was measured using an R-5021 ac bridge (Kiev, Ukraine) over 20 Hz to 200 kHz frequency range.

Potentiodynamic curves were taken using the SOLARTRON SI 1280B instrument. We used 0.5 M K_2SO_4 solution as indifferent electrolyte.

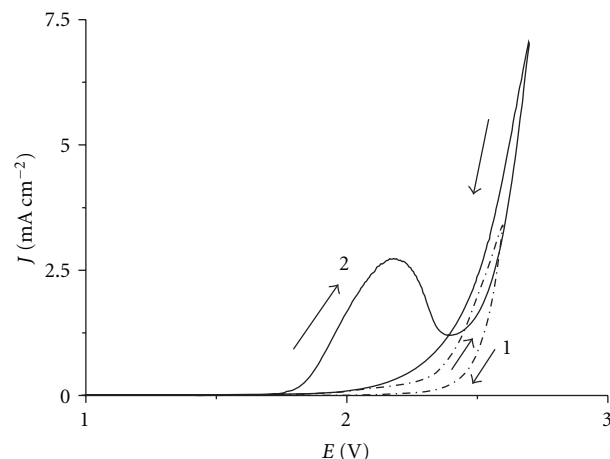


FIGURE 1: Cyclic voltammograms in 0.5 M K_2SO_4 solution: (1) benzene-free solution, (2) benzene-saturated solution. (In what follows, all experimental results are given for the 0.5 M K_2SO_4 solution, unless otherwise stated.) Potential scan rate 20 mV/s. Arrows show the direction of potential sweep.

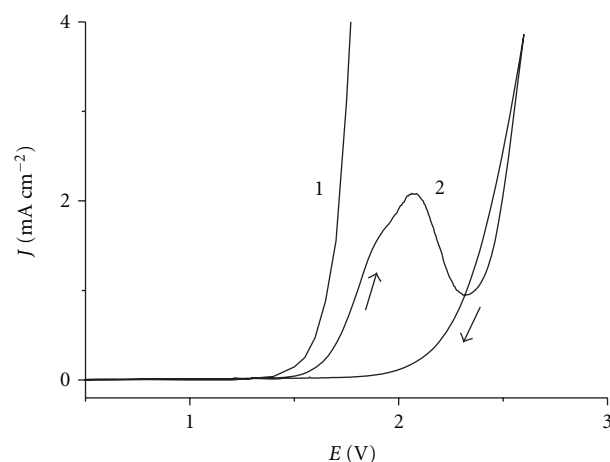


FIGURE 2: Cyclic voltammograms in 1 M KCl solution: (1) benzene-free solution, (2) benzene-saturated solution. Potential scan rate 20 mV/s.

The working solution was 0.5 M K_2SO_4 saturated with benzene (reagent grade, mass fraction 99.8%). The benzene solubility in water is 0.07% ($\sim 2 \cdot 10^{-2} \text{ M}$) at 22°C [7].

3. Results and Discussion

3.1. Potentiodynamic Curves. In Figure 1, we give cyclic voltammograms taken in benzene-free 0.5 M K_2SO_4 solution (curves 1) and in the benzene-containing solution (curves 2). The curves 1 measured in the pure indifferent electrolyte solution relate to the oxygen anodic evolution. The high overvoltage of the process should be emphasized; it is typical for diamond electrodes. On the curve 2 (direct run) taken in the presence of benzene, we see current maximum, followed by a minimum, then the second current rise occurred, which is due to the concurrent benzene oxidation and oxygen

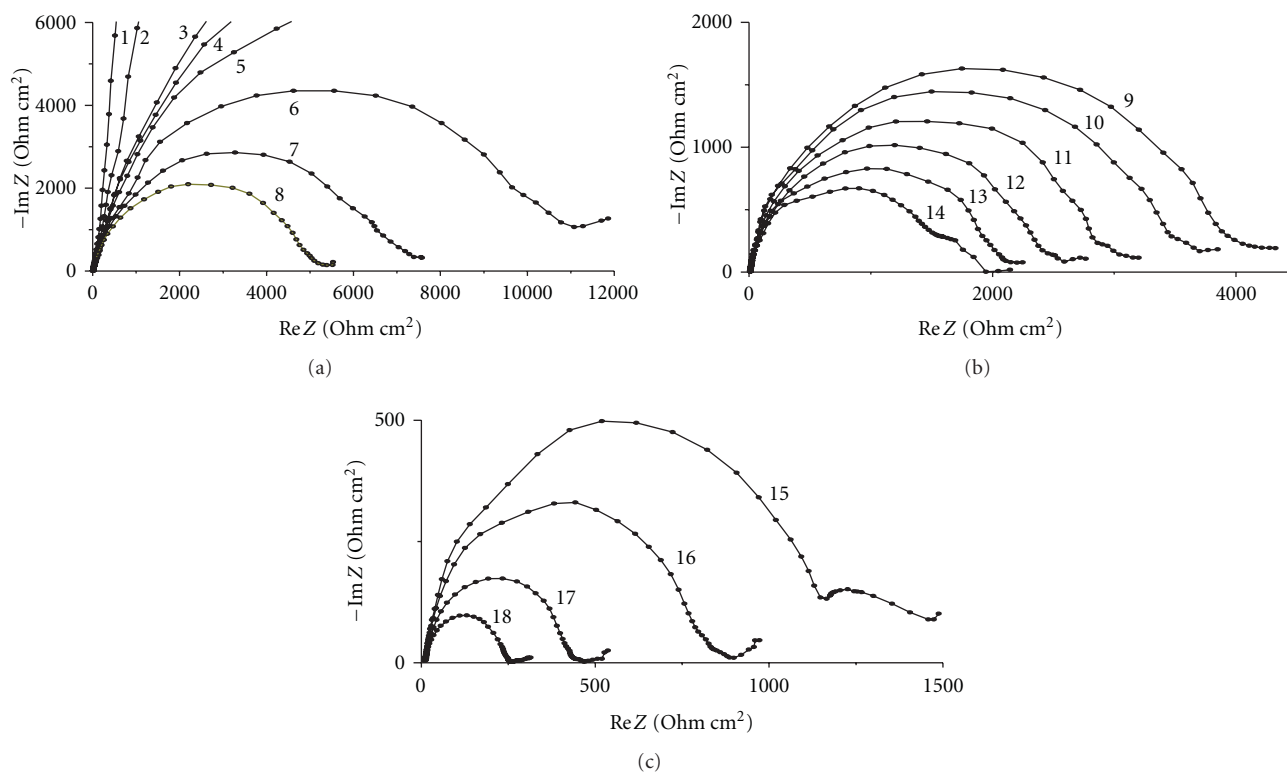


FIGURE 3: (a)–(c) Complex-plane plots of impedance spectra (f -sweep) in 0.5 M K_2SO_4 benzene-free solution at potentials E : (1) 0.80 V; (2) 1.40 V; (3) 1.60 V; (4) 1.65 V; (5) 1.70 V; (6) 1.75 V; (7) 1.80 V; (8) 1.85 V; (9) 1.95 V; (10) 2.00 V; (11) 2.05 V; (12) 2.10 V; (13) 2.15 V; (14) 2.20 V; (15) 2.25 V; (16) 2.30 V; (17) 2.35 V; (18) 2.40 V.

evolution. On basis of data on the differential capacitance (see below), we suggested that the decrease in the anodic current is mainly due to the blocking of anode surface by the benzene-oxidation intermediates that adsorb at the diamond electrode. This is confirmed, even if indirectly, by the fact that anodic curves taken repeatedly right after curve 2 lie much lower than this curve. This is analogous to the phenomenon described earlier for both benzene [6] and phenol [8] oxidation at BDD (see also Figure 2). As time goes by in currentless mode, the activity of electrode gradually restores. The electrode entire regeneration occurs in pure water after 12 h-exposure. We note that the loss of BDD-electrode activity during the benzene oxidation was not mentioned in [5].

For comparison, we give in Figure 2 similar potentiodynamic curves taken in another indifferent electrolyte, namely, 1 M KCl solution. As such, the benzene oxidation curves measured in K_2SO_4 and KCl are qualitatively similar. The difference is in the background curves: Cl^- ion is discharged (with chlorine gas evolution) at much less positive potential than that of benzene oxidation; hence, the electrode surface blocking by the benzene-oxidation intermediates affects this process too. Indeed, the Cl_2 evolution onset potential is shifted toward more positive potentials. By contrast, the oxygen evolution during water oxidation, which occurs at more positive potentials than the Cl_2 evolution, is not affected by the benzene oxidation.

3.2. The Impedance Spectra. The complex-plane plots of impedance spectra (that is, the $-ImZ$ versus ReZ dependences) were measured at constant potential E over the frequency f range from 0.1 Hz to 15 kHz (in what follows, we refer to them as f -sweep plots). The f -sweep plots were taken in benzene-free 0.5 M K_2SO_4 solution (Figure 3) and in the benzene-containing solution (Figure 4). In Figure 4, the potential range covered the ideal polarizability region (from 0.4 to 1.2 V) and the anodic current rise (from 1.2 to 1.9 V), Figure 4(a), the region of the current decay (1.9 to 2.0 V), Figure 4(b), and the region of the second rise of the current (from 2.0 to 2.40 V), Figure 4(c) (in Figure 3, we divided the entire potential region into the like segments.)

We now analyze the shape of the f -sweep complex-plane plots in more detail. At less positive potentials (curves 1, 2 in Figures 3 and 4), we have straight lines somewhat declined to vertical line, which is characteristic of equivalent circuits including a constant phase element (CPE). With the increasing of positive potential, the charge-transfer resistance decreased, and the plots became curved, eventually turning into somewhat depressed semicircles. The difference of the low-frequency and high-frequency cutoffs of the “semicircles” equals the charge-transfer “faradaic” resistance R_F . It should be emphasized that in the background electrolyte solution (Figure 3), the changing of R_F is monotonic, whereas in the benzene-containing solution (Figure 4), the value of R_F first decreased (see Figure 4(a), curves 1–8), then

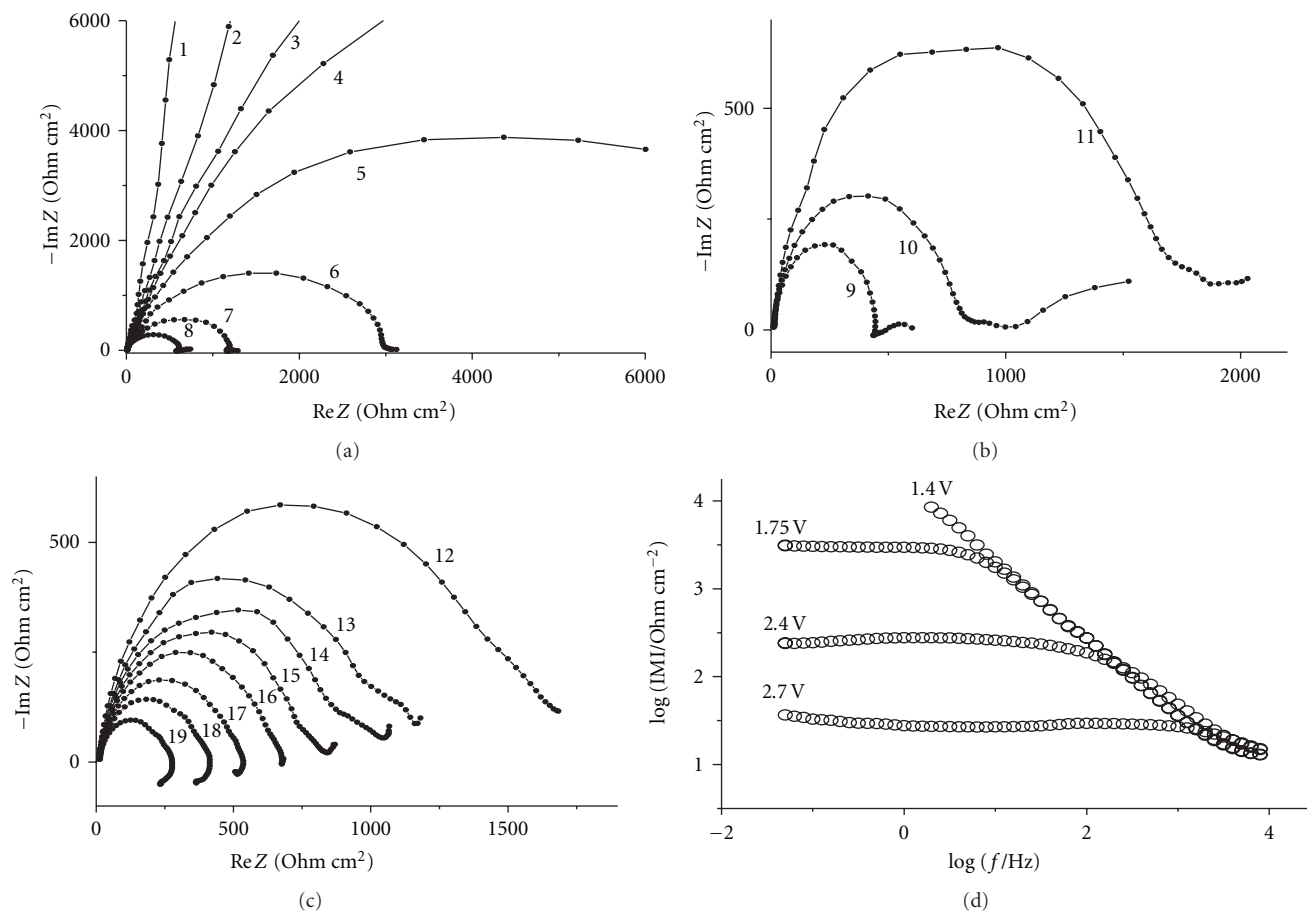


FIGURE 4: (a)–(c) Complex-plane plots of impedance spectra (f -sweep) in 0.5 M K_2SO_4 benzene-saturated solution at potentials E : (1) 0.80 V; (2) 1.40 V; (3) 1.60 V; (4) 1.65 V; (5) 1.70 V; (6) 1.75 V; (7) 1.80 V; (8) 1.85 V; (9) 1.90 V; (10) 1.95 V; (11) 2.00 V; (12) 2.05 V; (13) 2.10 V; (14) 2.15 V; (15) 2.20 V; (16) 2.25 V; (17) 2.30 V; (18) 2.35 V; (19) 2.40 V. (d) The Bode plot (bi-logarithmic dependence of the impedance modulus on the frequency).

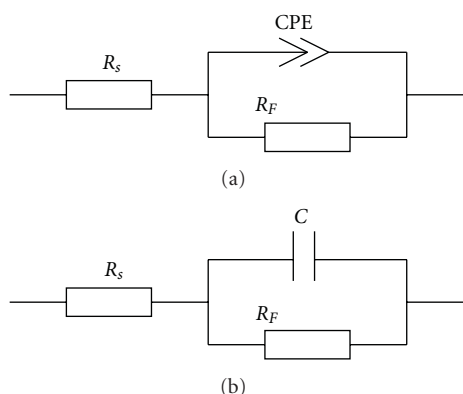


FIGURE 5: Equivalent circuits: (a) ZARC and (b) the Ershler-Randles circuit. CPE is the constant phase element, C is the differential capacitance, R_F is the charge-transfer resistance, and R_s is the series resistance.

increased (Figure 4(b), curves 9–11), and finally decreased again (Figure 4(c), curves 12–19). It is easy to see that the

character of changes in the value of R_F closely correlates with the shape of the potentiodynamic curve 2 in Figure 1.

The high-frequency “halves” of the f -sweep complex-plane plots of impedance spectra (from the high-frequency cutoff up to the maximum) resemble more or less perfect semicircles, whereas the low-frequency halves are distorted by some slow processes whose nature is unknown. (Some considerations thereon are given in our earlier work [6]).

The high-frequency “halves” of the impedance spectra plots were interpreted by using a modified Ershler-Randles equivalent circuit called ZARC [9] (Figure 5(a)), in which a constant phase element (CPE) is substituted for the differential capacitance C . The ZARC circuit is widely used in the electrochemical impedance spectroscopy practice. Here the CPE impedance is $Z_{CPE} = \sigma^{-1}(i\omega)^{-a}$, where σ is the frequency-independent factor; the exponent a determines the character of frequency dependence; $\omega = 2\pi f$ is the angular frequency; $i = \sqrt{-1}$ is the imaginary unity.

The elements of the circuit, namely, the CPE parameters (the frequency-independent factor σ and the exponent a), the charge-transfer resistance R_F and series resistance R_s , were calculated from the impedance spectra (Figures 3 and 4)

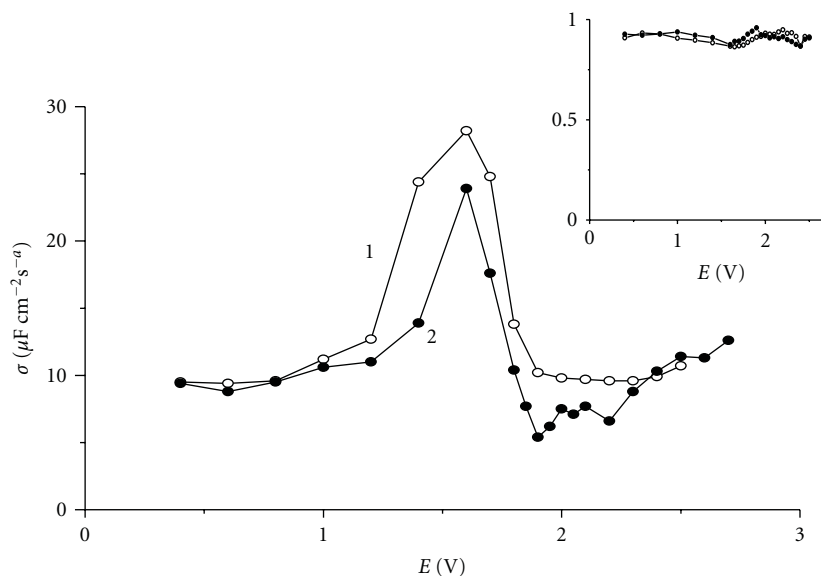


FIGURE 6: Potential dependence of σ and a (inset): (1) benzene-containing solution; (2) benzene-free solution.

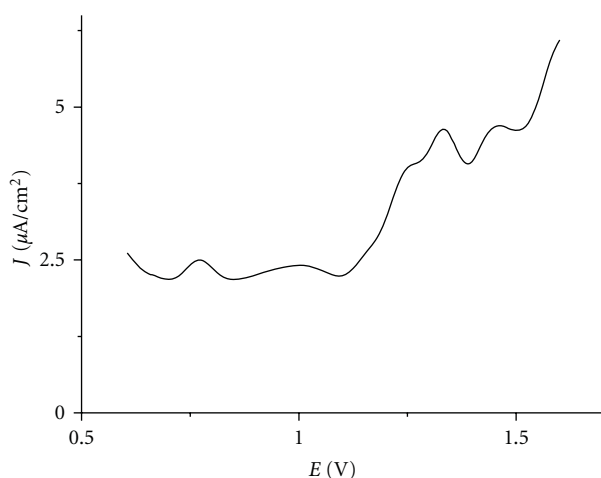


FIGURE 7: Residual current in indifferent electrolyte solution.

by a standard fitting procedure; the standard deviation of calculated values from those experimentally measured did not exceed 10^{-3} . (The experimentally measured impedance spectra were originally processed by using two equivalent circuits: the Ershler-Randles circuit (containing the capacitance C , see Figure 5(b)) and the ZARC circuit (containing the CPE, Figure 5(a)). When using Figure 5(a) circuit, the fitting relative error appeared being much less; therefore, we accepted this very circuit in our impedance calculations. We note that the numerical values of the differential capacitance C (in $\mu\text{F}/\text{cm}^2$) and the factor σ (in its accepted units) are quantities of the same order of magnitude, e.g., at $E = 0.7\text{V}$, we have $C = 5.7$, $\sigma = 11$. In what follows, we shall often refer to both C and σ as “capacitance”, without loss of generality).

The Bode plot (the frequency dependence of the impedance modulus $|M|$, Figure 4(d)) is consistent with

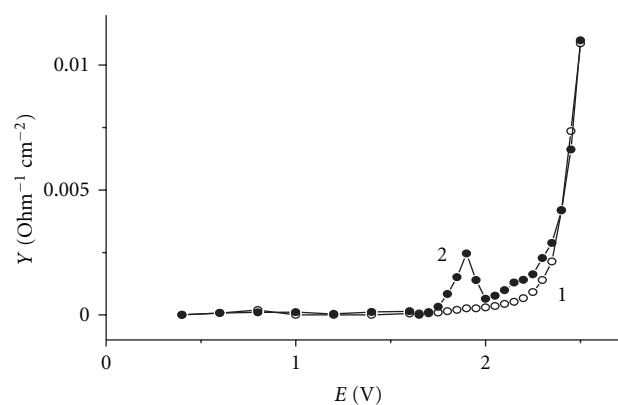


FIGURE 8: Potential dependence of differential conductivity: (1) benzene-free solution and (2) benzene-containing solution.

the results of the above analysis. At the potential of 1.4V (in the ideal polarizability region), the straight line reflects but the CPE in the equivalent circuit. When the oxidation current flows, the charge-transfer resistance R_F decreases (the more so, when the potential E increased from 1.75 to 2.7V) and thus contributes less to the $|M|$ value, the $\log|M|$ versus $\log f$ dependence saturates in the low-frequency region. In the high-frequency limit, we still have not reached saturation at $\sim 10\,000\text{Hz}$ with our instrument; yet, we see faint resemblance of the saturation at a value of $\leq 10\text{ Ohm cm}^2$, which is close to the high-frequency cutoff in the complex-plane plots (Figures 3(a) and 4(a)). It is the solution resistance R_s (see Figure 5) that contributes to $|M|$, along with the charge-transfer resistance R_F and manifests itself at the higher frequencies.

In Figure 6, we show the potential dependence of σ and a (inset). In the ideal polarizability region (at potentials E more negative than 1.2V), the differential capacitance (more

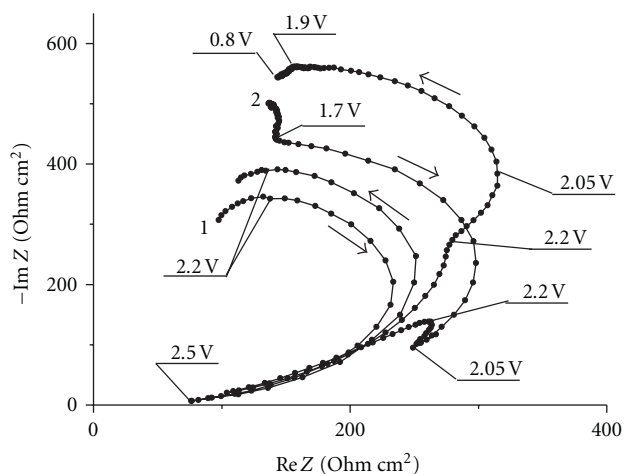


FIGURE 9: Complex-plane plots of impedance spectra (E -sweep): (1) benzene-free solution and (2) benzene-containing solution. Arrows show the direction of potential sweep; the relevant potential values are shown at the curves.

precisely, the factor σ) depends but little on E ; it is nearly the same both in the absence and in presence of benzene (compare curves 1 and 2 in Figure 6). Therefore, we conclude that in this potential region benzene does not adsorb on the diamond electrode (or its adsorption does not affect the electrode capacitance).

At potentials 1.5–1.6 V, the capacitance reaches its peak value. In the same potential region, the current-potential dependence in the indifferent electrolyte solution also reaches its peak value (a few $\mu\text{A}/\text{cm}^2$), see Figure 7. According to [10], this current maximum is caused by the anodic oxidation of nondiamond (sp^2 -)carbon composing intercrystalline boundaries; this material is less resistant toward oxidation than the crystalline (sp^3 -)diamond. It seems not unwise to relate the capacitance (or pseudocapacitance?) maximum to the sp^2 -carbon oxidation current.

At still more positive potentials where benzene is subject to active oxidation, the capacitance in the presence of benzene is somewhat lower than in benzene-free solution. This can be explained by the adsorption of some intermediate of the benzene oxidation on the electrode, which results in the formation of dielectric interlayer [11]. In all probability, it is the same intermediate that blocks the anodic current (see Figures 1 and 2). At the potential of 2.2 V, the adsorbed product desorbs from the electrode or is subjected to further anodic oxidation, and the capacitance increased again.

The exponent a somewhat differs from 1; it equals 0.8 to 0.9 (inset to Figure 6). Its weakly pronounced potential dependence may evidence some distribution of the reactants' charge-transfer and mass-transfer activation parameters over the electrode surface [12]. Alternatively, it may be caused by concurrent adsorption of several benzene-oxidation intermediates with different activation energies.

The potential dependence of the differential faradaic conductivity of the electrode/electrolyte interface $Y = 1/R_F$ (Figure 8) resembles qualitatively the potential dependence of anodic current. In the region of the current blocking,

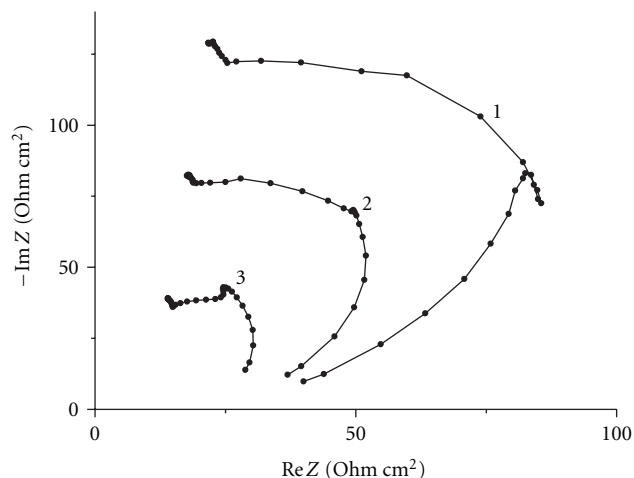


FIGURE 10: Complex-plane plots of impedance spectra (E -sweep, only direct runs), demonstrating the frequency effect on the *small arc* position: (1) 300 Hz, (2) 500 Hz, (3) 1000 Hz.

the conductivity drops down, due to the adsorption of an intermediate. Then Y increased again, thus reflecting the benzene oxidation and the parallel process of oxygen evolution (owing to water anodic oxidation).

3.3. The “ E -Sweep Complex-Plane Plots” of Impedance Spectra.

In addition to the complex-plane plots of impedance spectra obtained at constant potential and varying ac frequency (see the preceding Section), we measured complex-plane plots (the $-\text{Im} Z$ versus $\text{Re} Z$ dependences) of impedance at constant frequency, varying the potential E (the so-called E -sweep, Figure 9). They were taken both in the indifferent electrolyte (curves 1) and in the presence of benzene (curves 2).

By inspecting the spectra in Figure 9, we see that, to the first approximation, they comprise two parts, namely, nearly vertical lines in the ideal polarizability region (which are even better pronounced at higher frequencies, see Figure 11(b) below), and “vertically arranged semicircles” that can be related to the charge transfer process at the interface during the oxidation process. It is these second parts that give information on the electrode reaction [13].

The equation describing these “polarization complex-plane plots” of impedance spectra can be easily derived for the simplest model. When the charge-transfer impedance includes contributions from the differential capacitance C and faradaic conductivity Y_F (connected in parallel in equivalent circuit) to the charge transfer flux

$$Z_k = \frac{1}{i\omega C + Y_F}, \quad (1)$$

the equation for the complex-plane plot of the impedance is

$$\text{Re}^2 Z_k + \left(\text{Im} Z_k + \frac{1}{2\omega C} \right)^2 = \left(\frac{1}{2\omega C} \right)^2. \quad (2)$$

With varying Y_F , we obtain a semicircle whose radius is inversely proportional to the electrical double layer capacitance C and the angular frequency ω . The distance of the

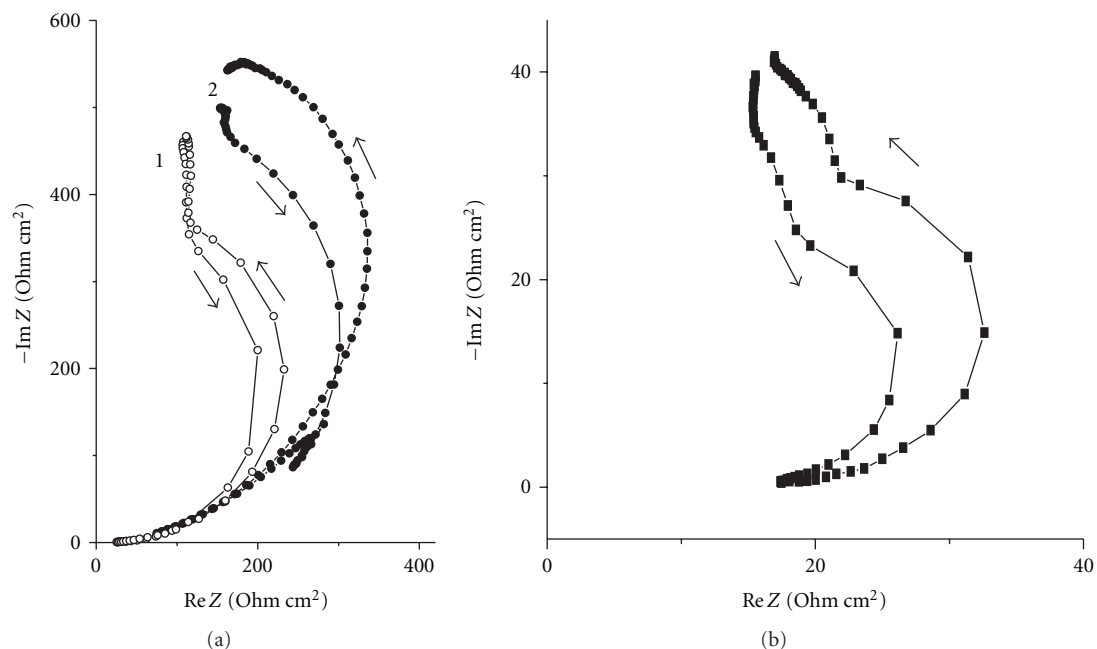


FIGURE 11: Complex-plane plots of impedance spectra (E -sweep) in 1 M KCl solution, demonstrating the frequency effect on the *small arc* position. (a) 60 Hz: (1) benzene-free solution and (2) benzene-containing solution. (b) 1000 Hz, benzene-containing solution. Arrows show the direction of potential sweep (0.4–2.5 V).

semicircle center to the real component axis equals the semicircle radius.

We note that after strong anodic polarization and subsequent return of potential to its initial (cathodic) value (see arrows in Figure 9, curves 1) the curve depicts a semicircle of larger radius (compare the curves obtained in the direct and the reverse run). At a fixed frequency, this can only be caused by decrease in the differential capacitance. The plausible reason of the decrease in the capacitance, hence, occurrence of the hysteresis may be irreversible adsorption of oxygen (formed during the water decomposition) and (in the presence of benzene) coadsorption of the benzene-oxidation intermediates.

When benzene is present in the solution (Figure 9, curves 2), the $-\text{Im}Z$ versus $\text{Re}Z$ plots of direct run, measured at relatively low frequencies (30–100 Hz), show a short segment shaped as *small arc*. It is observed right in the potential region where the voltammogram (Figure 1, curve 2) showed a current peak and subsequent current decay. The small arc separates the semicircle's segments of different radii. At the reverse run of the curves the small arc used to be absent, probably, due to the electrode surface blocking by the oxidation intermediates. Importantly, at the reverse run of the cyclic voltammograms in the benzene-containing solution (Figure 1, curve 2), the benzene oxidation current is also absent right in the potential region when the direct voltammogram shows the current peak. Evidently, it is due to the surface blocking by the benzene-oxidation intermediate products. Thus, the small arc in the E -sweep impedance curves is a reflection of the anodic current maximum in the voltammogram. In the absence of faradaic current, the small

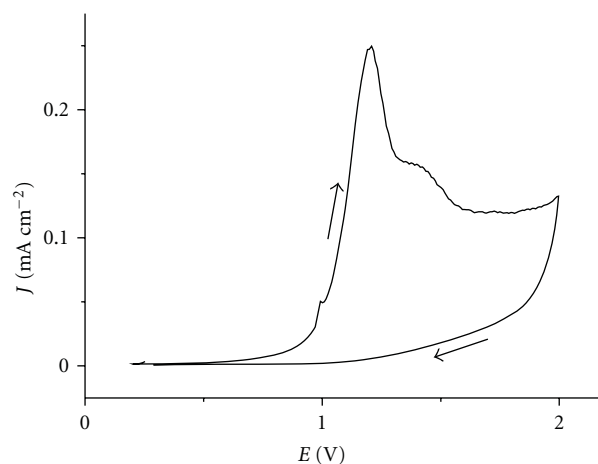


FIGURE 12: Cyclic voltammograms in phenol-containing solution. Potential scan rate 20 mV/s. Arrows show the direction of potential sweep.

arc in the reverse run of impedance complex-plane plots is also absent.

From the methodical point of view, it is of interest to reveal the effect of the ac measuring frequency on the position of the small arc in the impedance curve relative to the “central” (characteristic) point with the maximal $\text{Re}Z$. In the latter point, the capacitive and charge-transfer currents (hence, $|\text{Im}Z|$ and $\text{Re}Z$) are equal to each other. The position of the small arc relative to this characteristic point in the $-\text{Im}Z$ versus $\text{Re}Z$ plots is determined by the

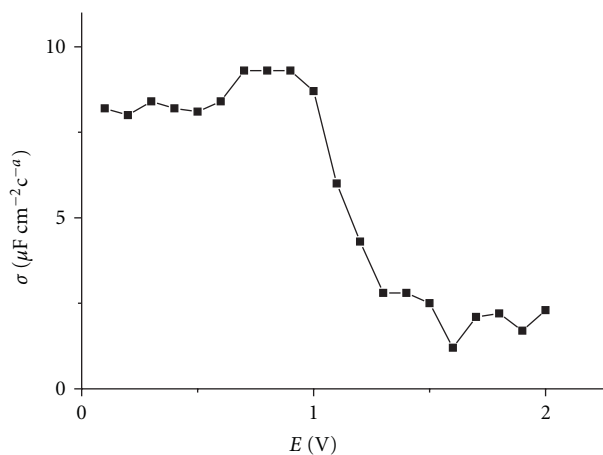


FIGURE 13: Potential dependence of σ in phenol-containing solution. Compare the background curve 2 in Figure 6.

capacitive-to-charge transfer current ratio. In Figure 10, we compare the small arc position for three frequency values. At the lower frequency (300 Hz, curve 1), the small arc is very well pronounced. With the increasing of the ac frequency (to 500 Hz), the current passing through the circuit's capacitive element increases; therefore, in the "new" characteristic point of the $-\text{Im}Z$ versus $\text{Re}Z$ plot, at the constant capacitance, the ohmic (charge-transfer) resistance appears being relatively less. And the small arc (corresponding to certain potential region with its characteristic charge-transfer resistance) at the higher frequency appeared being shifted closer to cathodic potentials, see curve 2. In this point, the capacitive-to-charge transfer current ratio is less than in the characteristic point. At still higher frequency (1000 Hz) the small arc almost reached the boundary of the ideal polarizability region (curve 3).

However, it appeared impossible to greatly increase the measuring frequency in the K_2SO_4 solution, in all probability due to its insufficiently large conductivity. We succeeded to do this in the better conducting KCl solution. In Figure 11, we clearly see that the small arc can be observed in KCl as well, however, at rather low frequencies (60 Hz, Figure 11(a)). By contrast, at higher frequencies (1–10 kHz), it disappeared (Figure 11(b)), in agreement with the above-given explanation.

3.4. Measurements in Phenol Solution. Above we showed that in the potential region of benzene oxidation the BDD-electrode surface is blocked by some intermediate products of the oxidative process. Among them, the former one in the reaction path is phenol that appears through a two-electron oxidation reaction (see, e.g., [8]). To reveal its possible effect on the impedance and charge transfer in the benzene system under study, we measured the potential dependences of anodic current (Figure 12) and differential capacitance (more precisely, the factor σ , Figure 13) in 0.5 M K_2SO_4 solution in the absence and in the presence of phenol.

The cyclic voltammogram (Figure 12) by and large is similar to that given in [8]. The potential dependences of

the capacitance in the ideal polarizability region both in the benzene- and phenol-containing solutions are basically similar (compare Figures 6 and 13). This allowed us to conclude that phenol, like benzene, does not adsorb on the diamond electrode. Hence, it is an intermediate other than phenol (that is, in higher oxidation state) that blocks the benzene oxidation current at the BDD electrode.

Interestingly, unlike Figure 6, no capacitance maximum is observed in the phenol solution at the potential of 1.5–1.6 V (Figure 13) where phenol is oxidized (whereas benzene is still stable against oxidation). Obviously, the phenol-oxidation intermediate adsorbs at the BDD and affect its surface properties in this potential region, in particular, lowering the capacitance.

4. Conclusions

Benzene oxidation at boron-doped diamond electrodes in 0.5 M K_2SO_4 aqueous solution is studied by cyclic voltammetry and electrochemical impedance spectroscopy. It is shown that in the ideal polarizability potential region benzene either does not adsorb at the diamond electrode or its adsorption does not affect the electrode capacitance. At more positive potentials, the "E-sweep" impedance measurements showed that the adsorption of some intermediate of benzene oxidation occurs at the electrode. The intermediate partially blocks the electrode surface and lowers the anodic current of benzene oxidation, however, without any effect on the oxygen evolution process. It is concluded that the electrode surface blocking is caused by an intermediate other than phenol.

Acknowledgment

This work was supported by the Russian Foundation for Basic Research, project no. 10-03-00011.

References

- [1] Yu.V. Pleskov, *Elektrokimiya Almaza (Electrochemistry of Diamond)*, URSS, Moscow, Russia, 2003.
- [2] Ch. Cominellis, I. Duo, P.-A. Michaud, D. Marselli, and S.-M. Park, "Application of synthetic boron-doped diamond electrodes in electrooxidation processes," in *Diamond Electrochemistry*, A. Fujishima, Ya. Einaga, T. N. Rao, and D. A. Tryk, Eds., Elsevier, Amsterdam, The Netherlands, 2005.
- [3] M. Fryda, T. Matthée, S. Mulcahy, A. Hampel, L. Schäfer, and I. Tröster, "Fabrication and application of Diachem electrodes," *Diamond and Related Materials*, vol. 12, no. 10-11, pp. 1950–1956, 2003.
- [4] W. Haenni, Ph. Rychen, M. Fryda, and C. Cominellis, "Industrial applications of diamond electrodes," in *Semiconductors and Semimetals*, C. E. Nebel and J. Ristein, Eds., vol. 77 of *Thin-film Diamond II*, p. 149, 2004.
- [5] R. T. S. Oliveira, G. R. Salazar-Banda, M. C. Santos et al., "Electrochemical oxidation of benzene on boron-doped diamond electrodes," *Chemosphere*, vol. 66, no. 11, pp. 2152–2158, 2007.
- [6] Yu.V. Pleskov, M. D. Krotova, V. V. Elkin, V. P. Varnin, and I. G. Teremetskaya, "Benzene oxidation on BDD anode: the electrochemical impedance study," *Elektrokimiya*. In press.

- [7] B. P. Nikol'skii et al., Ed., *Chemist's Handbook*, vol. 2, Gos. Khim. Izd., Leningrad, Russia, 1951.
- [8] J. Iniesta, P. A. Michaud, M. Panizza, G. Cerisola, A. Aldaz, and C. Comninellis, "Electrochemical oxidation of phenol at boron-doped diamond electrode," *Electrochimica Acta*, vol. 46, no. 23, pp. 3573–3578, 2001.
- [9] J. R. Macdonald, Ed., *Impedance Spectroscopy*, John Wiley & Sons, New York, NY, USA, 1988.
- [10] H. B. Martin, A. Argoitia, U. Landau, A. B. Anderson, and J. C. Angus, "Hydrogen and oxygen evolution on boron-doped diamond electrodes," *Journal of the Electrochemical Society*, vol. 143, no. 6, pp. L133–L136, 1996.
- [11] V. I. Melik-Gaikazyan, "The determination of kinetics of organics adsorption from impedance measurements," *Zhurnal Fizicheskoi Khimii*, vol. 26, p. 560, 1952.
- [12] Z. B. Stoynov, B. M. Grafov, B. S. Savova-Stoynova, and V. V. Elkin, *Elektrokhimicheskii Impedans (Electrochemical Impedance)*, Nauka, Moscow, Russia, 1991.
- [13] V. V. Elkin, V. Y. Mishuk, M. A. Abaturov, and B. M. Grafov, "Polarization hodograph of the second-order impedance for the charge transfer proceeding under kinetic control," *Russian Journal of Electrochemistry*, vol. 34, no. 2, pp. 126–132, 1998.

Review Article

Nanodiamond Films for Applications in Electrochemical Systems

A. F. Azevedo, M. R. Baldan, and N. G. Ferreira

LAS, Instituto Nacional de Pesquisas Espaciais (INPE), CP 515, 12227-010 São José dos Campos, SP, Brazil

Correspondence should be addressed to A. F. Azevedo, adriana@las.inpe.br

Received 29 March 2011; Accepted 21 May 2011

Academic Editor: Yasuaki Einaga

Copyright © 2012 A. F. Azevedo et al. This is an open access article distributed under the Creative Commons Attribution License, which permits unrestricted use, distribution, and reproduction in any medium, provided the original work is properly cited.

The purpose of the present paper is to give an overview on the current development status of nanocrystalline diamond electrodes for electrochemical applications. Firstly, we describe a brief comparison between the general properties of nanocrystalline diamond (undoped and boron-doped) and boron-doped microcrystalline diamond films. This is followed by a summary of the nanodiamond preparation methods. Finally, we present a discussion about the undoped and boron-doped nanocrystalline diamond and their characteristics, electrochemical properties, and practical applications.

1. Introduction

Diamond nanocrystal is a topic of considerable interest in the scientific community, as properties of these systems are expected to retain a large extent of singular characteristics concerning polycrystalline diamond films [1]. The first reference related to these materials as “nanocrystalline” was presented in the Workshop on Diamond Thin Films in 1990 [2]. In 1994, Gruen and coworkers have reported that the growth of “fine-grained” or nanocrystalline diamond (NCD) films was obtained by Chemical Vapor Deposition (CVD) under hydrogen-poor and argon/carbon-rich conditions [3–5]. And, in 1999, this new material was reviewed under the label of “Nanocrystalline-Diamond Films” [6].

As a class, NCD films cover a wide variety of materials ranging from films with properties approaching to single crystal diamond to others which are useful for specialized applications. In fact, there are intrinsic electrochemical properties of diamond that are independent of the grain size (nano or micro), unequivocally distinguishing them from other commonly used sp^2 -bonded carbon electrodes. These properties are (i) a low and stable background current; (ii) excellent structural and morphological stability at high temperatures and current density; (iii) good responsiveness for several aqueous and nonaqueous redox analytes without any conventional pretreatment; (iv) long-term response stability; (v) optical transparency in the UV/Vis and IR regions of the electromagnetic spectrum, useful properties for spectroelectrochemical measurements [7].

However, when the size of the structure is decreased, the surface/volume ratio increases considerably and the surface phenomena predominate over the chemistry and physics in the bulk. Thus, there are some specific properties for the NCD films that differentiate them from microcrystalline. In Table 1 are shown some of the differences between NCD (undoped and boron-doped) and boron-doped microcrystalline diamond (BDD).

Thus, there are important features of crystalline materials that need to be well understood in order to improve their application efficiency in a wide range of areas such as mechanics, biomedicine, electrochemistry, and electronics, among others.

2. The Preparation Methods of Nanodiamond Films

The main route towards nanocrystalline diamond films is to use standard techniques to grow polycrystalline diamond films on different substrates [16–19], for example, microwave plasma [20–29] or hot filament [30–36]. The growth of nanometric films may be performed by changing some growth parameters, such as, the application of negative bias on the substrate [37–40], the increase of the methane concentrations [41–45] or by the addition of noble gas to the precursor mixture [10, 46, 47].

The gas mixture, with a high percentage of CH_4 in H_2 (5–20%), provides a type of NCD morphology called cauliflower

TABLE 1: A comparison of the some properties of the NCD and BDD.

PROPERTY	NCD	BDD	References
working potential window	2.5 to 3.0 V	3.0 to 3.5 V	[7–11]
conductivity	undoped or doped	only doped	[1, 6, 8, 9]
roughness	low	high	[1, 10, 11]
ΔE_p (mV) – $\text{Fe}(\text{CN})_6^{-3/-4}$	60–170	60 to 80	[7, 11–14]
Effective surface area	high	low	[15]

or ballas type [48, 49]. Presumably the higher percentage of CH_4 in H_2 increases the twinning, and the non-diamond carbon incorporation thereby reducing the grain size [50]. Thus these NCD films can be grown without an appreciable increase of the roughness on growth surface, but at the cost of increasing the nondiamond component of the film (up to 50% nondiamond carbon).

The most used noble gas has been argon with concentrations above 70 vol.% [19, 22, 23, 42–44, 51]. It promotes an increase of CH_3 and C_2 (and/or C_2H) radical amounts close to the substrate surface which determines the growth morphology [6, 31]. Originally, it was suggested that the C_2 radical played an important role in the growth mechanism [6]. However, recent works have shown that the concentration of CH_3 and C_2H are much greater than C_2 , and these species may be more important growth precursors than C_2 under typical nanocrystalline deposition conditions [30, 31, 52].

In general, the other advantage of nanocrystalline diamond films is the possibility of deposition on different kind of substrates. However, two important regards must be considered when selecting a substrate: (i) tolerance of the high deposition temperature (1000–1200 K), and (ii) similarity in the thermal expansion coefficient with that of diamond ($1.1 \times 10^{-6} \text{ K}^{-1}$).

In relation to doped NCD films, they may be grown by adding nitrogen or boron in growth mixture mentioned above to obtain n-type or p-type semiconductor materials, respectively [1]. Boron is the most successful and widely used acceptor in diamond; and the doping can be achieved by adding substances as diborane, trimethyl borane, and boron trioxide. This is because of boron has a low charge carrier activation energy of 0.37 eV [53]. At low doping levels, the diamond acts as an extrinsic semiconductor. At high doping levels the material acts as a semimetal. The success of such a doping will be largely dependent on the dopant position within the films and the nature of the bonding of the dopant atoms to the surrounding of the carbon atoms. The possibility of n- and p-type diamond doping [54, 55] opens the door for a generation of bipolar devices, such as a diamond p–n junction reported by Koizumi et al. [56]. Other dopants have also been tried, such as sulfur and arsenic [57]; however, no systematic results have been obtained so far.

Therefore, this paper will present a short, up-to-date and compact review covering nearly all aspects of nanodiamond electrodes. In next topic will be reported the properties, characterizations, and applications of undoped and boron-doped nanocrystalline diamond electrodes separately.

3. Undoped and Boron-Doped Nanocrystalline Diamond Electrodes for Electrochemical Applications

New materials research for electrochemical applications has been a challenge in the last few years. The use of diamond films in electrochemistry is relatively a new field of research. The first article in the field was published in 1983 by Iwaki et al. [58], but the field was really initiated by the important article from Pleskov et al. [59] in 1987.

However, the doping is not a unique way to make dielectric diamond conducting. The NCD structures have the conductance caused by the same structural defects, and also due to continuous network formed by the amorphous carbons that are incorporated in the intercrystallite boundaries during the film growth process [6]. Gruen [6] has observed that when the crystalline size is reduced to nanometer scale, the percentage of carbon atoms located at grain boundary increases drastically with the decrease of grain size. Clearly, the magnitude of the effects on properties is directly proportional to the fraction of carbon atoms residing at the grain boundary. He has concluded that the conduction occurs via π states in the grain boundary and anything chemically or electrochemically that alters the grain boundary bonding influences the electrical conductivity, and as a consequence, the electrical properties of NCD.

Finally, we will report the characteristics, properties and applications of two types of nanocrystalline diamond electrodes, undoped and boron-doped.

3.1. Undoped Nanocrystalline Diamond Electrodes. As mentioned previously, the undoped NCD films are usually deposited from CH_4/H_2 or $\text{CH}_4/\text{H}_2/\text{Ar}$ gas mixture. Nowadays, high quality nanocrystalline and polycrystalline electrodes can be obtained from different commercial sources. Particularly, the film shown in Figure 1 was obtained in Diamond Laboratory of LAS/INPE (São Paulo, Brazil). It was prepared by hot filament chemical vapor deposition (HFCVD) technique on a silicon substrate using a gas mixture of $\text{CH}_4/\text{H}_2/\text{Ar}$ with a flow of 0.5/9.5/90 sccm [44]. The value of argon concentration is very close to values studied by other authors that obtained the smallest grains and better films with argon concentrations at or above 90 vol.% using HFCVD [60, 61] or microwaves system [28, 62]. This film presented a uniform morphology with grains around 50 nm. The micrograph obtained by Field Emission Gun Scanning Electron Microscopy (FEG-SEM) was performed using Zeiss-SUPRA 35 equipment.

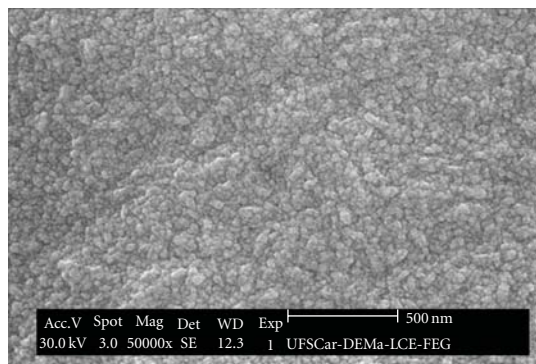


FIGURE 1: FEG-SEM image of undoped NCD film grown on a silicon substrate.

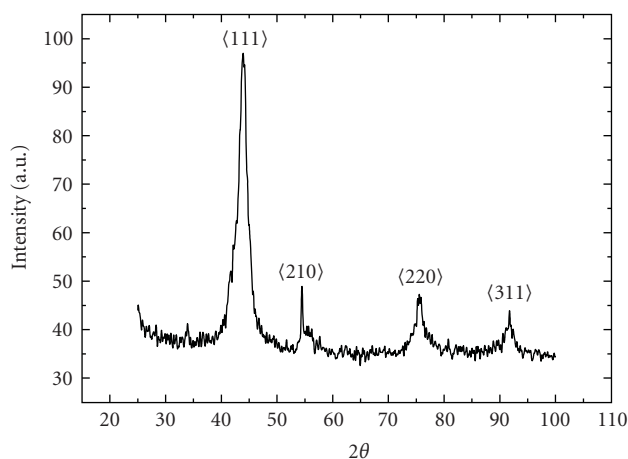


FIGURE 2: X-ray diffraction spectrum of undoped NCD film grown on a silicon substrate.

The nanodiamond crystallinity was investigated by X-ray diffraction (XRD) using a high resolution Philips diffractometer, X'Pert model, with the $\text{CuK}\alpha_1$ radiation ($\lambda = 1.54 \text{ \AA}$) in grazing incident mode with an incident angle of 5° . XRD pattern of film is shown in Figure 2. The XRD spectrum of the NCD film is dominated by the peaks at 43.9° , 54.57° , 75.3° , and 91.5° corresponding to the $\langle 111 \rangle$, $\langle 210 \rangle$, $\langle 220 \rangle$, and $\langle 311 \rangle$ diamond diffraction peaks that evidence the presence of crystalline diamond [63]. It should be noted that no peaks associated with graphite or features related to amorphous carbon could be identified in this film.

Raman spectroscopy has become one of the most used tools for the characterization of disordered polycrystalline graphitic carbons. This technique is simple, not destructive and it is possible to determine the quality of diamond film by the ratio of sp^3/sp^2 carbon bonds [64]. This film was analyzed by micro-Raman scattering spectroscopy (Renishaw microscope system 2000) using the 514.5 nm line of an argon ion laser taking the spectra covering the range from 1000 to 1800 cm^{-1} as shown in Figure 3.

The film spectrum is characteristic of NCD, showing a broad peak at 1345 cm^{-1} (D band) that represents a zone-edge A_{1g} mode due to the disorder and a G peak centered

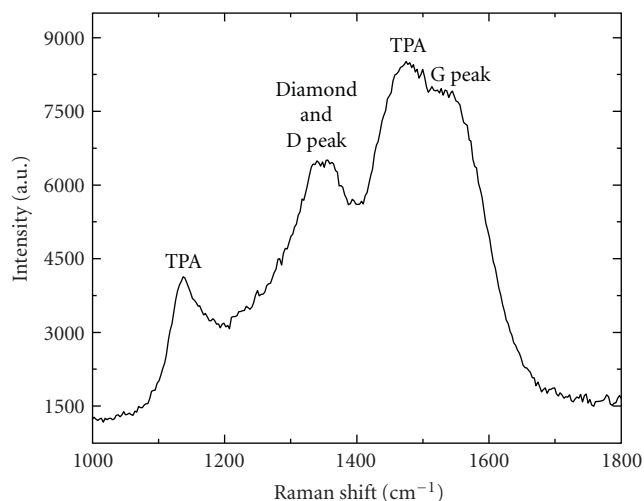


FIGURE 3: Raman spectrum of undoped NCD film grown on a silicon substrate.

at about 1550 cm^{-1} that corresponds to graphite [65]. The diamond peak at about 1332 cm^{-1} , not observed in visible Raman spectra of NCD films, is generally obscured by the overlapping of D peak, which is more sensitive to non-diamond phases. According to Ferrari and Robertson [66], the D peak is due to the breathing modes of A_{1g} symmetry involving phonons near the K zone boundary while the G peak is due to the bond stretching of all pairs of sp^2 atoms in both rings and chains [67]. This mode is forbidden in perfect graphite and only becomes active in the presence of disorder. The Raman spectrum also exhibited two bands at 1150 and 1490 cm^{-1} . This pair of peaks has already been discussed as the transpolyacetylene (TPA) segments at the grain boundaries of NCD surface [66].

Taking into account that the nanocrystalline grains are mainly surrounded by graphitic and oxygenated carbon forms, XPS spectrum should reveal a surface enrichment of graphitic, oxygen bonded, and dangling carbon components with respect to the diamond one. This suggestion is adequately confirmed by the analysis of $\text{C}1s$ XPS spectrum of this film. A better fitting of the experimental data was obtained assuming the concomitant presence of distinct groups of chemical species, emerging at separate Binding Energies (BE) maxima, in accordance with the analyzed spectrum. As a matter of fact, the residual curve suggests that this result was affected by minor errors. Moreover, the relevant physical parameters related to each component, for example, the mixing Gaussian factor, χ^2 and FWHM, are meaningful, thus allowing a reliable qualitative and quantitative XPS analysis.

The $\text{C}1s$ XPS film spectrum is shown in Figure 4. The $\text{C}1s$ peak evidenced the presence of several components, including graphitic (or sp^2 -like carbon), diamond (or sp^3 -hybridized carbon) species and, to a less variable extent, oxidation products containing oxygen—carbon bonds. Considering the fitting of data in Figure 4, the most intense peak (II), centered at 284.1 eV , may be attributed to the bulk diamond component ($\text{sp}^3 \text{ C-C}$) and the less intense

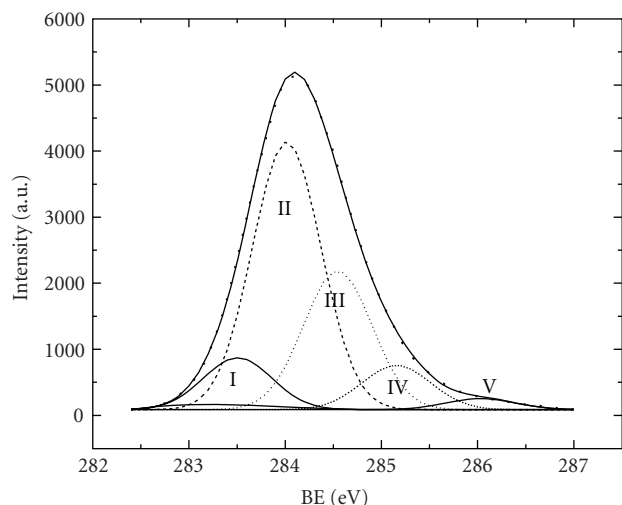


FIGURE 4: C1s XPS spectra of undoped NCD film grown on a silicon substrate.

component (I), shifted by -0.5 eV with respect to diamond peak, may be assigned to graphitic carbon species (sp^2 C–C). The peak (III) corresponds to C–H and the two remaining peaks, centered at higher BE values, could be reasonably assigned to alcoholic (peak IV) and carbonyls (peak V) functional groups, respectively [68].

The electrochemical characteristics of this undoped NCD electrode, immersed in aqueous electrolyte solution, are very close to be observed by others authors. Three electrodes, (work electrode, counter electrode and reference electrode) inside of a single-compartment electrochemical cell were used in this study. The electrodes were not submitted to surface pretreatment before electrochemical measurements and their geometric area in contact with the electrolyte was 0.10 cm². The platinum coil and Ag/AgCl electrodes were used as counter and reference electrodes, respectively. Solutions were deoxygenated with N₂ for at least 20 min prior to and blanketed with the gas during the measurements. The treatments of systems called quasireversible is associated to reactions that show electron's transfer kinetic limitations and consequently, for these systems, reverse reactions have to be considered [69]. In this way, NCD electrode was analyzed by the quasi-reversibility criteria: the separations between the anodic and cathodic peaks (ΔE_p) are larger than $59/n$ mV (where $n = 1$ is the number of electrons involved in the reaction).

In Figure 5 are shown (a) the Cyclic Voltammetric (CV) i-E curve in 0.5 mol L⁻¹ H₂SO₄ ($\nu = 0.1$ V s⁻¹) and (b) electrochemical response from a curve obtained in 1 mmol L⁻¹ of ferrocyanide + 0.1 mol L⁻¹ KCl ($\nu = 10$ mV s⁻¹) for the typical film obtained in our laboratory. CV measurements were carried out at room temperature using a potentiostat Omnimetra Instruments PG 3901.

Electrochemistry response for the NCD film showed a low capacitance and stable background currents. This result is attractive features of diamond for potentially improved signal-to-background in electrochemical assays. The curve

also revealed a working potential window around 2.6 V versus Ag/AgCl where the oxidation water begins at 1.8 V and the reduction water begins at -0.8 V ($i_{\text{baseline}} < 2$ μ A cm⁻²). This value was very close to the results observed by Hian et al. [70], ca. 2.5 V versus SCE, and Foord and Hu [71], ca. 2.8 V versus SCE. Well-defined oxidation (ca. 0.38 V) and reduction (ca. 0.18 V) peaks of the same current magnitude are seen for NCD electrode with a peak potential separation, ΔE_p , of 200 mV. The electrode reactions kinetics for this couple are strongly influenced by the amount of exposed edge planes on sp^2 -bonded carbon as well as the surface cleanliness [72]. Granger and Swain. [73] have shown that surface carbon-oxygen functionalities on microcrystalline diamond significantly influence ΔE_p with increasing oxygen content causing an increase in the peak potential separation. According to them, the oxygen blocks the surface site that is involved in the reaction on the film surface. Apparently, this affirmation can also be applied to this nanodiamond film.

Gruen et al. [12, 74] have demonstrated that smooth and high-quality diamond films can be produced using fullerene (C₆₀) and CH₄ precursors, taking into account the gas mixture. This result was obtained in argon microwave plasmas without the addition of H₂. Diamond films produced in this way are nanocrystalline, smooth (20 ± 50 nm rms surface roughness typically), electrochemically active (i.e., conductive), and highly reactive. The working potential window for the films is ca. 3.0 V versus SCE and is larger than the ca. 2.5 V window observed for freshly polished glassy carbon. The films also exhibited reasonably good voltammetric responses for Fe(CN)₆^{-3/-4} and Ru(NH₃)₆^{+2/+3}, with ΔE_p values of 167 and 90 mV, respectively. They concluded that the larger ΔE_p at the nanocrystalline film may be related to the presence of surface oxides. These results confirm that the surface cleanliness is important, as well as the electrolyte type and concentration [12].

In general, the porous materials are of scientific and technological interest because of their ability to interact with atoms, ions, and molecules not only at their surfaces, but throughout the bulk of the material. Not surprisingly, traditional applications of porous materials involve ion exchange, adsorption (for separation) and catalysis, and several of these benefits from the high order that can be achieved in solids such as zeolites. In the same way, the growth of microcrystalline diamond on porous silicon (PS) substrate has been studied with the objective of increasing the number of diamond nucleation sites, being a promising material for obtaining better crystalline structure and an excellent electrochemistry capacitor due to their large superficial area [75].

In this context, Ferreira et al. [36] have grown NCD films on a micrometric PS substrate to use as capacitor. The PS substrate was produced by anodic etching using n-type silicon wafers. From the micrographs in Figures 6(a) and 6(b), they observed nanograins with average size from 30 to 50 nm and uniform surface texture covered all the supports among the pores resulting in an apparent microhoneycomb structure.

NCD/PS presented a work potential window at 3.0 V versus Ag/AgCl and a large capacitive background current,

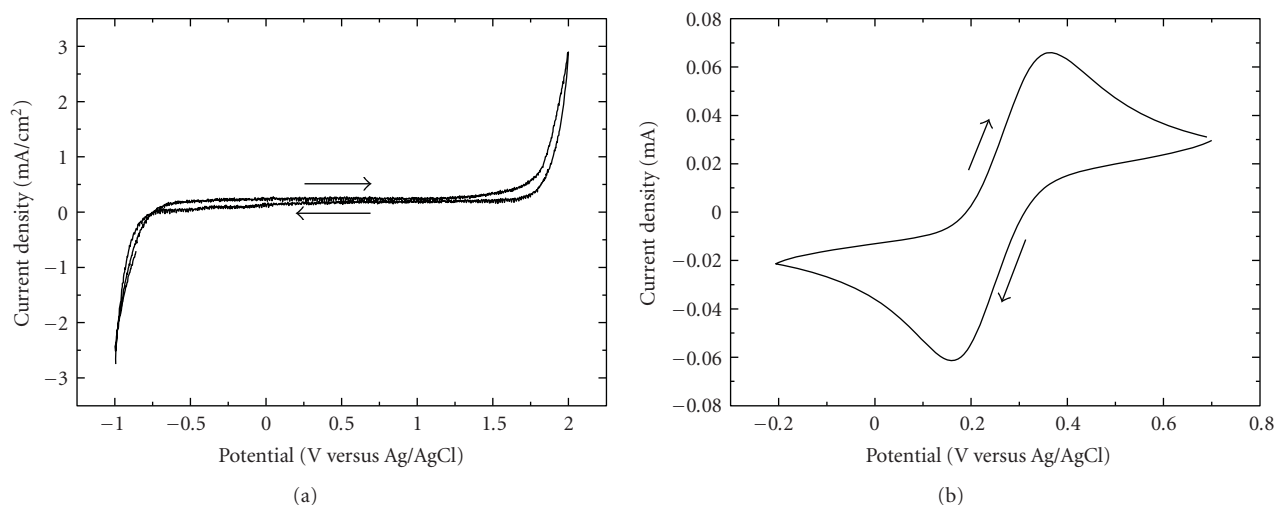


FIGURE 5: CV i - E curves for undoped NCD electrode in (a) $0.5 \text{ mol L}^{-1} \text{ H}_2\text{SO}_4$ (0.1 V.s^{-1}) and (b) 1 mmol L^{-1} ferrocyanide/ 0.1 mol L^{-1} KCl (10 mV.s^{-1}), respectively.

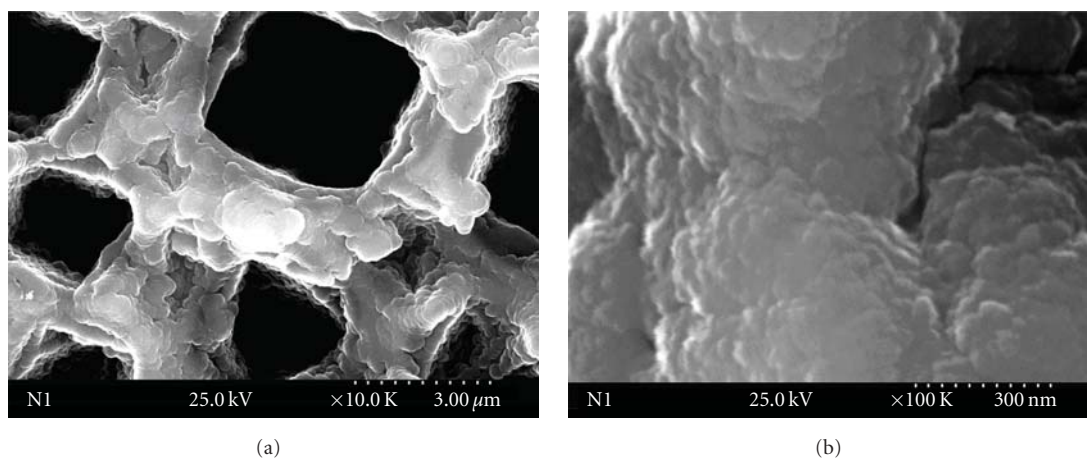


FIGURE 6: SEM images of undoped NCD grown on n-type PS sample. The magnification was increased from (a) to (b) for better visualization of nanograin.

mainly due to increase of electrode surface area as expected for such porous electrode. Taking into account the capacitor applications, they discussed that the double layer capacitive current for NCD/PS was 30 times larger than the as-deposited microcrystalline BDD electrodes. They evaluated the capacitance in the potential range of -0.5 up to 1.0 V versus Ag/AgCl and showed that for BDD electrode; the values in this range were 20 and $40 \mu\text{F cm}^{-2}$. However, NCD/PS electrodes presented superior capacitance in the same range from 230 to $990 \mu\text{F cm}^{-2}$ corresponding to an increase of around 25 times at 1.0 V versus Ag/AgCl. From all these results, they considered the possibility of NCD on PS substrates for electrochemical capacitor applications.

The use of silicon as a substrate for the diamond films growth is the most perfect due to their thermal expansion coefficients are very close. But for several practical applications the brittleness of silicon is forbidden, and then the metal substrates are used as an alternative. Beyond the

mechanical resistance, another advantage is the possibility to produce large area electrodes up to the square meter range. The titanium is widely used in many technological applications, such as aeronautics, bioimplants, dental prostheses, and commercial electrodes. Therefore, the combination of diamond films with titanium substrates may expand the range of possible applications [25, 40, 45, 76]. Hian et al. [70, 77, 78] have deposited an adherent nanodiamond film on titanium rods substrates for electroanalysis application. After the film deposition, they compared the metal deposition and stripping processes with gold and copper at nanodiamond and BDD electrodes and concluded that the processes were faster and more efficient at nanodiamond electrodes. They mentioned that the nanodiamond films exhibit significant electrical conductivity due to the graphitic content and high concentration of grain boundaries in the material and offer advantages over BDD in terms of enhanced reactivity [70]. They also observed that the nucleation of gold appeared to be

facile at edge sites, which are abundant on the nanodiamond surface. For the deposition and stripping of both gold and copper, a stripping efficiency (the ratio of electrodisolution charge to electrodeposition charge) of close to unity was detected even at low concentrations of analyte.

Braga et al. [79] have also shown to be possible to produce hybrid three-dimensional electrodes with NCD films on porous titanium (Ti) substrates. They used the power metallurgy technique to obtain the Ti substrates provided by interconnected and open porous among its volume. Electrochemical response revealed a working potential window around 3.3 V versus Ag/AgCl and a $\Delta E_p = 120$ mV. In the case of the NCD/Ti electrode, the high value of ΔE_p may be attributed to the presence of a high amount of the sp^2 -bonded carbon and film roughness. They concluded that such electrode may be applied to different electrochemical applications due to the structural advantages of the metallic Ti structure, the porosity introduced in the bulk material, and chemical properties of the diamond.

Mani et al. [80] have obtained a new nanocomposite containing nanocrystalline diamond and an amorphous sp^3 carbon phase that was synthesized by immersing a platinum wire substrate into the plasma. This material exhibited excellent electrochemical properties with wide potential window (>2.0 V in H_2SO_4) and high degree of reversibility for the dopamine redox couple (<100 mV peak separation). In addition, the nanocomposite was mechanically rugged and chemically stable in a variety of acidic and basic environments and did not require any surface preparation or any additional ohmic contacts. They suggested that these nanocomposites could directly be used in several analytical, biomedical, waste remediation, and electrosynthesis applications.

3.1.1. Applications of Undoped Nanocrystalline Diamond Electrodes. The undoped nanodiamond electrodes can be used in different applications due to their electrochemical properties. Besides, in some cases, these electrodes can be modified in multiple paths to change their properties. However, most of them have been used as a biosensor.

The interaction between electrode surface and the analyte that will be analyzed is very important. According to Lawrence and Don [81], the surface of as-grown CVD diamond films is typically terminated with hydrogen atoms. The unpolar hydrogen-terminated surface gives the electrodes a hydrophobic nature, while oxygen-terminated surface gives a hydrophilic nature. Klauser et al. [82] have shown the importance of this interaction when investigated the effect of fetal bovine serum (FBS) on cell adhesion on surfaces of identical roughness and topography but varying the surface chemistries of NCD terminations (hydrogen, fluorine and oxygen terminations). Two different cell lines, porcine renal epithelial cells (LLC-PK1) and carcinoma cells (PANC-1) were cultured on the NCD surfaces with and without 10% FBS in the growth medium. They concluded that the addition of FBS to the growth medium allowed cell adhesion on both hydrophilic and hydrophobic NCD surfaces. In contrast, in FBS-free medium, cell attachment could only be assessed on hydrophilic surfaces. Understanding basic cell-surface interactions on hydrophilic surfaces is complex, and

mechanisms of direct cell attachment on hydrophilic surfaces are not as well investigated as protein-mediated cell-surface interactions. Furthermore, protein adsorption is dependent on surface wettability and therefore more degrees of freedom have to be considered. Anyway, NCD offers the possibility to generate cell growth substrates with well-defined surface properties.

Huang et al. [83] have also studied the influence of surface treatments in the immobilization of antibodies on nanodiamond for biosensor applications. They analyzed the anti-*Salmonella* and the anti-*Staphylococcus aureus* antibodies. The efficacy of antibody immobilization was evaluated by enzyme-linked immunosorbent assay (ELISA) and the bacterial binding efficiency was analyzed by SEM pictures. They concluded that the immobilization efficacy of both antibodies and bacterial binding efficiency on air plasma treated nanodiamond are better than those of the hydrogen plasma treated. The explanation for this is that the nanodiamond electrodes treated by air plasma had oxidized surfaces, consequently, is more hydrophilic. Thus, the contact between the hydrophilic antibody solution and the hydrophilic nanodiamond surfaces was enhanced.

Indeed, recent works have shown different applications to oxygen-terminated nanodiamond surfaces, including as transducer material for the detection of pH and penicillin concentration [84, 85]. Poghosian et al. [84] have developed a field-effect capacitive EDIS (electrolyte-diamond-insulator-semiconductor) structure as a platform for (bio) chemical sensing. According to them, in contrast to transistor structures, EDIS sensors are simple in layout and cost-effective in fabrication. Usually, no photolithographic process steps or complicated encapsulation procedures are required in case of the capacitive field-effect EDIS structure. Consequently, they characterized the NCD-based field-effect sensors by means of constant-capacitance method. The average pH sensitivity of the O-terminated NCD film was 40 mV/pH. A low detection limit of $5 \mu M$ and a high penicillin G sensitivity of 65–70 mV/decade was obtained for an EDIS penicillin biosensor with the adoptively immobilized enzyme penicillinase. Finally, they proposed a model of the drift mechanism in EDIS sensors, as well as an immobilization of biomolecules (DNA and proteins) on NCD films for extending the biosensor capabilities of the EDIS platform.

Another possibility is to obtain modified nanodiamond electrodes, which can be performed by the deposition of layers of different chemistry or biological compounds, for biosensor device as studied by Rubio-Retama et al. [86] and Yang et al. [87]. Rubio-Retama et al. [86] have investigated the functionalization of NCD thin films with horseradish peroxidase (HRP). The electrochemical behavior of the modified NCD surface was characterized by impedance spectroscopy and CV. The proximity of HRP heme groups to the NCD surface allowed direct electron transfer between them. The heterogeneous electron-transfer constant for both processes was calculated to be $0.066 s^{-1}$, the charge-transfer coefficient $\alpha = 0.49$, and the immobilized enzymatic layer about $2 \times 10^{-10} mol cm^{-2}$. The modified NCD electrode was used as a third generation biosensor for hydrogen peroxide

determination showing a linear response in the 0.1–45 mmol H_2O_2 range, at +0.05 V versus Ag/AgCl. Thus, they concluded that the immobilized enzyme maintains its activity and good stability. These results confirmed that modified NCD electrodes could be used for *in vivo* applications or for optimizing clinical methodologies that are based on the measurement of hydrogen peroxide produced during the analytical process.

Meanwhile, Yang et al. [87] have shown that NCD thin films covalently modified with DNA oligonucleotides provide an extremely stable, highly selective platform in subsequent surface hybridization processes. They used a photochemical modification scheme to modify chemically the NCD surface, producing a homogeneous layer of amine groups that serve as sites for DNA attachment. After linking DNA to the amine groups, hybridization reactions with fluorescently tagged complementary and noncomplementary oligonucleotides showed no detectable non-specific adsorption, with extremely good selectivity between matched and mismatched sequences. Comparison of DNA-modified NCD film with other commonly used surfaces for biological modification, such as gold, silicon, glass, and glassy carbon, showed that diamond was unique in achieve a high stability and high sensitivity and while it also was compatible with microelectronics processing technologies.

In general, the use of carbon materials has promoted great interest for fuel cells and supercapacitor electrodes [88]. Also called electrochemical capacitor, they have been extensively studied due to the increasing demand for a new kind of electrical energy accumulators of long durability (over 10^6 cycles) and high specific power (more than 10 kW/kg) [89]. Then, the study of new hybrid nanomaterials is very important for understanding and promoting new technologies in this area. Almeida et al. [90] have shown that the NCD formation on carbon fiber (CF) structures produces an innovative material, the diamond porous electrode, with a large surface area and high capacitive response. Furthermore, NCD grown directly on CF substrate promotes an electrode with low electric resistance, improving the device performance. In Figure 7 is showed the CV of NCD/CF electrode in $0.5 \text{ mol L}^{-1} \text{ H}_2\text{SO}_4$ solution at the scan rates of 100 and 10 mV s^{-1} .

This result showed that the NCD/CF electrode has the characteristic behavior of an ideal capacitor with rectangular current-potential responses curves. As discussed by Chen et al. [91], using carbon nanotubes, the achievement of rectangular-shaped CV over a wide range of scan rate is the ultimate goal for electrochemical double-layer capacitors. This behavior is very important for practical applications when two contributions are assigned: a higher energy density due to the wide potential range and a higher power density associated to the scan rate increase. This behavior was confirmed by the inset in Figure 7. The currents at 0.6 V were plotted as a function of scan rate, assuming that there is a contribution of non-Faradaic reactions at this potential. The plot of the NCF/CF electrode depicts a linear dependence with scan rate for the whole range studied up to 100 mV s^{-1} . This result should also be pointed out since for an ideal capacitor, its capacitance is independent of the

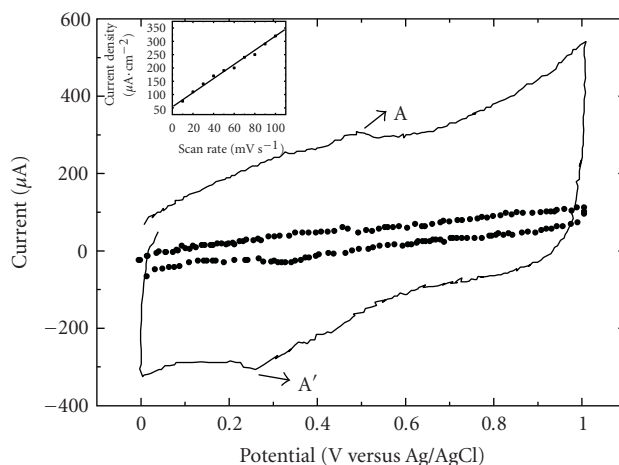


FIGURE 7: CV *i*-*E* curves for NCD/CF electrode in $0.5 \text{ mol L}^{-1} \text{ H}_2\text{SO}_4$ aqueous solution. Scan rate: 100 mV s^{-1} (solid line) and 10 mV s^{-1} (dash line).

frequency, so the charge stored by a capacitor is proportional to the imposed potential. Apparently, the pair of broad redox peaks (A and A') that appear in Figure 7 may be the oxidation/reduction of surface functional groups on CF substrate.

They also measured the specific capacity from the linear regression of the graph of current density in function of the scan rate (inset in Figure 7). The value for NCD/CF was 2.6 mF cm^{-2} . Finally, they compared this value with other values reported in the literature. The best comparison with data already presented in the literature was the nanohoneycomb structures of the BDD films that were investigated by Yoshimura et al. [92]. Particularly, the specific capacity for a nanohoneycomb electrode ($60 \times 500 \text{ nm}$) in an aqueous solution was 1.83 mF cm^{-2} , which is lower but in the same order of magnitude for this NCF/CF electrode studied.

3.2. Boron-Doped Nanocrystalline Diamond Electrodes. A second type of nanodiamond electrodes which seems to become more important is a boron-doped nanocrystalline diamond (BDND). These films can be obtained using the same conditions of undoped-NCD film growth as mentioned previously. The doping can be reached by adding substances containing boron in the gas mixture. Rarely, the morphology is different from that shown for undoped-NCD. However it may vary slightly according to the experimental conditions, substrate used, and so forth [93–95]. In Figure 8 is shown the surface of BDND film grown on a silicon substrate obtained in Diamond Laboratory of LAS/INPE (São Paulo, Brazil). Scanning Electron Microscopy (SEM) image of BDND was performed using a JEOL JSM-5310 microscope system. It showed that the morphology is quite similar to that of unfaceted CVD ballas diamond, with grains tended to form agglomerates. These agglomerates have approximately $1.5 \mu\text{m}$ of diameter with grains smaller than 30 nm. NCD films with agglomerates grown on a silicon substrate were also reported by Yang et al. [28]. They observed the cauliflower or ball-shaped diamond formation, so-called

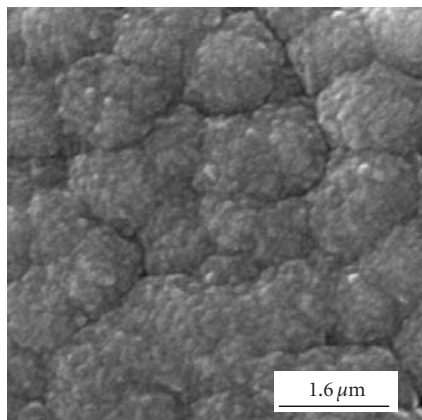


FIGURE 8: SEM image of BDND film grown on a silicon substrate.

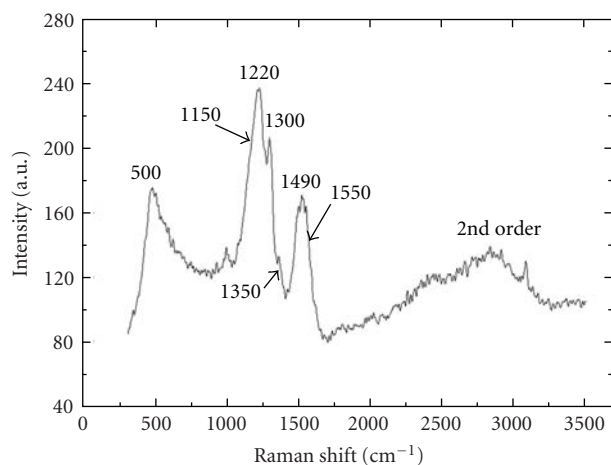


FIGURE 9: Raman spectrum of BDND film grown on a silicon substrate.

CVD ballas diamond, when argon concentrations above 30% were used. They discussed that ballas diamond is nearly pure diamond with strongly twinned microstructure and grows at the transition from faceted diamond to graphite depositions. This film was prepared by HFCVD technique using the following growth parameters: temperature of the 900 K, pressure of the 6.7 KPa, deposition time of the 6 h, and gas mixture of $\text{CH}_4/\text{H}_2/\text{Ar}$ with a flow of 1/19/80 sccm.

Boron doping was obtained by forcing H_2 through a bubbler with B_2O_3 dissolved in methanol. The doping level corresponds to the acceptor concentrations at about 10^{20} cm^{-3} atoms B/C, calculated from Mott-Schottky plot analysis. The presence of boron incorporation in the film can be observed from Raman spectrum shown in Figure 9. The spectrum covered a range from 300 to 3500 cm^{-1} .

Eight features were identified in the Raman spectrum of BDND film. The diamond peak is visible, and shifted to lower wavenumber (1300 cm^{-1}) that is related to impurities formed in heavily doped films showing a metallic conductivity [96]. The bands at 1350 and 1550 cm^{-1} correspond to the D and G band, respectively. Besides, the spectrum exhibited a shoulder at 1150 cm^{-1} and a peak at 1490 cm^{-1}

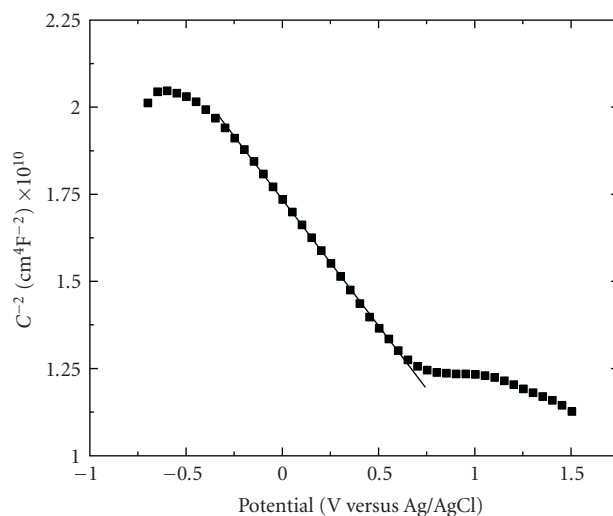


FIGURE 10: Room temperature Mott-Schottky plot C^{-2} versus the potential in $0.5 \text{ mol L}^{-1} \text{ H}_2\text{SO}_4$ obtained at 1000 Hz for as-grown BDND film.

related to TPA at the grain boundaries of NCD surface. The broad bands at about 500 and 1220 cm^{-1} present in these films are still subject to an intense debate. They have been associated with the actual boron incorporation in the lattice, rather than the hole concentration [97]. The presence of the 500 cm^{-1} peak is attributed to the concentration increase of the boron pairs. These boron pairs have local vibration modes giving wide bands at about 500 cm^{-1} [97]. In addition, the band centered at 1220 cm^{-1} is attributed to the Fano interference between the discrete phonon state and the electronic continuum. Pruvost and Deneuille [98] have suggested that the Fano effect appears above a critical percolation threshold for the achievement of the metallic conductivity on the boron impurity band. Meanwhile, Ager et al. [99] have reported that the Fano effect is attributed to the transition from the broadened impurity band to continuum states composed of the excited acceptor and valence band sates.

In the following, the graph of Figure 10 represents the Mott-Schottky plot of as-grown BDND electrode. The physical meaning of a Mott-Schottky plot is related to the effect of potential E on the thickness of the space-charge layer in the semiconductor. The intercept of the linear part of the curve with the potential axis at $C^{-2} = 0$ represents the flat-band potential (E_{FB}), while the slope of the curve allows to determine the acceptor densities in the semiconductor [100]. The value of E_{FB} was about $+2.4 \text{ V}$ versus Ag/AgCl.

Several works describe the use of electrochemical impedance spectroscopy as well as the capacitance-potential measurements to demonstrate the differences in electrode behavior after cathodic or anodic pretreatment of the BDD films [101–103]. For example, Actis et al. [101] have mentioned that the values of the flat band potentials for H-terminated BDD and for photochemically oxidized BDD were 0.52 V and 1.11 V versus SCE, respectively. Becker and Jüttner [104] have explained the occurrence of the

resistance associated to the high-frequency element in the BDD impedance by a partial blocking of the diamond electrode surface. However, this resistance is reduced when the BDD surface undergoes the cathodic treatment. This could be related to a superficial conductive layer (SCL) that exists on hydrogen-terminated diamond surface and it can improve the charge transfer and may explain the enhanced electrochemical response [103]. Furthermore, according to Girard et al. [105], a notable positive shift for E_{FB} in the BDD as-grown electrode from 1.0 to 3.0 V versus Hg/Hg₂SO₄ was observed after the anodic process that contributed to the increase of oxygen terminations. This is also supported by Simon et al. [106] that have reported a positive shift in E_{FB} as characteristic for the formation of C–O structures. Considering the fact that the source of boron doping is a solution of methanol and B₂O₃, it is expected that there was the presence of oxygen-terminated on the surface of this film.

In relation to the electrochemical characteristics of this BDND electrode, its properties are very close to be observed by other authors. CV i - E curve for this film in 0.5 mol L⁻¹ H₂SO₄ (0.1 V·s⁻¹) and the curve obtained in 1 mM of Fe(CN)₆^{-3/-4} + 0.5 mol L⁻¹ H₂SO₄ (0.1 V·s⁻¹) as shown in Figure 11.

Electrochemistry response for the BDND film showed a low capacitance and stable background current, around 3 μA cm⁻² at 500 mV. The working potential window for this film is approximately 2.3 V versus Ag/AgCl where the oxidation water begins at 1.8 V and the reduction water begins at -0.5 V. This value is approximately the same as observed by Siew et al. [15], ca. 2.6 V versus Ag/AgCl, and Zhao et al. [107], ca. 2.8 V versus SCE, but, slightly lower than the values obtained by Hupert et al. [7], Wang et al. [11], and Show et al. [72], ca. 3.0 V versus Ag/AgCl. Regardless of differences between the values of working potential window, the value of the peak potential separation (ΔE_p) observed for all the films [7, 13, 107] was very similar to ours results, approximately 80 mV. Remembering that a lower ΔE_p (~59 mV) reflects the rapid reaction kinetics at the electrode surface and is compatible with the activity of the same.

3.2.1. Applications of Boron-Doped Nanocrystalline Diamond Electrodes. Boron-doped nanocrystalline diamond electrodes can be used for a multitude of applications because of their unique electrochemical properties that largely differ from that of conventional electrode materials. The electrochemical process of these electrodes permit to obtain results that was not possible with conventional electrodes. Some of the results are related to organic substances which have been determined so far with BDND electrodes, such as aminobiphenyls [108], ganciclovir [109], oxalic acid [110], DNA [111], glucose [107, 112, 113], protein [114], and dopamine [15].

The determination of heavy metal ultratracés is a tough challenge for analysts. Human activity, principally during the last two centuries, has released these toxic metals into the environment and now the impact on the health of humans, animals, and plants is obvious. Spectroscopic and electroanalytical techniques have been widely used, but the principal difference between them is related to the

TABLE 2: Quantification limit (ppb) of different heavy metals for BDND electrodes using ASV.

Metals	Ref. [72]	Ref. [115]	Ref. [117]
Ag(I)	0.11	—	1.0
Cu(II)	0.64	3.0	10.0
Pb(II)	2.07	3.8	5.0
Cd(II)	1.12	1.2	1.0
Zn(II)	6.54	5.0	50.0

instrumental cost. Electroanalytical techniques are simple to use in situ and the apparatus is easy to handle for measurements in rivers or lakes.

In the recent past and nowadays, inductively coupled plasma atomic emission spectroscopy (ICP-AES), inductively coupled plasma mass spectroscopy (ICP-MS), and related techniques have been widely used to determine low levels of heavy metals in pharmaceutical drugs, food and fish, wine, highly concentrated salt water, or marine microalgae Fucus [115]. However, electroanalytical techniques may compete with spectral methods for selected heavy metals such as copper, lead, cadmium, and zinc because these four metals are known as reversible (rapid electron exchange) and their signals are wide even at low concentration [72, 115, 116]. Using anodic stripping voltammetry (ASV), Tall et al. [115] and Show et al. [72] were able to detect and quantify Ag(I), Cu(II), Pb(II), Cd(II), and Zn(II) as shown in Table 2. The difference of values presented in Table 2 is related to the experimental conditions used by each author. The results using BDD obtained by McGaw and Swain. [117] were also included in Table 2 to show the advantages of BDND to detect these metals.

Both authors [72, 115] concluded that for the metals studied, the BDND electrode provides good sensitivity, low limits of detection, valuable response precision, and superb response stability for several contaminated samples, such as lake and well water, tap water, wastewater treatment sludge, and contaminated soil.

Some BDND electrodes have been modified superficially with the purpose to absorb a specific substance on their surfaces. The modifying agents of surface can promote selective recognition due to charge transfer, adsorption and ion exchange, or specific biological interactions. Yang et al. [118] have shown the possibility to use a surface electrochemical reaction to achieve electrically addressable biomolecular functionalization of BDND films. They provided a pathway for arrays fabrication of distinct biomolecular recognition elements on diamond surfaces, without the use of microfluidics or spotting methods. The electrically addressable functionalization started with BDND films, followed by functionalization of the diamond with nitro groups. The key to achieve electrically addressable biomolecular functionalization lies in the ability to reduce nitro groups selectively on specific electrodes to primary amines, followed by reaction with bifunctional linkers that will selectively react with the amines and covalently link them to DNA or other biomolecules of interest.

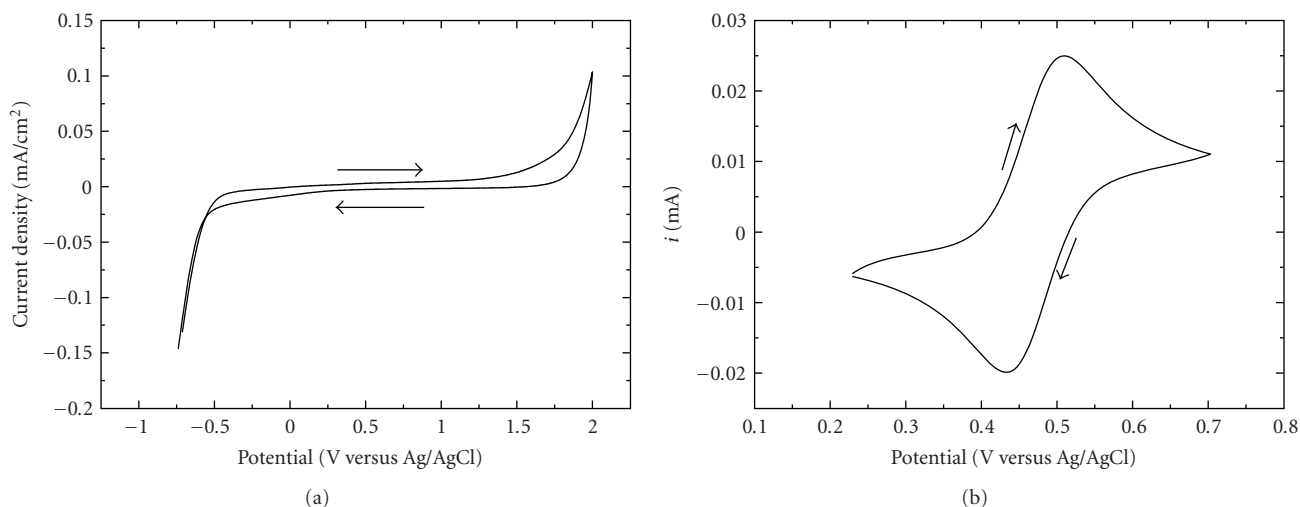


FIGURE 11: CV i - E curve in (a) $0.5 \text{ mol L}^{-1} \text{ H}_2\text{SO}_4$ and (b) 1 mmol L^{-1} ferrocyanide + $0.5 \text{ mol L}^{-1} \text{ H}_2\text{SO}_4$ for BDND electrode. ($\nu = 0.1 \text{ V s}^{-1}$).

Zhou et al. [13] have also got some interesting results from the use of photochemical functionalization on BDND electrodes. They used a photochemical reaction scheme to modify hydrogen-terminated BDND surfaces chemically using a vinyl group of undecylenic acid methyl esters, followed by hydrolyzation of the esters under basic conditions to produce a monolayer of carboxylic groups on the surfaces. Cyt c was covalently immobilized on the resulting carboxyl-terminated BDND electrode through carbodiimide coupling reaction. For comparison, they prepared counterpart biosensors in which Cyt c was immobilized on BDD and glassy carbon (GC) electrodes prepared by the same procedure. The reproducibility and stability of the Cyt c -modified BDND electrode were investigated by the measurement of the response to $100 \mu\text{M H}_2\text{O}_2$ in 0.1 M PBS (pH 7.0). The relative standard deviation (RSD) is 2.1% for 10 successive assays. The long-term stability of the developed enzyme electrode was determined every 3 days, and 85% of its initial activity can be obtained after 6 weeks, while the Cyt c -modified BDD and GC electrodes retained 80% and 25% of their initial activity after 6 weeks. This result suggests that the stability of Cyt c -modified BDND electrode is nearly equivalent to that of the Cyt c -modified BDD electrode, but is significantly higher than that of the Cyt c -modified GC electrode. The superior stability of the Cyt c -modified BDND electrode may be the result of the biocompatible microenvironment for the enzyme provided by the doped diamond electrodes and the high chemical and electrochemical stability of them. Furthermore, the direct electron transfer between Cyt c -modified and the electrodes was obtained and the electron transfer is faster on the BDND than BDD because of the incorporated sp^2 state carbon as charge transfer mediators on BDND surface. So, they concluded that these results make the BDND thin film an interesting candidate for the study of the direct electrochemistry of redox proteins and their sensing applications.

Currently, the water treatment is the application that most has been investigated with diamond electrode. The

high overvoltage for oxygen evolution and the possibility to produce anodically hydroxyl radicals with high current efficiency makes the diamond electrodes especially interesting for destruction/detection of organic pollutants in water. The aromatic compounds, and particularly the phenolics, have high toxicity and low water solubility and are released in the wastewaters from a considerable number of industries [119, 120]. The phenol is potentially fatal if ingested, inhaled, and absorbed by skin and may cause severe burns and affect central nervous system, liver, and kidney [120]. Although effective, existing treatments require the addition of large quantities of reagents (chemical oxidation) or considerable physical areas, long retention time, and difficult process control (biological degradation). The ease of phenol electrochemical oxidation on different electrodes prompted the use of electrochemical methods for the determination of this compound [120]. However, sensitive and stable electrochemical detection of phenols is generally impossible with most materials used for manufacturing the electrode because of irreversible adsorption of reactive intermediates that form a passive film on the electrode surface [120]. The BDND electrode described in Figure 8 (obtained in Diamond Laboratory of LAS/INPE) was used to analyze the detection of different phenolic compounds.

In Figure 12 are shown three CV of 1 mmol L^{-1} of 4-chlorophenol, 4-nitrophenol, and phenol in $0.5 \text{ mol L}^{-1} \text{ H}_2\text{SO}_4$ ($\nu = 0.1 \text{ mV s}^{-1}$). After each subsequent measurement, the BDND surfaces were treated by anodic polarization (2.8 V versus Ag/AgCl) for 10 s followed by cathodic polarization (-2.8 V versus Ag/AgCl) for 10 s. This procedure was necessary to restore the initial electrode activity [121, 122]. The electrode presented a well-defined current profile for each phenol compound and the electrode efficiency was maintained even after several measurements. The oxidation peak potential at 1.16 V , 1.22 V , and 1.52 V versus Ag/AgCl corresponds to 4-chlorophenol, phenol, and 4-nitrophenol, respectively.

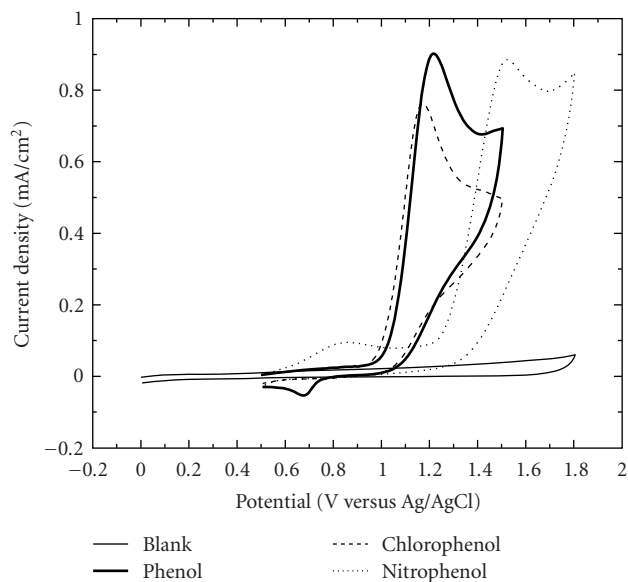


FIGURE 12: CV i - E curve of 1 mmol L^{-1} of 4-chlorophenol, 4-nitrophenol and phenol in $0.5 \text{ mol L}^{-1} \text{ H}_2\text{SO}_4$ for BDND electrode ($\nu = 0.1 \text{ V s}^{-1}$).

For any quantitative method there is a range of analyte concentrations on which the method can be applied. In the low concentration range, the limiting factors are the values of detection and quantification limits [123]. The detection limit of phenol was investigated by square wave voltammetry (SWV) [124]. In this technique, the net current (i_{net}), centered on the redox potential, is obtained by taking the difference between the forward and reverse currents ($i_{\text{for}} - i_{\text{rev}}$). The current peak height is directly proportional to electroactive species concentration and the direct determination of the detection limit is possible. Figure 13 shows the square wave voltammogram for BDND electrode. The BDND electrode presented a well-defined current profile as a function of the phenol concentration and an excellent accuracy of phenol oxidation peak at 1.12 V versus Ag/AgCl. In Figure 13, the inset corresponds to the analytical curve in the current peak versus the concentration in the range of 30 to $130 \mu\text{mol L}^{-1}$ for each electrode. From linear regression analysis of an analytical curve was found this equation:

$$i_p = (-2.5057 \times 10^{-7} \pm 1.1783 \times 10^{-7}) + (1.3522 \times 10^{-7} \pm 1.1716 \times 10^{-9}) \times [\text{phenol}]. \quad (1)$$

This equation was used to evaluate the detection limit (DL) and quantification limit (QL). The DL and QL were calculated from the criterion $\text{DL} = 3\sigma/\theta$ and $\text{QL} = 10\sigma/\theta$, respectively, where σ denotes the standard deviation of arithmetic media of the currents obtained from ten voltammograms of blanks and θ is the slope of analytical curves [124]. The BDND electrode presented a phenol DL of 0.1 mg L^{-1} and phenol QL of 0.4 mg L^{-1} .

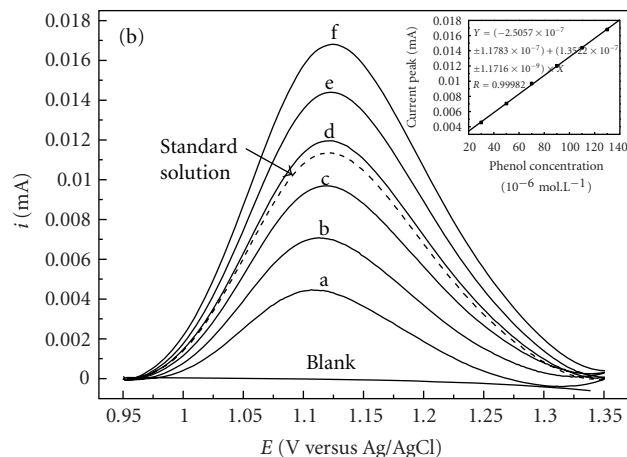


FIGURE 13: Square wave voltammogram in $0.5 \text{ mol L}^{-1} \text{ H}_2\text{SO}_4$ for different phenol concentrations from (a) 30; (b) 50; (c) 70; (dash style) standard solution; (d) 90; (e) 110 and (f) $130 \mu\text{mol L}^{-1}$, using BDND electrode. $f = 60 \text{ Hz}$, step potential = 2 mV and amplitude = 70 mV . Inset: analytical curve for phenol peak.

In Figure 13 also appears a voltammogram identified as “standard solution”, but it was not considered in the previous analytical curve. This solution of 8 mg L^{-1} was prepared from a phenol standard solution of SPECSOL (SRM 136f NIST-USA) to validate the results obtained from the BDND electrode using SWV and chromatographic techniques. The chromatography analyses were performed using Ion Chromatograph (850 Professional IC, Metrohm) equipped with an amperometric detector (791 VA) and a phenol column (Protonsil Enviro PHE $3 \mu\text{m}$). The eluent used for this analysis was $20 \text{ mmol L}^{-1} \text{ KNO}_3 + 0.5 \text{ mmol L}^{-1} \text{ H}_2\text{SO}_4 + 30\% \text{ methanol} + \text{ultrapure deionized water}$.

The values presented below were obtained from the average of three measurements. From the equations it was possible to determine the values of phenol standard sample measured using the BDND electrode. The value was $8.2 \pm 0.2 \text{ mg L}^{-1}$. The same standard solution sample was also injected in the Ion Chromatograph and the value obtained was $7.9 \pm 0.1 \text{ mg L}^{-1}$. As preliminary tests, the results showed that the methodology using the BDND electrode and SWV was very efficient.

Muna et al. [119] have also studied the efficiency of BDND electrode using other analytical techniques. They showed the results of amperometric detection of phenol coupled with Flow Injection Analysis (FIA) and High Performance Liquid Chromatography (HPLC). The values of QL presented were 0.3 mg L^{-1} and 0.1 mg L^{-1} using the FIA and HPLC, respectively. In addition, they mentioned that the QL for the phenolic analytes in their HPLC-EC method is comparable to those reported for Environmental Protection Agency (EPA) methods 1625. So, they confirmed a new possibility for use of this electrode.

4. Conclusions and Outlook

The nanotechnology seeks to study the properties of nanoscale objects and their use in developing devices with these dimensions. This study includes a search by a decrease in materials, targeting a space-saving and energy, and an exploration of new effects that occur at the nanometer scale. Its applications represent a new challenge that includes the fields of physics, chemistry, biology, engineering, and pharmacy, and due to its recent development the nanotechnology has enormous potential to impact science and economics.

Conducting nanodiamond with exceptional hardness, inertness, and stability has been proven as a versatile electrode material for a wide variety of applications. There are several commercial sources that market conducting diamond thin-film electrodes with affordable cost. Undoped or doped nanodiamond electrodes can function in aggressive solution environments without any microstructural or morphological degradation. With favorable mass transport, nanoscale devices enable the study of very fast electrode kinetics and enhance the response of many electroanalytical sensors. Apparently, the undoped nanodiamond occupies a special place as an electrode material in biosensing applications, while the BDND can be considered as one of the most ideal electrode materials for electroanalysis of many chemistry compounds.

Acknowledgments

The authors are very grateful to FAPESP, CNPq, and CAPES for financial support, and Mrs. Maria Lúcia Brison de Mattos (LAS/INPE), Mr. Peter Hammer (UNESP/Araraquara) and UFSCar for SEM, XPS, and FEG-SEM analyses.

References

- [1] J. E. Butler and A. V. Sumant, "The CVD of nanodiamond materials," *Chemical Vapor Deposition*, vol. 14, no. 7-8, pp. 145–160, 2008.
- [2] T. P. Ong, W. A. Chiou, F. R. Chen, and R. P. H. Chang, "Preparation of nanocrystalline diamond films for optical coating applications using a pulsed microwave plasma CVD method," *Carbon*, vol. 28, no. 6, p. 799, 1990.
- [3] D. M. Gruen, X. Z. Pan, A. R. Krauss, S. Z. Liu, J. S. Luo, and C. M. Foster, "Deposition and characterization of nanocrystalline diamond films," *Journal of Vacuum Science & Technology A*, vol. 12, no. 4, pp. 1491–1495, 1994.
- [4] D. M. Gruen, S. Liu, A. R. Krauss, J. Luo, and X. Pan, "Fullerenes as precursors for diamond film growth without hydrogen or oxygen additions," *Applied Physics Letters*, vol. 64, no. 12, pp. 1502–1504, 1994.
- [5] D. M. Gruen, S. Liu, A. R. Krauss, and X. Pan, "Bucky-ball microwave plasmas: fragmentation and diamond-film growth," *Journal of Applied Physics*, vol. 75, no. 3, pp. 1758–1763, 1994.
- [6] A. Gruen, "Nanocrystalline diamond films," *Journal of Psychohistory*, vol. 29, pp. 211–259, 1999.
- [7] M. Hupert, A. Muck, J. Wang et al., "Conductive diamond thin-films in electrochemistry," *Diamond and Related Materials*, vol. 12, no. 10-11, pp. 1940–1949, 2003.
- [8] A. Kraft, "Doped diamond: a compact review on a new, versatile electrode material," *International Journal of Electrochemical Science*, vol. 2, pp. 355–385, 2007.
- [9] J. H. T. Luong, K. B. Male, and J. D. Glennon, "Boron-doped diamond electrode: synthesis, characterization, functionalization and analytical applications," *Analyst*, vol. 134, no. 10, pp. 1965–1979, 2009.
- [10] D. Zhou, D. M. Gruen, L. C. Qin, T. G. McCauley, and A. R. Krauss, "Control of diamond film microstructure by Ar additions to CH₄/H₂ microwave plasmas," *Journal of Applied Physics*, vol. 84, no. 4, pp. 1981–1989, 1998.
- [11] S. Wang, V. M. Swope, J. E. Butler, T. Feygelson, and G. M. Swain, "The structural and electrochemical properties of boron-doped nanocrystalline diamond thin-film electrodes grown from Ar-rich and H₂-rich source gases," *Diamond and Related Materials*, vol. 18, no. 4, pp. 669–677, 2009.
- [12] B. Fausett, M. C. Granger, M. L. Hupert, J. Wang, G. M. Swain, and D. M. Gruen, "The electrochemical properties of nanocrystalline diamond thin-films deposited from C₆₀/argon and methane/nitrogen gas mixtures," *Electroanalysis*, vol. 12, no. 1, pp. 7–15, 2000.
- [13] Y. Zhou, J. Zhi, Y. Zou, W. Zhang, and S. T. Lee, "Direct electrochemistry and electrocatalytic activity of cytochrome *c* covalently immobilized on a boron-doped nanocrystalline diamond electrode," *Analytical Chemistry*, vol. 80, no. 11, pp. 4141–4146, 2008.
- [14] A. E. Fischer, Y. Show, and G. M. Swain, "Electrochemical performance of diamond thin-film electrodes from different commercial sources," *Analytical Chemistry*, vol. 76, no. 9, pp. 2553–2560, 2004.
- [15] P. S. Siew, K. P. Loh, W. C. Poh, and H. Zhang, "Biosensing properties of nanocrystalline diamond film grown on polycrystalline diamond electrodes," *Diamond and Related Materials*, vol. 14, no. 3–7, pp. 426–431, 2005.
- [16] W. Kulisch, C. Popov, V. Vorlicek, P. N. Gibson, and G. Favaro, "Nanocrystalline diamond growth on different substrates," *Thin Solid Films*, vol. 515, no. 3, pp. 1005–1010, 2006.
- [17] M. Amaral, F. J. Oliveira, M. Belmonte, A. J. S. Fernandes, F. M. Costa, and R. F. Silva, "Hot-filament chemical vapour deposition of nanodiamond on silicon nitride substrates," *Diamond and Related Materials*, vol. 13, no. 4–8, pp. 643–647, 2004.
- [18] M. R. Baldan, S. C. Ramos, E. C. Almeida, A. F. Azevedo, and N. G. Ferreira, "Homogeneous micro and nanocrystalline diamond coating on reticulated vitreous carbon treated at different temperatures," *Diamond and Related Materials*, vol. 17, no. 7–10, pp. 1110–1115, 2008.
- [19] C. R. B. Miranda, N. A. Braga, M. R. Baldan, A. F. Beloto, and N. G. Ferreira, "Improvements in CVD/CVI processes for optimizing nanocrystalline diamond growth into porous silicon," *Diamond and Related Materials*, vol. 19, no. 7–9, pp. 760–763, 2010.
- [20] G. Cicala, P. Bruno, F. Bénédic, F. Silva, K. Hassouni, and G. S. Senesi, "Nucleation, growth and characterization of nanocrystalline diamond films," *Diamond and Related Materials*, vol. 14, no. 3–7, pp. 421–425, 2005.
- [21] F. Silva, F. Bénédic, P. Bruno, and A. Gicquel, "Formation of <110> texture during nanocrystalline diamond growth: an X-ray diffraction study," *Diamond and Related Materials*, vol. 14, no. 3–7, pp. 398–403, 2005.

- [22] Sh. Michaelson, A. Stacey, J. Orwa et al., "Bulk and surface thermal stability of ultra nanocrystalline diamond films with 10–30 nm grain size prepared by chemical vapor deposition," *Journal of Applied Physics*, vol. 107, pp. 093521-1–093521-7, 2010.
- [23] W. S. Huang, D. T. Tran, J. Asmussen, T. A. Grotjohn, and D. Reinhard, "Synthesis of thick, uniform, smooth ultrananocrystalline diamond films by microwave plasma-assisted chemical vapor deposition," *Diamond and Related Materials*, vol. 15, no. 2-3, pp. 341–344, 2006.
- [24] H. Kozak, A. Kromka, E. Ukraintsev et al., "Detecting sp^2 phase on diamond surfaces by atomic force microscopy phase imaging and its effects on surface conductivity," *Diamond and Related Materials*, vol. 18, no. 5–8, pp. 722–725, 2009.
- [25] A. F. Azevedo, E. J. Corat, N. F. Leite, and V. J. Trava-Airoldi, "Chemical vapor deposition diamond thin films growth on Ti6Al4V using the Surfatron system," *Diamond and Related Materials*, vol. 11, no. 3-6, pp. 550–554, 2002.
- [26] A. F. Azevedo, E. J. Corat, N. F. Leite, N. G. Ferreira, and V. J. Trava-Airoldi, "Raman analyses of residual stress in diamond thin films grown on Ti6Al4V alloy," *Materials Research*, vol. 6, no. 1, pp. 51–56, 2003.
- [27] S. G. Wang, Q. Zhang, S. F. Yoon et al., "Electron field emission properties of nano-, submicro- and micro-diamond films," *Physica Status Solidi A*, vol. 193, no. 3, pp. 546–551, 2002.
- [28] T. S. Yang, J. Y. Lai, C. L. Cheng, and M. S. Wong, "Growth of faceted, ballas-like and nanocrystalline diamond films deposited in $CH_4/H_2/Ar$ MPCVD," *Diamond and Related Materials*, vol. 10, no. 12, pp. 2161–2166, 2001.
- [29] J. A. Carlisle and O. Auciello, "Ultrananocrystalline diamond: properties and applications in biomedical devices," *Electrochemical Society Interface*, vol. 12, no. 1, pp. 28–31, 2003.
- [30] P. W. May and Y. A. Mankelevich, "Experiment and modeling of the deposition of ultrananocrystalline diamond films using hot filament chemical vapor deposition and $Ar/CH_4/H_2$ gas mixtures: a generalized mechanism for ultrananocrystalline diamond growth," *Journal of Applied Physics*, vol. 100, no. 2, Article ID 024301, 9 pages, 2006.
- [31] P. W. May, J. A. Smith, and Y. A. Mankelevich, "Deposition of NCD films using hot filament CVD and $Ar/CH_4/H_2$ gas mixtures," *Diamond and Related Materials*, vol. 15, no. 2-3, pp. 345–352, 2006.
- [32] J. G. Buijnsters, L. Vázquez, G. W. G. Van Dreumel, J. J. Ter Meulen, W. J. P. Van Enckevort, and J. P. Celis, "Enhancement of the nucleation of smooth and dense nanocrystalline diamond films by using molybdenum seed layers," *Journal of Applied Physics*, vol. 108, no. 10, Article ID 103514, 9 pages, 2010.
- [33] G. F. Zhang and V. Buck, "Lower filament temperature limit of diamond growth in a hot-filament CVD system," *Surface and Coatings Technology*, vol. 160, no. 1, pp. 14–19, 2002.
- [34] K. K. Hirakuri, T. Kobayashi, E. Nakamura, N. Mutsukura, G. Friedbacher, and Y. Machi, "Influence of the methane concentration on HF-CVD diamond under atmospheric pressure," *Vacuum*, vol. 63, no. 3, pp. 449–454, 2001.
- [35] Y. H. Tang, X. T. Zhou, Y. F. Hu, C. S. Lee, S. T. Lee, and T. K. Sham, "A soft X-ray absorption study of nanodiamond films prepared by hot-filament chemical vapor deposition," *Chemical Physics Letters*, vol. 372, no. 3-4, pp. 320–324, 2003.
- [36] N. G. Ferreira, A. F. Azevedo, A. F. Beloto et al., "Nanodiamond films growth on porous silicon substrates for electrochemical applications," *Diamond and Related Materials*, vol. 14, no. 3–7, pp. 441–445, 2005.
- [37] S. Potocky, A. Kromka, J. Potmesil et al., "Investigation of nanocrystalline diamond films grown on silicon and glass at substrate temperature below 400 °C," *Diamond and Related Materials*, vol. 16, no. 4–7, pp. 744–747, 2007.
- [38] T. S. Yang, J. Y. Lai, M. S. Wong, and C. L. Cheng, "Substrate bias effect on the formation of nanocrystalline diamond films by microwave plasma-enhanced chemical vapor deposition," *Journal of Applied Physics*, vol. 92, no. 4, pp. 2133–2138, 2002.
- [39] V. J. Trava-Airoldi, A. F. Azevedo, E. J. Corat, J. R. Moro, and N. F. Leite, "Diamond deposition using surface wave system with high microwave power," *Brazilian Journal of Vacuum Applications*, vol. 19, no. 1, pp. 6–10, 2000.
- [40] A. F. Azevedo, N. G. Ferreira, E. J. Corat, and V. J. Trava-Airoldi, "Adherence measurements of nanodiamond thin films grown on Ti6Al4V alloy," *Journal of Metastable and Nanocrystalline Materials*, vol. 20-21, pp. 753–757, 2004.
- [41] K. Wu, E. G. Wang, Z. X. Cao, Z. L. Wang, and X. Jiang, "Microstructure and its effect on field electron emission of grain-size-controlled nanocrystalline diamond films," *Journal of Applied Physics*, vol. 88, no. 5, pp. 2967–2974, 2000.
- [42] A. F. Azevedo, J. T. Matsushima, F. C. Vicentin, M. R. Baldan, and N. G. Ferreira, "Surface characterization of NCD films as a function of sp^2/sp^3 carbon and oxygen content," *Applied Surface Science*, vol. 255, no. 13-14, pp. 6565–6570, 2009.
- [43] S. C. Ramos, A. F. Azevedo, M. R. Baldan, and N. G. Ferreira, "Effect of methane addition on ultrananocrystalline diamond formation: morphology changes and induced stress," *Journal of Vacuum Science and Technology A*, vol. 28, no. 1, pp. 27–32, 2010.
- [44] A. F. Azevedo, S. C. Ramos, M. R. Baldan, and N. G. Ferreira, "Graphitization effects of CH_4 addition on NCD growth by first and second Raman spectra and by X-ray diffraction measurements," *Diamond and Related Materials*, vol. 17, no. 7–10, pp. 1137–1142, 2008.
- [45] A. F. Azevedo, V. J. Trava-Airoldi, and N. G. Ferreira, "Bias-Enhanced nucleation of NCD on high-adherent diamond/Ti6Al4V films," *International Journal of Nanomanufacturing*, vol. 2, no. 1-2, pp. 70–79, 2008.
- [46] Y. F. Zhang, F. Zhang, Q. J. Gao, X. F. Peng, and Z. D. Lin, "The roles of argon addition in the hot filament chemical vapor deposition system," *Diamond and Related Materials*, vol. 10, no. 8, pp. 1523–1527, 2001.
- [47] M. Vila, M. Amaral, F. J. Oliveira, R. F. Silva, A. J. S. Fernandes, and M. R. Soares, "Residual stress minimum in nanocrystalline diamond films," *Applied Physics Letters*, vol. 89, no. 9, Article ID 093109, 3 pages, 2006.
- [48] Y. Lifshitz, C. H. Lee, Y. Wu, W. J. Zhang, I. Bello, and S. T. Lee, "Role of nucleation in nanodiamond film growth," *Applied Physics Letters*, vol. 88, no. 24, Article ID 243114, 3 pages, 2006.
- [49] T. Soga, T. Sharda, and T. Jimbo, "Precursors for CVD growth of nanocrystalline diamond," *Physics of the Solid State*, vol. 46, no. 4, pp. 720–725, 2004.
- [50] J. E. Butler and I. Oleynik, "A mechanism for crystal twinning in the growth of diamond by chemical vapour deposition," *Philosophical Transactions of the Royal Society A*, vol. 366, no. 1863, pp. 295–311, 2008.
- [51] D. C. Barbosa, L. L. Melo, V. J. Trava-Airoldi, and E. J. Corat, "The activation energy for nanocrystalline diamond films deposited from an $Ar/H_2/CH_4$ hot-filament reactor," *Journal of Nanoscience and Nanotechnology*, vol. 9, no. 6, pp. 3944–3948, 2009.

- [52] D. C. Barbosa, P. R. P. Barreto, V. J. Trava-Airoldi, and E. J. Corat, "Growth and characterization of diamond micro and nano crystals obtained using different methane concentration in argon-rich gas mixture," *Diamond and Related Materials*, vol. 19, no. 7–9, pp. 768–771, 2010.
- [53] W. Haenni, P. Rychen, M. Fryda, and C. Comninellis, "Semiconductors and Semimetals series," in *Thin-Film Diamond B*, Ch. Nebel, Ed., p. 149, Academic Press, Elsevier, 2004.
- [54] Q. Liang, J. G. Harrison, and Y. K. Vohra, "Modeling of nitrogen/diborane/methane/hydrogen plasma for nanocrystalline diamond growth: comparison with experimental data," *Diamond and Related Materials*, vol. 17, no. 12, pp. 2067–2070, 2008.
- [55] P. Hartmann, R. Haubner, and B. Lux, "Effects of simultaneous boron and nitrogen addition on hot-filament CVD diamond growth," *Diamond and Related Materials*, vol. 6, no. 2–4, pp. 456–462, 1997.
- [56] S. Koizumi, K. Watanabe, M. Hasegawa, and H. Kanda, "Ultraviolet emission from a diamond pn junction," *Science*, vol. 292, no. 5523, pp. 1899–1901, 2001.
- [57] S. J. Sque, R. Jones, J. P. Goss, and P. R. Briddon, "Shallow donors in diamond: chalcogens, pnictogens, and their hydrogen complexes," *Physical Review Letters*, vol. 92, no. 1, Article ID 017402, 4 pages, 2004.
- [58] M. Iwaki, S. Sato, K. Takahashi, and H. Sakairi, "Electrical conductivity of nitrogen and argon implanted diamond," *Nuclear Instruments and Methods In Physics Research*, vol. 209–210, no. 2, pp. 1129–1133, 1983.
- [59] Y. V. Pelskov, A. Y. Sakharova, M. D. Krotova, L. L. Bouilov, and B. V. Spitsyn, "Photoelectrochemical properties of semiconductor diamond," *Journal of Electroanalytical Chemistry*, vol. 228, no. 1–2, pp. 19–27, 1987.
- [60] A. N. Jones, W. Ahmed, I. U. Hassan et al., "The impact of inert gases on the structure, properties and growth of nanocrystalline diamond," *Journal of Physics Condensed Matter*, vol. 15, no. 39, pp. S2969–S2975, 2003.
- [61] M. J. Jackson, A. N. Jones, and W. Ahmed, "Experimental and gas phase modeling of nanocrystalline diamond films grown on titanium alloys for biomedical applications," *Journal of Materials Engineering and Performance*, vol. 14, no. 5, pp. 565–568, 2005.
- [62] T. Ikeda and K. Teii, "Comparative study on nanocrystalline diamond growth from acetylene and methane," *Diamond and Related Materials*, vol. 15, no. 4–8, pp. 635–638, 2006.
- [63] K. Brühne, K. V. Kumar, H. J. Fecht, P. Gluche, and A. Flöter, "Nanocrystalline HF-CVD-grown diamond and its industrial applications," *Reviews on Advanced Materials Science*, vol. 10, no. 64, pp. 224–228, 2005.
- [64] J. Birrell, J. E. Gerbi, O. Auciello, J. M. Gibson, J. Johnson, and J. A. Carlisle, "Interpretation of the Raman spectra of ultrananocrystalline diamond," *Diamond and Related Materials*, vol. 14, no. 1, pp. 86–92, 2005.
- [65] P. K. Chu and L. Li, "Characterization of amorphous and nanocrystalline carbon films," *Materials Chemistry and Physics*, vol. 96, no. 2–3, pp. 253–277, 2006.
- [66] A. C. Ferrari and J. Robertson, "Raman spectroscopy of amorphous, nanostructured, diamond-like carbon, and nanodiamond," *Philosophical Transactions of the Royal Society A*, vol. 362, no. 1824, pp. 2477–2512, 2004.
- [67] J. K. Shin, C. S. Lee, K. R. Lee, and K. Y. Eun, "Effect of residual stress on the Raman-spectrum analysis of tetrahedral amorphous carbon films," *Applied Physics Letters*, vol. 78, no. 5, pp. 631–633, 2001.
- [68] S. Ferro, M. Dal Colle, and A. De Battisti, "Chemical surface characterization of electrochemically and thermally oxidized boron-doped diamond film electrodes," *Carbon*, vol. 43, no. 6, pp. 1191–1203, 2005.
- [69] P. Chen and R. L. McCreery, "Control of electron transfer kinetics at glassy carbon electrodes by specific surface modification," *Analytical Chemistry*, vol. 68, no. 22, pp. 3958–3965, 1996.
- [70] L. C. Hian, K. J. Grehan, R. G. Compton, J. S. Foord, and F. Marken, "Influence of thin film properties on the electrochemical performance of diamond electrodes," *Diamond and Related Materials*, vol. 12, no. 3–7, pp. 590–595, 2003.
- [71] J. Foord and J. P. Hu, "Electrochemical oxidation and reduction processes at diamond electrodes of varying phase purity," *Physica Status Solidi (A) Applications and Materials*, vol. 203, no. 12, pp. 3121–3127, 2006.
- [72] Y. Show, M. A. Witek, P. Sonthalia, and G. M. Swain, "Characterization and electrochemical responsiveness of boron-doped nanocrystalline diamond thin-film electrodes," *Chemistry of Materials*, vol. 15, no. 4, pp. 879–888, 2003.
- [73] M. C. Granger and G. M. Swain, "The influence of surface interactions on the reversibility of ferri/ferrocyanide at boron-doped diamond thin-film electrodes," *Journal of the Electrochemical Society*, vol. 146, no. 12, pp. 4551–4558, 1999.
- [74] D. M. Gruen, A. R. Krauss, D. Zhou et al., "Nanocrystalline diamond films from argon microwave plasmas: phase purity, microstructure, growth mechanism, and applications," in *Electrochemical Society Proceedings*, vol. PV 97-25, p. 325, Pennington, NJ, USA, 1997.
- [75] V. Raiko, R. Spitzl, J. Engemann, V. Borisenko, and V. Bondarenko, "MPCVD diamond deposition on porous silicon pretreated with the bias method," *Diamond and Related Materials*, vol. 5, no. 10, pp. 1063–1069, 1996.
- [76] A. F. Azevedo, E. J. Corat, N. G. Ferreira, and V. J. Trava-Airoldi, "Wettability and corrosion tests of diamond films grown on Ti6Al4V alloy," *Surface and Coatings Technology*, vol. 194, no. 2–3, pp. 271–275, 2005.
- [77] L. C. Hian, K. J. Grehan, C. H. Goeting, R. G. Compton, J. S. Foord, and F. Marken, "Nanodiamond thin film electrodes: metal electro-deposition and stripping processes," *Electroanalysis*, vol. 15, no. 3, pp. 169–174, 2003.
- [78] L. C. Hian, K. J. Grehan, R. G. Compton, J. S. Foord, and F. Marken, "Nanodiamond thin films on titanium substrates growth and electrochemical properties," *Journal of the Electrochemical Society*, vol. 150, no. 1, pp. E59–E65, 2003.
- [79] N. A. Braga, C. A. A. Cairo, J. T. Matsushima, M. R. Baldan, and N. G. Ferreira, "Diamond/porous titanium three-dimensional hybrid electrodes," *Journal of Solid State Electrochemistry*, vol. 14, no. 2, pp. 313–321, 2010.
- [80] R. C. Mani, S. Sharma, M. K. Sunkara et al., "Synthesis and electrochemical characteristics of a nanocomposite diamond electrode," *Electrochemical and Solid-State Letters*, vol. 5, no. 6, pp. E32–E35, 2002.
- [81] S. P. Lawrence and R. K. Don, *Diamond: Electronic Properties and Applications*, Kluwer Academic Publishers, Boston, Mass, USA, 1995.
- [82] F. Klauser, M. Hermann, D. Steinmüller-Nethl et al., "Direct and protein-mediated cell attachment on differently terminated Nanocrystalline diamond," *Chemical Vapor Deposition*, vol. 16, no. 1–3, pp. 42–49, 2010.
- [83] T. S. Huang, Y. Tzeng, Y. K. Liu et al., "Immobilization of antibodies and bacterial binding on nanodiamond and carbon nanotubes for biosensor applications," *Diamond and Related Materials*, vol. 13, no. 4–8, pp. 1098–1102, 2004.

- [84] A. Poghossian, M. H. Abouzar, A. Razavi et al., "Nanocrystalline-diamond thin films with high pH and penicillin sensitivity prepared on a capacitive Si-SiO₂ structure," *Electrochimica Acta*, vol. 54, no. 25, pp. 5981–5985, 2009.
- [85] M. H. Abouzar, A. Poghossian, A. Razavi et al., "Characterisation of capacitive field-effect sensors with a nanocrystalline-diamond film as transducer material for multi-parameter sensing," *Biosensors and Bioelectronics*, vol. 24, no. 5, pp. 1298–1304, 2009.
- [86] J. Rubio-Retama, J. Hernando, B. Lopez-Ruiz et al., "Synthetic nanocrystalline diamond as a third-generation biosensor support," *Langmuir*, vol. 22, pp. 5837–5842, 2006.
- [87] W. Yang, O. Auciello, J. E. Butler et al., "DNA-modified nanocrystalline diamond thin-films as stable, biologically active substrates," *Nature Materials*, vol. 1, no. 4, pp. 253–257, 2002.
- [88] C. V. Guterl, E. Frackowiak, K. Jurewicz, M. Friebe, J. Parmentier, and F. Béguin, "Electrochemical energy storage in ordered porous carbon materials," *Carbon*, vol. 43, no. 6, pp. 1293–1302, 2005.
- [89] E. Frackowiak and F. Béguin, "Carbon materials for the electrochemical storage of energy in capacitors," *Carbon*, vol. 39, no. 6, pp. 937–950, 2001.
- [90] E. C. Almeida, A. F. Azevedo, M. R. Baldan, N. A. Braga, J. M. Rosolen, and N. G. Ferreira, "Nanocrystalline diamond/carbon felt as a novel composite for electrochemical storage energy in capacitor," *Chemical Physics Letters*, vol. 438, no. 1–3, pp. 47–52, 2007.
- [91] J. H. Chen, W. Z. Li, D. Z. Wang, S. X. Yang, J. G. Wen, and Z. F. Ren, "Electrochemical characterization of carbon nanotubes as electrode in electrochemical double-layer capacitors," *Carbon*, vol. 40, no. 8, pp. 1193–1197, 2002.
- [92] M. Yoshimura, K. Honda, R. Uchikado et al., "Electrochemical characterization of nanoporous honeycomb diamond electrodes in non-aqueous electrolytes," *Diamond and Related Materials*, vol. 10, no. 3–7, pp. 620–626, 2001.
- [93] E. L. Silva, M. A. Neto, A. J. S. Fernandes et al., "Fast coating of ultramicroelectrodes with boron-doped nanocrystalline diamond," *Diamond and Related Materials*, vol. 19, no. 10, pp. 1330–1335, 2010.
- [94] Y. Show, V. M. Swope, and G. M. Swain, "The effect of the CH₄ level on the morphology, microstructure, phase purity and electrochemical properties of carbon films deposited by microwave-assisted CVD from Ar-rich source gas mixtures," *Diamond and Related Materials*, vol. 18, no. 12, pp. 1426–1434, 2009.
- [95] Z. Gao, V. Carabelli, E. Carbone et al., "Transparent diamond microelectrodes for biochemical application," *Diamond and Related Materials*, vol. 19, no. 7–9, pp. 1021–1026, 2010.
- [96] C. Lévy-Clément, N. A. Ndao, A. Katty et al., "Boron doped diamond electrodes for nitrate elimination in concentrated wastewater," *Diamond and Related Materials*, vol. 12, no. 3–7, pp. 606–612, 2003.
- [97] M. Bernard, C. Baron, and A. Deneuve, "About the origin of the low wave number structures of the Raman spectra of heavily boron doped diamond films," *Diamond and Related Materials*, vol. 13, no. 4–8, pp. 896–899, 2004.
- [98] F. Pruvost and A. Deneuve, "Analysis of the Fano in diamond," *Diamond and Related Materials*, vol. 10, no. 3–7, pp. 531–535, 2001.
- [99] J. W. Ager III, W. Walukiewicz, M. McCluskey, M. A. Plano, and M. I. Landstrass, "Fano interference of the Raman phonon in heavily boron-doped diamond films grown by chemical vapor deposition," *Applied Physics Letters*, vol. 66, pp. 616–618, 1995.
- [100] Y. V. Pleskov, "Electrochemistry of diamond: a review," *Russian Journal of Electrochemistry*, vol. 38, pp. 1275–1291, 2002.
- [101] P. Actis, A. Denoyelle, R. Boukherroub, and S. Szunerits, "Influence of the surface termination on the electrochemical properties of boron-doped diamond (BDD) interfaces," *Electrochemistry Communications*, vol. 10, pp. 402–406, 2008.
- [102] H. B. Suffredini, V. A. Pedrosa, L. Codognoto, S. A. S. Machado, R. C. Rocha-Filho, and L. A. Avaca, "Enhanced electrochemical response of boron-doped diamond electrodes brought on by a cathodic surface pre-treatment," *Electrochimica Acta*, vol. 49, no. 22–23, pp. 4021–4026, 2004.
- [103] H. Girard, N. Simon, D. Ballutaud, E. Rochefoucauld, and A. Etcheberry, "Effects of controlled anodic treatments on electrochemical behavior of boron doped diamond," *Diamond and Related Materials*, vol. 16, pp. 888–891, 2007.
- [104] D. Becker and K. Jüttner, "Impedance measurements on boron-doped diamond electrodes at different doping levels," *New Diamond and Frontier Carbon Technology*, vol. 13, pp. 67–78, 2003.
- [105] H. Girard, N. Simon, D. Ballutaud, M. Herlem, and A. Etcheberry, "Effect of anodic and cathodic treatments on the charge transfer of boron doped diamond electrodes," *Diamond and Related Materials*, vol. 16, no. 2, pp. 316–325, 2007.
- [106] N. Simon, H. Girard, D. Ballutaud et al., "Effect of H and O termination on the charge transfer of moderately boron doped diamond electrodes," *Diamond and Related Materials*, vol. 14, no. 3–7, pp. 1179–1182, 2005.
- [107] J. Zhao, J. Wang, J. Zhi, and Z. Zhang, "Preparation of grain size controlled boron-doped diamond thin films and their applications in selective detection of glucose in basic solutions," *Science China Chemistry*, vol. 53, no. 6, pp. 1378–1384, 2010.
- [108] J. Barek, K. Jandova, K. Peckova, and J. Zima, "Voltammetric determination of aminobiphenyls at a boron-doped nanocrystalline diamond film electrode," *Talanta*, vol. 74, pp. 421–426, 2007.
- [109] Y. Zhou, J. Zhi, X. Zhang, and M. Xu, "Electrochemical studies of ganciclovir at boron-doped nanocrystalline diamond electrodes," *Diamond and Related Materials*, vol. 20, no. 1, pp. 18–22, 2011.
- [110] A. F. Azevedo, N. A. Braga, F. A. Souza, J. T. Matsushima, M. R. Baldan, and N. G. Ferreira, "The effect of surface treatment on oxidation of oxalic acid at nanocrystalline diamond films," *Diamond and Related Materials*, vol. 19, no. 5–6, pp. 462–465, 2010.
- [111] T. Clukers, B. Van Grinsven, T. Vandenryt et al., "Boron doped nanocrystalline diamond temperature regulator for sensing applications," *Physica Status Solidi A*, vol. 207, pp. 2110–2113, 2010.
- [112] J. Zhao, D. Wu, and J. Zhi, "A direct electrochemical method for diabetes diagnosis based on as-prepared boron-doped nanocrystalline diamond thin film electrodes," *Journal of Electroanalytical Chemistry*, vol. 626, no. 1–2, pp. 98–102, 2009.
- [113] D. Luo, L. Wu, and J. Zhi, "Fabrication of boron-doped diamond nanorod forest electrodes and their application in nonenzymatic amperometric glucose biosensing," *ACS Nano*, vol. 3, no. 8, pp. 2121–2128, 2009.

- [114] S. Haymond, G. T. Babcock, and G. M. Swain, "Direct electrochemistry of cytochrome C at nanocrystalline boron-doped diamond," *Journal of the American Chemical Society*, vol. 124, no. 36, pp. 10634–10635, 2002.
- [115] O. El Tall, N. Jaffrezic-Renault, M. Sigaud, and O. Vittori, "Anodic stripping voltammetry of heavy metals at nanocrystalline boron-doped diamond electrode," *Electroanalysis*, vol. 19, no. 11, pp. 1152–1159, 2007.
- [116] P. Sonthalia, E. McGaw, Y. Show, and G. M. Swain, "Metal ion analysis in contaminated water samples using anodic stripping voltammetry and a nanocrystalline diamond thin-film electrode," *Analytica Chimica Acta*, vol. 522, no. 1, pp. 35–44, 2004.
- [117] E. A. McGaw and G. M. Swain, "A comparison of boron-doped diamond thin-film and Hg-coated glassy carbon electrodes for anodic stripping voltammetric determination of heavy metal ions in aqueous media," *Analytica Chimica Acta*, vol. 575, no. 2, pp. 180–189, 2006.
- [118] W. Yang, S. E. Baker, J. E. Butler et al., "Electrically addressable biomolecular functionalization of conductive nanocrystalline diamond thin films," *Chemistry of Materials*, vol. 17, no. 5, pp. 938–940, 2005.
- [119] G. W. Muna, N. Tasheva, and G. M. Swain, "Electro-oxidation and amperometric detection of chlorinated phenols at boron-doped diamond electrodes: a comparison of microcrystalline and nanocrystalline thin films," *Environmental Science & Technology*, vol. 38, pp. 3674–3682, 2004.
- [120] B. Šljukić, C. E. Banks, A. Crossley, and R. G. Compton, "Lead(IV) oxide-graphite composite electrodes: application to sensing of ammonia, nitrite and phenols," *Analytica Chimica Acta*, vol. 587, no. 2, pp. 240–246, 2007.
- [121] M. A. Rodrigo, P. A. Michaud, I. Duo, M. Panizza, G. Cerisola, and C. Comninellis, "Oxidation of 4-chlorophenol at boron-doped diamond electrode for wastewater treatment," *Journal of the Electrochemical Society*, vol. 148, no. 5, pp. D60–D64, 2001.
- [122] J. Iniesta, P. A. Michaud, M. Panizza, G. Cerisola, A. Aldaz, and C. Comninellis, "Electrochemical oxidation of phenol at boron-doped diamond electrode," *Electrochimica Acta*, vol. 46, no. 23, pp. 3573–3578, 2001.
- [123] L. A. Currie, "Detection and quantification limits: basic concepts, international harmonization, and outstanding ("low-level") issues," *Applied Radiation and Isotopes*, vol. 61, no. 2–3, pp. 145–149, 2004.
- [124] L. Codognoto, S. A. S. Machado, and L. A. Avaca, "Square wave voltammetry on boron-doped diamond electrodes for analytical determinations," *Diamond and Related Materials*, vol. 11, no. 9, pp. 1670–1675, 2002.

Review Article

The Use of Diamond for Energy Conversion System Applications: A Review

**K. I. B. Eguiluz,¹ J. M. Peralta-Hernández,² A. Hernández-Ramírez,³ J. L. Guzmán-Mar,³
L. Hinojosa-Reyes,³ C. A. Martínez-Huitle,⁴ and G. R. Salazar-Banda¹**

¹*Instituto de Tecnologia e Pesquisa e Programa de Pós-Graduação em Engenharia de Processos, Universidade Tiradentes, 49032-490 Aracaju, SE, Brazil*

²*Centro de Innovación Aplicada en Tecnologías Competitivas, Departamento de Investigación Ambiental, Omega-201, Fraccionamiento Industrial Delta, 37545 León, Guanajuato, Mexico*

³*Laboratorio de Fotocatálisis y Electroquímica Ambiental, Facultad de Ciencias Químicas, Universidad Autónoma de Nuevo León, 64570 Monterrey, NL, Mexico*

⁴*Departamento de Química, Centro de Ciências Exatas e da Terra, Universidade Federal do Rio Grande do Norte, Lagoa Nova 59078-970 Natal, RN, Brazil*

Correspondence should be addressed to G. R. Salazar-Banda, gianrsb@gmail.com

Received 1 May 2011; Revised 20 June 2011; Accepted 21 June 2011

Academic Editor: Yasuaki Einaga

Copyright © 2012 K. I. B. Eguiluz et al. This is an open access article distributed under the Creative Commons Attribution License, which permits unrestricted use, distribution, and reproduction in any medium, provided the original work is properly cited.

Catalytic layers of polymer electrolyte membrane fuel cell (PEMFC) electrodes are usually composed of platinum nanoparticles dispersed on an electron conductive carbon support, which can undergo several degradation processes like dissolution of Pt and carbon corrosion under PEMFC working conditions. In this context, the major advantage of conductive boron-doped diamond (BDD) surfaces is their mechanical and chemical stability. BDD is also considered as a good substrate for studying the intrinsic properties of deposited catalysts, avoiding some problems encountered with other substrates, that is, surface corrosion, oxide formation, or electronic interactions with the deposit. Thus, the first part of this review summarized the surface modification of BDD materials, with emphasis in different techniques, to improve the catalytic efficiency of supported catalysts for PEMFCs. In addition, it is known that graphite carbon or lithium metal alloys used in advanced lithium-ion high-energy batteries suffer morphological changes during the charge-discharge cycling, which in turn results in a very poor cycle life. Thus, the use of diamond materials in these applications was also reviewed, since they have very stable surfaces and exhibits excellent electrochemical properties when compared with other carbon forms like glassy carbon and highly oriented pyrolytic graphite.

1. Introduction

The continuous use of petroleum as the main source of energy has caused considerable atmospheric pollution and global warming. At the same time, with the continued climbing of crude oil price and increase of energy demand, research on alternative energy resources becomes an urgent task for scientists around the world. In that manner, electrochemists intensified their research in order to develop the fuel cell technology. Fuel cells can convert chemical fuels, including some renewable, directly into electricity. The main advantage of this technology over traditional energy production is that the fuel cell energy efficiency is Carnot cycle independent. Fuel cells, in particular polymer

electrolyte membrane fuel cells (PEMFCs), represent an attractive technology to meet future energy needs because of their potentially high efficiency in converting stored chemical energy to electrical energy. However, their widespread deployment has been hampered by materials limitations, as exemplified in the catalysts by their high cost, intolerance to fuel contaminants, and degradation leading to short fuel cell lifetimes. The possible use of methanol and other small organic molecules as PEMFC fuels is promising because of their high energy density and ease of transport, compared to H₂.

The catalytic layers of PEMFC electrodes are usually composed of platinum nanoparticles dispersed on an electron conductive carbon support, in weight ratios higher

TABLE 1: Survey of recent publications on metal/metal oxide particles from microemulsions deposited onto BDD thin film electrodes with applications in fuel cells.

Catalyst	Microemulsion system	Metal precursor	Reducing/precipitating agent	Particle diameter (nm)	Catalytic reaction	Reference
Pt	BRIJ-30 ¹ /n-heptane	H ₂ PtCl ₆	NH ₂ NH ₂	2–3	Methanol oxidation	[20]
Pt-Ru	BRIJ-30 ¹ /n-heptane	H ₂ PtCl ₆ , RuCl ₃	NaBH ₄	2–5	Methanol and ethanol oxidation	[21]
Pt-Sn	BRIJ-30 ¹ /n-heptane	H ₂ PtCl ₆ , SnCl ₂	NaBH ₄	2–5	Ethanol oxidation	[22]
Pt/Ru/Sn	BRIJ-30 ¹ /n-heptane	H ₂ PtCl ₆ , RuCl ₃ , SnCl ₂	NaBH ₄	2–5	Methanol and ethanol oxidation	[23]

¹BRIJ-30: Polyoxyethylene (4) lauryl ether (non ionic surfactant).

than 10 wt% [1, 2]. Under PEMFC working conditions, the catalytic layers undergo several degradation processes: dissolution of platinum [3] and carbon corrosion [4], increase of the particle size due to agglomeration [5], and so forth. In this context, in recent years, conductive films of boron-doped diamond (BDD) have been used for many researches as an outstanding electrode material for electrosynthesis [6], a conductive support in electrocatalysis and mainly in environmental applications [7–13]. Boron-doped diamond (BDD) exhibits attractive properties such as wide potential window, low background current, a high chemical and dimensional stability, making it feasible for many electrochemical processes [14]. Recently, Shao et al. [15], in a critical review about novel catalyst support materials for PEMFCs, discussed that BDD materials can be used as a potential support in these systems. In this context, the major advantage of conductive BDD is the mechanical and chemical stability that it offers to modify this substrate.

BDD can be considered as a good substrate for studying the intrinsic properties of deposited catalysts, avoiding the problems encountered with other common substrates, that is, surface corrosion, oxide formation, or electronic interactions with the deposit. This is advantageous for the fundamental study of electrocatalysis.

Part of the aims of this review is to summarize the basic surface modification of BDD materials, with emphasis on different techniques to improve the catalytic efficiency of supported catalysts for PEM fuel cells (methanol and ethanol oxidation) using BDD materials.

In addition, it is known that graphite carbon or lithium metal alloys used in advanced lithium-ion high-energy batteries suffer morphological changes during the charge-discharge cycling, which in turn results in a very poor cycle life. Thus, BDD electrode materials, that have very stable surfaces and exhibits excellent electrochemical properties when compared with other carbon forms like glassy carbon and highly oriented pyrolytic graphite, has been proposed as an alternative material for battery applications. Thus, the use of diamond materials in these applications is also reviewed.

2. Application of Modified BDD Films for Fuel Cell Applications

The deposition of metal or metal oxide clusters onto BDD film surfaces as nanoparticles is used to exploit the much

higher catalytic activity of such nanoparticles using very small amounts only compared to the conventional bulk material [16]. Many deposition techniques have been tested in an effort to improve particle adherence and dispersion. A wide range of methods for nanoparticles synthesis has been explored. These methods are well known to be efficient ways to prepare particles and nanoparticles; however, the shape and size distribution of the obtained particles are strongly dependent on the synthesis technique. The deposition technique should be simple and yield good dispersion of the particles on the substrate surface. In this section we present a general review of the techniques used for the modification of BDD surfaces to studies as electrodes for fuel cell systems. Some fundamentals of each technology are also briefly discussed to better understand its advantages and limitations for the modification of BDD surfaces.

2.1. Microemulsion Synthesis. A microemulsion is defined as a thermodynamically stable isotropic dispersion of two immiscible liquids consisting of microdomains of one or both liquids stabilized by an interfacial film of surface active molecules. The microemulsion system is characterized by transparency (optical isotropic), droplet size (from 6 to 80 nm), and stability (thermodynamic) [17, 18]. The synthesis of inorganic nanoparticles is usually carried out in water-in-oil microemulsions (w/o). The microemulsion method has been used as microreactors to produce nanoparticles with narrow size distribution, since the first work described by Boutonnet et al. [19]. Water-in-oil microemulsion consists in the coexistence of an excess water phase and the surfactant molecules which aggregate in the oil phase in the form of reverse micelle. The water core of these aggregates is surrounded by surfactant molecules which have the nonpolar part of their molecule towards the oil phase. In the water core of this aggregate metal salts can be solubilized. These metals will be then transformed into inorganic precipitates by using an appropriate reducing or precipitating agent. The final size and shape of the nanoparticles can be controlled by varying the water-to-surfactant molar ratio or by varying the microemulsion itself.

Since the development of the microemulsion technique [19], a few publications have been presented in which the technique has been used for the synthesis of metallic nanoparticles where the catalyst has been supported in BDD (Table 1). BDD has been investigated as substrate of

Pt [20], Pt-Ru [21], Pt-Sn [22], and Pt-Ru-Sn [23]. The choice of Pt and Pt-based particles was motivated by its useful potential application in alcohol (methanol or ethanol) electro-oxidation.

Siné and Comminellis [20] obtained platinum nanoparticles by reduction of chloroplatinic acid (H_2PtCl_6) with hydrazine at room temperature in a water-in-oil (w/o) microemulsion of tetraethylene glycol monododecylether (BRIJ-30)/n-heptane using a two microemulsion steps method. The catalyst displayed similar particle size 2–5 nm. Platinum nanoparticles were deposited onto the BDD substrate putting of the suspension on the diamond substrate and the excess water was dried under nitrogen atmosphere. Nafion films were used to mechanically stabilize the electrode in order to avoid the detachment of Pt nanoparticles from the BDD surfaces by the addition of Nafion solution.

Anodic treatment at high overpotentials activates Pt deposit that is mechanically stabilized by a Nafion layer. Activation of the Pt deposit by hydroxyl radicals produced by water discharge becomes feasible when a Nafion layer is added to the BDD-Pt electrode. The polymer layer strongly stabilizes the particles under these conditions, and optimum activation times, for which activity reaches by a maximum, were found to be close to 3 s in all cases. Such activation resulted in enhancement of activity towards methanol electro-oxidation, due to additional cleaning of the particles by oxidation of the residual surfactant by electrogenerated hydroxyl radicals.

Subsequently, Siné and coworkers prepared bimetallic binary Pt-Ru [21], Pt-Sn [22], and ternary Pt-Ru-Sn [23] nanoparticles supported on BDD substrates by mixing the microemulsion with solid sodium borohydride as reducing agent.

They also used transmission electron microscopy (TEM) and X-ray photoelectron spectroscopy (XPS) techniques to characterize particle sizes and morphology and to determine the effective particle compositions and the identification of oxidation states of metals in the different samples, respectively. On the other hand, the morphology and microstructure of metal-BDD electrodes were characterized by X-ray diffraction (XRD), and the specific electrochemical surface activity and stability were analyzed by cyclic voltammetry (CV). Pt/Ru nanoparticles of different compositions were synthesized by mixing appropriate ratios of Pt and Ru precursors in the aqueous phase of the microemulsion; and the size distributions obtained by them were similar for all the samples and the size domain of the particles was approximately 2–3 nm of diameter. In addition, CV was used as a surface analytical tool to provide information on the surface state of BDD-supported nanoparticles.

In fact, other syntheses were carried out by the same authors in order to understand the effect of particles size and morphology on the efficiency. Therefore, bimetallic Pt/Sn particles of several compositions with theoretical atomic contents $\text{Pt}_{80}\text{Sn}_{20}$, $\text{Pt}_{60}\text{Sn}_{40}$, $\text{Pt}_{50}\text{Sn}_{50}$, $\text{Pt}_{40}\text{Sn}_{60}$, $\text{Pt}_{20}\text{Sn}_{80}$ were synthesized via the microemulsion method [22].

TEM micrographs of the catalysts revealed small isolated and well-spherical units of diameter in the 2–5 nm range, whereas XRD analyses confirmed the deposition of

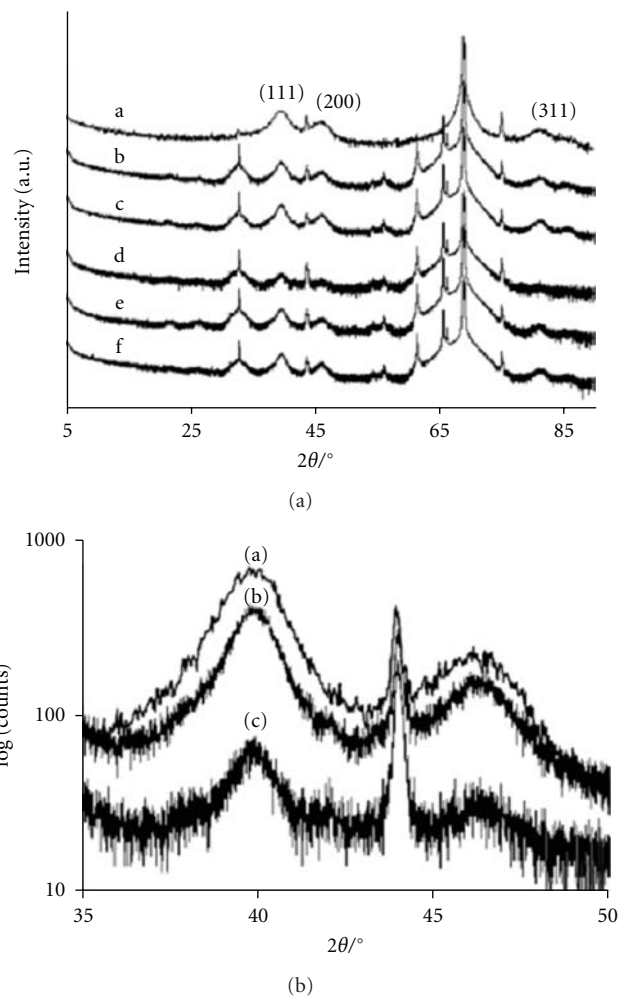


FIGURE 1: (a) XRD patterns of microemulsion-synthesized Pt/Sn nanoparticles deposited on BDD; (a) Pt, (b) $\text{Pt}_{80}\text{Sn}_{20}$, (c) $\text{Pt}_{60}\text{Sn}_{40}$, (d) $\text{Pt}_{50}\text{Sn}_{50}$, (e) $\text{Pt}_{40}\text{Sn}_{60}$ and (f) $\text{Pt}_{20}\text{Sn}_{80}$ nanoparticles. (b) XRD patterns of microemulsion-synthesized Pt (a), $\text{Pt}_{80}\text{Sn}_{20}$ (b) and $\text{Pt}_{50}\text{Sn}_{50}$ (c) nanoparticles deposited on BDD in the Pt(111) and Pt(200) reflections region (Reprinted with permission from [22]).

crystalline Pt and Sn structures together with the peaks attributed to diamond (44° and 75.3°) and silicon (70°) from the substrate (Figure 1(a)). The (101), (200), (112), (211) (202), and (213) planes of Sn (located at 2θ values of 33.1° , 56.5° , 61.8° , 66° , 66.5° , and 86.7° , resp.) are also observed in Figure 1(a). Furthermore, the (111) and (200) peaks of Pt are well defined and discernable on all the XRD patterns and were not altered by the gradual addition of Sn in the particles. This indicates that there was no loss of crystallinity in the Pt lattice with two different crystalline phases coexisting as bimetallic nanoparticles rather than true alloys [22].

This result was confirmed with the data obtained in Figure 1(b). Peak displacements of Pt (111) and Pt (200) reflections were not observed for the contributions of $\text{Pt}_{80}\text{Sn}_{20}$ and $\text{Pt}_{50}\text{Sn}_{50}$ nanoparticles that clearly indicated that the microemulsion route leads to the formation of

bimetallic nanoparticles rather than true alloys. The fact that Pt/Sn nanoparticles were not true alloys seemed not to be a limitation to their use as electrocatalysts.

The Pt-rich bimetallic surfaces displayed the better electrocatalytic activities and the higher tolerance to CO poisoning, due to their superior alcohol adsorption properties at room temperature. In this sense, microemulsion-synthesized Pt₈₀Sn₂₀ nanoparticles can be considered as good electrocatalysts of ethanol oxidation [22].

compositions (80 : 10 : 10) were synthesized by Siné et al. [23]. The particle size measured by TEM was in the 2–5 nm range. XPS analyses of Pt₈₀Ru₁₀Sn₁₀ nanoparticles produced by microemulsion technique showed that the relative atomic amounts of Pt, Ru, and Sn in the nanoparticles were 90, 3, and 7%, respectively. XPS Pt4f spectra for Pt/Ru, Pt/Sn and Pt/Ru/Sn alloy nanoparticles have shown that Pt4f binding energies for the Pt/Ru and Pt/Sn alloy nanoparticles were lower than those for clean Pt nanoparticles. The change in the electronic structure of the Pt component in the alloys (Pt/Sn and Pt/Ru) could modify the Pt work function and thus weakens bonding of adsorbed intermediates Pt-CO that could produce an enhancement in rates of methanol oxidation.

Compared to bimetallic Pt/Ru and Pt/Sn catalysts, the Pt₈₀Ru₁₀Sn₁₀ ternary nanoparticles exhibit enhanced catalytic activity toward both methanol and ethanol electro-oxidation.

The cyclic voltammograms of Figure 2 show the electro-oxidation of methanol, ethanol, acetaldehyde, and acetic acid on BDD-supported Pt₈₀Ru₁₀Sn₁₀ nanoparticles recorded at 20 mV s⁻¹ in 1 M HClO₄ + 0.1 M electroactive species solutions. Although the ethanol oxidation began at lower potentials than the methanol oxidation, the specific molar current reached a high value for the latter fuel (Figure 2(a)).

The cyclic voltammograms relative to acetic acid and acetaldehyde electro-oxidation (Figure 2(b)) showed that the electrocatalytic activity of ternary nanoparticles toward oxidation of any of these potential intermediates of ethanol oxidation was negligible compared to that toward oxidation of ethanol itself. As a result, the complete oxidation of ethanol was less efficient than the methanol oxidation due to its apparent inability to activate the C–C bond scission. Hence, electro-oxidation of ethanol with ternary Pt₈₀Ru₁₀Sn₁₀ catalyst was stopped at the formation of C₂ oxidation products (acetaldehyde and/or acetic acid). The Pt₈₀Ru₁₀Sn₁₀ ternary catalyst did not exhibit any chemical shift of the XPS Pt 4f_{7/2} line compared to that of pure Pt catalyst, indicating no electronic transfer involving Pt. A possible electronic transfer, between Sn and Ru, may create a new and specific *OH state, weakly adsorbed on Ru and of higher mobility and reactivity. This new *OH state could well explain the lowered onset potential of alcohol oxidation [23].

2.2. Thermal Deposition. The thermal decomposition of appropriate precursors that have been dissolved in suitable solvents and spread on a metallic support [24] has been

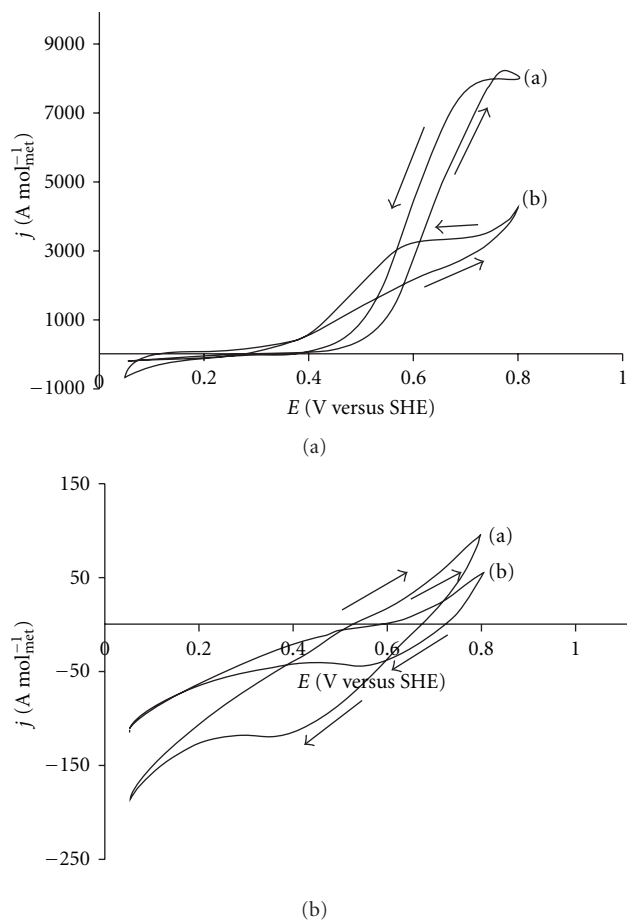


FIGURE 2: (a) Cyclic voltammograms of (a) methanol and (b) ethanol electro-oxidation at BDD-supported Pt₈₀Ru₁₀Sn₁₀ nanoparticles. (b) Cyclic voltammograms of (c) acetaldehyde, and (d) acetic acid electro-oxidation at BDD-supported Pt₈₀Ru₁₀Sn₁₀ nanoparticles. Scan rate of 20 mV s⁻¹ in 1 M HClO₄ + 0.1 M electroactive species solutions, $T = 25^{\circ}\text{C}$ (Reprinted with permission from [23]).

applied to deposit iridium oxide [21, 25], gold [21, 26], and platinum nanoparticles [27] onto BDD films. The nature of the precursor and the decomposition temperature must be controlled during the procedure since these parameters affect the particle size, nonstoichiometry, and morphology of the oxide layer. The goal of the modification of doped diamond with IrO₂, Au, or Pt nanoparticles was to produce electrodes with the well-known properties of iridium oxide, gold or platinum electrodes by using only very low amounts of these precious metals. However, long-term stability is not sufficient at the current state of development.

Siné et al. [21] deposited IrO₂ onto BDD film electrode using as precursor H₂IrCl₆ at different precursor concentrations, in order to vary the amount of deposited IrO₂. The calcinations were performed at 450°C. At low IrO₂ loading, isolated IrO₂ particles had a size of about 2-3 nm and were concentrated at the grain boundaries of the diamond crystals. At higher IrO₂ loading, the particles were larger (10 nm) and their concentration at the grain boundaries of

the diamond crystals was significantly higher. The voltammetric curves obtained with BDD-IrO₂ electrodes provided a fingerprint of electrode surface transitions occurring during the potential scan. The high capacitive current showed by the BDD-IrO₂ electrode was related to changes in the oxidation state of the IrO₂ surface during the potential scan (i.e., Ir(III)/Ir(II) and Ir(IV)/Ir(III)) at 0.4 and 0.95 V, respectively. The very low currents recorded at a BDD electrode were certainly related to the absence of electroactive surface functionalities on the electrode surfaces.

The effect of IrO₂ particles deposited on diamond on the oxygen evolution reaction (OER), an inner-sphere reaction, was investigated by CV performed in 0.5 M H₂SO₄. A potential shift of almost 1 V was noticed between BDD and BDD-IrO₂ electrodes (Figure 3). At bare diamond, the process took place at very high overpotentials while at BDD-IrO₂, oxygen evolution took place at 1.45 V, close to the equilibrium potential of the redox system Ir(VI)/Ir(IV) (1.35 V). The current increased sharply at the OER potential, indicating a high electrocatalytic activity of BDD-IrO₂ electrodes. The behavior of the BDD-IrO₂ electrodes can be interpreted entirely as that of IrO₂ continuous-film electrodes. Diamond merely acts as an inert substrate on which the catalytic activity of deposited IrO₂ particles can be investigated without interference.

On the other hand, platinum particles were deposited on p-Si/BDD substrate by thermal decomposition procedure [27]. The reaction of methanol oxidation in acidic media was used as reaction test of the prepared p-Si/BDD/Pt electrode. This method consisted in the application of 5 μ L of a platinum precursor solution (0.2–3 mM H₂PtCl₆ in 2-propanol) on the diamond surface (1 cm²), evaporation of the solvent at 60 °C during 5 min, and finally, thermal decomposition of the precursor by treatment in an oven at 350 °C during 1 h.

Irregular distribution of platinum clusters (around 3 μ m) on the diamond surface was observed in this study. The agglomeration of the Pt particles was related to the inhomogeneity of the interfacial surface tension of the BDD support.

The stability of the deposits was tested by cycling between oxygen and hydrogen evolution reactions. After 500 cycles at 50 mV s⁻¹ the obtained cyclic voltammogram did not show the characteristic peaks for the formation and reduction of the platinum oxide. Furthermore, the SEM images obtained after this treatment showed the absence of platinum particles on the diamond surface. These facts indicated the dissolution/detachment of the platinum by the potential cycling. Therefore, the authors concluded that thermal decomposition procedure was not a suitable method to obtain a well-dispersed and electrochemically stable nanoparticle catalyst.

2.3. Electrodeposition. The electrodeposition is one of the most widely used methods for the preparation and deposition of particles on BDD. As an electroanalytical tool, BDD has been used in the detection of numerous analytes, but it has also been successfully employed as an inert substrate for catalytically active metals and metal oxides [28, 29]. The

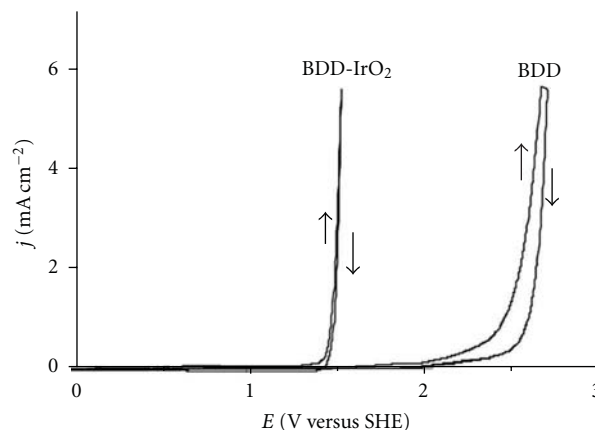


FIGURE 3: Cyclic voltammograms recorded at BDD and BDD-IrO₂ ($G = 6.4$) electrodes in 0.5 M H₂SO₄. Scan rate: 100 mV s⁻¹. Geometric surface area 1 cm². $G = 1$ corresponds to 10¹⁵ molecules IrO₂ cm⁻² (reprinted with permission from [21]).

modification of a BDD electrode surface has been reported for a limited range of metal nanoparticles, including Ag, Au, Pt, Pd, Cu, Bi, Ni, Hg, Pb, Co, Ir, Ru, Te, Ti, and Fe [30–32].

One important feature of the BDD electrode is the nonuniform electroactivity across its surface. This is due to the boron doped nature of the polycrystalline diamond, leading to areas of increased reactivity depending on the concentration of B atoms, which are present in an approximate ratio of 1 boron atom to 1000 carbon atoms [33]. Increased activity at the diamond grain boundaries is a feature suggested by the SEM images of polished polycrystalline high quality BDD surfaces [34, 35], and varied local reactivity has also been reported via confocal Raman imaging, photoluminescence [36] and AC impedance experiments [37, 38]. As such BDD is an excellent electrode material to promote the formation of nanoparticles as opposed to films. Nanoparticles are well known to be ideal for use in catalysis owing to their high surface area to volume ratio and often improved catalytic behavior due to their changed properties from the corresponding bulk material [39].

The advantages of electrodeposition include the fact that most compound semiconductor is obtained at or near room temperature, which is considered low temperature deposition. Electrodeposition also promotes controlled growth and it is generally a low cost methodology when compared to the dry methods. The deposition and co-deposition of the different metals on diamond films have been the most studied systems due to their high interest in electrocatalysis. Deposits in BDD received great attention due to their applicability in fuel cell systems, the methanol oxidation with being the preferred test reaction [40].

As Pt is one of the more deposited metals by electrodeposition technique, the electrodeposition of Pt particles on a BDD electrode is generally performed by applying a potential step to a deaerated 2 mM H₂PtCl₆ solution in 1 M HClO₄ [27]. The potential is shifted from an equilibrium potential (1 V, where no reduction of platinum ions takes place) to

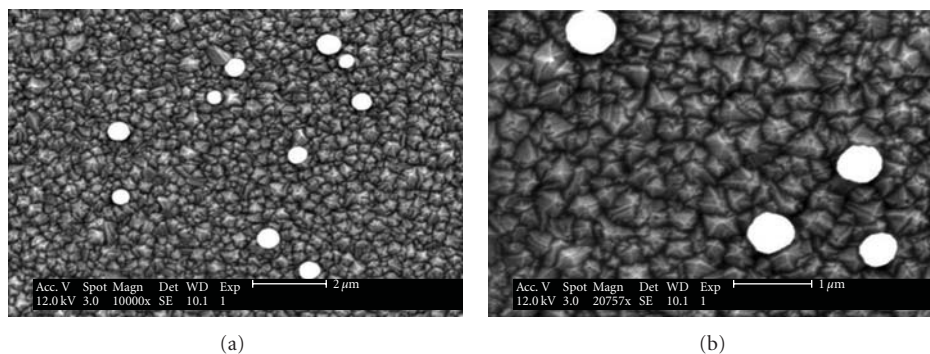


FIGURE 4: SEM images at two different magnification scales of a BDD-Pt electrode prepared by electrodeposition with a single potential step (5 s) from 1 to 0.02 V in a N_2 -saturated 2 mM H_2PtCl_6 + 1 M $HClO_4$ solution (reprinted with permission from [21]).

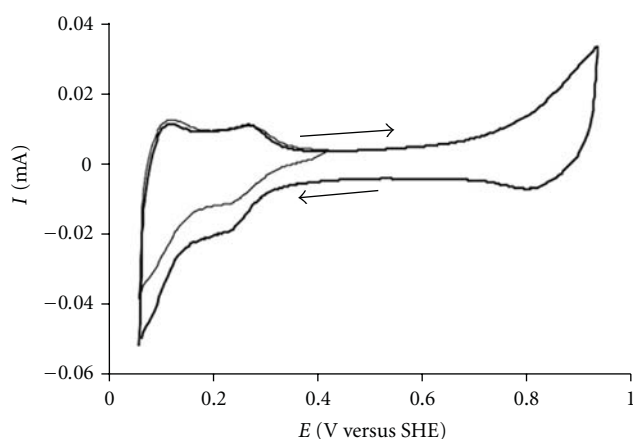


FIGURE 5: Cyclic voltammograms of electrodeposited Pt particles on BDD electrode. Recorded in a N_2 -saturated 1 M $HClO_4$ solution at 50 mV s^{-1} and 25°C . Conditions of electrodeposition: single potential step (5 s) from 1 to 0.02 V in a N_2 -saturated 2 mM H_2PtCl_6 + 1 M $HClO_4$ solution (reprinted with permission from [21]).

a potential at which the reduction of Pt^{4+} to metallic Pt occurs (0.02–0.15 V). The electrodeposition mechanism was studied by multistep chronoamperometry.

Montilla et al. [27] showed that the electrodeposition of Pt on BDD film electrodes follows a mechanism of progressive nucleation, which favors a higher dispersion of the platinum particles, increasing the amount of new nuclei for Pt deposition on the BDD support. The stability of the electrochemically deposited electrodes was tested by cycling the potential (1000 cycles) between oxygen and hydrogen evolution reactions in a 0.5 M H_2SO_4 solution at a sweep rate of 50 mV s^{-1} . This treatment resulted in a dissolution/detachment of an important fraction of the deposited Pt, since the amount of Pt presents on the electrode surface (estimated from the electrical charge in the cyclic voltammograms) after the potential cycling was reduced by approximately 65% with respect to the initial conditions.

The most important techniques for characterization of electrodeposits on BDD are SEM, XRD, energy-dispersive X-ray spectroscopy (EDS), atomic force microscopy (AFM),

Raman spectroscopy, scanning electrochemical microscopy (SECM), XPS, and CV. Figure 4 shows SEM micrographs of a BDD-Pt electrode prepared by performing a potential step from 1 V to 0.02 V in a 2 mM H_2PtCl_6 + 1 M $HClO_4$ solution for 5 s [21]. Spherical and isolated particles are observed with a quite large size variation that covers the 40–700 nm range. This is indicative of continuous formation of new nuclei during deposition and it is in agreement with the progressive mechanism of nucleation of Pt on BDD.

A typical CV for electrodeposited Pt particles on BDD is shown in Figure 5 [21]. This voltammogram exhibits the characteristic feature of Pt, that is, two distinctive H adsorption-desorption peaks between 0.05 and 0.35 V, followed by a fine double layer region corresponding to metallic Pt. The electrochemical response of this BDD-Pt composite electrode can be attributed solely to the deposited Pt particles—even at very low Pt loadings, due to the chemical inertness and low background current of the diamond substrate. This justifies the choice of BDD for the electrochemical study of supported catalytic nanoparticles.

Although electrodeposited Pt particles on BDD are efficient for methanol electro-oxidation, their size domain is so broad that they cannot be strictly classified as nanoparticles. The literature attributes this heterodispersity to the inhomogeneous nature of the BDD substrates [41], mainly to the presence of nondiamond sp^2 impurities that act as preferential deposition sites. Therefore, a “size effect” cannot be reasonably expected in this case, and some alternative synthesis techniques have to be employed to deposit real Pt nanoparticles on BDD.

The Pt-Ru binary metallic catalyst is commonly accepted as the best electrocatalyst for methanol oxidation. The fundamental mechanism studies for Pt-Ru catalysts indicate that methanol is oxidized according to bifunctional mechanism [42]. Surface-sited Pt atoms oxidatively dehydrogenate the chemisorbed methyl moiety in consecutive steps to yield a residual Pt-CO fragment that cannot be oxidized to CO_2 at direct methanol fuel cell potentials. Pt adsorbed CO is removed via an oxygen-transfer step from electrogenerated Ru-OH. Ru transfers oxygen more effectively than Pt due to its ability to oxidatively absorb water at less positive potentials [43].

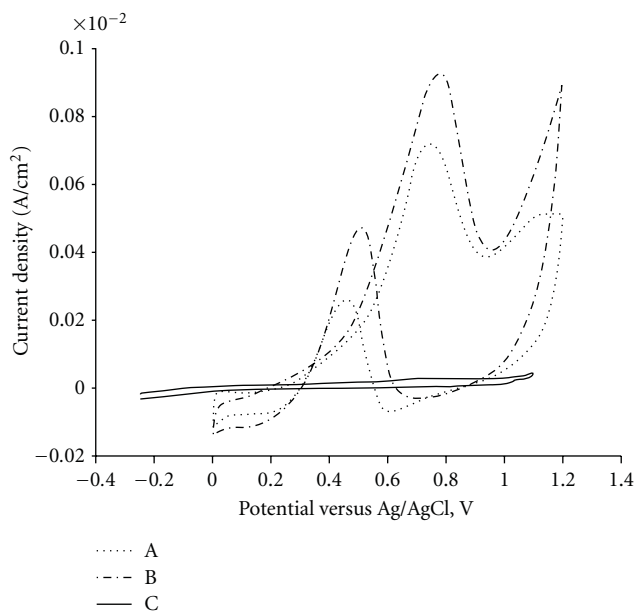


FIGURE 6: Study of cyclic voltammetry of diamond films with electrocatalyst deposition on 0.1 MeOH/0.5 M H_2SO_4 at 50 mV s^{-1} : (A) Pt/BDD, (B) Pt-Ru/BDD, and (C) BDD (reprinted with permission from [44]).

In this sense, polycrystalline BDD films were proposed by González-González et al. [44] as the alternative material to obtain high-area carbon supports using electrodeposition, with potential application for direct methanol fuel cell electrocatalysts. The electrocatalytic behavior of Pt/BDD, Pt-Ru/BDD and BDD electrodes towards the oxidation of methanol in acidic media was evaluated by CV in Figure 6. Thus, the maximum current densities obtained for methanol oxidation were about 0.73 mA cm^{-2} for Pt and 0.94 mA cm^{-2} for Pt-Ru deposited on BDD. However, as indicated by the authors, the fact that Pt-Ru exhibited lower potentials than Pt may be expected in the basis of previous studies [42]; nevertheless, more investigation is necessary to completely understand the composition and particle size effects.

The electrodeposition of Pt-Ru electrocatalytic particles was recently studied by comparing simultaneous and sequential deposition on BDD supports using a potentiostatic method [45]. Smooth cluster morphologies were observed for simultaneous deposition and a dendritic structure was observed for sequential deposition from SEM studies (Figure 7). The morphology of sequential deposition was dominated by Pt deposition in the first step, while a change of aggregate morphology due to the presence of Ru was observed for simultaneous deposition. This different morphology and microstructure contributed to different electrochemical performance.

Pt-Ru deposits from simultaneous deposition showed stable cyclic voltammograms in sulfuric acid, in contrast to the severe dissolution of Ru which was seen for the deposits from sequential deposition.

An enhanced electrocatalytic performance for the oxidation of methanol was observed for binary Pt-Ru deposits

from both sequential and simultaneous deposition, in comparison to that seen on pure Pt, both in terms of onset potential and current density for methanol oxidation. Compared to sequential deposition, Pt-Ru electrocatalysts from simultaneous deposition exhibited higher activity and more tolerance to CO poisoning for methanol oxidation, and this could be further optimized by choice of the electrodeposition potential. The best catalytic performance was obtained at Pt/Ru ratio of around 0.3 in used experimental conditions. Differing rate-determining steps were identified from Tafel plots for methanol oxidation for the different catalysts (Figure 8).

The Tafel curves of simultaneously deposited Pt/Ru had the same slope of around 173 mV/dec , indicating that the dehydrogenation of methanol molecules was very fast at even relatively low overpotential and the first rate-determining step was the migration of CO_{ads} between Pt sites and Ru sites [46]. However, the Tafel plot of sequential deposited Pt-Ru presented two linear regions: a slope of around 115 mV/dec in the first region below 0.45 V which indicated a rate-determining step of dehydrogenation of methanol molecules, and a slope of around 289 mV/dec in the second region above 0.45 V ; indicating a change of rate-determining step to the oxidation of CO like absorbents on catalytic surfaces [47]. The differing Tafel plots and rate-limiting steps highlighted how subtle changes in the properties of the Pt-Ru particles could significantly influence catalytic properties and performance.

In a different approach, Pt/BDD powder electrocatalyst was prepared via electrochemical deposition of platinum, and the electrochemical behavior was compared with that for Pt/graphite powder [48]. The conductive diamond powder (particle size range, less than $150 \mu\text{m}$) was obtained from the Element Six Co and used as support for the Pt deposition. Initially a small amount (e.g., 50 mg) of BDD powder was preheated at 110°C in air and then poured into 5 mL of warm H_2PtCl_6 solution (10 mM) in ethanol. The suspension was blended for 30 min in an ultrasonic bath, and then the solvent was evaporated under continuous stirring. After further drying at 110°C , the resulting agglomerates were ground in an agate mortar. Secondly, the deposition of platinum was performed by continuously cycling the potential of the coated electrodes (20 mV s^{-1}) within the potential range 0.5 to -0.2 V in a nitrogen-saturated $0.5 \text{ M H}_2\text{SO}_4$ solution. Cyclic voltammograms were recorded, and the deposition process was continued until a stable voltammetric response was obtained (typically, after *ca.* 30 cycles).

The results of the steady state and long-time polarization measurements suggested that, when deposited on conductive diamond powder, platinum may be slightly less susceptible to deactivation, for example, via CO poisoning, during methanol oxidation. This behavior was ascribed to the increased hydrophilicity of the oxidized diamond, to a possible electronic effect of the oxygen-terminated support, or to the absence of the adsorption of reaction intermediates that could foul the Pt surface. The finding of this study could indicate that by using BDD powder as a support, it is possible to minimize the loading of alloying metals such as ruthenium, while maintaining high catalytic activity.

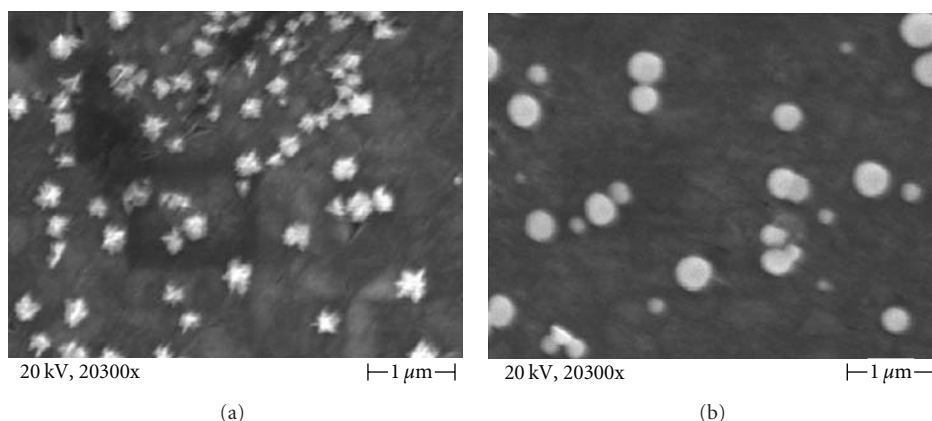


FIGURE 7: SEM images of Pt-Ru deposited on BDD electrode at -0.2 V for 10 min, (a) sequential deposition, and (b) simultaneous deposition (reprinted with permission from [45]).

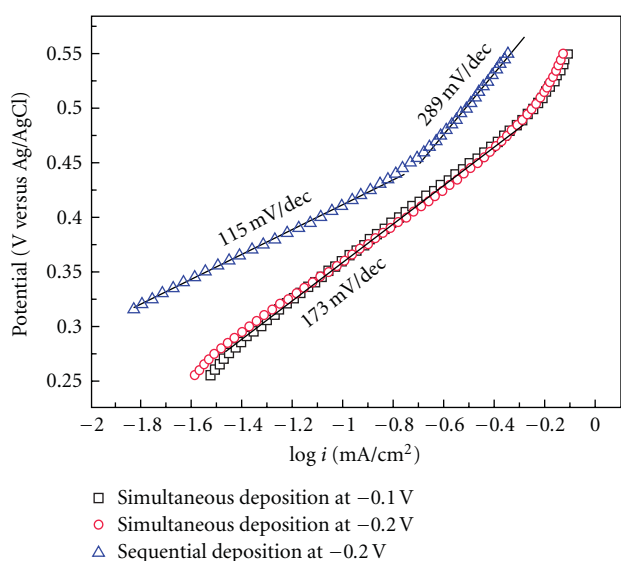


FIGURE 8: Tafel plots of anode polarization curve in 1.0 M methanol and 0.5 M H_2SO_4 solution for (\square) simultaneous deposition at -0.1 V, (\circ) simultaneous deposition at -0.2 V, and (\triangle) sequential deposition at -0.2 V (reprinted with permission from [45]).

2.4. Sol-Gel Method. Surface modifications of BDD electrodes have been carried out with several metal oxides and some mixed composites using the sol-gel method [49, 50]. It is well known that sol-gel technique is a suitable process for coating substrates for energy storage materials and electrochemical devices; in either case, there are many interfaces between components and many components that have to perform reliably and safely. There are interfaces between electrodes and current collectors, between electrodes and electrolyte and between electrodes and interconnects. In some cases, the interfaces are the location of failure in an operating fuel cell and problems due to chemical reactions and increased contact resistance can occur. Also, elevated temperatures lead to microstructure changes, crystallization, thermal expansion mismatch, and delamination. In these

complicated materials systems, the use of sol-gel processing is well suited to the need for accurate placement of critical materials [51].

The sol-gel method starts with a solution consisting of metal compounds, such as metal alkoxides, and acetylacetonates as source of oxides, water as hydrolysis agent, alcohol as solvent, and acid or base as catalyst. Metal compounds undergo hydrolysis and polycondensation at room temperature, giving rise to sol, in which polymers or fine particles are dispersed. Further reaction connects the particles, solidifying the sol into wet gel, which still contains water and solvents. Vaporization of water and solvents produces a dry gel (xerogel), an aerogel results from a supercritical drying process. Heating gels to several hundred degrees produces dense oxides as products. Coating films can be made by dip-coating or spin-coating of the sol. Unsupported films can be made by synthesizing the film at the interface between alkoxide solution and water. Membranes are prepared by pouring the sol on the porous oxide with coarse pores. Particles with sharp size distribution can be precipitated and grown in the sol [52].

The advantages of sol-gel technique in the preparation of ceramics include better homogeneity, lower temperature processing, and more uniform phase distribution in multicomponent systems, easy preparation of thin films and coatings, better size and morphological control in powder synthesis and opportunities for the preparation of new crystalline and noncrystalline solids [53]. The main factors that are important in development of thin films are the uniformity and thickness of film, its adhesion to the substrate, and resistance to cracking. In this context, some research groups are working on the BDD surface modification by sol-gel technique for different catalytic coatings such as metallic oxides (MO_2 , $M = \text{Pb}, \text{Ru}$, and Ir) [49] or metal catalyst like platinum.

Suffredini et al. [54] reported the preparation of Pt-RuO₂ deposits on a carbon black substrate using the sol-gel method; their activity toward methanol electro-oxidation was investigated and they found superior activity of the Pt-RuO₂/C anodes prepared by sol-gel than those of

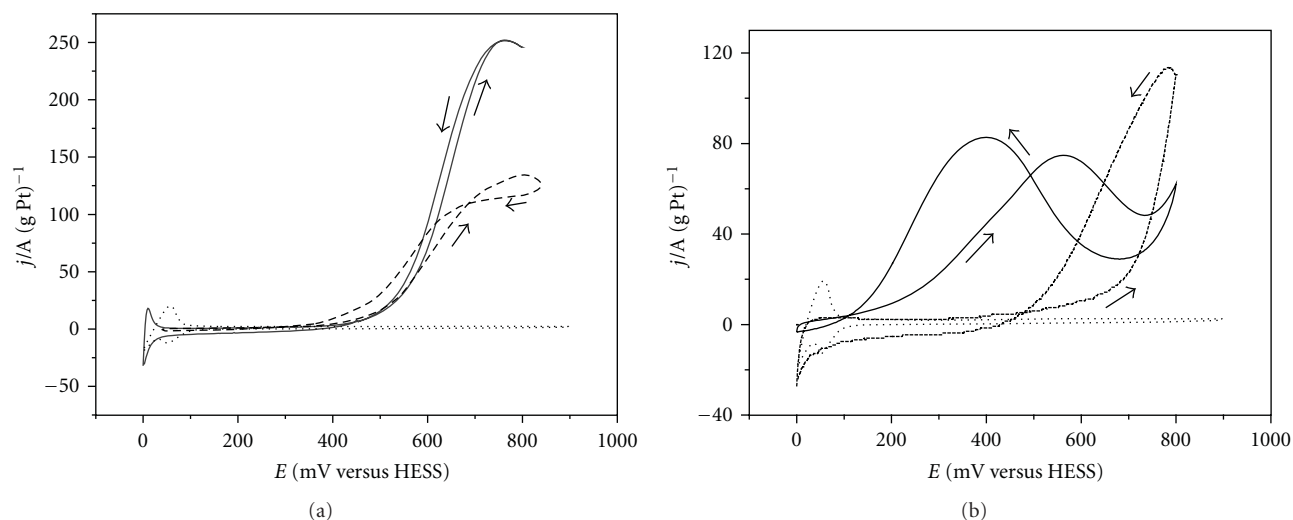


FIGURE 9: Voltammetric oxidation of 1.0 M of methanol (a) and ethanol (b) in 0.5 M H₂SO₄ on Pt-RuO₂/C (full lines) and Pt/C (traced lines) composites fixed on BDD surfaces. Baselines (dotted lines) were included as a comparison. Scan rate $\nu = 10 \text{ mV s}^{-1}$ (reprinted with permission from [50]).

similar composition but prepared by alternative methods. Later, Suffredini et al. [50] reported the electro-oxidation of methanol and ethanol using a Pt-RuO₂/C composite prepared by sol-gel method supported on BDD which were evaluated by CV. Catalytic properties of Pt-RuO₂/C supported over BDD were evaluated by means of cyclic voltammetric technique. In this context, electrochemical assays were also conducted using a glassy carbon (GC) electrode as the substrate for the composite. The capacitance in the potential window 100–400 mV versus HESS using a GC electrode was $1.26 \times 10^{-5} \text{ C}$ which was considerably larger than that calculated at BDD (i.e., $2.69 \times 10^{-6} \text{ C}$), indicating that BDD can be used as substrate with lower substrate interferences than GC. The potential region of methanol oxidation for forward and reverse scans as well as for the peak showed that the Pt-RuO₂/C composite on the BDD substrate presented a higher current density than the composite supported on GC electrode. In this frame, the authors emphasized an interesting difference between the two voltammograms, indicating that the forward and backward lines of BDD substrate were almost coincident while a large difference was observed for GC electrode. However, other tests using the same Pt-RuO₂/C material, indicating that the differences should be attributed to the substrate and that probably reflect the great capacitive effect of the GC.

In light of this discussion, the most important contribution to the larger oxidation currents was that the use of BDD surfaces practically avoids the substrate contribution and thus, the response of electrode was only dependent on the catalyst. Results presented in Figures 9(a) and 9(b) correspond to methanol and ethanol oxidation responses, respectively, for Pt-RuO₂/C catalyst over BDD studied by CV at 10 mV s^{-1} . As well, they included in this figure the responses of a commercial 10% Pt/C catalyst on BDD as a comparison. As observed in Figure 9(a), the oxidation of

methanol started at 380 mV versus HESS on both substrates and these results were in agreement with the data reported by He et al. [43] where Pt-Ru nanoparticles were electrodeposited on carbon nanotubes. For the case of ethanol oxidation (Figure 9(b)), the electrochemical responses were extremely different for both cases, showing the presence of a reactivation process on the catalyst surface, but in the case of Pt-RuO₂/C material, the onset potential of the ethanol oxidation was much lower than for the Pt/C. However, the response in current density for Pt-RuO₂/C material was fairly large for an extended potential window, indicating a multistep processes during ethanol oxidation.

The composite catalysts Pt-PbO_x/C, Pt-IrO₂/C, Pt-(RuO₂-IrO₂)/C, Pt-(RuO₂-PbO_x)/C, and Pt-(IrO₂-PbO_x)/C were prepared by sol-gel and fixed on BDD substrate to be used as anodes for studies of direct ethanol fuel cells (DEFCs) [55]. The sol-gel method gives as a result the formation of the nanometric crystallite dimensions of the composites which can be responsible for the enhanced catalytic activity toward ethanol oxidation. The XRD analysis revealed that Pb was deposited as a mixture of PbO and PbO₂ and the EDX measurements indicated that Pb is preferentially deposited as compared with Pt.

Quasi-steady-state polarization curves showed that the composites Pt-(RuO₂-PbO_x)/C and Pt-(RuO₂-IrO₂)/C started the oxidation process in very low potentials (155 and 178 mV, resp.), presenting good performance to promote the ethanol oxidation. In fact, the composite Pt-(RuO₂-PbO_x)/C presented a gain of about 467 mV in the onset potential as compared to the Pt/C composite and, as a consequence, very high currents can be obtained on this catalyst at low potentials. On the contrary, the combination of IrO₂ with PbO_x disfavors the catalytic activity for the ethanol oxidation, showing a nonsynergic behavior [55].

These catalysts studied for ethanol oxidation were also tested as anode composites for the oxidation of methanol

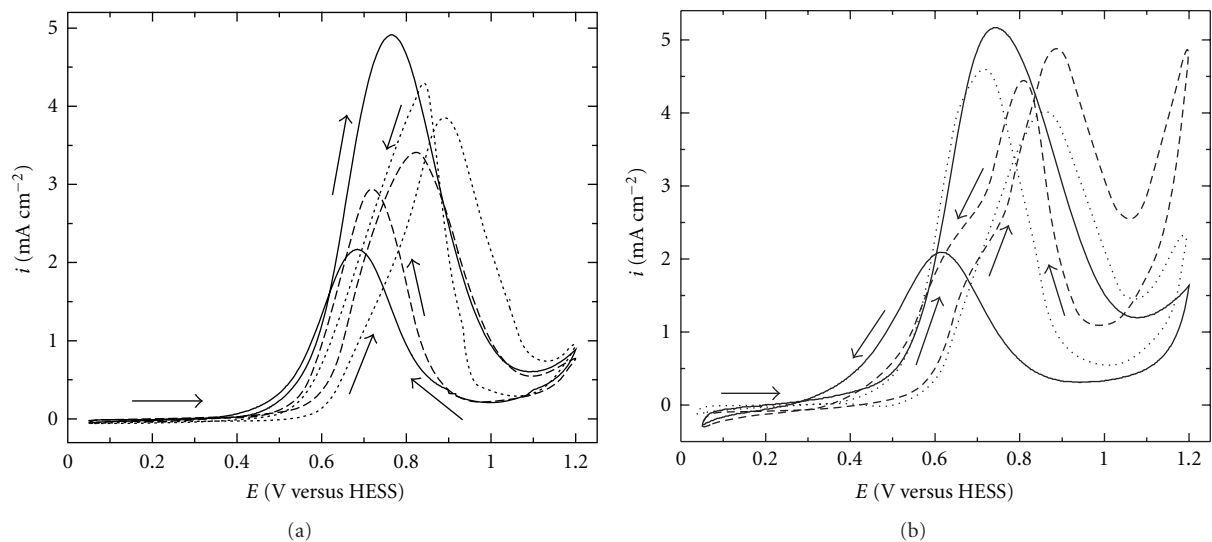


FIGURE 10: Cyclic voltammetric study (second cycle) for electrochemistry oxidation of 0.5 M of (a) methanol and (b) ethanol. Dotted line correspond to Pt/BDD, dashed line Pt-RuO₂/BDD, and solid line Pt-RuO₂-RhO₂/BDD electrodes materials ($\nu = 0.005 \text{ V s}^{-1}$) (reprinted with permission from [58]).

[56]. CV and quasistationary polarization experiments showed that the new Pb-based catalysts presented good performance to promote the oxidation of methanol in acidic media. Current-time measurements also proved the good performance of the Pt-(RuO₂-PbO_x)/C, Pt-PbO_x, and Pt-(RuO₂-IrO₂)/C catalysts to oxidize methanol in acidic media. Therefore, the authors concluded that the addition of metallic Pt and PbO_x onto high-area carbon powder, by the sol-gel route, constitutes an interesting way to prepare anodes with high catalytic activity for further applications in direct methanol fuel cell systems.

On the other hand, Salazar-Banda et al. [57] carried out the direct deposition of platinum oxide particles (PtO_x) on BDD surfaces by the sol-gel method and testing several pre- and posttreatments of the surface for electrochemical experiments. They studied the electrochemical stability of the catalytic coatings indicating that the electrodes retained 91.6% of the coated material after 1000 voltammetric cycles conducted in the water decomposition electrochemical window. Their results demonstrate that the sol-gel method produces more stable PtO_x deposits on BDD surfaces than other reported techniques.

In addition, covering the modified electrode surface (PtO_x/BDD) with a Nafion film (40 μL of a 0.5% Nafion solution evaporated on the electrode surface using a hot air stream) made negligible the clusters detachment/dissolution after the extensive potential cycling test describe above. In another study carried out by Suffredini et al. [49] that used a similar electrode configuration (Pt/BDD + Nafion film), showed that 1000 voltammetric cycles for the ethanol oxidation reaction also left the surface practically unchanged.

In a following study [58] the BDD electrode surface was modified with Pt, Pt-RuO₂, Pt-RuO₂-RhO₂ by the sol-gel process to study the oxidation of methanol and ethanol. Each catalyst was deposited as coating film on BDD electrodes,

previously pretreated at 400°C for 30 min in air, using as precursors the corresponding metallic acetylacetonates. The sol-gel solutions were prepared with Pt(II), Ru(II) and Rh(III) acetylacetonates in a mixture of isopropyl alcohol and acetic acid (3:2, v/v) obtaining a 0.01 M as a final concentration of each solution. These solutions were transferred onto BDD surfaces by painting and the solvents were evaporated at 80°C for 5 min in an oven. This procedure was repeated 15 times and finally the electrodes were annealed at 400°C for 1 h in an argon atmosphere.

The physical characterization of the different composite materials deposited on BDD demonstrated that the relatively simple and low-cost sol-gel method is a very useful technique to modify BDD electrodes producing catalysts nanoparticles with a well-controlled atomic composition and a homogeneous distribution on the surface.

The voltammetric responses for bare BDD and BDD after modification with Pt, Pt-RuO₂ and Pt-RuO₂-RhO₂, evidenced that the electrochemical potential window was greatly diminished due to the catalytic effect of the deposited metals after modification. Cyclic voltammetric assays were carried out for methanol and ethanol oxidation at a scan rate of 0.005 V s⁻¹, in acidic media (H₂SO₄) adding 0.5 M alcohol concentration; their results are shown in Figure 10. These studies revealed that the CO poisoning effect for both alcohols oxidation reaction was mainly inhibited on the ternary alloy Pt-RuO₂-RhO₂/BDD electrode (solid lines in Figure 10) due to the Rh presence, which promotes a better catalytic effect for these reactions by either prompting the oxidation of the adsorbed intermediate species to CO₂ or diminishing the absorption of CO and the others intermediates over Pt surface.

Moreover, chronoamperometric experiments analyzed by a modified Cottrell's law strongly suggest that poisoning of the surface by CO is greatly inhibited on the ternary

TABLE 2: Catalysts or composite catalysts on BDD support synthesized by the sol-gel method.

Fuel studied	Catalyst deposited on BDD electrode	Characterization techniques	Precursors	Reference
Methanol and ethanol	Pt Pt-RuO ₂ Pt-RuO ₂ -RhO ₂	XRD, EDX, AFM, SEM	Pt (II), Ru (III), Rh (III) acetylacetonates in a mixture of isopropyl alcohol and acetic acid	[58]
Ethanol	PtO _x PtO _x -RuO ₂ RuO ₂ IrO ₂ PbO ₂	AFM	Pt (II), Ru (III), Pb (II), Ir (III) acetylacetonates in a mixture of isopropyl alcohol and acetic acid	[49]
Methanol and ethanol	Pt-RuO ₂ /C	XRD, EDX	Pt (II), Ru (III) acetylacetonates in a mixture of isopropyl alcohol and acetic acid/carbon black powder (Vulcan XC72R)	[50]
Methanol	Pt-RuO _x	SEM, DRX	Pt (II), Ru (III) acetylacetonates in a mixture of isopropyl alcohol and acetic acid	[59]
Ethanol	Pt-RuO ₂ /C Pt-PbO _x /C Pt-IrO ₂ /C Pt-(RuO ₂ -IrO ₂)/C Pt-(RuO ₂ -PbO _x)/C Pt-(IrO ₂ -PbO _x)/C	XRD, EDX	Pt (II), Ru (III), Pb (II), Ir (III) acetylacetonates in a mixture of ethanol and acetic acid/carbon black powder (Vulcan XC72R)	[55]
Methanol and ethanol	Pt Pt-SnO ₂ Pt-Ta ₂ O ₅	XRD, EDX, SEM, AFM	Pt (II) acetylacetonate, Sn (IV) bis(acetylacetonate) dibromide, Ta (V) ethoxide in a mixture of isopropyl alcohol and acetic acid	[61]
—	Pt oxides	TEM, XPS	Pt (II) acetylacetonate in a mixture of ethanol and acetic acid	[64]

composite electrode (Pt-RuO₂-RhO₂/BDD) if compared to the other two materials. Consequently, the current densities on that coating remain higher and diffusion controlled for a considerable amount of time (or charge) thus making the catalyst containing Pt, RuO₂, and RhO₂ deposited on BDD by the sol-gel method a promising composite material to be used in fuel cell anodes.

The modification of the BDD electrode with other Pt-metal oxide catalysts prepared by sol-gel has been investigated with the aim to improve its electrocatalytic response to be used as a fuel cell anode. In this context, BDD electrodes with IrO₂, PbO₂, SnO₂, Ta₂O₅ and some mixed composites prepared by sol-gel have been investigated by electrochemical techniques to establish their catalytic activity towards methanol and/or ethanol oxidation reactions [49–61]. In Table 2 are presented different coating catalysts synthesized by sol-gel technique on BDD support electrode, indicating the precursors used in the synthesis, and the electro-oxidation reaction that was studied. In all cases a Nafion film was incorporated onto the modified BDD to improve the stability of the coating on the diamond surface. It is worthwhile noticing that all the routes proposed are those using metallic alkoxides dissolved in alcohol prepared by an acid catalyzed hydrolysis.

The surface modification of BDD with IrO₂ and PbO₂ was studied by AFM technique and the results indicated the existence of sites with heterogeneous deposition; both

catalysts showed good electrocatalytic activity; however, IrO₂/BDD electrode exhibits better performance for the OER with respect to diamond (unmodified) and PbO₂/BDD electrodes, as demonstrated by Suffredini et al. [49].

Recently, Salazar-Banda et al. [61] presented similar study, for the preparation of BDD film surfaces modified with Pt, Pt-SnO₂, and Pt-Ta₂O₅ nanocrystalline deposits by means of sol-gel method, to evaluate the methanol and ethanol oxidation. The characterization of the BDD modified electrodes was accomplished by XRD, AFM, SEM, and EDX studies. The authors estimated (from XRD diffractograms) the mean crystallite size for Pt, Pt-SnO₂, and Pt-Ta₂O₅ coatings, achieving values of 4.6, 5.0, and 9.1 nm, respectively.

Figure 11 shows the voltammograms obtained on a nonmodified BDD electrode without (solid line curve) and in the presence of 0.5 M of methanol, and ethanol (dashed and dotted lines, resp.). In this figure it is possible to observe that methanol and ethanol are not electroactive in the potential region commonly used to evaluate the fuel cell systems (from 0.4 to 0.8 V versus HESS). Based on these results, it is possible to observe that this electrode showed onset potential (taken at $i = 0.5 \text{ mA cm}^{-1}$), respectively, to 1.49 and 1.54 V for the methanol and ethanol oxidation process, in accordance with the insert in Figure 11. The possible explanation for this behavior is maybe due to the low adsorption of species characteristics of diamond surfaces. In light of these results, the substrate, when modified

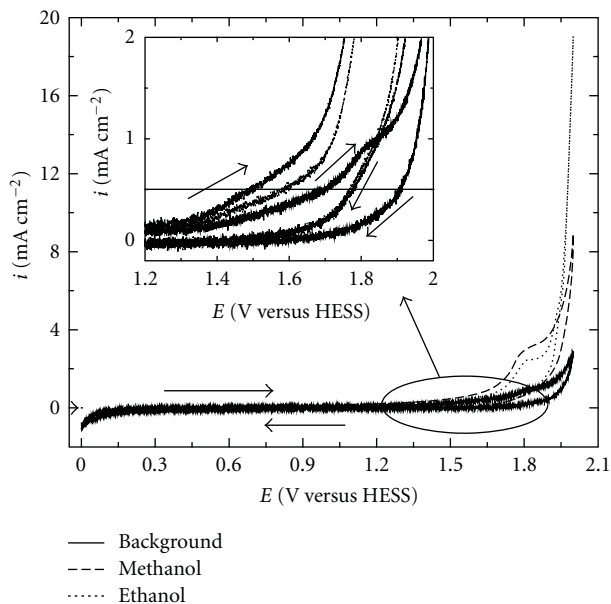


FIGURE 11: Comparative voltammetric study (first cycle) for the oxidation of methanol (dashed line) and ethanol (dotted line) in 0.5 M H_2SO_4 and background responses in the supporting electrolyte (solid line), recorded using a nonmodified BDD electrode, $\nu = 5 \text{ mV s}^{-1}$ (reprinted with permission from [61]).

presents, a small capacitive current, and the study of the alcohols oxidation processes is facilitated, because they do not compete with these reactions.

Potentiostatic polarization experiments (data obtained in the potentiostatic mode after 300 s polarization at each potential) showed in Figure 12 indicate that the addition of Ta_2O_5 to a Pt-containing catalyst decreases the poisoning effect caused by the strongly adsorbed CO species generated during the oxidation of methanol, changing the reaction onset 170 mV toward less positive potentials, whereas the addition of SnO_2 moderately enhances the catalytic activity toward this alcohol oxidation.

On the other hand, the mixture of SnO_2 or Ta_2O_5 to Pt compounds produces more reactive electrocatalysts for the oxidation of ethanol in acidic media and changes the reactions onsets by 190 or 150 mV toward less positive potentials, respectively. This synergic effect indicates that the addition of these cocatalysts inhibits the poisoning effect caused by the strongly adsorbed intermediary species. Since the Pt- SnO_2 catalyst was more efficient than Pt- Ta_2O_5 for the oxidation of ethanol, it suggests that probably the tin oxide co-catalyst facilitates the cleavage of the C–C bond of the adsorbed intermediate fragments better than tantalum oxide. However, additional studies to confirm this point must be performed.

Since no loss or diminution of the catalytic activities of the electrodes was observed during the whole experiments, these deposits also showed a high stability on the diamond surfaces as already demonstrated for sol-gel-made composites deposited on BDD surfaces.

These authors concluded that the catalysts containing Pt and SnO_2 deposited on BDD by the sol-gel method are very promising composite materials to be further studied as anodes (high-area BDD substrates) for ethanol oxidation. In addition, catalyst containing Pt and Ta_2O_5 are very interesting composite materials to be used in direct methanol fuel cell anodes. Finally the authors suggested the Pt- SnO_2 and Pt- Ta_2O_5 deposition on high-area BDD material (powder or felt) to further test as anodes in fuel cells applications.

In this context, in 2007, Salazar-Banda et al. [59], reported an interesting and innovate research where they carried out the modification of BDD powder with metallic oxides (Pt- RuO_x) using the sol-gel technique to prepare high-area and stable surface electrodes to methanol oxidation, and its comparison with a commercial catalyst (Pt- Ru/C). Pt- RuO_x/BDD powder electrode was electrochemically evaluated by means of CV, obtaining that the incorporation of ruthenium presents the inhibition of the hydrogen adsorption/desorption signals. Additionally, good performances on currents were observed in the double layer region due to an increase of the capacitive currents and to the ruthenium redox processes, in accordance with the inset of Figure 13. As seen in Figure 13, methanol oxidation, onset potentials ($i = 0.04 \text{ mA cm}^{-2}$), displayed close values on both electrodes ($\sim 0.40 \text{ V}$ versus HESS). Furthermore, the magnitude of the current densities in the common fuel cell operation was approximately from 0.4 to 0.8 V versus HESS. As a consequence, the BDD powder modification presented an important enhancement of the catalytic activity to methanol oxidation with respect to other materials such as carbon-modified composites.

At the same time, analogous idea was recently proposed by Swope et al. [62], where they have prepared conductive diamond powders as a new catalyst for fuel cells. They have reported the development of higher surface area, approximately $100 \text{ m}^2 \text{ g}^{-1}$, and good corrosion resistance by conductive diamond powders for application as the electrocatalyst support, using electrodeposition. For this investigation, they carried out the electrochemical measurements using a glassy carbon rotating disk electrode (GC RDE) as the substrate. As illustrated in Figure 14, the larger background current for the 500 nm diamond powder electrode was due to higher specific area. However, no reduction and oxidation signal was observed between -500 to 700 V , suggesting that the electrode surface is largely free of sp^2 carbon impurities. Moreover, they affirmed that the featureless backgrounds for the voltammograms are evidence of good particle conductive.

The same research group [63] subsequently reported the platinization of boron-doped ultrananocrystalline diamond (B-UNCD). Clearly, B-UNCD possesses the requisite electrical conductivity (ca. 0.5 S/cm) and specific surface area (ca. $170 \text{ m}^2/\text{g}$) for a viable electrocatalyst support and, more importantly, the material exhibited excellent carbon corrosion resistance in the presence of Pt. XRD and TEM were used to characterize the Pt particle size and distribution on the diamond powder. A chemical impregnation-reduction method was used for Pt deposition. Pt particles

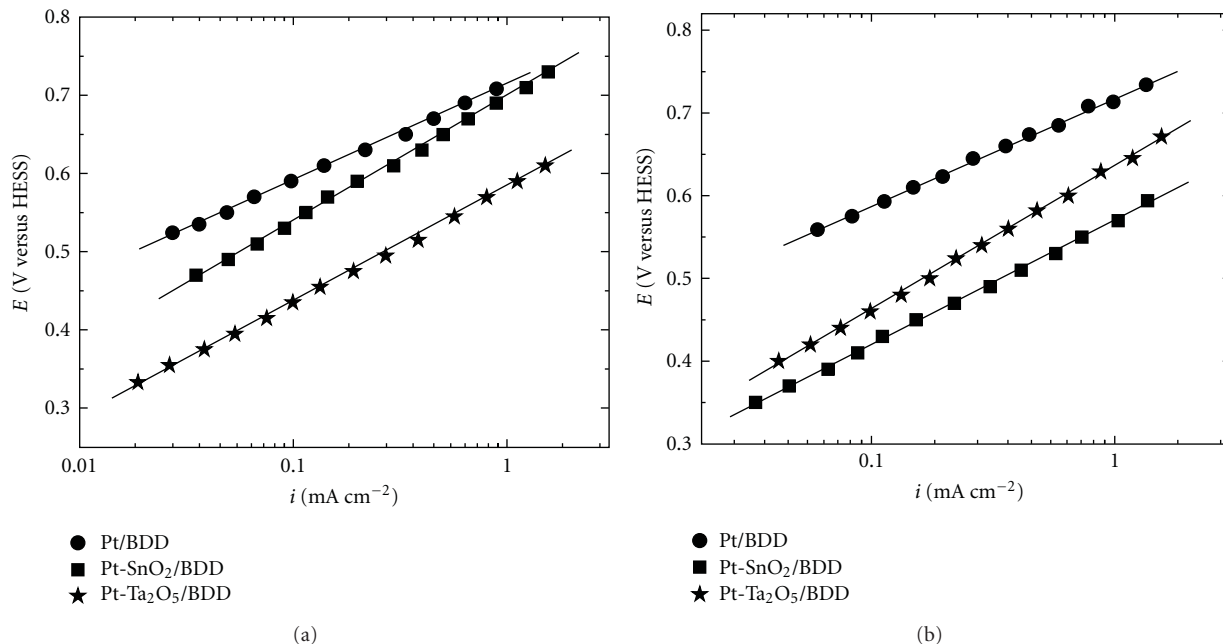


FIGURE 12: Steady-state polarization curves plotted as the corresponding Tafel plots for the electrochemical oxidation of methanol 0.5 M (a) and ethanol 0.5 M (b) dissolved in 0.5 M H_2SO_4 and recorded for the Pt/BDD (spheres), Pt-SnO₂/BDD (squares), and Pt-Ta₂O₅/BDD (stars) electrode surfaces (reprinted with permission from [61]).

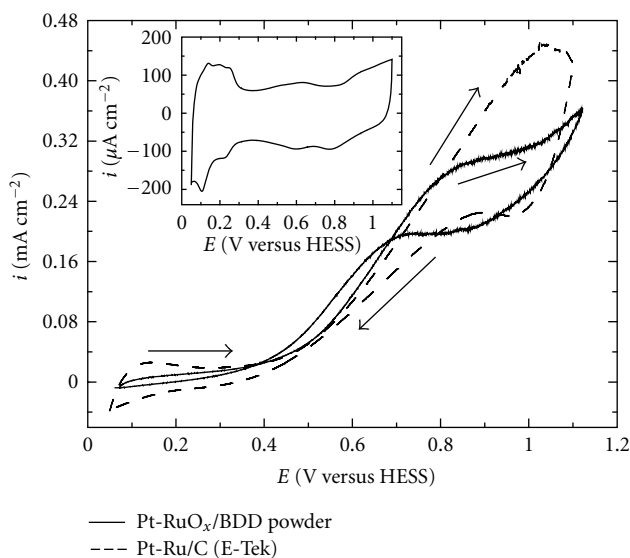


FIGURE 13: Cyclic voltammograms for the electrochemical oxidation of 0.5 M of methanol in 0.5 M H_2SO_4 aqueous solution carry out on the Pt-RuO_x/BDD powder/BDD (solid line) and on the Pt-Ru/C/BDD (dashed line) electrodes at $\nu = 10 \text{ mV s}^{-1}$. Insert correspond to the Cyclic voltammogram recorded on the Pt-RuO_x/BDD powder/BDD electrode in 0.5 M H_2SO_4 aqueous solution at $\nu = 50 \text{ mV s}^{-1}$ (reprinted with permission from [59]).

were uniformly distributed on B-UNCD using this method. The nominal particle size was approximately 5 nm. A high-resolution TEM image of a Pt nanoparticle formed on diamond particle is shown in Figure 15. The Pt metal

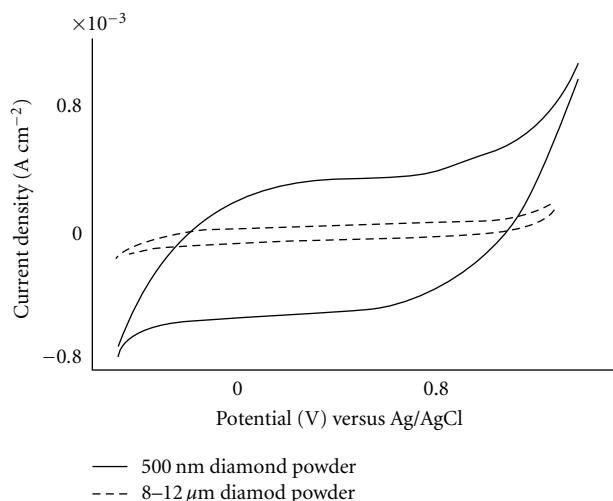


FIGURE 14: Cyclic Voltammogram for an 8–12 μm diamond powder electrode, grown under microcrystalline conditions, and a 500 nm diamond powder electrode, grown under nanocrystalline conditions. Experiments were carried out in 1 M KCl at 100 mV s^{-1} (reprinted with permission from [62]).

particles bonded directly to the diamond surface with no graphitic interfacial layer. The small lattice misfit of 10% between the Pt (111) and diamond (111) crystallographic orientations is good for bond formation between the two phases with low internal stress. Good electronic coupling between Pt and diamond was indicated by the Pt 4f binding energy shift of 0.6 eV from 70.8 eV for the bulk metal

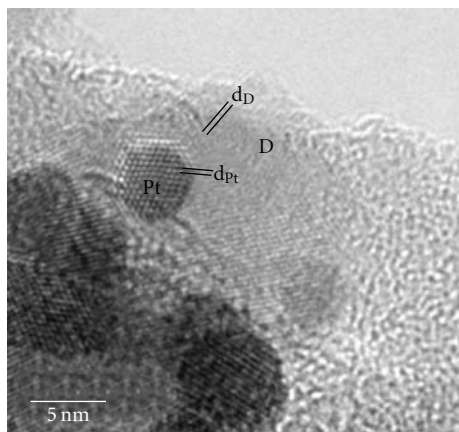


FIGURE 15: High-resolution TEM image of a Pt particle formed on B-UNCD-D. The Pt loading was 5% Pt/C and the metal at layer was formed by a chemical impregnation method. P is the platinum particle, D is the diamond, and d_{Pt} and d_D are the lattice spacing for Pt and diamond (Reprinted with permission from [63]).

to 71.4 eV for Pt on diamond; a binding energy that was close to that for Pt supported on sp^2 -bonded carbon supports. The gas-phase oxidation of the bare and platinized powders in air was studied by TGA (Thermogravimetric Analysis). Commercial Vulcan XC-72 and platinized Vulcan XC-72 at a 20% wt% were used for comparison. A more rapid and reliable assessment of the dimensional stability of carbon electrocatalyst supports is possible using this method, in comparison with traditional long-term fuel cell testing. There are parallels between the relative thermal stability in an oxygen-containing atmosphere and the relative support stability in an operating fuel cell. The results clearly demonstrate that platinized diamond is more resistant to gas phase oxidation than is platinized Vulcan at elevated temperatures. Those results could indicate that the platinized diamond material possesses greater resistance to electrochemical corrosion.

Boron-doped diamond nanoparticles were recently prepared in nanosize undoped diamond particles showing a great improvement in conductivity and surface capacitance with a negligible activity in its potential window [64]. The sol-gel method deposited Pt oxide nanoparticles on the undoped diamond nanoparticles as well as on the BDD nanoparticles. The CV of the depositions was consistent with the higher conductivity and lower surface capacitance of the BDD nanoparticles shown by the comparison between the doped and undoped diamond nanoparticles. Also, BDD nanoparticles favored the formation of different planes of Pt in the deposition. Since, the first peak (lowest potential) in Figure 16 was at the same potential for each material, and the other peaks differ from each different configuration, showing different Pt planes. The authors concluded that the accomplishment of this letter paper opens unlimited opportunities, the use as a support for catalysts for alkaline fuel cells as well as for waste water management, among others.

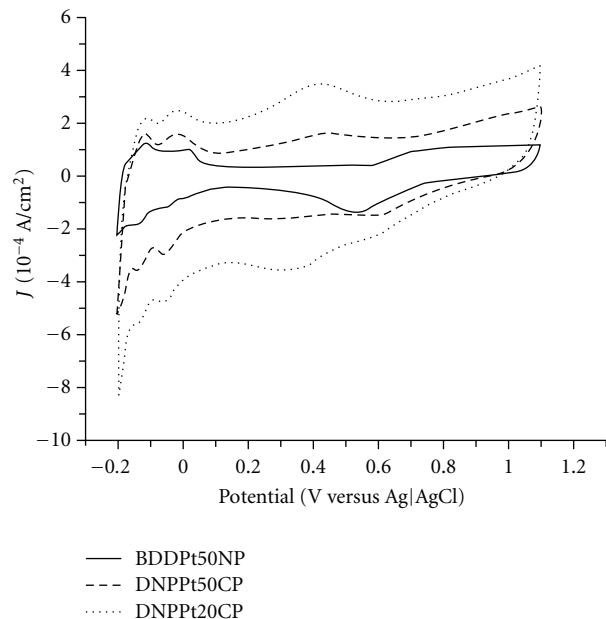


FIGURE 16: Cyclic voltammetry of BDD nanoparticles with 50 wt% Pt (BDDPt50NP), undoped diamond nanoparticles with 50 wt% Pt (DNPPt50CP), and with 20 wt% Pt (DNPPt20CP) in 0.5 M H_2SO_4 (reprinted with permission from [64]).

3. Application of BDD Films in Batteries

Both primary and rechargeable batteries, which can generate clean electric energy from the stored chemical energy through the desired electrochemical reactions, are essential to the convenience and sustainability of human development in the modern mobile society [65]. Rechargeable batteries are currently prevailing portable power sources because they are material saving due to repeated charge and discharge. Nowadays, environmental awareness and high energy density demand lead to the popularity of Li ion and Ni-MH batteries, which have gradually become an alternative power source to traditional lead acid and Ni-Cd batteries [65]. Rechargeable Li ion battery systems have become a prominent technology in the global battery market, since they offer the highest energy density available to date for rechargeable batteries.

Current research and development of Li ion batteries can hardly keep up with the growing demand of the ever-increasing 3C (computer, communication, and consumer electronics) market. New-generation wireless communication technologies require batteries with lighter weight, higher energy/power density, and longer cycle life. Commercial Li ion batteries generally utilize classic Li^+ intercalation compounds ($LiCoO_2$) and carbons as active materials, which fall in short with limited inherent capacity [66].

Although the lithium anode has superior theoretical capacity (3.862 mAh g^{-1}) and a high redox potential, there are several problems like dendrite and poor cyclability to be resolved before it can have practical applications [67–69]. In the last two decades, numerous researchers have endeavored to find solutions to this problem by introducing



FIGURE 17: SEM image of BDD/CF electrode with a doping level of 10^{18} part cm^{-3} (reprinted with permission from [78]).

different solvent mixtures [70], novel electrolyte salts [71], and additives to the electrolytes [72, 73].

Carbonaceous anodes are the most used anodic materials due to their low cost and availability. However, the theoretical capacity (372 mAh g^{-1}) is poor compared with the charge density of lithium (3.862 mAh g^{-1}). Some efforts with novel graphite varieties and carbon nanotubes have tried to increase this reversible capacity. Reported measurements to date of the lithium ion capacity for single walled carbon nanotubes (SWCNTs) are generally between 400 and 460 mAh g^{-1} [74, 75]. However, there is a large first cycle hysteresis that leads to high irreversible capacity loss for SWCNTs. This effect has been attributed to the high surface area of SWCNTs, which affects the extent of solvent decomposition leading to the solid-electrolyte-interface formation [74].

As a substitute material, BDD electrodes have very interesting properties (see Section 1). BDD films were early used as substrates for the deposition of Al thin films for the study of the underpotential deposition (UPD) of lithium as an indirect application of diamond for battery systems [76]. Thus, the electrochemical properties of clean aluminum in $\text{LiClO}_4(\text{poly}(\text{ethylene oxide}))$ solutions have been investigated in ultrahigh vacuum using as electrodes both foils and thin films vapor deposited on BDD layers supported on Si substrates. Voltammetric scans recorded at temperatures of about 55°C yielded a set of deposition/stripping peaks at potentials more positive to the onset of Li/Al alloy formation, attributed to Li UPD on Al. The amount of stored Li was found to increase with the thickness of the Al film; however, uncertainties in the real amount of Al did not allow more quantitative conclusions to be drawn.

The use of diamond materials in studies for further battery applications is rather recent. The direct insertion of lithium into as prepared H-terminated BDD electrodes with different levels of boron doping (10^{18} – 10^{21} B cm^{-3}) and grown on cloth of graphite fibers was demonstrated in 2003 by Ferreira and coworkers [77].

The effect of boron concentration was evident. Electrodes with lower boron content displayed higher capacity for reversible lithium insertion, although they present a smaller electronic conductivity that increases the ohmic drop of the electrode. The electrode with 10^{21} part cm^{-3} reached a

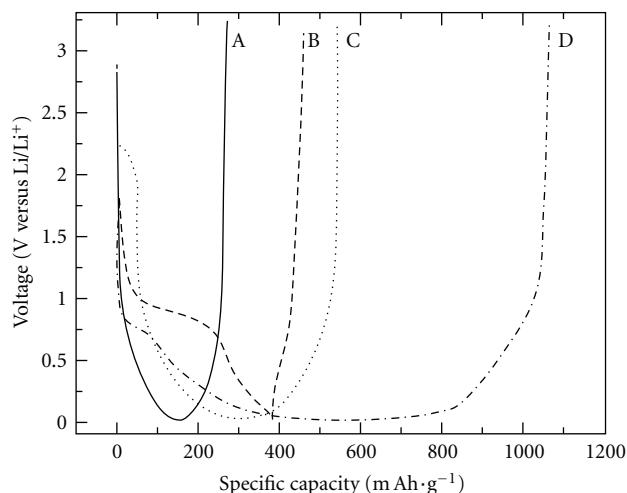


FIGURE 18: First charge/discharge for carbon felt (A) and BDD/CF electrodes doped from 10^{18} up to 10^{21} part cm^{-3} (B, C, D) (reprinted with permission from [77]).

specific capacity, during the first insertions, of 95.7 mAh g^{-1} , while the sample with 10^{18} part cm^{-3} reached 234.9 mAh g^{-1} .

A continuation of this research was reported in 2005 when the authors investigated the lithium electrochemical intercalation into BDD films grown on carbon felt (BDD/CF electrodes, see Figure 17) also with different boron doping levels (10^{18} – 10^{21} B cm^{-3}) [78]. The grain sizes and conductivity of the BDD layers had great influence in the lithium intercalation process.

In contrast to the first study (BDD grown on graphite fibers) [77], higher electronic conductivity (higher boron doping level) increased the reversible electrode capacity of the BDD grown on carbon felt. Composite electrodes containing diamond layers with higher boron concentration (10^{21} part cm^{-3} , curve D in Figure 18) have also smaller grain sizes, and as a consequence are rich in grain boundaries or sp^2 sites, displayed the highest reversible capacity for lithium storage. On the contrary, the low doped diamond layer with a boron concentration of 10^{18} part cm^{-3} (curve B in Figure 18), that has large grain sizes and low electronic conductivity, was not efficient for lithium storage and intercalation. Nevertheless, the reason for these incongruous results from the two studies was unclear and was not fully explored in the study.

According to these authors, this new class of electrodes can be very useful since they are free of the binder polymers traditionally used in the preparation of lithium batteries. Hypothetically, BDD composite electrodes can become very competitive if a boron-diamond layer providing an elevated sp^2/sp^3 sites ratio. In this sense, nanodiamond layers, with a large quantity of grain boundaries, grown on felt substrates deserve further investigation.

The study of the cycling performance of BDD powder prepared by the chemical vapor deposition method by assembling Li/BDD cells at ambient temperature was recently reported [79]. BDD powders with a doping level of 3500 ppm

of B were prepared on single crystal p-type Si (100) wafers. The as-grown BDD contained some graphitic (sp^2) phase and was hydrogen-terminated. Activation of BDD by anodic polarization (in H_2SO_4 1 M at $25^\circ C$ for 30 min) was carried out to eliminate most of the sp^2 -type carbon and absorbed hydrogen from the surface.

According to Christy and coworkers [79] the diamond grains of the BDD layer have effective participation in the lithium storage, and electron reaches the diamond through the sp^2 carbons located in the grain boundaries. Both graphitic and nongraphitic carbons should provide sites for lithium insertion. Graphitic sp^2 -type carbons accommodate Li between grapheme layers while the sp^3 -type carbons can accommodate only in defect sites caused by the presence of the trivalent boron, although it was reported that the lithium insertion in the interstitial sites of the sp^3 -bonded carbon structure is energetically favorable and that the mobility of Li in the diamond lattice seems to be elevated [80].

It is worthwhile mentioning that the defect structure and, therefore, the sp^2 character can be enhanced by incorporation of more boron in the carbons. Thus the results of Christy and coworkers suggested that BDD anode materials could be very promising if BDD provides an elevated number of both sp^2 carbon sites and also sp^3 sites with good intercalation kinetics. This supposition is reinforced if it is considered that a high fraction of sp^2 carbon is preferred for high lithium storage capacity when as-deposited diamond-like carbon (DLC) films with different sp^2/sp^3 ratios were characterized as anode materials for Li-ion batteries [81]. DLC is a metastable form of amorphous carbon containing sp^2 -bonded clusters interconnected by a random network of sp^3 -bonded atomic sites [82].

In a different approach, functional sp^2 - sp^3 carbon composite materials (carbon nanotube/nanohoneycomb BDD, CNT-NANO) were fabricated by introducing multiwalled carbon nanotubes (MWCNs) into the pores of nanohoneycomb diamond of 400 nm diam. using the CVD method [83].

Highly BDD films were deposited by microwave-assisted plasma CVD. Nanohoneycomb structures were prepared by oxygen plasma etching through anodic alumina masks with 400 nm pore diameter on polished diamond films, as observed in Figure 19, while, the MWCNs were prepared by pyrolysis of phthalocyanine with an Fe catalyst using CVD.

The electrochemical behavior of these electrodes was examined using CV, electrochemical impedance spectroscopy, and galvanostatic measurements in $LiClO_4$ /propylene carbonate electrolyte. In contrast to the studies above discussed [77–79], neither Li^+ intercalation nor deintercalation was observed on the cyclic voltammograms for the as-deposited BDD. On the other hand, the behavior of Li^+ insertion into CNTs was observed in the cathodic sweep at $-3.3 V$ (versus Ag/Ag^+) in CV. The current density for Li^+ intercalation at HD CNT-NANO was $-343 \mu A cm^{-2}$ (geometric area), and this at LD CNT-NANO was $-173 \mu A cm^{-2}$ (geometric) at $-3.3 V$ (versus Ag/Ag^+).

Alternating current (AC) impedance measurements have indicated that at the nanohoneycomb diamond densely deposited CNTs (HD CNT-NANO), only the Li^+

intercalation process is observed. In contrast, the nanohoneycomb diamond modified with CNTs in low density (LD CNT-NANO) exhibited the combination behavior of Li^+ intercalation at CNTs and the electrochemical double-layer discharging on the diamond surface.

In galvanostatic measurements, HD CNT-NANO behaved as a pure Li^+ ion battery anode, and the specific capacity (per 1 g of activated material) was found to be $894 mAh g^{-1}$, which is higher than that obtained for mesophase carbon materials. For LD CNT-NANO, in the initial time following the start of discharging, the behavior of the double-layer discharging was observed in addition to Li^+ deintercalation. Suppression of the potential drops associated with Li^+ deintercalation by rapid discharging from the electrical double layer could increase the specific power for LD CNT-NANO. The combination function of the super capacitor and the Li^+ -ion battery that works simultaneously supporting each other in one electrochemical cell suggests the possible realization of a hybrid electrode material with high energy density and high-specific power.

In summary, two different functionalities were simultaneously realized by combining two different materials with totally different electrochemical characteristics. In this case, the increase in the performance of the one functionality results in the tradeoff of the other functionality. Therefore, in the case of the actual use of this hybrid electrode, the ratio of the combination of sp^2 and sp^3 carbon must be selected according to the requirement from the application.

4. Concluding Remarks

The deposition of metal or metal oxide clusters onto the BDD film electrodes has been used to exploit the much higher catalytic activity of such nanoparticles using only very small catalyst amounts compared to the conventional bulk material. The modification of BDD surfaces with micro- and nanometric metallic and/or metallic oxide deposits using different methods has been broadly investigated in the last two decades [15–61]. The use of these hybrid systems containing BDD as new anode supports for future fuel cell applications has been widely evaluated and investigated. However, it is difficult to choose the most suitable method for the modification of BDD surfaces at this time, since each method has its own advantages and limitations. The available literature covered in this review clearly indicates that while the microemulsion method produces a well-defined nanoparticles size (2–5 nm) and good dispersion, the alloy degree is poor. The electrodeposition method produces well-dispersed particles at the BDD surface, but with higher sizes (40–700 nm) and low stability. The sol-gel method produce the highest stable nanoparticles with low particle sizes (<10 nm) and good dispersion on the BDD surface; however, the control of the alloy degree between the Pt and the ad-atom used is difficult to achieve by this method. The thermal deposition appears as the less suitable method for this purpose due to the low degree of dispersion, high particle size, low stability, and the difficulty to control the degree of alloying when this method is used.

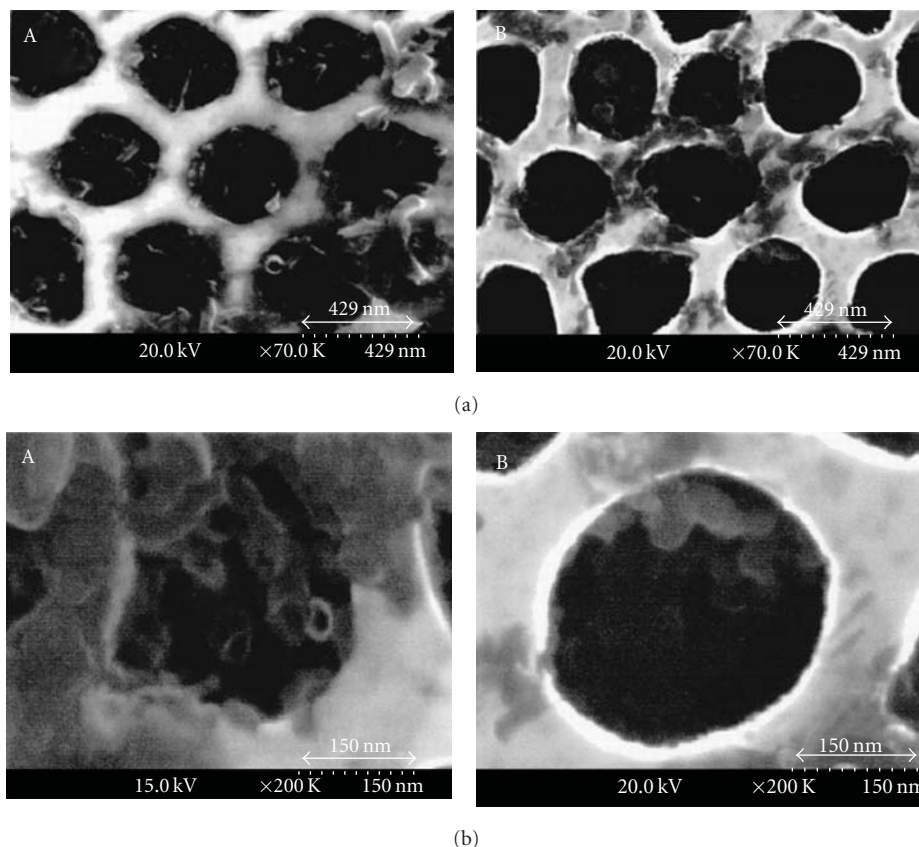


FIGURE 19: Top view of SEM images for a carbon nanotubes/nanoporous diamond composite electrode; (a) low magnification, and (b) high magnification images for (A) HD CNT-NANO and (B) LD CNT-NANO (reprinted with permission from [83]).

Therefore, further developments should be carried out upon the close collaboration of analytical chemists, engineers, and electrochemists to ensure effective application and exploitation of new catalysts to increase the efficiency of fuel cells using BDD anodes tested in real fuel cell operating conditions.

On the other hand, some efforts should be carried out for the application of BDD materials on rechargeable battery or electrochemical capacitors systems. However, considering the scarce quantity of reports available in the literature and due to the controversial results discussed in this section for the intercalation of lithium ion on BDD materials, it is clear that this issue is in the beginning of development. Several studies must be carried out for the application of BDD materials on rechargeable battery systems. Studies with emphasis on the quantification and understanding of the relationship within the properties of the diamond materials, like sp^2 -type carbon content, grain boundary size (micro, and nanodiamond), level of doping, diamond conductivity, surface termination, among others, on the lithium intercalation behavior are still needed. Future outlooks are apparently related to the use of boron-doped nanodiamond materials with high levels of doping, joining both, a high sp^2/sp^3 carbon ratio and a high quantity of atomic defect sites. This direction would be a worthwhile area to pursue for research and technological applications for anode materials for battery systems.

Acknowledgment

The authors wish to thank National Council of Technological and Scientific Development-CNPq (Proc. 304018/2009-0) for the scholarships and financial support to this work.

References

- [1] H. A. Gasteiger, S. S. Kocha, B. Sompalli, and F. T. Wagner, "Activity benchmarks and requirements for Pt, Pt-alloy, and non-Pt oxygen reduction catalysts for PEMFCs," *Applied Catalysis B*, vol. 56, no. 1-2, pp. 9–35, 2005.
- [2] M. S. Saha, R. Li, and X. Sun, "High loading and monodispersed Pt nanoparticles on multiwalled carbon nanotubes for high performance proton exchange membrane fuel cells," *Journal of Power Sources*, vol. 177, no. 2, pp. 314–322, 2008.
- [3] S. Mitsushima, S. Kawahara, K. I. Ota, and N. Kamiya, "Consumption rate of Pt under potential cycling," *Journal of the Electrochemical Society*, vol. 154, no. 2, pp. B153–B158, 2007.
- [4] D. A. Stevens, M. T. Hicks, G. M. Haugen, and J. R. Dahn, "Ex situ and in situ stability studies of PEMFC catalysts," *Journal of the Electrochemical Society*, vol. 152, no. 12, pp. A2309–A2315, 2005.
- [5] S. Brimaud, C. Coutanceau, E. Garnier et al., "Influence of surfactant removal by chemical or thermal methods on structure and electroactivity of Pt/C catalysts prepared by water-in-oil microemulsion," *Journal of Electroanalytical Chemistry*, vol. 602, no. 2, pp. 226–236, 2007.

- [6] U. Griesbach, D. Zollinger, H. Pütter, and C. Comninellis, "Evaluation of boron doped diamond electrodes for organic electrosynthesis on a preparative scale," *Journal of Applied Electrochemistry*, vol. 35, no. 12, pp. 1265–1270, 2005.
- [7] P. Cañizares, A. Gadri, J. Lobato et al., "Electrochemical oxidation of azoic dyes with conductive-diamond anodes," *Industrial and Engineering Chemistry Research*, vol. 45, no. 10, pp. 3468–3473, 2006.
- [8] R. T. S. Oliveira, G. R. Salazar-Banda, M. C. Santos et al., "Electrochemical oxidation of benzene on boron-doped diamond electrodes," *Chemosphere*, vol. 66, no. 11, pp. 2152–2158, 2007.
- [9] M. A. Rodrigo, P. A. Michaud, I. Duo, M. Panizza, G. Cerisola, and C. Comninellis, "Oxidation of 4-chlorophenol at boron-doped diamond electrode for wastewater treatment," *Journal of the Electrochemical Society*, vol. 148, no. 5, pp. D60–64, 2001.
- [10] B. Boye, P. A. Michaud, B. Marselli, M. M. Dieng, E. Brillas, and C. Comninellis, "Anodic oxidation of 4-chlorophenoxyacetic acid on synthetic boron-doped diamond electrodes," *New Diamond and Frontier Carbon Technology*, vol. 12, no. 2, pp. 63–72, 2002.
- [11] I. Sirés, N. Oturan, M. A. Oturan, R. M. Rodríguez, J. A. Garrido, and E. Brillas, "Electro-fenton degradation of antimicrobials triclosan and triclocarban," *Electrochimica Acta*, vol. 52, no. 17, pp. 5493–5503, 2007.
- [12] C. Flox, J. A. Garrido, R. M. Rodríguez et al., "Mineralization of herbicide mecoprop by photoelectro-fenton with UVA and solar light," *Catalysis Today*, vol. 129, no. 1–2, pp. 29–36, 2007.
- [13] G. S. Garbellini, G. R. Salazar-Banda, and L. A. Avaca, "Effects of ultrasound on the degradation of pentachlorophenol by boron-doped diamond electrodes," *Portugaliae Electrochimica Acta*, vol. 28, no. 6, pp. 405–415, 2010.
- [14] J. H. T. Luong, K. B. Male, and J. D. Glennon, "Boron-doped diamond electrode: synthesis, characterization, functionalization and analytical applications," *Analyst*, vol. 134, no. 10, pp. 1965–1979, 2009.
- [15] Y. Shao, J. Liu, Y. Wang, and Y. Lin, "Novel catalyst support materials for PEM fuel cells: current status and future prospects," *Journal of Materials Chemistry*, vol. 19, no. 1, pp. 46–59, 2009.
- [16] A. Kraft, "Doped diamond: a compact review on a new, versatile electrode material," *International Journal of Electrochemical Science*, vol. 2, pp. 355–385, 2007.
- [17] M. Boutonnet, S. Lögdberg, and E. E. Svensson, "Recent developments in the application of nanoparticles prepared from w/o microemulsions in heterogeneous catalysis," *Current Opinion in Colloid and Interface Science*, vol. 13, no. 4, pp. 270–286, 2008.
- [18] S. Eriksson, U. Nylén, S. Rojas, and M. Boutonnet, "Preparation of catalysts from microemulsions and their applications in heterogeneous catalysis," *Applied Catalysis A*, vol. 265, no. 2, pp. 207–219, 2004.
- [19] M. Boutonnet, J. Kizling, P. Stenius, and G. Maire, "The preparation of monodisperse colloidal metal particles from microemulsions," *Colloids and Surfaces*, vol. 5, no. 3, pp. 209–225, 1982.
- [20] G. Siné and C. Comninellis, "Nafion[®]-assisted deposition of microemulsion-synthesized platinum nanoparticles on BDD: activation by electrogenerated ·OH radicals," *Electrochimica Acta*, vol. 50, no. 11, pp. 2249–2254, 2005.
- [21] G. Siné, I. Duo, B. El Roustom, G. Fóti, and C. Comninellis, "Deposition of clusters and nanoparticles onto boron-doped diamond electrodes for electrocatalysis," *Journal of Applied Electrochemistry*, vol. 36, no. 8, pp. 847–862, 2006.
- [22] G. Siné, G. Fóti, and C. Comninellis, "Boron-doped diamond (BDD)-supported Pt/Sn nanoparticles synthesized in microemulsion systems as electrocatalysts of ethanol oxidation," *Journal of Electroanalytical Chemistry*, vol. 595, no. 2, pp. 115–124, 2006.
- [23] G. Siné, D. Smida, M. Limat, G. Fóti, and C. Comninellis, "Microemulsion synthesized Pt/Ru/Sn nanoparticles on BDD for alcohol electro-oxidation," *Journal of the Electrochemical Society*, vol. 154, no. 2, pp. B170–B174, 2007.
- [24] F. Cardarelli, P. Taxil, A. Savall, C. Comninellis, G. Manoli, and O. Leclerc, "Preparation of oxygen evolving electrodes with long service life under extreme conditions," *Journal of Applied Electrochemistry*, vol. 28, no. 3, pp. 245–250, 1998.
- [25] I. Duo, P. A. Michaud, W. Haenni, A. Perret, and C. Comninellis, "Activation of boron-doped diamond with IrO₂ clusters," *Electrochemical and Solid-State Letters*, vol. 3, no. 7, pp. 325–326, 2000.
- [26] B. E. Roustom, G. Fóti, and C. Comninellis, "Preparation of gold nanoparticles by heat treatment of sputter deposited gold on boron-doped diamond film electrode," *Electrochemistry Communications*, vol. 7, no. 4, pp. 398–405, 2005.
- [27] F. Montilla, E. Morallón, I. Duo, C. Comninellis, and J. L. Vázquez, "Platinum particles deposited on synthetic boron-doped diamond surfaces. Application to methanol oxidation," *Electrochimica Acta*, vol. 48, no. 25–26, pp. 3891–3897, 2003.
- [28] A. De Battisti, S. Ferro, and M. Dal Colle, "Electrocatalysis at conductive diamond modified by noble-metal oxides," *Journal of Physical Chemistry B*, vol. 105, no. 9, pp. 1679–1682, 2001.
- [29] J. S. Gao, T. Arunagiri, J. J. Chen et al., "Preparation and characterization of metal nanoparticles on a diamond surface," *Chemistry of Materials*, vol. 12, no. 11, pp. 3495–3500, 2000.
- [30] M. Li, G. Zhao, R. Geng, and H. Hu, "Facile electrocatalytic redox of hemoglobin by flower-like gold nanoparticles on boron-doped diamond surface," *Bioelectrochemistry*, vol. 74, no. 1, pp. 217–221, 2008.
- [31] V. Saez, J. Gonzalez-Garcia, M. A. Kulandainathan, and F. Marken, "Electro-deposition and stripping of catalytically active iron metal nanoparticles at boron-doped diamond electrodes," *Electrochemistry Communications*, vol. 9, no. 5, pp. 1127–1133, 2007.
- [32] K. E. Toghill, G. G. Wildgoose, A. Moshar, C. Mulcahy, and R. G. Compton, "The fabrication and characterization of a bismuth nanoparticle modified boron doped diamond electrode and its application to the simultaneous determination of cadmium(II) and lead(II)," *Electroanalysis*, vol. 20, no. 16, pp. 1731–1737, 2008.
- [33] G. M. Swain and R. Ramesham, "The electrochemical activity of boron-doped polycrystalline diamond thin film electrodes," *Analytical Chemistry*, vol. 65, no. 4, pp. 345–351, 1993.
- [34] K. B. Holt, A. J. Bard, Y. Show, and G. M. Swain, "Scanning electrochemical microscopy and conductive probe atomic force microscopy studies of hydrogen-terminated boron-doped diamond electrodes with different doping levels," *Journal of Physical Chemistry B*, vol. 108, no. 39, pp. 15117–15123, 2004.
- [35] C. H. Goeting, F. Jones, J. S. Foord et al., "Electrochemistry at boron-doped diamond films grown on graphite substrates: redox-, adsorption and deposition processes," *Journal of Electroanalytical Chemistry*, vol. 442, no. 1–2, pp. 207–211, 1998.

- [36] M. Mermoux, B. Marcus, G. M. Swain, and J. E. Butler, "A confocal raman imaging study of an optically transparent boron-doped diamond electrode," *Journal of Physical Chemistry B*, vol. 106, no. 42, pp. 10816–10821, 2002.
- [37] D. Becker and K. Jüttner, "Influence of surface inhomogeneities of boron doped CVD-diamond electrodes on reversible charge transfer reactions," *Journal of Applied Electrochemistry*, vol. 33, no. 10, pp. 959–968, 2003.
- [38] D. Becker and K. Jüttner, "The impedance of fast charge transfer reactions on boron doped diamond electrodes," *Electrochimica Acta*, vol. 49, no. 1, pp. 29–38, 2003.
- [39] N. R. Stradiotto, K. E. Toghill, L. Xiao, A. Moshar, and R. G. Compton, "The fabrication and characterization of a nickel nanoparticle modified boron doped diamond electrode for electrocatalysis of primary alcohol oxidation," *Electroanalysis*, vol. 21, no. 24, pp. 2627–2637, 2009.
- [40] J. Wang and G. M. Swain, "Fabrication and evaluation of platinum/diamond composite electrodes for electrocatalysis," *Journal of the Electrochemical Society*, vol. 150, no. 1, pp. E24–E32, 2003.
- [41] O. Enea, B. Riedo, and G. Dietler, "AFM study of Pt clusters electrochemically deposited onto boron-doped diamond films," *Nano Letters*, vol. 2, no. 3, pp. 241–244, 2002.
- [42] H. A. Gasteiger, N. Marković, P. N. Ross, and E. J. Cairns, "Methanol electrooxidation on well-characterized Pt-Ru alloys," *Journal of Physical Chemistry*, vol. 97, no. 46, pp. 12020–12029, 1993.
- [43] Z. He, J. Chen, D. Liu, H. Zhou, and Y. Kuang, "Electrodeposition of Pt-Ru nanoparticles on carbon nanotubes and their electrocatalytic properties for methanol electrooxidation," *Diamond and Related Materials*, vol. 13, no. 10, pp. 1764–1770, 2004.
- [44] I. González-González, D. A. Tryk, and C. R. Cabrera, "Polycrystalline boron-doped diamond films as supports for methanol oxidation electrocatalysts," *Diamond and Related Materials*, vol. 15, no. 2-3, pp. 275–278, 2006.
- [45] X. Lu, J. Hu, J. S. Foord, and Q. Wang, "Electrochemical deposition of Pt-Ru on diamond electrodes for the electrooxidation of methanol," *Journal of Electroanalytical Chemistry*, vol. 654, no. 1-2, pp. 38–43, 2011.
- [46] H. A. Gasteiger, N. Markovic, P. N. Ross, and E. J. Cairns, "Temperature-dependent methanol electro-oxidation on well-characterized Pt-Ru alloys," *Journal of the Electrochemical Society*, vol. 141, no. 7, pp. 1795–1803, 1994.
- [47] J. Zhu, F. Cheng, Z. Tao, and J. Chen, "Electrocatalytic methanol oxidation of $\text{Pt}_{0.5}\text{Ru}_{0.5-x}\text{Sn}_x/\text{C}$ ($x = 0 - 0.5$)," *Journal of Physical Chemistry C*, vol. 112, no. 16, pp. 6337–6345, 2008.
- [48] N. Spătaru, X. Zhang, T. Spătaru, D. A. Tryk, and A. Fujishima, "Platinum electrodeposition on conductive diamond powder and its application to methanol oxidation in acidic media," *Journal of the Electrochemical Society*, vol. 155, no. 3, pp. B264–B269, 2008.
- [49] H. B. Suffredini, G. R. Salazar-Banda, S. T. Tanimoto, M. L. Calegaro, S. A. S. Machado, and L. A. Avaca, "AFM studies and electrochemical characterization of boron-doped diamond surfaces modified with metal oxides by the sol-gel method," *Journal of the Brazilian Chemical Society*, vol. 17, no. 2, pp. 257–264, 2006.
- [50] H. B. Suffredini, V. Tricoli, N. Vastistas, and L. A. Avaca, "Electro-oxidation of methanol and ethanol using a Pt-RuO₂/C composite prepared by the sol-gel technique and supported on boron-doped diamond," *Journal of Power Sources*, vol. 158, no. 1, pp. 124–128, 2006.
- [51] L. C. Klein, M. Aparicio, and F. Damay, "Sol-gel processing for battery and fuel cell applications," in *Sumio Sakka Applications of Sol-Gel Technology*, vol. 3, Kluwer Academic Publisher, 2004.
- [52] S. Sakka, *Applications of Sol-gel Technology*, Kluwer Academic Publisher, 2004.
- [53] C. P. Ballard and A. J. Fanelli, "Sol-gel route for materials synthesis," in *Chemistry of Advanced Materials*, C. N. R. Rao, Ed., Blackwell Scientific Publications, 1993.
- [54] H. B. Suffredini, V. Tricoli, L. A. Avaca, and N. Vastistas, "Sol-gel method to prepare active Pt-RuO₂ coatings on carbon powder for methanol oxidation," *Electrochemistry Communications*, vol. 6, no. 10, pp. 1025–1028, 2004.
- [55] H. B. Suffredini, G. R. Salazar-Banda, and L. A. Avaca, "Enhanced ethanol oxidation on PbO_x-containing electrode materials for fuel cell applications," *Journal of Power Sources*, vol. 171, no. 2, pp. 355–362, 2007.
- [56] H. B. Suffredini, G. R. Salazar-Banda, and L. A. Avaca, "Carbon supported electrocatalysts prepared by the sol-gel method and their utilization for the oxidation of methanol in acid media," *Journal of Sol-Gel Science and Technology*, vol. 49, no. 2, pp. 131–136, 2009.
- [57] G. R. Salazar-Banda, H. B. Suffredini, and L. A. Avaca, "Improved stability of PtO_x sol-gel-modified diamond electrodes covered with a Nafion[®] film," *Journal of the Brazilian Chemical Society*, vol. 16, no. 5, pp. 903–906, 2005.
- [58] G. R. Salazar-Banda, H. B. Suffredini, M. L. Calegaro, S. T. Tanimoto, and L. A. Avaca, "Sol-gel-modified boron-doped diamond surfaces for methanol and ethanol electro-oxidation in acid medium," *Journal of Power Sources*, vol. 162, no. 1, pp. 9–20, 2006.
- [59] G. R. Salazar-Banda, K. I. B. Eguiluz, and L. A. Avaca, "Boron-doped diamond powder as catalyst support for fuel cell applications," *Electrochemistry Communications*, vol. 9, no. 1, pp. 59–64, 2007.
- [60] G. R. Salazar-Banda, H. B. Suffredini, M. L. Calegaro, S. T. Tanimoto, and L. A. Avaca, "Diamond-supported binary and ternary nano-size catalyst for advanced direct-alcohol PEM fuel cells," in *Proceedings of the 57th Annual Meeting of the International Society of Electrochemistry*, 2006.
- [61] G. R. Salazar-Banda, H. B. Suffredini, L. A. Avaca, and S. A. S. Machado, "Methanol and ethanol electro-oxidation on Pt-SnO₂ and Pt-Ta₂O₅ sol-gel-modified boron-doped diamond surfaces," *Materials Chemistry and Physics*, vol. 117, no. 2-3, pp. 434–442, 2009.
- [62] V. M. Swope, I. Sasaki, T. Ay, and G. M. Swain, "Conductive diamond powder: a new catalyst support for the polymer electrolyte membrane fuel cell," *Electrochemical Society Transactions*, vol. 3, no. 28, pp. 27–36, 2007.
- [63] L. Guo, V. M. Swope, B. Merzougui et al., "Oxidation resistance of bare and pt-coated electrically conducting diamond powder as assessed by thermogravimetric analysis," *Journal of the Electrochemical Society*, vol. 157, no. 1, pp. A19–A25, 2010.
- [64] L. Cunci and C. R. Cabrera, "Preparation and electrochemistry of boron-doped diamond nanoparticles on glassy carbon electrodes," *Electrochemical and Solid-State Letters*, vol. 14, no. 3, pp. K17–K19, 2011.
- [65] M. Winter and R. J. Brodd, "What are batteries, fuel cells, and supercapacitors?" *Chemical Reviews*, vol. 104, no. 10, pp. 4245–4270, 2004.
- [66] M. S. Whittingham, "Lithium batteries and cathode materials," *Chemical Reviews*, vol. 104, no. 10, pp. 4271–4302, 2004.
- [67] J. J. Zhang and Y. Y. Xia, "Co-Sn alloys as negative electrode materials for rechargeable lithium batteries," *Journal of the*

- Electrochemical Society*, vol. 153, no. 8, Article ID 012608JES, pp. A1466–A1471, 2006.
- [68] J. Hassoun, S. Panero, and B. Scrosati, “Electrodeposited Ni-Sn intermetallic electrodes for advanced lithium ion batteries,” *Journal of Power Sources*, vol. 160, no. 2, pp. 1336–1341, 2006.
- [69] H. Jusef, S. Panero, P. Simon, P. L. Taberna, and B. Scrosati, “High-rate, long-life Ni-Sn nanostructured electrodes for lithium-ion batteries,” *Advanced Materials*, vol. 19, no. 12, pp. 1632–1635, 2007.
- [70] X. Wang, E. Yasukawa, and S. Kasuya, “Electrochemical properties of tetrahydropyran-based ternary electrolytes for 4 V lithium metal rechargeable batteries,” *Electrochimica Acta*, vol. 46, no. 6, pp. 813–819, 2001.
- [71] M. Ishikawa, S. I. Machino, and M. Morita, “Electrochemical control of a Li metal anode interface: improvement of Li cyclability by inorganic additives compatible with electrolytes,” *Journal of Electroanalytical Chemistry*, vol. 473, no. 1-2, pp. 279–284, 1999.
- [72] K. Kanamura, H. Takezawa, S. Shiraishi, and Z. I. Takehara, “Chemical reaction of lithium surface during immersion in LiClO₄ or LiPF₆/DEC electrolyte,” *Journal of the Electrochemical Society*, vol. 144, no. 6, pp. 1900–1906, 1997.
- [73] R. Mogi, M. Inaba, S. K. Jeong, Y. Iriyama, T. Abe, and Z. Ogumi, “Effects of some organic additives on lithium deposition in propylene carbonate,” *Journal of the Electrochemical Society*, vol. 149, no. 12, pp. A1578–A1583, 2002.
- [74] E. Frackowiak and F. Béguin, “Electrochemical storage of energy in carbon nanotubes and nanostructured carbons,” *Carbon*, vol. 40, no. 10, pp. 1775–1787, 2002.
- [75] I. Mukhopadhyay, S. Kawasaki, F. Okino, A. Govindaraj, C. N. R. Rao, and H. Touhara, “Electrochemical Li insertion into single-walled carbon nanotubes prepared by graphite arc-discharge method,” *Physica B*, vol. 323, no. 1–4, pp. 130–132, 2002.
- [76] L. F. Li, Y. Luo, G. G. Totir, D. A. Totir, G. S. Chottiner, and D. A. Scherson, “Underpotential deposition of lithium on aluminum in ultrahigh-vacuum environments,” *Journal of Physical Chemistry B*, vol. 103, no. 1, pp. 164–168, 1999.
- [77] N. G. Ferreira, L. L. Mendonça, V. J. T. Airoidi, and J. M. Rosolen, “Electrochemical intercalation of lithium into boron-doped CVD diamond electrodes grown on carbon fiber cloths,” *Diamond and Related Materials*, vol. 12, no. 3–7, pp. 596–600, 2003.
- [78] E. C. Almeida, V. J. Trava-Airoidi, N. G. Ferreira, and J. M. Rosolen, “Electrochemical insertion of lithium into a doped diamond film grown on carbon felt substrates,” *Diamond and Related Materials*, vol. 14, no. 10, pp. 1673–1677, 2005.
- [79] A. Y. M. T. Christy, K. S. Nahm, Y. J. Hwang et al., “Lithium insertion studies on boron-doped diamond as a possible anode material for lithium batteries,” *Ionics*, vol. 14, no. 2, pp. 157–161, 2008.
- [80] S. A. Kajihara, A. Antonelli, and J. Bernholc, “Nitrogen and potential n-type dopants in diamond,” *Physical Review Letters*, vol. 66, no. 15, pp. 2010–2013, 1991.
- [81] Z. G. Lu and C. Y. Chung, “Electrochemical characterization of diamond like carbon thin films,” *Diamond and Related Materials*, vol. 17, no. 11, pp. 1871–1876, 2008.
- [82] J. Robertson, “Diamond-like amorphous carbon,” *Materials Science and Engineering R*, vol. 37, no. 4–6, pp. 129–281, 2002.
- [83] K. Honda, M. Yoshimura, K. Kawakita et al., “Electrochemical characterization of carbon nanotube/nanohoneycomb diamond composite electrodes for a hybrid anode of Li-ion battery and super capacitor,” *Journal of the Electrochemical Society*, vol. 151, no. 4, pp. A532–A541, 2004.

Research Article

Automated Online Solid-Phase Extraction Coupled with Sequential Injection-HPLC-EC System for the Determination of Sulfonamides in Shrimp

Pimkwan Chantaratepra,¹ Weena Siangproh,² Shoji Motomizu,³
and Orawon Chailapakul^{4,5}

¹ Program in Biotechnology, Faculty of Science, Chulalongkorn University, Patumwan, Bangkok 10330, Thailand

² Department of Chemistry, Faculty of Science, Srinakharinwirot University, Sukhumvit 23, Wattana, Bangkok 10110, Thailand

³ Department of Chemistry, Faculty of Science, Okayama University, 3-1-1 Tsushima-ka, Okayama 700-8530, Japan

⁴ Department of Chemistry, Faculty of Science, Chulalongkorn University, Patumwan, Bangkok 10330, Thailand

⁵ Center for Excellence Petroleum, Petrochemicals and Advanced Materials, Chulalongkorn University, Patumwan, Bangkok 10330, Thailand

Correspondence should be addressed to Orawon Chailapakul, corawon@chula.ac.th

Received 26 April 2011; Accepted 20 June 2011

Academic Editor: Carlos Alberto Martinez-Huitle

Copyright © 2012 Pimkwan Chantaratepra et al. This is an open access article distributed under the Creative Commons Attribution License, which permits unrestricted use, distribution, and reproduction in any medium, provided the original work is properly cited.

The use of fully automated online solid-phase extraction (SPE) coupled with sequential injection analysis, high-performance liquid chromatography (HPLC), and electrochemical detection (EC) for the separation and determination of sulfonamides has been developed. A homemade microcolumn SPE system coupled with sequential injection analysis (SIA) was used to automate the sample cleanup and extraction of sulfonamides. The optimal flow rate of sample loading and elution was found to be 10 $\mu\text{L/s}$, and optimal elution time of zone was 20–24 s. Under the optimal conditions, a linear relationship between peak area and sulfonamide concentrations was obtained in the range of 0.01–8.0 $\mu\text{g mL}^{-1}$. Detection limits for seven sulfonamides were between 1.2 ng mL^{-1} and 11.2 ng mL^{-1} . The proposed method has been applied for the determination of sulfonamides in shrimp. Recoveries in the range of 84–107% and relative standard deviations (RSDs) below 6.5% for intraday and 13% for inter-day were received for three concentration levels of spiking. The results showed that the present method was simple, rapid, accurate and highly sensitive for the determination of sulfonamides.

1. Introduction

Sulfonamides (SAs) have been widely used as effective chemotherapeutics and growth promoters in animals' feeding. They are a group of synthetic antibiotic agents that played important role for the treatment in both human and veterinary medicines. SAs represent one of the most commonly used families of antibiotics in veterinary medicine because of their low cost, low toxicity, and excellent activity against common bacterial diseases. Nowadays, they are much used for therapy, prophylaxis, and growth promotion in livestock in cattle farm [1, 2]. Residues of SAs may occur in animal tissues if the adequate withdrawal time has not been observed

or if SAs have been improperly administered. Therefore, long-term use of sulfonamide agents can cause serious side effects, such as Stevens-Johnson syndrome and carcinogenicity because of human consumption [3, 4]. Additionally, antibacterial drug in food can cause anaphylaxis in sensitive patients and can foster the development of antibiotic resistance in pathogenic organisms. With considerable attention to the potential human health, the European Union (EU) has set the maximum residual level of sulfonamides at 100 ng g^{-1} in edible tissues and in milk [5]. In Thailand, shrimp is one of the top ten of our exports sent to other countries. To safeguard human health and to overcome the limitations of trade based on SAs residues, a rapid, accurate, selective, sensitive,

and efficient method for the monitoring of SAs in shrimp is of great significance.

Several conventional methods have been successfully applied for the separation and determination of the sulfonamide content in different samples including gas chromatography (GC), gas chromatography-mass spectrometry (GC/MS), capillary electrophoresis (CE) [6, 7], enzyme-linked immunosorbent assay (ELISA) [8, 9], thin-layer chromatography (TLC), high-performance liquid chromatography (HPLC-UV) [10–17], and high-performance liquid chromatography-mass spectrometry (HPLC/MS) [18–25]. Although the mentioned methods offer good resolution of organic compound, their sensitivities are often insufficient for direct determination of trace sulfonamides residue in food. Therefore, sample preparation is required in order to obtain higher concentration and avoid interference by matrix constituents. Recently, offline sample preparation procedures such as liquid-liquid extraction (LLE) [14, 26], matrix solid-phase dispersion (MSPD) [27], solid-phase microextraction (SPME) [15], and solid-phase extraction (SPE) [1, 16, 18, 20–24, 28] have been reported for the extraction of sulfonamides. Unfortunately, the recovery of the analytes and analytical precision of these methods are reduced during the preparation of samples. Moreover, they also consume the large volumes of sample and solvent. To overcome those problems, online solid-phase extraction (SPE) coupled with HPLC has been developed [29–36]. Online SPE is an attractive sample preparation technique because it not only improves analytical precision but also reduces the solvent consumption.

In recent years, sequential injection analysis (SIA) has become apparent that the scope of SIA can be extended to encompass a variety of more complex, online, sample manipulation, and pretreatment procedure. Therefore, the use of SIA for a fully automated online SPE procedure prior to subsequently analyzing on HPLC to enhance productivity and reproducibility as well as reduce labor intensive is an attractive choice.

From our previous report, offline SPE using Oasis HLB material was successfully proposed and applied to extract the residual sulfonamides in shrimp [28]. This material is a hydrophilic-lipophilic balanced (HLB) sorbent that is composed of two monomers (N-vinylpyrrolidone and divinylbenzene). It exhibited excellent retention capacity for a wide polarity of analytes [18, 24]. To increase the performance and sensitivity in HPLC-EC by means of fully automation, in this work, we used online Oasis HLB SPE procedure to extend our previous efforts on the determination of sulfonamides instead of using offline SPE before their HPLC separation. The common detectors for chromatography with online SPE are ultraviolet (UV) [10–17], fluorescence [1, 4, 37] and MS [18–25]. Even though these methods provide high sensitivity and selectivity, there are the expensive equipment and a requirement for significant labor and analytical resources. Nowadays, the alternative detection for the determination of sulfonamides is the electrochemical detection (EC) due to its high sensitivity, low cost, fastness, and simplicity [26, 28, 38].

In this paper, the ultimate goal was to develop a fully automatic online SPE technique coupled with SIA-HPLC-EC for the separation and determination of seven sulfonamides (sulfaguanidine (SG), sulfadiazine (SDZ), sulfamethazine (SMZ), sulfamonomethoxine (SMM), sulfamethoxazole (SMX), sulfadimethoxine (SDM), and sulfaquinoxaline (SQ)). A silica-based monolithic column was employed for sulfonamides separation because of its high tolerance for organic solvent, which led to a longer lifetime and lower back-pressure, compared to other traditional columns. A meticulous optimization process was carried out in order to get an optimum performance of the online system. Likewise, a detailed evaluation of the methodology was developed to demonstrate that this method can be satisfactorily applied to determine residual concentrations of the seven sulfonamides in shrimp using the Oasis HLB SPE material for sample extraction.

2. Experimental

2.1. Reagents and Standards. All solvents and reagents used were HPLC or analytical grade. Acetonitrile was purchased from Sigma-Aldrich (St. Louis, MO, USA). Ethanol was obtained from Carlo Erba (Val de Reuil, France). Methanol, disodium hydrogen phosphate dehydrate (Na_2HPO_4), and citric acid were obtained from Merck (Darmstadt, Germany). Potassium dihydrogen orthophosphate (KH_2PO_4) was obtained from BDH (VWR International Ltd., England). Ethylene diamine tetraacetic acid disodium salt dehydrate (Na_2EDTA) was purchased from Sigma-Aldrich (St. Louis, MO, USA). Ultrapure Water ($R \geq 18.2 \text{ M}\Omega \text{ cm}^{-1}$) from a Milli-Q system (Millipore) was used throughout the experiment. The extraction solution (Na_2EDTA -McIlvaine buffer, pH 4) was prepared by dissolving 13.52 g of Na_2HPO_4 , 13.02 g of citric acid and 3.72 g of Na_2EDTA in one liter of ultrapure water. Prior to use, all solution and solvents were filtered with $0.45 \mu\text{m}$ nylon membranes.

Sulfadiazine, sulfadimethoxine, sulfamethazine, sulfamethoxazole, sulfamonomethoxine, and sulfaquinoxaline were purchased from Sigma-Aldrich (St. Louis, MO, USA). Sulfaguanidine was obtained from ICN Biomedicals Inc. (USA). A stock standard solution ($100 \mu\text{g mL}^{-1}$) of each SA was prepared by dissolving 3 mg of SA in 30 mL of an acetonitrile:ultrapure water solution in (1:1 v/v) and stored at 4°C in the dark. The working solutions were prepared by diluting the stock standard solutions with the mobile phase.

2.2. Materials and Instrumentations. Oasis HLB with particle size of $30 \mu\text{m}$ was obtained from Water (Milford, MA, USA). A homemade microcolumn SPE ($4.0 \text{ cm} \times 1.59 \text{ mm i.d.}$) packed with 60 mg of Oasis HLB was used for the sample cleanup and extraction of SAs.

The HPLC-EC system consisted of an HPLC compact pump model 2250 (Bischoff, Germany) and a thin-layer flow cell (Bioanalytical system Inc., Japan) consisting of three electrodes: a BDD working electrode, an Ag/AgCl reference electrode (Bioanalytical system Inc., Japan), and a stainless

steel tube counter electrode. The chromatographic column was a Chromolith Performance RP-18 silica-based monolithic column (100 mm × 4.6 mm i.d.) from Merck (Darmstadt, Germany). The HPLC was carried out in the mobile phase, which consisted of a phosphate buffer solution (0.05 M KH_2PO_4 , pH 3), acetonitrile, and ethanol in the ratio of 80 : 15 : 5 (v/v/v). The flow rate was set at 1.5 mL min^{-1} . The amperometric detection was used in this experiment, with an applied potential at +1.2 V versus Ag/AgCl. The sequential injection system, Auto-Pret ECD-01P (M&G CHEMATECHS Japan Co. Ltd., Okayama Japan) with 2.5 mL syringe pump, 2.5 mL holding coil, 8-port selection valve (Hamilton, Nevada, USA) and 6-port switching valve (Rheodyne MXT 715-000, USA) was used for sample processing. The experiment was performed at room temperature (25 °C). The CHI1232A (CH Instrument, USA) was used for amperometric controlling and signals processing.

2.3. Online SPE-HPLC Procedure. A schematic diagram for the online solid-phase extraction coupled to SIA-HPLC-EC for the determination of SAs in shrimp is depicted in Figure 1. The online SPE-HPLC-EC consists of three parts. Part I is online SPE consisting of a 3-way syringe pump (2.5 mL), 8-port selection valve, 6-port switching valve, holding coil (2.5 mL), loop (34 μL), and SPE microcolumn. Part II is HPLC system including an HPLC pump and analytical column. Part III is an EC detector consisting of a thin-layer flow cell and a data acquisition system (CHI1232A). The online SPE procedure consists of six steps including conditioning, loading, washing, elution, reconditioning, and injection summarized in Table 1. The first is the column condition step. The SPE microcolumn was conditioned with 1 mL of Na_2EDTA -McIlvaine buffer. In the second, sample loading, 1 mL of sulfonamides solution is introduced into the SPE microcolumn. In the third step, washing, 1 mL of ultrapure water is used to remove the interferences from SPE microcolumn, while the analyte was retained on the sorbent. For the fourth step, elution, 0.2 mL of methanol is used to elute sulfonamides from the sorbent, and then the eluate zone was kept in sample loop. In the fifth step, the SPE microcolumn is cleaned. 5 mL of methanol and 2.5 mL of ultrapure water are sequentially passed through the sorbent to solvate the functional groups of the sorbent. In the final step, eluate was transferred to the analytical column by changing the switching valve from loading to injection position. Next, the separation was performed on RP-18 silica-based monolithic analytical column.

2.4. Sample Preparation. The apparatuses for sample preparation consisted of a vortex mixer (Mixer Uzusio LMS. Co. Ltd., Japan), an ultrasonic bath (ESP chemicals, Inc., MA, USA), and a centrifuge (Cole Parmer, Illinois, USA). Shrimps were obtained from a local supermarket (Bangkok, Thailand). One gram of a homogeneous shrimp sample was placed in a 15 mL amber glass bottle, and 5 mL of Na_2EDTA -McIlvaine's buffer solution was then added into the bottle. The mixture was well mixed on a vortex mixer for 5 min at high speed. Then, the mixture was placed in an ultrasonic

water bath for 10 min following centrifugation at 20,000 rpm for 10 min. Prior to loading the supernatant into online system, it was filtered through a 0.20 μm nylon membrane filter.

3. Results and Discussion

3.1. Optimization of SPE Condition. In order to obtain the optimal conditions, the effects of various parameters were investigated. These included the effect of eluent component, sample loading flow rate, and elution time zone. During the optimization of these parameters, a 10 $\mu\text{g mL}^{-1}$ of SAs standard mixture solution was utilized, and the results were evaluated as the highest current signal.

3.1.1. Optimization of the Eluent Component. From our previous report [28], methanol was selected as the most suitable eluent for offline SPE to achieve the complete extraction of sulfonamides (SAs) in shrimp and the mixture of phosphate buffer : acetonitrile : ethanol (80 : 15 : 5; v/v/v) was used as a mobile phase to obtain the high separation efficiency. In this work, seven SAs were eluted from online SPE and directly flowed through the analytical column (RP-18 silica-based monolithic column) and then detected by electrochemical detection, respectively. The eluent was not only used to elute SAs from SPE but also used to carry analytes into a monolithic column and electrochemical cell. Therefore, the eluent component has directly affected on the efficiency of elution, performance of separation, and sensitivity of electrochemical signal. The ratio of methanol to mobile phase was studied across 50 : 50, 60 : 40, 70 : 30, 80 : 20, 90 : 10, and 100 : 0 (v/v) ratios. The results were illustrated in Figure 2. By the use of 50% methanol, there are only three peaks of SG, SDZ, and SMZ observed. Interestingly, increasing percentage methanol up to 90% and 100%, all seven peaks of SAs can be recorded. However, the retention time of all analytes decreased with increasing the methanol ratio. Hence, an eluent of 100% methanol was selected as the best eluent for the next experiment because this condition led to the complete elution of SAs from SPE column, good separation of seven SAs following their HPLC, and highest electrochemical signals.

3.1.2. Optimization of the Sample Loading Flow Rate. The sample loading flow rate will influence on the retention of SAs on the SPE column. The sample loading flow rate was therefore studied in the range of 0.48, 0.54, 0.60, and 0.66 mL min^{-1} . From the results as shown in Figure 3, it can be observed that the peak current decreased at sample loading flow rate higher than 0.60 mL min^{-1} . This effect is caused from the short interaction time between analyte and sorbent in SPE column. The higher retention efficiency can be got at the lower sample loading flow rate; however, the total analysis time is also increased. Therefore, the sample loading flow rate of 0.60 mL min^{-1} was selected as an optimal value to compromise between the interaction time and the total analysis time. Moreover, the changing of sample loading flow rate did not affect on the resolution of the seven SAs.

3.1.3. Optimization of the Elution Time Zone. After SAs were eluted from the SPE column, the eluate would be kept in

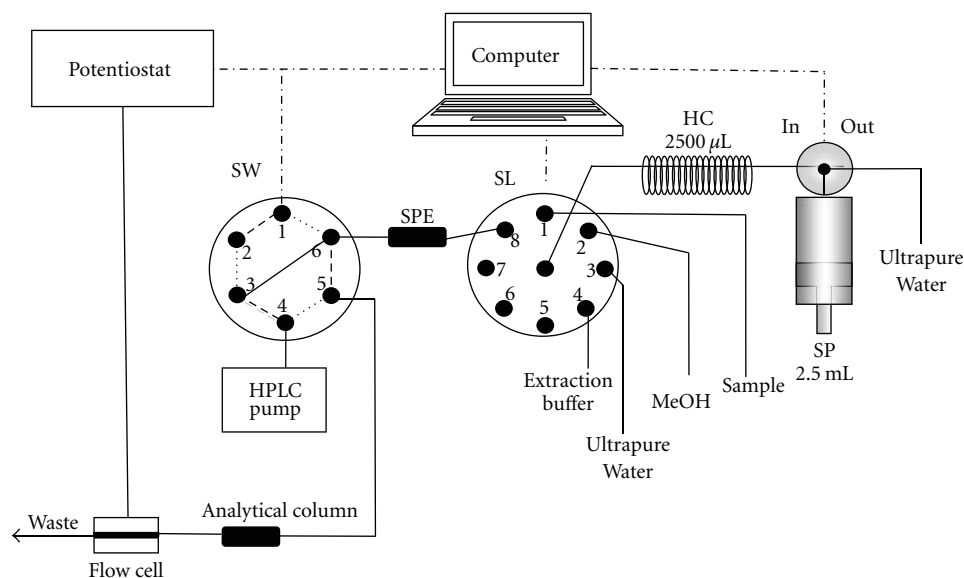


FIGURE 1: The manifold diagram of online SPE-HPLC system. SP: syringe pump; SL: selection valve; SW: switching valve (loading position in dot line and injection position in dashed line); HC: holding coil; L: sample loop; SPE: solid-phase extraction.

TABLE 1: The SIA operating sequence for sulfonamides analysis.

Step	Syringe pump Action	Position SL	Position SW	Volume (mL)	Flow rate (mL min ⁻¹)
(1) Column condition	(a) Aspirate	4		1	3
	(b) Dispense	8		1	0.6
(2) Sample loading	(a) Aspirate	1		1	3
	(b) Dispense	8		1	0.6
(3) Washing	(a) Aspirate	3		1	3
	(b) Dispense	8	Loading	1	0.6
(4) Elution	(a) Aspirate	2		0.24	3
	(b) Dispense	8		0.24	0.6
(5) Column cleaning	(a) Aspirate	2		5	3
	(b) Dispense	8		5	0.6
	(c) Aspirate	3		2.5	3
	(d) Dispense	8		2.5	0.6
(6) Injection	HPLC pump	—	Injection	—	1.5

the sample loop ($34 \mu\text{L}$) whereas the switching valve was set at loading position. Then, this solution was transferred to the analytical column via the left position of injection. According to the different distribution of SAs in eluted zone, the eluate zone with the highest SAs concentration is preferably injected in the HPLC system in order to obtain maximum sensitivity. To deliver the most concentrated zone of eluate into the sample loop, optimization was needed. From the manifold diagram (Figure 1), it was found that the eluent (100% methanol), at least $200 \mu\text{L}$, was used to completely fill eluent in SPE column and SIA line between port 6 of the switching valve and port 8 of the selection valve. In this online SIA-HPLC system, the elution time zone was varied from 20–24 s, 25–29 s to 30–34 s at constant eluting flow rate of 0.60 mL min^{-1} ($10 \mu\text{L s}^{-1}$) using syringe pump. The movement of the eluate zone was then passed to the analytical column and monitored by EC system, respectively. Results

showed that the peak current for the seven SAs decreased when elution time increased as shown in Figure 4. The maximum signal was obtained at approximately 20–24 s from the start of the elution step. This indicated that the concentration of SAs in eluate zone was related to the elution time zone from the start to the stop of elution step. Hence, the elution time zone of 20–24 s was regarded as optimum for the delivery of the eluate zone into sample loop and then analytical HPLC system.

3.2. Analytical Performances. The methodology was validated with respect to linearity, accuracy, precision, and sensitivity in order to evaluate the reliability of results provided by methodology. Under the optimal condition, the calibration curves were established by measuring the peak areas of seven compounds of various concentrations with three injections of each concentration of standard SAs. The studied

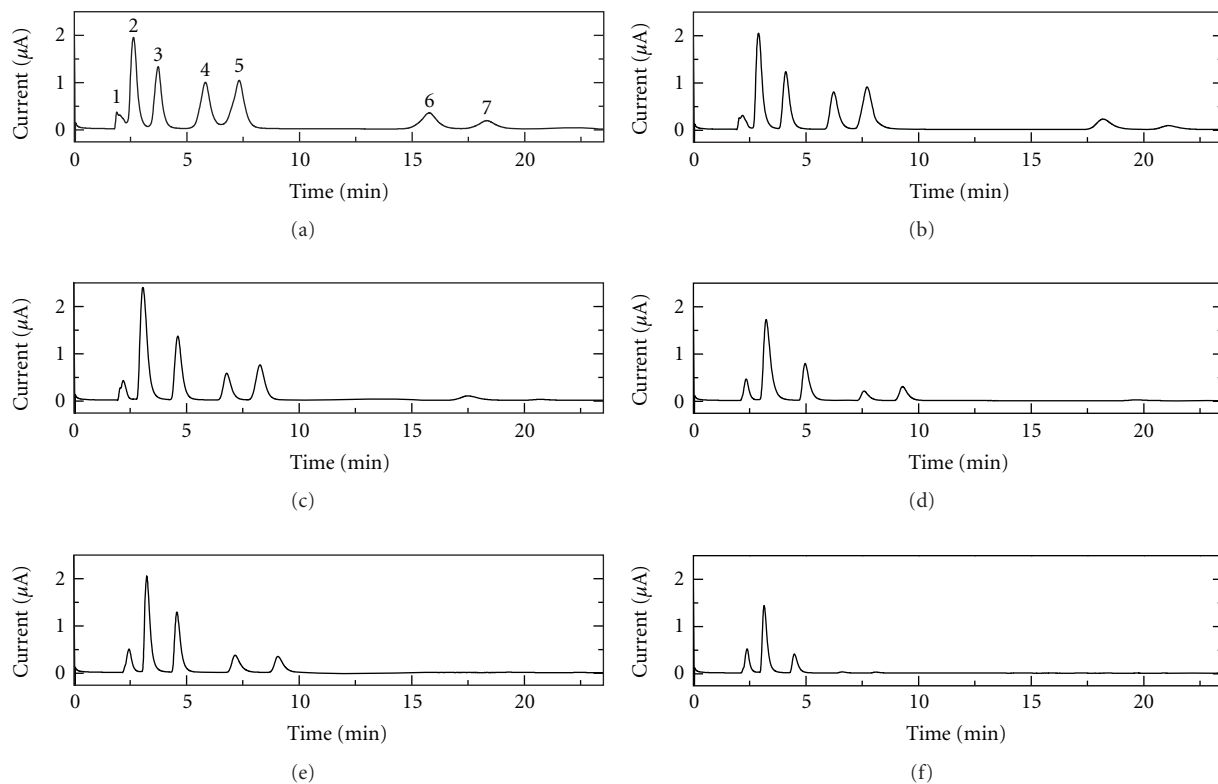


FIGURE 2: HPLC chromatograms of SAs ($10 \mu\text{g mL}^{-1}$) at different ratio of methanol and mobile phase (a) 100% methanol, (b) 90% methanol and 10% mobile phase, (c) 80% methanol and 20% mobile phase, (d) 70% methanol and 30% mobile phase, (e) 60% methanol and 40% mobile phase, and (f) 50% methanol and 50% mobile phase. HPLC pump flow rate was set at 1.0 mL min^{-1} .

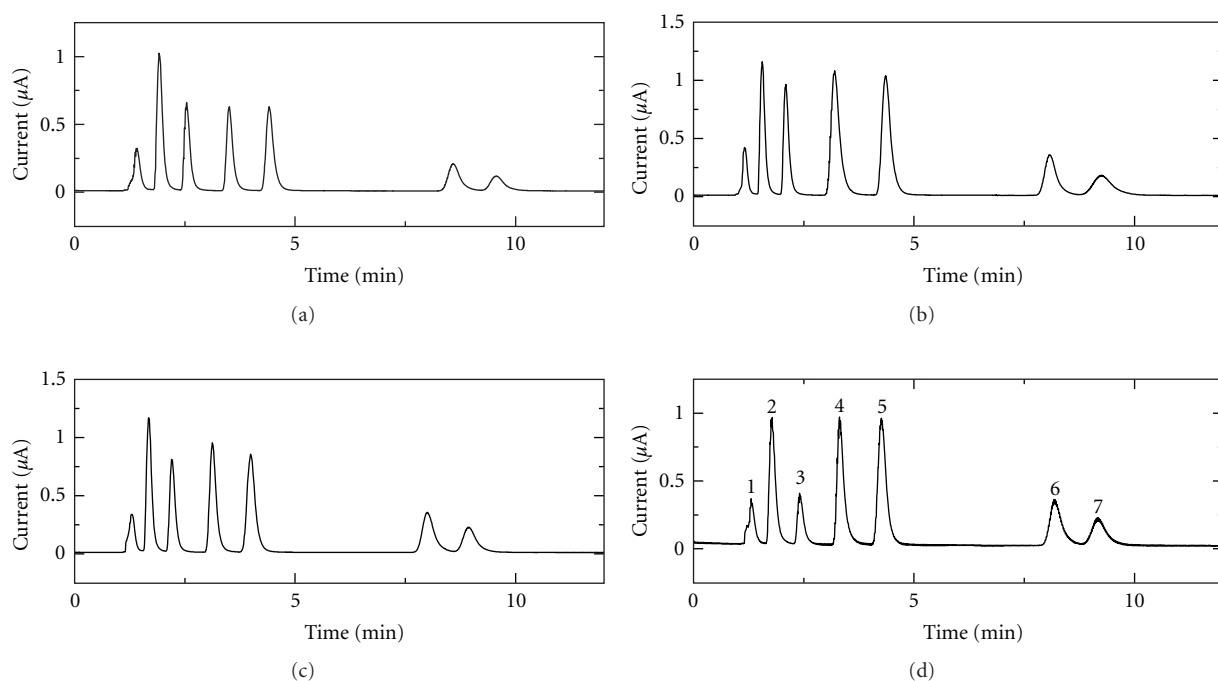


FIGURE 3: HPLC chromatograms of seven SAs ($10 \mu\text{g mL}^{-1}$) at different sample loading flow rates (a) 0.66, (b) 0.60, (c) 0.54, (d) 0.48 mL min^{-1} . HPLC pump flow rate was set at 1.5 mL min^{-1} . (1) SG, (2) SDZ, (3) SMZ, (4) SMM, (5) SMX, (6) SDM, and (7) SQ. Other conditions are the same as in Figure 2.

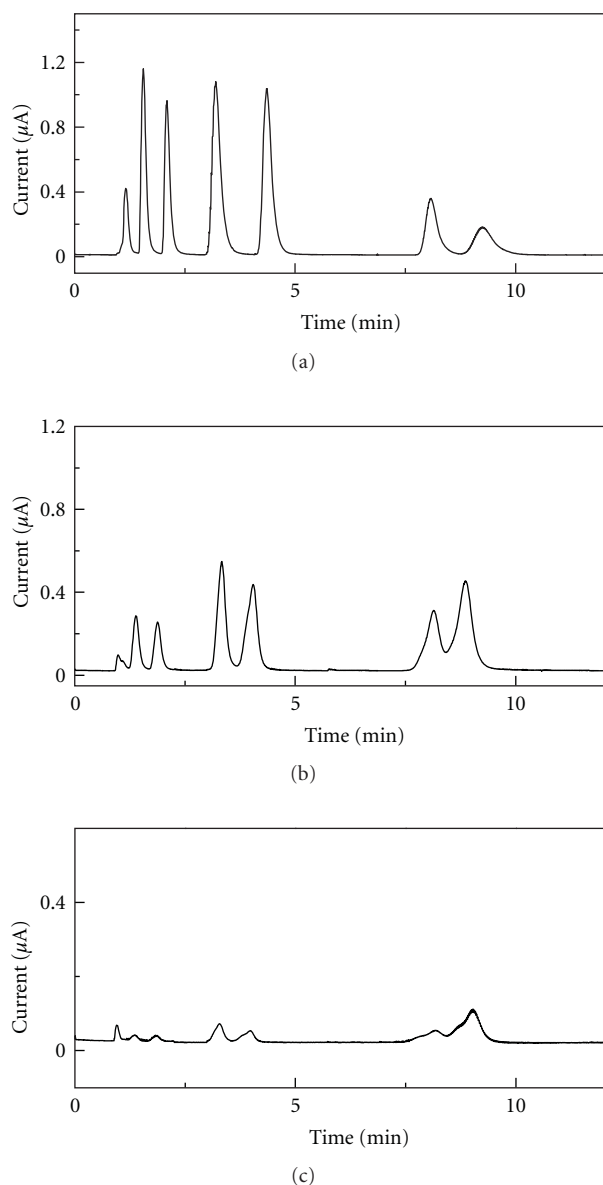


FIGURE 4: HPLC chromatograms of SAs ($10 \mu\text{g mL}^{-1}$) at different elution time zone (a) 20–24 s, (b) 25–29 s, (c) 30–34 s. Other conditions are the same as in Figure 2.

concentrations were in the range of $0.05\text{--}10.0 \mu\text{g mL}^{-1}$. The calibration curves were found to be linear in the concentration range $0.01\text{--}8.0 \mu\text{g mL}^{-1}$ for SG, SDZ, SMZ, SMM, and SMX and $0.1\text{--}8.0 \mu\text{g mL}^{-1}$ for SDM and SQ. The correlation coefficients generally exceeded 0.994. The limits of detection (LOD) and limits of quantitation (LOQ) were calculated from $3S_{\text{bl}}/S$ and $10S_{\text{bl}}/S$, where S_{bl} is the standard deviation of the blank measurement ($n = 10$) and S is the sensitivity of the method or the slope of the linearity. The data are summarized in Table 2.

3.3. Application to Shrimp Samples. To demonstrate the utilization of the proposed method, online SPE-HPLC-EC was applied for the determination of SG, SDZ, SMZ, SMM, SMX,

SDM, and SQ in shrimp samples that were sampled from the local supermarkets by standard addition. Typically, the important problem for shrimp analysis is large lipid content in shrimp. Prior to loading sample into online system, the Na_2EDTA -MacIlvaine's buffer solution (pH 4) was used to extract SAs from shrimp. This method can be used to determine SMZ, SMM, SMX, SDM, and SQ, but SG and SDZ peaks overlapped with interfering compound. This may concern the very large protein and lipid content in shrimp that could not be precipitated by high-speed centrifugation and cleanup with SPE.

The accuracy of the present method was expressed as a parameter of percentage recovery. The recovery was calculated at three concentration levels of 2, 4, and $6 \mu\text{g g}^{-1}$ by measurement of responses from spiked blank shrimp. These concentrations of SAs were chosen to demonstrate the accuracy at overall SAs level: the low, medium, and high levels. The average recoveries of five SAs (SMZ, SMM, SMX, SDM, and SQ) in shrimp were obtained in the range of 84–107% as shown in Table 3. The precision of the method was characterized by parameter of repeatability. The relative standard deviation was calculated for three consecutive measurements of the repeated injections of solution containing the complete set of standard compounds. Three spiked concentrations (2, 4, and $6 \mu\text{g g}^{-1}$) of SAs were studied to evaluate the repeatability of the proposed method. Intraday and interday precision were determined by injection of the spiked blank shrimp in the same day ($n = 3$), and, similarly, these methods were analyzed three times at different day ($n = 3$); results are shown in Table 3. The relative standard deviations of all concentrations of SAs were less than 6.5% for intraday and 13% for interday, respectively. The results indicated that this method provided the acceptable accuracy and precision for the SAs determination in shrimp.

To validate the developed method, the results from the developed method were compared to those obtained by HPLC-MS from Laboratory Center for Food and Agricultural Products Company Limited (Table 4). It can be seen that no significant difference was found at the 95% confidence level of the paired t -test method. Thus, the analyzed values of SAs in shrimp can be acceptable and reliable.

4. Conclusion

Fully automated sample preparation, separation, and determination of SAs in shrimp were developed using an online SPE coupled with SIA prior to HPLC electrochemical detection. This work is the extension of our previous efforts on the determination of sulfonamides with a diamond electrode using chromatography in “real-world” contaminated samples. Particular attention was focused on the online sample preparation. Automated online coupling of SPE to SIA-HPLC electrochemical detection has not been previously proposed to determine sulfonamides; therefore, for the first time, we have employed the present system for the automatic sample preparation and determination of SAs in real samples. Method exhibits similar sensitivity as our previous work. Anyhow, the developed method can reduce sample

TABLE 2: Linearity, limit of detection (LOD), and limit of quantitation (LOQ) of the online SPE-HPLC-EC method ($n = 3$).

Analytes	Linearity ($\mu\text{g mL}^{-1}$)	Slope (peak area units/ $\mu\text{g mL}^{-1}$)	Intercept (μA)	R^2	LOD (ng mL^{-1})	LOQ (ng mL^{-1})
SG	0.01–8	0.5277	0.1085	0.9943	11.2	33.6
SDZ	0.01–8	7.6757	0.0403	0.9982	1.2	4.0
SMZ	0.01–8	6.5834	0.0769	0.9990	1.3	4.2
SMM	0.01–8	5.2178	0.3764	0.9965	1.5	5.0
SMZ	0.01–8	2.4536	0.0679	0.9994	2.9	9.8
SDM	0.1–8	2.3970	0.2668	0.9957	3.1	10.3
SQ	0.1–8	0.8786	0.0419	0.9997	7.4	24.6

TABLE 3: Intra- and Interday precision and recoveries of the proposed method.

Analyte	Spiked level ($\mu\text{g g}^{-1}$)	Intraday		Interday	
		Mean of recovery (%) \pm SD*	RSD (%)	Mean of recovery (%) \pm SD*	RSD (%)
SMZ	2	87.8 \pm 5.5	6.2	84.6 \pm 8.7	10.3
	4	86.3 \pm 2.7	3.1	96.5 \pm 9.9	10.3
	6	97.6 \pm 2.2	2.3	99.8 \pm 2.3	2.3
SMM	2	100.3 \pm 6.5	6.5	94.5 \pm 5.2	5.5
	4	85.2 \pm 3.7	4.3	92.5 \pm 6.4	6.9
	6	104.6 \pm 3.4	3.2	102.8 \pm 1.5	1.4
SMX	2	106.5 \pm 5.3	4.9	103.5 \pm 5.6	5.4
	4	94.0 \pm 1.9	2.0	95.0 \pm 1.3	1.3
	6	95.6 \pm 1.9	2.0	100.9 \pm 4.9	4.9
SDM	2	102.1 \pm 3.0	3.0	101.2 \pm 9.7	9.6
	4	93.0 \pm 3.9	4.2	90.6 \pm 2.8	3.1
	6	101.0 \pm 5.6	5.5	103.1 \pm 1.8	1.8
SQ	2	105.6 \pm 1.3	1.2	96.9 \pm 12.6	13.0
	4	91.2 \pm 1.2	1.3	96.2 \pm 5.6	5.8
	6	102.5 \pm 1.1	1.0	100.9 \pm 1.3	1.3

* SD: standard deviation ($n = 3$).

TABLE 4: Determination of SAs levels in shrimp samples by the traditional HPLC-MS method and the developed online SPE-HPLC-EC method.

Spiked level ($\mu\text{g g}^{-1}$)	Analytes	Online SPE-HPLC-EC method (conc. \pm SD*, $\mu\text{g g}^{-1}$)	HPLC-MS (conc. \pm SD*, $\mu\text{g g}^{-1}$)
2	SMZ	1.76 \pm 0.11	1.77 \pm 0.10
	SMM	2.01 \pm 0.13	1.82 \pm 0.11
	SMX	2.13 \pm 0.11	2.04 \pm 0.11
	SDM	2.04 \pm 0.06	1.70 \pm 0.09
	SQ	2.11 \pm 0.03	1.49 \pm 0.09
4	SMZ	3.45 \pm 0.11	4.39 \pm 0.14
	SMM	3.41 \pm 0.15	4.44 \pm 0.14
	SMX	3.76 \pm 0.08	4.57 \pm 0.16
	SDM	3.72 \pm 0.16	4.34 \pm 0.14
	SQ	3.65 \pm 0.05	4.34 \pm 0.14
6	SMZ	5.85 \pm 0.13	6.56 \pm 0.18
	SMM	6.28 \pm 0.21	6.30 \pm 0.18
	SMX	5.74 \pm 0.12	6.61 \pm 0.18
	SDM	6.06 \pm 0.34	6.02 \pm 0.17
	SQ	6.15 \pm 0.07	5.79 \pm 0.15

* SD: standard deviation ($n = 3$).

preparation time, reagent consumption, and labor intensive while the enable effective cleanup of sample can be obtained. Additionally, method also permits the simultaneous determination of seven SAs with good recoveries, precision, and detection limits. Overall, the present method is promising for the automation of online sample preparation before HPLC analysis. Therefore, the proposed method could be recommended as alternative method for the routine analysis of residual SAs in shrimp.

Acknowledgments

This work was supported by the 90th Anniversary of Chulalongkorn University Fund, Innovation for the Improvement of Food Safety and Food Quality for New World Economy Project. This work is also supported by the Thai Government Stimulus Package 2 (TKK2555), under the Project for Establishment of Comprehensive Center for Innovative Food, Health Products and Agriculture (PERFECTA), University Project of CHE and the Ratchadaphisaksomphot Endowment Fund (Project code AM1009I).

References

- [1] T. A. Gehring, B. Griffin, R. Williams, C. Geiseker, L. G. Rushing, and P. H. Siitonen, "Multiresidue determination of sulfonamides in edible catfish, shrimp and salmon tissues by high-performance liquid chromatography with postcolumn derivatization and fluorescence detection," *Journal of Chromatography B*, vol. 840, no. 2, pp. 132–138, 2006.
- [2] G. Z. Fang, J. X. He, and S. Wang, "Multiwalled carbon nanotubes as sorbent for on-line coupling of solid-phase extraction to high-performance liquid chromatography for simultaneous determination of 10 sulfonamides in eggs and pork," *Journal of Chromatography A*, vol. 1127, no. 1-2, pp. 12–17, 2006.
- [3] F. J. Lara, A. M. García-Campaña, C. Neusüss, and F. Alés-Barrero, "Determination of sulfonamide residues in water samples by in-line solid-phase extraction-capillary electrophoresis," *Journal of Chromatography A*, vol. 1216, no. 15, pp. 3372–3379, 2009.
- [4] K. E. Maudens, G. F. Zhang, and W. E. Lambert, "Quantitative analysis of twelve sulfonamides in honey after acidic hydrolysis by high-performance liquid chromatography with post-column derivatization and fluorescence detection," *Journal of Chromatography A*, vol. 1047, no. 1, pp. 85–92, 2004.
- [5] Commission of the European Community, "The rules governing medical products in the European Community IV," 1991, Brussels, Belgium.
- [6] T. You, X. Yang, and E. Wang, "Determination of sulfadiazine and sulfamethoxazole by capillary electrophoresis with end-column electrochemical detection," *Analyst*, vol. 123, no. 11, pp. 2357–2360, 1998.
- [7] M. R. S. Fuh and S. Y. Chu, "Quantitative determination of sulfonamide in meat by solid-phase extraction and capillary electrophoresis," *Analytica Chimica Acta*, vol. 499, no. 1-2, pp. 215–221, 2003.
- [8] X. Wang, K. Li, D. Shi et al., "Development of an immunochromatographic lateral-flow test strip for rapid detection of sulfonamides in eggs and chicken muscles," *Journal of Agricultural and Food Chemistry*, vol. 55, no. 6, pp. 2072–2078, 2007.
- [9] C. Cháfer-Pericás, Á. Maquieira, R. Puchades, J. Miralles, and A. Moreno, "Fast screening immunoassay of sulfonamides in commercial fish samples," *Analytical and Bioanalytical Chemistry*, vol. 396, no. 2, pp. 911–921, 2010.
- [10] N. Furusawa, "Rapid high-performance liquid chromatographic determining technique of sulfamonomethoxine, sulfadimethoxine, and sulfaquinoxaline in eggs without use of organic solvents," *Analytica Chimica Acta*, vol. 481, no. 2, pp. 255–259, 2003.
- [11] R. H. M. M. Granja, A. M. M. Niño, F. Rabone, and A. G. Salerno, "A reliable high-performance liquid chromatography with ultraviolet detection for the determination of sulfonamides in honey," *Analytica Chimica Acta*, vol. 613, no. 1, pp. 116–119, 2008.
- [12] M. Gratacós-Cubarsí, M. Castellari, A. Valero, and J. A. García-Regueiro, "A simplified LC-DAD method with an RP-C12 column for routine monitoring of three sulfonamides in edible calf and pig tissue," *Analytical and Bioanalytical Chemistry*, vol. 385, no. 7, pp. 1218–1224, 2006.
- [13] J. He, S. Wang, G. Fang, H. Zhu, and Y. Zhang, "Molecularly imprinted polymer online solid-phase extraction coupled with high-performance liquid chromatography-UV for the determination of three sulfonamides in pork and chicken," *Journal of Agricultural and Food Chemistry*, vol. 56, no. 9, pp. 2919–2925, 2008.
- [14] J. E. Roybal, A. P. Pfenning, S. B. Turnipseed, and S. A. Gonzales, "Application of size-exclusion chromatography to the analysis of shrimp for sulfonamide residues," *Analytica Chimica Acta*, vol. 483, no. 1-2, pp. 147–152, 2003.
- [15] Y. Wen, M. Zhang, Q. Zhao, and Y. Q. Feng, "Monitoring of five sulfonamide antibacterial residues in milk by in-tube solid-phase microextraction coupled to high-performance liquid chromatography," *Journal of Agricultural and Food Chemistry*, vol. 53, no. 22, pp. 8468–8473, 2005.
- [16] H. Niu, Y. Cai, Y. Shi et al., "Evaluation of carbon nanotubes as a solid-phase extraction adsorbent for the extraction of cephalosporins antibiotics, sulfonamides and phenolic compounds from aqueous solution," *Analytica Chimica Acta*, vol. 594, no. 1, pp. 81–92, 2007.
- [17] B. Roudaut and M. Garnier, "Sulphonamide residues in eggs following drug administration via the drinking water," *Food Additives and Contaminants*, vol. 19, no. 4, pp. 373–378, 2002.
- [18] H. Chang, J. Hu, M. Asami, and S. Kunikane, "Simultaneous analysis of 16 sulfonamide and trimethoprim antibiotics in environmental waters by liquid chromatography-electrospray tandem mass spectrometry," *Journal of Chromatography A*, vol. 1190, no. 1-2, pp. 390–393, 2008.
- [19] E. L. McClure and C. S. Wong, "Solid phase microextraction of macrolide, trimethoprim, and sulfonamide antibiotics in wastewaters," *Journal of Chromatography A*, vol. 1169, no. 1-2, pp. 53–62, 2007.
- [20] R. Sheridan, B. Policastro, S. Thomas, and D. Rice, "Analysis and occurrence of 14 sulfonamide antibacterials and chloramphenicol in honey by solid-phase extraction followed by LC/MS/MS analysis," *Journal of Agricultural and Food Chemistry*, vol. 56, no. 10, pp. 3509–3516, 2008.
- [21] U. Koesukwiwat, S. Jayanta, and N. Leepipatpiboon, "Solid-phase extraction for multiresidue determination of sulfonamides, tetracyclines, and pyrimethamine in Bovine's milk," *Journal of Chromatography A*, vol. 1149, no. 1, pp. 102–111, 2007.
- [22] M. S. Díaz-Cruz, M. J. García-Galán, and D. Barceló, "Highly sensitive simultaneous determination of sulfonamide antibiotics and one metabolite in environmental waters by liquid

- chromatography-quadrupole linear ion trap-mass spectrometry," *Journal of Chromatography A*, vol. 1193, no. 1-2, pp. 50–59, 2008.
- [23] H. Li, P. J. Kijak, S. B. Turnipseed, and W. Cui, "Analysis of veterinary drug residues in shrimp: a multi-class method by liquid chromatography-quadrupole ion trap mass spectrometry," *Journal of Chromatography B*, vol. 836, no. 1-2, pp. 22–38, 2006.
- [24] Z. Ye, H. S. Weinberg, and M. T. Meyer, "Trace analysis of trimethoprim and sulfonamide, macrolide, quinolone, and tetracycline antibiotics in chlorinated drinking water using liquid chromatography electrospray tandem mass spectrometry," *Analytical Chemistry*, vol. 79, no. 3, pp. 1135–1144, 2007.
- [25] K. J. Choi, S. G. Kim, C. W. Kim, and S. H. Kim, "Determination of antibiotic compounds in water by on-line SPE-LC/MSD," *Chemosphere*, vol. 66, no. 6, pp. 977–984, 2007.
- [26] A. Preechaworapun, S. Chuanuwatanakul, Y. Einaga, K. Grudpan, S. Motomizu, and O. Chailapakul, "Electroanalysis of sulfonamides by flow injection system/high-performance liquid chromatography coupled with amperometric detection using boron-doped diamond electrode," *Talanta*, vol. 68, no. 5, pp. 1726–1731, 2006.
- [27] K. Kishida and N. Furusawa, "Matrix solid-phase dispersion extraction and high-performance liquid chromatographic determination of residual sulfonamides in chicken," *Journal of Chromatography A*, vol. 937, no. 1-2, pp. 49–55, 2001.
- [28] H. Sangjarusvichai, W. Dungchai, W. Siangproh, and O. Chailapakul, "Rapid separation and highly sensitive detection methodology for sulfonamides in shrimp using a monolithic column coupled with BDD amperometric detection," *Talanta*, vol. 79, no. 4, pp. 1036–1041, 2009.
- [29] M. J. García-Galán, M. S. Díaz-Cruz, and D. Barceló, "Determination of 19 sulfonamides in environmental water samples by automated on-line solid-phase extraction-liquid chromatography-tandem mass spectrometry (SPE-LC-MS/MS)," *Talanta*, vol. 81, no. 1-2, pp. 355–366, 2010.
- [30] A. V. Pereira and Q. B. Cass, "High-performance liquid chromatography method for the simultaneous determination of sulfamethoxazole and trimethoprim in bovine milk using an on-line clean-up column," *Journal of Chromatography B*, vol. 826, no. 1-2, pp. 139–146, 2005.
- [31] R. V. Oliveira, A. C. De Pietro, and Q. B. Cass, "Quantification of cephalexin as residue levels in bovine milk by high-performance liquid chromatography with on-line sample cleanup," *Talanta*, vol. 71, no. 3, pp. 1233–1238, 2007.
- [32] L. Oliferova, M. Statkus, G. Tsyin, and Y. Zolotov, "On-line solid-phase extraction and high performance liquid chromatography determination of polycyclic aromatic hydrocarbons in water using polytetrafluoroethylene capillary," *Talanta*, vol. 72, no. 4, pp. 1386–1391, 2007.
- [33] E. Yamamoto, S. Takakuwa, T. Kato, and N. Asakawa, "Sensitive determination of aspirin and its metabolites in plasma by LC-UV using on-line solid-phase extraction with methylcellulose-immobilized anion-exchange restricted access media," *Journal of Chromatography B*, vol. 846, no. 1-2, pp. 132–138, 2007.
- [34] L. Tasso and T. D. Costa, "High performance liquid chromatography for quantification of gatifloxacin in rat plasma following automated on-line solid phase extraction," *Journal of Pharmaceutical and Biomedical Analysis*, vol. 44, no. 1, pp. 205–210, 2007.
- [35] F. Gosetti, U. Chiuminatto, D. Zampieri, E. Mazzucco, E. Marengo, and M. C. Gennaro, "A new on-line solid phase extraction high performance liquid chromatography tandem mass spectrometry method to study the sun light photodegradation of mono-chloroanilines in river water," *Journal of Chromatography A*, vol. 1217, no. 20, pp. 3427–3434, 2010.
- [36] G. Z. Fang, J. X. He, and S. Wang, "Multiwalled carbon nanotubes as sorbent for on-line coupling of solid-phase extraction to high-performance liquid chromatography for simultaneous determination of 10 sulfonamides in eggs and pork," *Journal of Chromatography A*, vol. 1127, no. 1-2, pp. 12–17, 2006.
- [37] R. Fernandez-Torres, M. O. Consentino, M. A. B. Lopez, and M. C. Mochon, "Simultaneous determination of 11 antibiotics and their main metabolites from four different groups by reversed-phase high-performance liquid chromatography-diode array-fluorescence (HPLC-DAD-FLD) in human urine samples," *Talanta*, vol. 81, no. 3, pp. 871–880, 2010.
- [38] T. N. Rao, B. V. Sarada, D. A. Tryk, and A. Fujishima, "Electroanalytical study of sulfa drugs at diamond electrodes and their determination by HPLC with amperometric detection," *Journal of Electroanalytical Chemistry*, vol. 491, no. 1-2, pp. 175–181, 2000.

Review Article

A Brief Review on Environmental Application of Boron Doped Diamond Electrodes as a New Way for Electrochemical Incineration of Synthetic Dyes

J. M. Peralta-Hernández,¹ M. Méndez-Tovar,¹ R. Guerra-Sánchez,¹
C. A. Martínez-Huitle,² and J. L. Nava³

¹Departamento de Investigación Ambiental, Centro de Innovación Aplicada en Tecnologías Competitivas, Omega 201, Fraccionamiento Industrial Delta, 37545 León, Guanajuato, Mexico

²Departamento de Química, Centro de Ciências Exatas e da Terra, Universidade Federal do Rio Grande do Norte, Lagoa Nova, 59078-970 Natal, RN, Brazil

³Departamento de Ingeniería Geomática e Hidráulica, Universidad de Guanajuato, Avenida Juárez 77, 36000, Guanajuato, Mexico

Correspondence should be addressed to J. M. Peralta-Hernández, jperalta@ciatec.mx

Received 29 April 2011; Revised 23 June 2011; Accepted 24 June 2011

Academic Editor: Yasuaki Einaga

Copyright © 2012 J. M. Peralta-Hernández et al. This is an open access article distributed under the Creative Commons Attribution License, which permits unrestricted use, distribution, and reproduction in any medium, provided the original work is properly cited.

The present study was stimulated by an authoritative review on decontamination of wastewaters containing synthetic organic dyes by electrochemical methods published in Martínez-Huitle and Brillas (2009). As reviewed by the authors, there have been significant efforts on investigating the decontamination of wastewaters containing synthetic dyes by electrochemical methods, and currently, more studies are being published. A high number of electrodes have been tested in this method, including boron doped diamond (BDD) anodes. In this context, many papers have demonstrated that the use of a BDD thin film in electrochemical oxidation provides total mineralization with high current efficiency of different organics in real wastewaters. And this synthetic material deposited on several supports has been recently applied to dyestuff treatment. Although, in the last two years, more reports have been published treating electrochemically synthetic dyes wastewaters using BDD, there are few reports on the use of electrooxidation processes to degrade real textile effluents. The aim of this paper is to summarize and discuss the most important and recent results available in the literature about the application of BDD electrodes for removing azo dyes in synthetic and real wastewaters.

1. Introduction

Azo dyes are used in a wide variety of industrial processes such as, food production, cosmetics, and pharmaceuticals manufacturing and paper printing. Therefore, these dyes are frequently found in industrial wastewater effluents and are a principal cause of pollution around the world [1]. The release of colored effluents into the environment is undesirable, not only for aesthetic reasons but also because many azo dyes and their degradation byproducts are toxic to aquatic life and mutagenic to humans [2]. The effluents from the textile industry are frequently characterized by high alkalinity, biological oxygen demand, chemical oxygen demand, and total dissolved solids in addition to high

dye concentrations (>1000 ppm). The synthetic origin and complex aromatic structures of dyes make them stable and difficult to biodegrade.

Dyes are classified as anionic (direct, acid, and reactive dyes), cationic (basic dyes), and nonionic (disperse dyes). The chromophores in ionic and nonionic dyes mostly consist of azo groups or anthraquinone types [3]. In this context, azo dye compounds constitute about one-half of the dyes that are used in the textile industry [4]. The chemical structure of this group of compounds is characterized by the presence of the azo group ($-N=N-$) chromophore, associated with aromatic systems and other groups, such as hydroxyls ($-OH$) and sulfonic groups ($-SO_3H$) [5]. The azo group can be present one or more times in the molecular structure of the

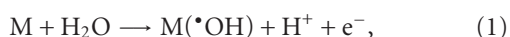
compound. Additionally, another environmental problem with respect to the use of azo dyes in the textile industry is the consumption of large amounts of potable water. In many countries where potable water is scarce, this high consumption of water has become undesirable, and wastewater recycling has been recommended in order to decrease the water requirements [2].

To avoid azo dye accumulation in aquatic systems, different methods are being developed to carry out the elimination of these compounds from wastewater. These include biological and physicochemical methods such as flocculation combined with flotation, membrane filtration, coagulation, ion exchange, irradiation, and katox treatment method [3, 6]. However, these methods are generally unsuccessful in color removal, expensive, and less adaptable to a wide range of dye wastewaters.

In recent years, electrochemical technologies have caused great interest because they offer effective means to solve environmental problems related to industrial processes [7, 8] such as wastewater contamination. The highest advantage of these methods is their environmental compatibility. Their principal reagent is the electron, which is an inherently clean species whose energy can be carefully controlled by means of an applied potential, thus avoiding parallel reactions. In traditional chemistry, secondary reactions often result in subproducts which sometimes increase removal costs [8–10].

The principal electrochemical methods are the following:

- (a) *direct electrochemical oxidation*, where the organic compound degradation occurs directly over the anode through the adsorbed $\cdot\text{OH}$, or chemisorbed active oxygen in the anode surface (often called “anodic oxidation, direct oxidation or electrochemical incineration”), by means of the following general equation [10–12]:



where the pollutants are first adsorbed on the anode surface (M) and then destroyed by the anodic electron transfer reaction,

- (b) *indirect electrochemical oxidation*, where the organic compounds are treated in the bulk solution by means of species generated in the electrode, such as $\cdot\text{OH}$ (by means of the Fenton reaction), Cl_2 , hypochlorite, peroxodisulfate, and ozone, as the most common electrochemically generated oxidants [6, 13].

In recent decades, several electrodes have been evaluated to rank anode material in terms of high stability, high activity toward organic oxidation, and cost. The types of electrodes tested included graphite, platinum, IrO_2 , RuO_2 , SnO_2 , PbO_2 , Ti/Pt , Ti/Pt-Ir , Ti/PbO_2 , $\text{Ti/PdO-Co}_3\text{O}_4$, and $\text{Ti/RhO}_x\text{-TiO}_2$, Ti coated with oxides of Ru/Ir/Ta [14, 15], BDD thin films, and others.

In this context, several groups have proposed the use of BDD as anode material. The electrochemical behavior of such BDD thin films deposited on different substrates (Si, Ti, Nb, or Pt) has also been studied with the aim of

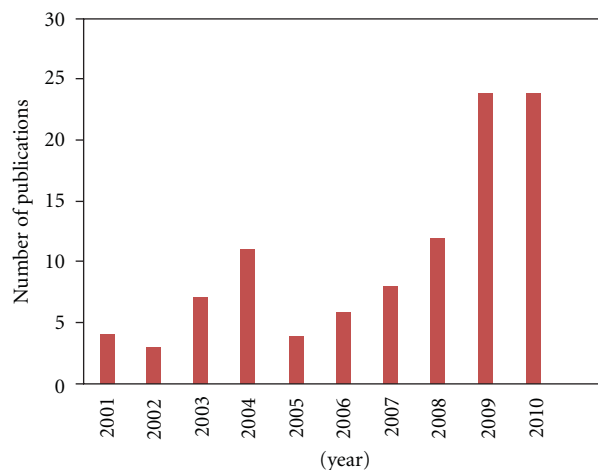


FIGURE 1: Tendency in the number of publications versus year for wastewater treatment using BDD anodes.

developing applications for the electrochemical oxidation of different organic compounds for wastewater treatment, as reviewed by Martinez-Huitle and Brillas [16], there have been significant efforts made in investigating the decontamination of wastewaters containing synthetic dyes by electrochemical methods, using especially BDD anodes. Although more reports involving electrochemical treatment of synthetic dye wastewater have been published in the last two years, there are few reports on the use of this process to degrade real textile effluents. The aim of this paper is to present the recent progress in electrochemical treatment by anodic oxidation of synthetic dye wastewaters and real effluents using BDD electrodes, focusing on the elimination of azo dyes.

2. BDD Anodes for Wastewater Treatment Applications

In the last 10 years, the boron-doped diamond anode has been an attractive material for numerous environmental applications. Figure 1 illustrates the tendency to use this kind of electrode for the degradation of different refractory or priority pollutants in wastewater. Although relatively few articles were published between 2001 and 2005, the amount of articles involving BDD electrodes increased considerably between 2006 and 2010 (by means of Scopus).

2.1. Hydroxyl Radical (BDD($\cdot\text{OH}$)) Generation. Considerable $\cdot\text{OH}$ amounts may be electrogenerated on BDD anodes. These radicals, due to their weak interaction with the BDD film, present high reactivity towards organics (Rx 2–4); these processes have been efficiently used in wastewater treatment [10, 17] as follows:



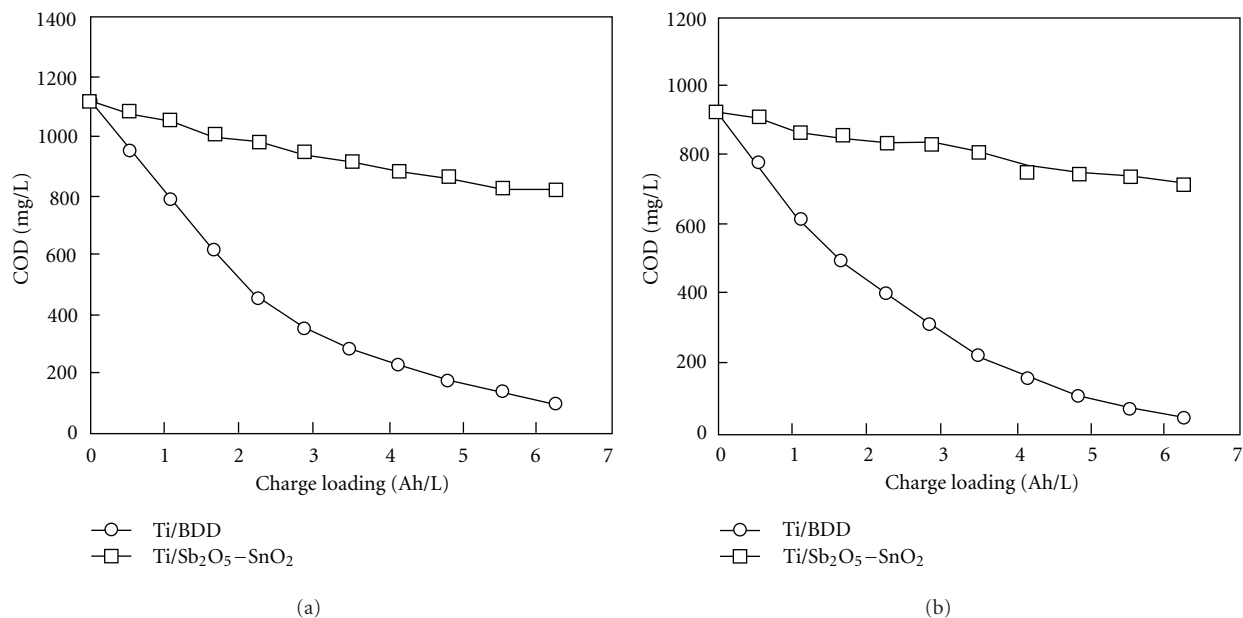
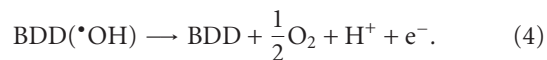


FIGURE 2: COD decay for comparison of Ti/BDD versus Ti/Sb₂O₅-SnO₂ for incineration (a) Orange II and (b) Reactive red HE-3B at current density 200 A/cm² and $T = 30^{\circ}\text{C}$ [19].

According to the literature, reaction (3) is in competition with the side reaction of free $\cdot\text{OH}$ discharge to O_2 without any participation of BDD surface, following the next reaction:



However, many authors have reported that during incineration process of BDD anodes at high potentials, a great number of organic pollutants are completely mineralized by the reaction with electrogenerated free $\cdot\text{OH}$ species [18]. In this context, some papers have reported (period from 2003 to 2010) the incineration of a great number of synthetic azo dyes by reaction with electrogenerated $\cdot\text{OH}$ species over BDD anode.

2.2. Electrochemical Treatment of Synthetic Dye Solutions.

The study of the treatment of synthetic dyes using BDD anodes started in 2003, when Chen and coworkers [19] tested the mineralization of Orange II and Reactive red HE-3B. They proposed the comparison of physicochemical and electrochemical properties for two different electrodes, Ti/BDD and Ti/Sb₂O₅-SnO₂, using a thermostatic reactor controlled with a water bath. They evaluated the efficiency for mineralization of 750 mg/L of Orange II and 1500 mg/L of Reactive red HE-3B in each electrode, measuring the chemical oxygen demand (COD) decay using a supporting electrolyte, 2 g/L of Na₂SO₄. It was observed that the rate of COD decay considerably increased when the Ti/BDD electrode was used. Figure 2(a) shows that the decay of Orange II at the Ti/BDD anode was 91%, and this removal efficiency was higher than that obtained at the Ti/Sb₂O₅-SnO₂ anode (26%). In the case of Reactive red HE-3B, Figure 2(b) shows that the performance of COD abatement was very similar.

The Ti/BDD electrode achieved about 95% removal, whereas Ti/Sb₂O₅-SnO₂ only 22%. In light of these results, Ti/BDD anodes are much more efficient than those composed of Ti/Sb₂O₅-SnO₂.

After that, this application motivated other researchers to investigate the use of BDD anodes for removing dyes from synthetic wastewaters, such as the degradation of the azo dye Eriochrome Black T (EBT) by Cañizares et al. [20]. Figure 3 shows the abatement of 100 mg/dm³ of EBT where TOC 70% and COD 90%, after that 20 Ah dm⁻³ was applied. When 1813 mg/dm³ has been treated, both TOC and COD decreased considerably after 80 Ah dm⁻³, achieving closely 100% of degradation. During the BDD oxidation of EBT molecules, a great variety of intermediates (changes in the COD) was observed, attaining complete incineration at the final electrolysis time. Sakalis et al. [21] compared the use of two different anodes: platinumized titanium (Pt/Ti) and Niobium/synthetic diamond (Nb/D), in order to improve the electrochemical incineration of synthetic samples containing four reactive azo dyes. Different experimental conditions were evaluated, such as supporting electrolyte, concentration of electrolyte, effect of applied potential, pH, and temperature. Under the optimum electrochemical conditions, complete elimination of dyes was achieved, using both electrodes Pt/Ti and Nb/D. However, the use of Nb/D anodes showed the best performances on removal efficiency for the most important parameters such as biochemical oxygen demand (BOD₅), COD, and TOC.

The influence of the anode on the electrochemical oxidation of methylene blue (MB) was evaluated by Panizza et al. [22]. Direct electrolysis using boron-doped diamond and the indirect electrolysis mediated by active chlorine electrogenerated on a TiRuO₂ oxide anode, was compared for

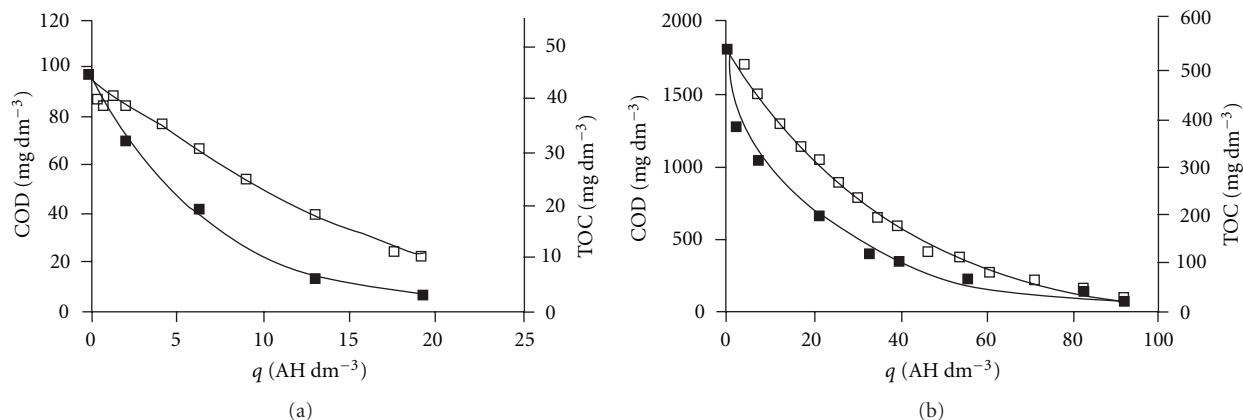


FIGURE 3: Changes in the COD (■) and in the TOC (□) with the current charge passed during electrolyses of EBT-polluted synthetic wastes. Operation conditions: current density, $300 \text{ A}\cdot\text{m}^{-2}$; $T = 25^\circ\text{C}$. Waste composition: sodium sulfate Na_2SO_4 , $5000 \text{ mg}\cdot\text{dm}^{-3}$; natural pH. COD_0 : (a) 100 and (b) $1813 \text{ mg}\cdot\text{dm}^{-3} \text{ O}_2$ [20].

removing MB. The study was carried out on COD and color removal efficiencies as a function of time, for each type of electrochemical processes. Figure 4 shows the comparison of COD abatement and color removal for both processes (direct and indirect electrolysis). As can be observed, the graph shows interesting results, because indirect electrolysis facilitates faster mineralization and decolorization of the solution. The authors attributed this behavior to the strong bleaching properties of active chlorine, and the efficiency of direct electrolysis is limited by the mass transport of pollutants to the anode surface in solutions containing low concentrations of organics.

Based on the literature results reported by Panizza and Cerisola, the ability to remove organic pollutants, like azo dyes, is more evident when diamond electrodes are used. These assertions were confirmed when the electrocatalytic properties of different materials are compared; the anodic oxidation of methyl red was studied comparing the electrocatalytic properties of Ti–Ru–Sn ternary oxide, platinum, lead dioxide, and boron-doped diamond anodes. The results of the study demonstrated a different reactivity of electrogenerated hydroxyl radicals for each electrode, limiting the removal efficiency of methyl red removal and COD abatement.

The authors speculate that on BDD, which is well known to have weak adsorption properties due to its inert surface, hydroxyl radicals are very weakly adsorbed and consequently they are very reactive toward organics oxidation. On the contrary, lead dioxide is hydrated and hydroxyl radicals are expected to be more strongly adsorbed on its surface and consequently less reactive. For these reasons, TiRuSnO₂ and Pt anodes, which are good electrocatalysts for the oxygen evolution reaction due to their low oxygen evolution overpotential, showed poor elimination efficiencies. Contrarily PbO₂ and BDD anodes, with high oxygen evolution overpotential making those poor electrocatalysts for the oxygen evolution reaction, had higher rates of COD and color removals. The same behavior was observed when Panizza and Cerisola [23] compared the electrocatalytic

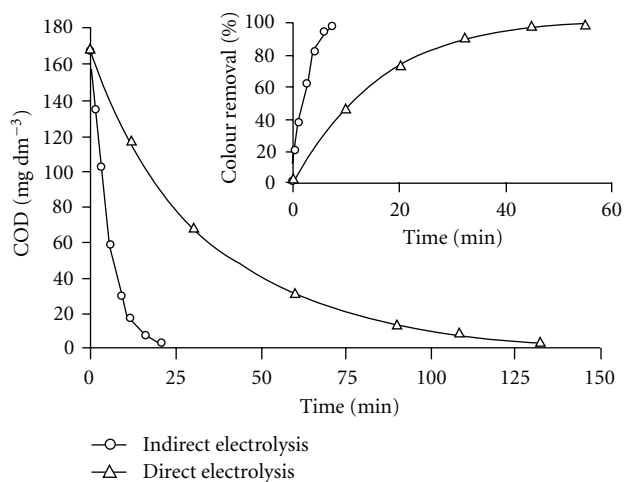


FIGURE 4: Comparison of the COD evolution and colour removal (inset) during the direct and mediated electrolysis of the methylene blue. Indirect electrolysis: Cl^- concentration = 1.2 g dm^{-3} ; $i = 60 \text{ mA cm}^{-2}$; flow rate: $180 \text{ dm}^3 \text{ h}^{-1}$; $T = 40^\circ\text{C}$. Direct electrolysis: $i = 20 \text{ mA cm}^{-2}$; flow rate: $180 \text{ dm}^3 \text{ h}^{-1}$, $T = 40^\circ\text{C}$ [22].

properties between lead dioxide (PbO₂) and BDD anodes for the electrochemical incineration of methyl red, using an electrolytic flow cell with parallel plate electrodes. Results indicated that, for all of the applied currents, the COD decreased to zero, after 8 hours of treatment using a PbO₂ anode. Whereas, the COD decreased to zero with all applied currents after 4 h of treatment using a BDD anode, resulting in complete mineralization of the dye by means of the electrogenerated $\cdot\text{OH}$ radicals. The influence of the current density on the COD and CE during the electrochemical oxidation of methyl red at the BDD anode is shown in Figure 5.

The influence of different operational conditions (such as initial dye concentration, Na_2SO_4 concentration as supporting electrolyte, current density, flow rate, and initial pH) during azo dye degradation has received great attention by

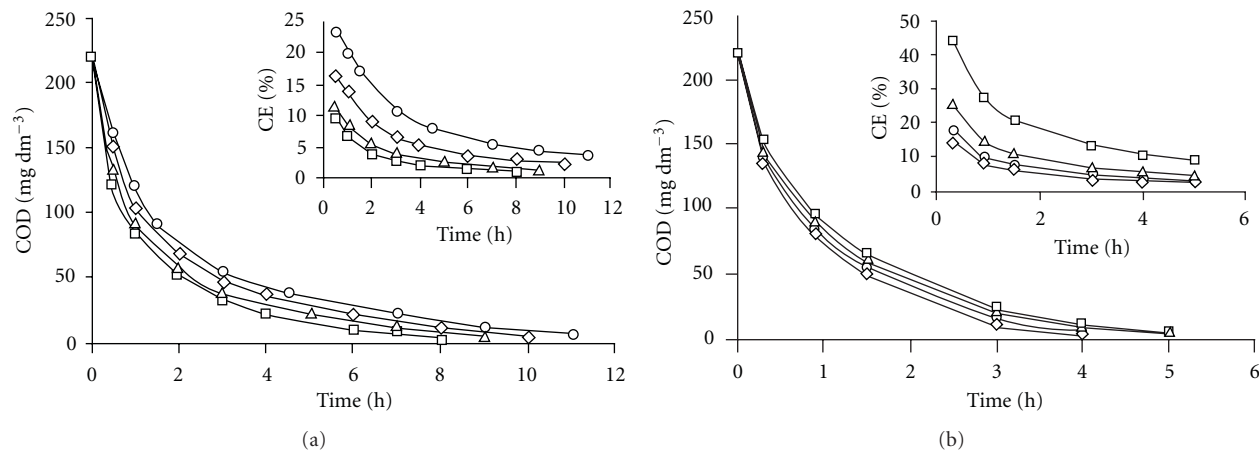


FIGURE 5: Influence of the applied current on the evolution of the COD and current efficiency (inset) as a function of time during the electrolysis of methyl red on the (a) PbO_2 and (b) BDD anodes, respectively. Flow rate = $180 \text{ dm}^3 \text{ h}^{-1}$; pH = 3; applied current = (○) 0.5, (◇) 1, (△) 1.5, (□) 2 A [23].

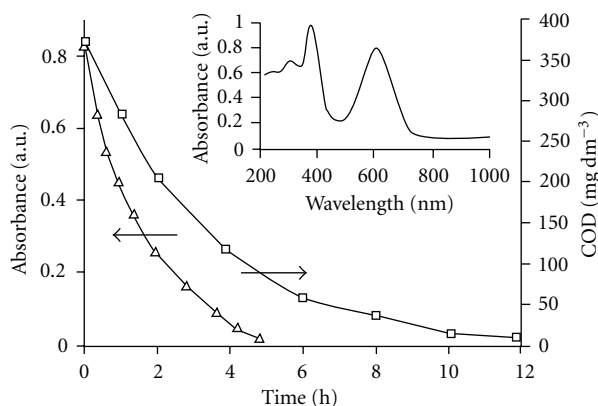


FIGURE 6: Trend of absorbance band at 594 nm (△) and COD (□) during the anodic oxidation solution of acid blue 22 at a 0.3 mM concentration on the BDD electrode at $i = 20 \text{ mA cm}^{-2}$, flow rate = $300 \text{ dm}^3 \text{ h}^{-1}$, $T = 25^\circ\text{C}$. UV spectrum of the acid blue 22 is shown in the inset [24].

several authors (Panizza and Cerisola [24], Bensalah et al. [25], Kopal et al. [26], Carvalho et al. [27], and Saez et al. [28]).

For example, Panizza and Cerisola evaluated the electrochemical oxidation of synthetic wastewater containing acid blue 22 dye using a BDD electrode [24]. This study investigated the influence of certain variables such as current density, dye concentration flow rate, and temperature on the abatement of COD and color. Figure 6 presents an interesting comparison between color removal and COD abatement for 0.3 mM of acid blue 22 by applying 20 mA cm^{-2} current density. Complete solution decoloration after about 4 h of electrolysis was achieved, while 7 h was necessary to complete COD elimination, indicating that acid blue 22 was oxidized initially to colorless intermediates and then to carbon dioxide. Figure 7 compares energy consumption (kWh m^{-3}) for COD and color removal of acid blue 22 at a 0.3 mM concentration during electrochemical oxidation

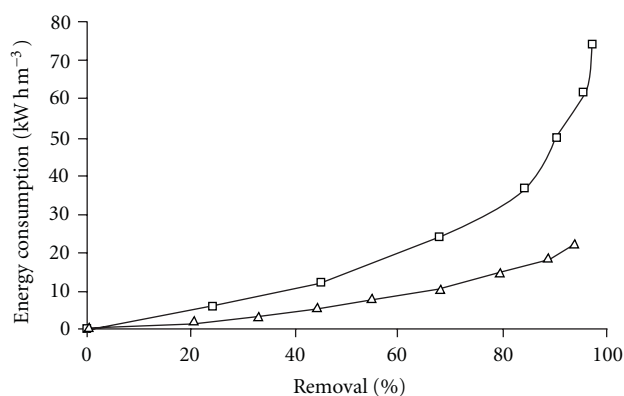


FIGURE 7: Evolution of the specific energy consumption against the removal of COD (□) and color (△) during the anodic oxidation of acid blue 22. Acid blue 22 concentration: 0.3 mmol; current density 20 mA cm^{-2} ; flow rate $300 \text{ dm}^3 \text{ h}^{-1}$; $T = 25^\circ\text{C}$ [24].

using a BDD anode. The result is very important from an economic point of view because the energy consumption increased almost linearly with color removal but had a sharp increase with COD removal. On the other hand, Bensalah et al. [25] investigated the treatment of synthetic wastewaters containing Alphazurine A (AZA) by anodic oxidation using BDD anodes, monitoring COD and color removal under different operational conditions. According to the experimental results obtained in this work, the electrochemical oxidation process is suitable for removing COD and decolorizing wastewaters containing AZA dye, due to the production of hydroxyl radicals and other oxidants on the anode surface. Whereas, the energy requirements for removing 95% of initial COD during galvanostatic electrolyses of AZA synthetic solutions depends mainly on the applied current density, temperature and agitation rate; it passes from 57 kWh at 30 mA cm^{-2} to 138 kWh at 90 mA cm^{-2} per kg COD removed; from 102 kWh at 25°C to 89 kWh at

TABLE 1: Percentage of color removal and COD decay obtained for the electrochemical oxidation treatment with BDD anodes of selected synthetic dyes solutions under optimized conditions at ambient temperature or 25°C.

Dye	Solution	Electrolytic system	$j^a/\text{mA cm}^{-2}$	Color removal/%	COD decay/%	Ref.
<i>Si/BDD</i> 3,4,5-trihydroxybenzoic acid)	1000 mg dm ⁻³ in HClO ₄	A one-compartment electrolytic flow cell with parallel plate electrodes.	20–60	100	100	[43]
Remazol Brilliant Blue	50 mg dm ⁻³ RBBR, 0.05 M Na ₂ SO ₄ and 0.01 M NaCl with an initial pH of 5.8 and conductivity 8.5 ms cm ⁻¹	Batch mode in a 100-mL single-compartment cell with a boron-doped diamond anode of geometric area 5 cm ² .	20–40	99	98	[29]
Acid Yellow 1	1000 mg dm ⁻³ in 0.5 M HClO ₄	A one-compartment electrolytic flow cell with a BDD of 50 cm ² .	0.5–1.5 ^b	100	100	[30]
O-toluidine	1 × 10 ⁻⁴ –1 × 10 ⁻³ M ^c	A two compartments thermostated cell under different current densities, temperatures, and COT concentration.	20–100	— ^d	70–90	[33]
Basic Blue 3	1000 mg dm ⁻³	thermojacketed BTT reactor was used with BDD Raschig's rings.	0.5–0.875	99	87	[34]
Crystal violet	33–600 mg dm ⁻³	In a 150 mL, one-compartment electrolytic cell with a BDD of 4 cm ² .	2.5–15	100	80–95	[44]
Acid Black 210	500 mg dm ⁻³	In an one-compartment filter-press flow cell.	25–100	100	80–97	[35]
<i>Nb/BDD</i> Orange II	50 mg dm ⁻³ in the presence of different supporting electrolytes, 200 mL in each run	Batch recirculation reactorcontaining one-compartment cell equipped with boron-doped diamond anode and Pt cathode.	1.29–7.68	80–98	80–95	[31]
<i>Ti/BDD</i> Alizarin Red S	0.278 mM ^c	Electrolytic cell with a single compartment without diaphragm with Ti/BDD (1.5 cm ²) anode and Ti/RuO ₂ –TiO ₂ –SnO ₂ (9 cm ²) cathode.	40	100	100	[41]

^a Applied current density, ^b potential, ^c molar concentration, ^d not determined.

60°C and from 141 kWh at 100 rpm to 29 kWh at 400 rpm. Based on results reported by several authors (Panizza and Cerisola [24], Bensalah et al. [25], Koparal et al. [26], Carvalho et al. [27] and Saez et al. [28]), the electrochemical technique is economically suitable for waste pre-treatment to remove color. However, although complete COD removal is technically feasible, its high-energy cost makes this technique unsuitable for a refining process.

Nevertheless, the application of electrochemical technologies for decolorization and degradation of azo dyes has been investigated and reported by several scientific groups, as recently reviewed in details by Martínez-Huitle and Brillas [16]. However, since this review was published, new results have been published and more statements have been established. The destruction by EO with BDD of dyes such as Remazol Brilliant Blue Reactive [29], Acid Yellow 1 [30], Orange II [31], Reactive Orange 16

[32], O-Toluidine [33], Basic Blue 3 [34], acid black 210 [35], Trichloroethylene [36], methylene blue [37], 3-amino-4-hydroxy-5-nitrobenzenesulfonic acid (A1), 5-amino-2-methoxybenzenesulfonic acid (A2), 2,4-dihydroxyaniline hydrochloride (A3) and benzene-1,4-diamine (A4) [38], methyl orange [39], Reactive brilliant red X-3B [40], Alizarin Red S [41], Aniline (AN) and Ortonilic (OA), Metanilic (MA) and Sulfanilic (SA) acids [42], Gallic acid [43] and Crystal Violet [44], has been studied. In these studies the influence of pH, dye content, temperature, supporting electrolyte, cathode material, current density, and anode potential was investigated for optimizing degradation conditions. Many of these authors also estimated the color removal, current efficiency and decay in COD and/or TOC, which mainly depended on the above parameters. Data are collected in Table 1, and the most relevant papers will be discussed and commented below.

The electrochemical oxidation of aniline (AN) and orfanilic (OA), metanilic (MA), and sulfanilic (SA) acids (dyes precursors) was studied by Santos et al. [42] using a BDD electrode. Model solutions of the different amines with concentrations of 200 mg L^{-1} in $0.035 \text{ M Na}_2\text{SO}_4$ were oxidized using a batch cell by applying 200 and 300 A m^{-2} . Results showed a good elimination of the persistent pollutants, with COD and TOC removals always higher: AN: 91% and 90%, OA: 75% and 82%, MA: 88% and 87%, and SA: 85% and 79% (for 200 and 300 A m^{-2} , resp.). The combustion efficiencies, calculated for the first hour of the runs, for the 300 A m^{-2} assays, were the following: AN: 0.93, OA: 0.28, MA: 0.82, and SA: 0.83, indicating the efficiency of the BDD anode for removing these dyes precursors. For all the amines studied, after 6 h degradation, only oxalic and maleic acids were identified by HPLC. Additionally, analysis performed to the content of different forms of nitrogen in solution led to the conclusion that, in the case of the sulfonated amines, the amino group was mainly eliminated in the form of ammonia, since AMN content increases while TKN decreases.

Another study evaluated the electrochemical oxidation of several dyes precursors [38], such as 3-amino-4-hydroxy-5-nitrobenzenesulfonic acid (A1), 5-amino-2-methoxybenzenesulfonic acid (A2), 2,4-dihydroxyaniline hydrochloride (A3), and benzene-1,4-diamine (A4), using a BDD electrode as the anode. Tests were run at room temperature with model solutions of the different amines at concentrations of 200 ppm, using $0.035 \text{ M Na}_2\text{SO}_4$ aqueous solutions as electrolytes, in a batch cell with recirculation at different current densities (200 and 300 A m^{-2}).

From the results obtained by these authors, the anodic oxidation of four dyes precursors, using a BDD anode, showed high COD and TOC removals (see Figure 8). For the assays run with the first two compounds, after 4 h, no amine was detected by HPLC. For the tests with the other two compounds, small amounts of the amines were still present at the end of the assay, and higher combustion efficiencies were observed. Apparently, a high initial amine removal rate leads to a lower degree of mineralization. Additionally, the substituent has an effect on the rate of degradation mainly due to its contribution to the molar volume, since diffusivity and, consequently, mass transfer coefficient decrease with its increase. The anodic oxidation of 2,4-dihydroxyaniline hydrochloride and benzene-1,4-diamine was the only instance where hydroquinone and maleic acid were identified as metabolites, after a 6 h run. These particular oxidations also produced higher combustion efficiencies. It seems that the early formation of oxalic acid reduces the ability to obtain mineralization. On the other hand, the formation of other intermediates, like hydroquinone, may lead to an easier complete combustion of the organic matter. Analysis performed to different forms of nitrogen content led to the conclusion that the amino group is mainly eliminated in the form of ammonia, since AN content increases while TKN decreases during the anodic oxidation.

Zhou and Särkkä [39] compared the electrochemical degradation of methyl orange on the mixed metal oxide

(MMO) and BDD electrodes. The effect of several parameters such as current density, pH, electrolyte types, and initial dye concentration were investigated in terms of decolorization. COD and TOC removals, as well as energy consumption, were estimated. The degradation on two electrodes presented different trends in operative parameters. High current density enhanced the decolorization on both electrodes, but the promotion on MMO was not as significant as that on the BDD electrode, which led to a sharp increase of specific energy consumption, as shown in Figure 9. The decolorization of MMO performed better at acidic conditions for two electrodes, but the dependence of pH on BDD was not as obvious as that on MMO electrodes.

The presence of NaCl favored the indirect oxidation of active chlorines on MMO electrodes, which greatly improved the decolorization rate. High initial concentration enhanced general current efficiency (GCE) although the COD and TOC removal efficiency was decreased. The GCE on BDD was much higher than that on MMO, indicating that it was much more efficient. The BDD electrode yielded high combustion efficiency, while on MMO is greatly improved in the presence of NaCl.

Due to the applicability of mediated oxidation using DSA or BDD anodes, other groups have focused attention on this electrochemical process, evaluating different operating conditions. For example, the electrochemical degradation of chloride-mediated and chloride-free dye wastewaters (a synthetic solution containing high concentration methylene blue (MB), with 1000 mg L^{-1}), was investigated by Wu and coworkers [37]. In chloride-free wastewater, the electrochemical degradation efficiency of dye on BDD electrode was much higher than that on DSA, with a COD removal of 100% and 26% for BDD and DSA, respectively. In chloride-mediated dye wastewater, COD removal was faster than that in chloride-free wastewater on both BDD and DSA electrodes with COD removal efficiencies higher than 95%, whereas the rate of COD removal on DSA was faster than that on BDD electrode. The investigation indicated that DSA is more suitable than BDD electrode in degradation of dye wastewaters containing chloride in terms of energy and time saving. However, for chloride-free dye wastewaters, BDD electrode is more appropriate, in regards to environmental protection, because of its ability to achieve complete mineralization. These assumptions are confirmed by the results reported in Figure 10.

As shown by several authors [16] and Wu et al. [37], the high chlorine evolution potential in Cl^- -mediated wastewater may cause difficulty in the formation of active chlorine from wastewater and decrease the rate of electrochemical degradation of organic compounds, leading to a slower electrochemical degradation process on BDD. The lower chlorine evolution potential of 1.0 V on the DSA probably makes the formation of active chlorine on DSA surface much easier, so that the oxidation rate of MB on DSA is much higher than that on BDD due to the strong oxidative property of active chlorine. As the electrolysis takes place, the concentration of chloride in electrolyte decreases gradually, and the amount of active chlorine on the electrode surface

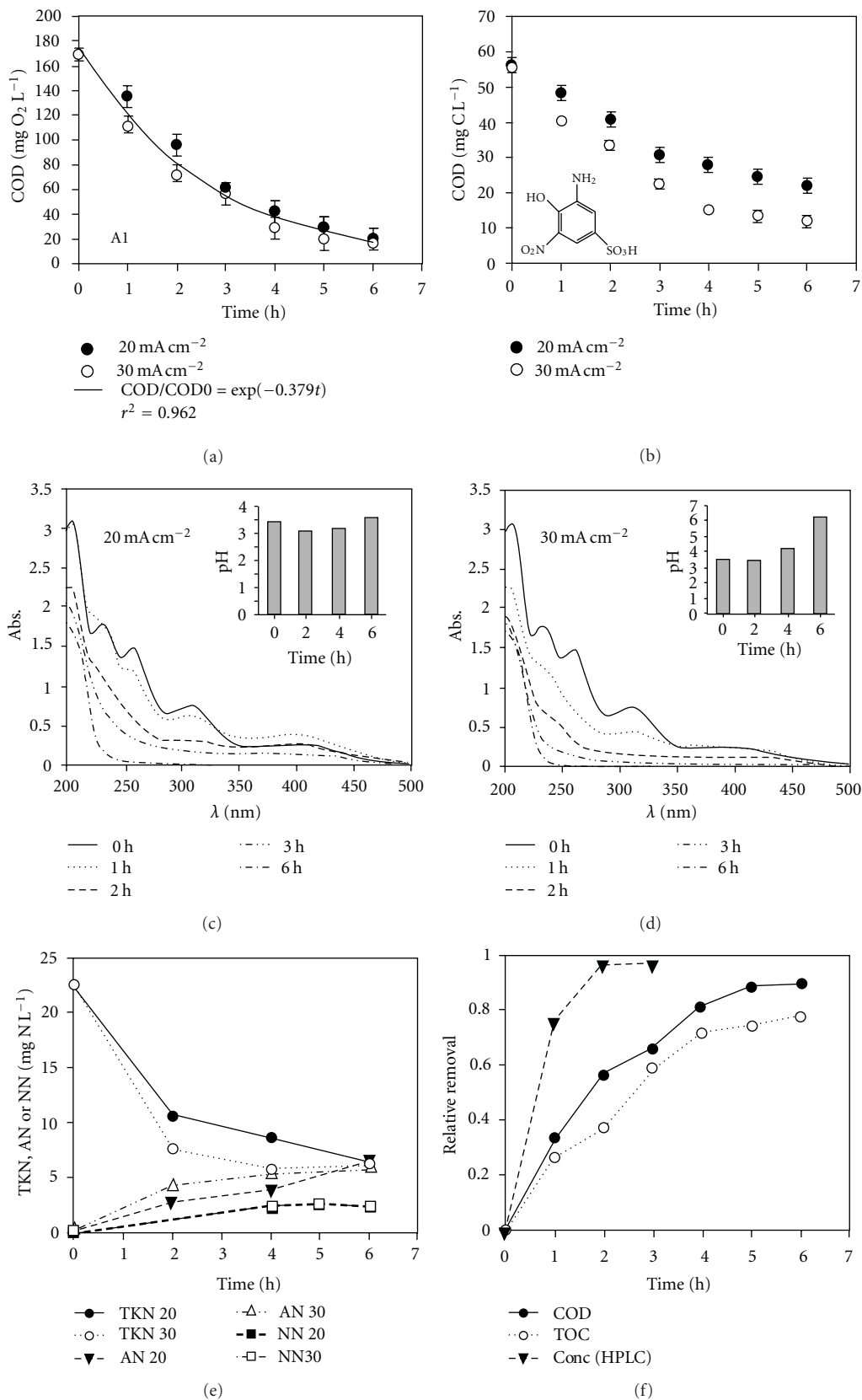


FIGURE 8: Variations of COD (a), TOC (b), absorbance and pH (c, d), TKN, AN and NN (e) and relative removals of COD, TOC and concentration (f) versus. time observed during the degradation assays of the amine A1, with an initial concentration of 200 mg L⁻¹, performed with a BDD anode (8 cm²). Cathode: stainless steel (8 cm²); current density: 20 and 30 mA cm⁻²; electrolyte 0.035 M Na₂SO₄ aqueous solution [38].

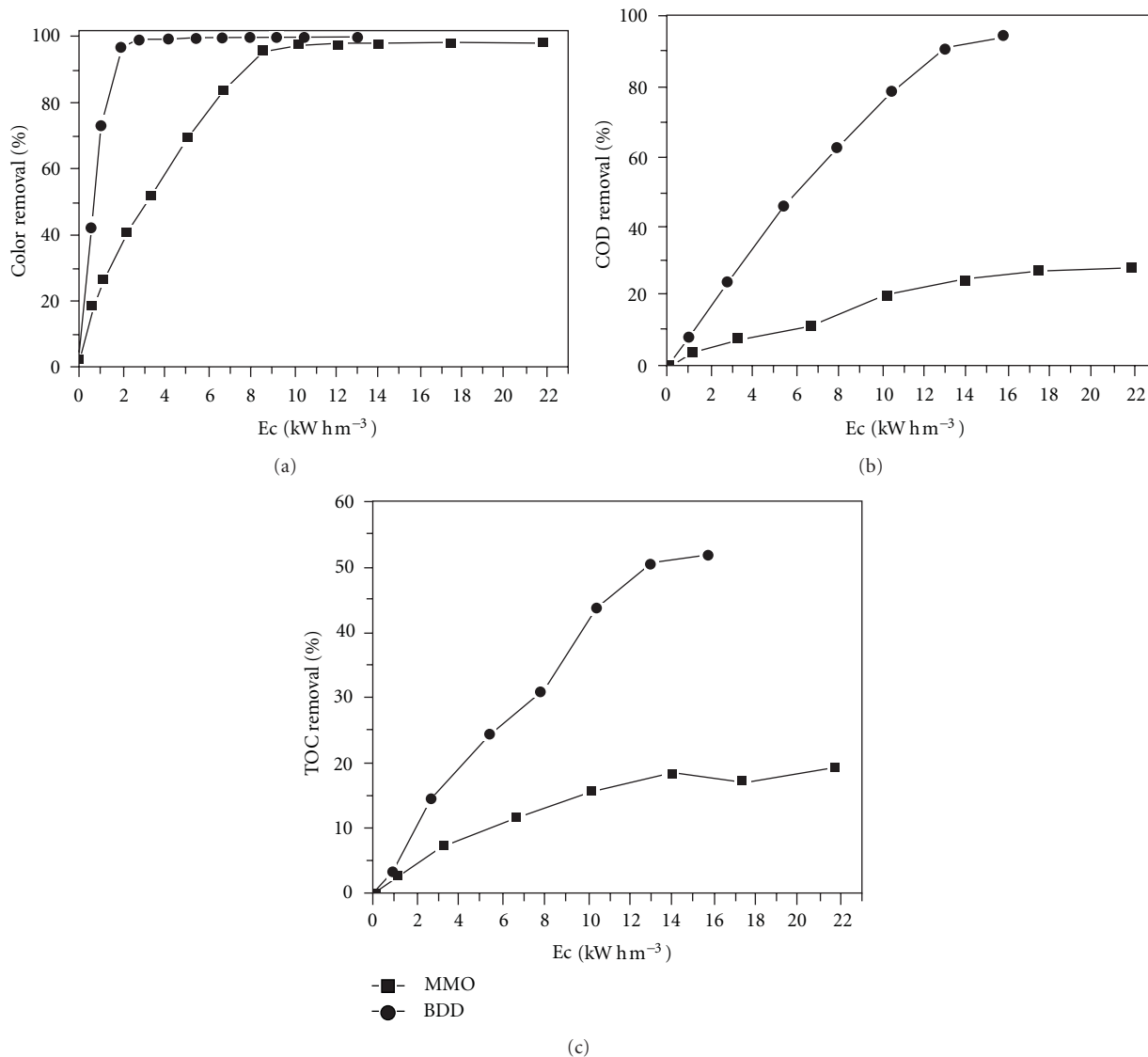


FIGURE 9: The removal of color, COD, and TOC on two electrodes. Conditions: electrolyte: Na_2SO_4 0.1 M + NaCl 0.05 M; pH 3; MO 200 mg L^{-1} ; current density: 50 mAcm^{-2} . Reprinted with permission of Separation and Purification Technology [39].

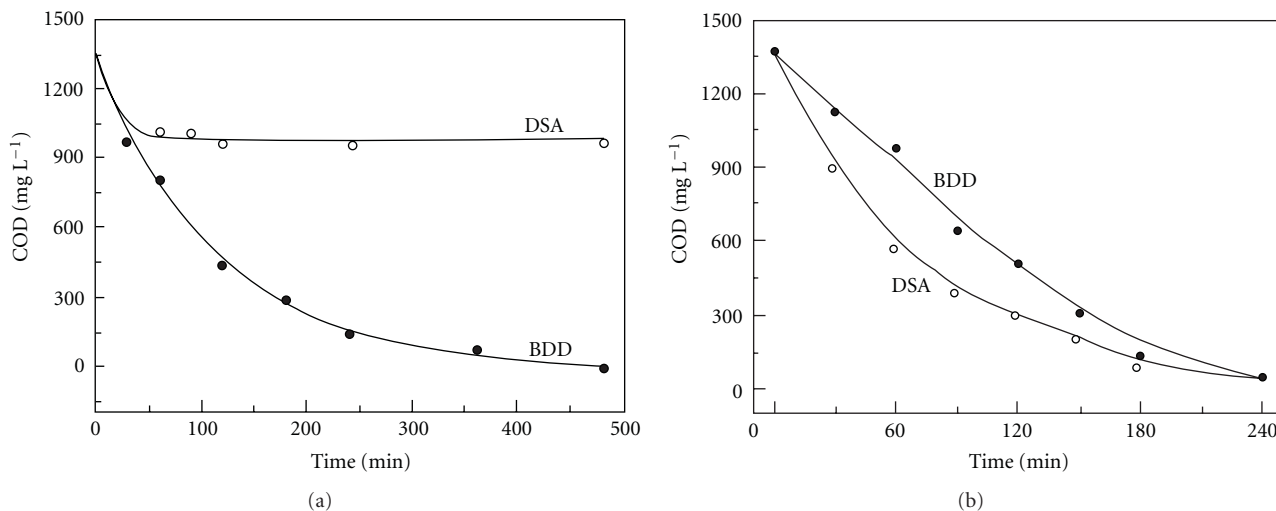


FIGURE 10: COD (a) in MB degradation in chloride-free wastewater and COD (b) in MB degradation in chloride-mediated wastewater [37].

decreases, so that the rate of electrochemical decontamination of wastewater is lowered. However, this electrochemical treatment of chloride-containing wastewater will introduce strong toxic halogen compounds and requires a second step to remove this chlorinated organic compound (e.g., by adsorption on activated carbon, coupled/integrated methods [45], or emerging technologies [16]).

Therefore, new electrochemical processes are being studied. For example, photocatalysis on nanosized TiO_2 and electrocatalysis on BDD electrode, two advanced oxidation processes (AOPs) in the field of wastewater treatment, were combined into one batch reactor by Zhang and coworkers [40]. Reactive brilliant red X-3B dye was used as a model compound to study the combinatory effect between photocatalysis and electrocatalysis. The aim of this study was to confirm that the oxidants produced on BDD anodes such as hydrogen peroxide, ozone, and peroxydisulfate could raise the quantum efficiency of photocatalytic processes. Initially, the performances of the separate processes in the elimination of X-3B were compared and different reaction systems of the same size were employed to study the performance in X-3B decolorization, listed as (1) BDD alone; (2) BDD with UV light, without TiO_2 ; (3) TiO_2 photocatalysis with UV light; (4) BDD + UV + TiO_2 ; (5) BDD + UV + TiO_2 + aeration. The air rate was set to 5.0 L/h by a small magnetic air pump.

The experimental conditions were set as follows: initial concentration of X-3B (C_0) 50 mg/L; current density 25.2 mA/cm²; pH 2.72 (adjusted with 1.0 M H_2SO_4). The time for removing color completely was studied for each reaction system, and the results were illustrated in Figures 11(a) and 11(b). It can be deduced that photocatalysis coupled with electrocatalysis in one reactor will degrade pollutants faster than either process alone. The results obtained show some interesting phenomena, commonly called synergistic effect. Both BDD electrode and TiO_2 film produces $\cdot\text{OH}$ on their surfaces, and a portion of them may react directly with X-3B. As have been well established by the literature, oxidation of pollutants at the BDD anode occur under mass transfer control mainly in a thin liquid film near the electrode surface, where the concentration of $\cdot\text{OH}$ is very high. Similar phenomenon also exists in photocatalytic systems. But the adding of salts (SO_4^{2-}) can trap part of these $\cdot\text{OH}$ to form peroxides and diffuse into the whole solution to allow full contact with X-3B. Then $\cdot\text{OH}$ are set "free" by activating these mixture of oxidants (H_2O_2 , $\text{S}_2\text{O}_8^{2-}$) with UV light, thus promotes the performance as well as the generation of more $\cdot\text{OH}$ on the surfaces of both BDD electrode and TiO_2 film. These experimental results revealed the suitability of the combination of the two oxidation processes for accelerating the removal of dye pollutants from solution.

Other scientific groups are studying the preparation of new electrocatalytic materials with similar characteristics of BDD anodes in order to decrease the cost of treatment and increase removal efficiency. In this context, interesting results have been reported by Andrade and Tasso [46] who studied the performances of the Ti-Pt/ β - PbO_2 and BDD electrodes in the electrooxidation of simulated wastewaters containing 85 mg L⁻¹ of the Reactive Orange 16 dye using

a filter-press reactor. The electrolyses were carried out at the flow rate of 7 L min⁻¹, at different current densities (10–70 mA cm⁻²), and in the absence or the presence of chloride ions (10–70 mM NaCl). In the absence of NaCl, total decolorisation of the simulated dye wastewater was attained independently of the electrode used. However, according to the results reported by the authors, the performance of the BDD electrode was better than that of the Ti-Pt/ β - PbO_2 electrode; the total decolorizations were achieved by applying only 1.0 Ah L⁻¹ and 2.0 Ah L⁻¹, respectively. In the presence of NaCl, with the electrogeneration of active chlorine, the times needed for total color removal were markedly decreased; the addition of 50 mM Cl⁻ or 35 mM Cl⁻ (for Ti-Pt/ β - PbO_2 or BDD, resp.) to the supporting electrolyte led to a 90% decrease of these times (at 50 mA cm⁻²). On the other hand, total mineralization of the dye in the presence of NaCl was attained only when using the BDD electrode (for 1.0 Ah L⁻¹); for the Ti-Pt/ β - PbO_2 electrode, a maximum mineralization of 85% was attained (for 2.0 Ah L⁻¹). For total decolorization of the simulated dye wastewater, the energy consumption per unit mass of dye oxidized was only 4.4 kWh kg⁻¹ or 1.9 kWh kg⁻¹ using the Ti-Pt/ β - PbO_2 or BDD electrode, respectively. Clearly the BDD electrode proved to be the best anode for the electrooxidative degradation of the dye, either in the presence or the absence of chloride ions. In the absence of chloride, this high performance is due to the fact that the electrogenerated hydroxyl radicals are weakly adsorbed on the BDD because of its inertness; consequently, they are very reactive towards the dye oxidation. On the Ti-Pt/ β - PbO_2 surface, the hydroxyl radicals are more strongly adsorbed, thus being less reactive. Whereas, the addition of chloride to the simulated dye wastewater had a very marked effect on the dye degradation; the time needed for total decolorization of the dye decreased by 90%. This increased performance is most probably related to the weak chlorohydroxyl adsorption strength on the BDD surface, as it is the case with the hydroxyl radical.

2.3. Electrochemical Treatment of Real Wastewaters Polluted with Dyes. Few papers have demonstrated that the use of a BDD thin film in EO provides total mineralization with high current efficiency of real textile wastewaters [16]. However, more studies have been published in the last three years.

Chatzisyseon et al. [47], using a titanium (grade II/VII) anode covered by a thin film of tantalum, platinum, and iridium alloy, attained 98% decolorization within 10–15 min, regardless of the applied current. From their best data (use of 5 A for 10 min, 8 L of effluent), one infers that only 0.38 kC L⁻¹ was used, which is much lower than the value used in our best case (5.8 kC L⁻¹); however, they added NaCl to the effluent to have a minimum concentration of 10 g L⁻¹ while we used only 1.5 g L⁻¹.

Fytianos et al. [48] compared the use of two different anodes: platinized titanium (Pt/Ti) and Nb/BDD, in order to improve the electrochemical incineration of synthetic samples containing four reactive azo dyes and real wastewater. They compare their treatment through biochemical oxygen

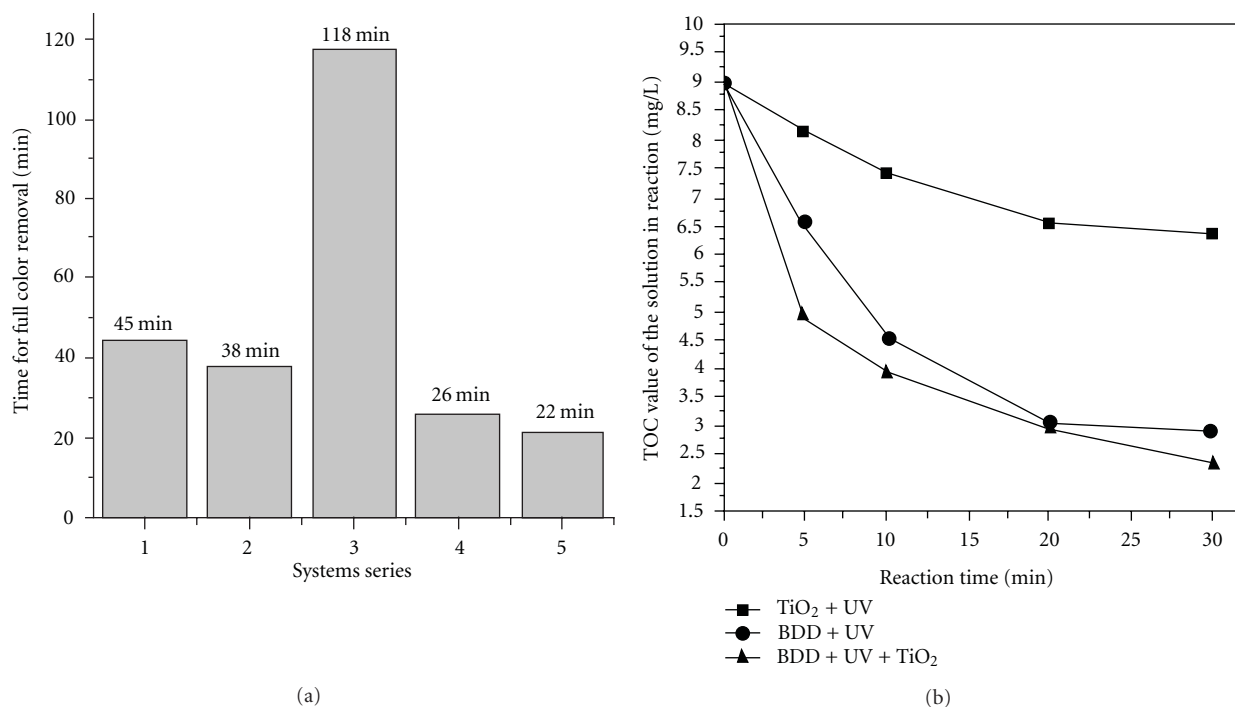


FIGURE 11: (a) Comparison on degradation performance of different reaction systems and (b) TOC decay with reference to electrolysis time for the mineralization of X-3B with three different systems (C_0 : 50 mg/L, $I_{\text{appl}} = 25.2 \text{ mA/cm}^2$, pH 2.72) [40].

TABLE 2: Initial and final values of the most important environmental parameters of electrochemically treated wastewater under optimal conditions [48].

Environmental parameter	Initial wastewater	Electrochemically treated wastewater	
		Pt/Ti	Nb/D
pH	9	8	8
% Dye removal (436 nm)	—	67.3	81.2
% Dye removal (526 nm)	—	82.4	89.1
% Dye removal (620 nm)	—	80.3	89.5
Chlorides (mg/L)	224	174	112
Hypochlorites (mg/L)	—	0.2	82.4
BOD ₅ (mg/L)	149	25	75
COD (mg/L)	150	70	10
COD/BOD ₅	1	2.8	0.13
TOC (mg/L)	164	100	78
Temperature (°C)	25	28	40.5

Time of treatment: 30 min.

demand (BOD₅), COD, TOC, energy consumption, and efficiency of the anodes. In this context, the authors evaluated

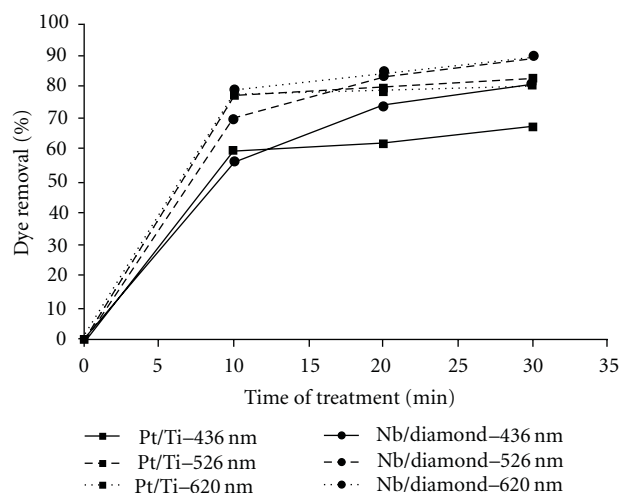


FIGURE 12: Decoloration efficiency of Nb/D and Pt/Ti, treating real wastewater. Applied potential: 18 V; time of treatment: 30 min [48].

different experimental conditions such as type and concentration of supporting electrolyte, effect of applied potential, pH, and temperature. Table 2 shows initial and final values of the most important environmental parameters of electrochemically treated wastewater under optimal conditions using both Pt/Ti and Nb/BDD electrodes. As can be seen, the use of Nb/BDD anode increased the efficiency removal for the most important parameters such as BOD₅, COD, TOC, and dye removal. An interesting result was shown in Figure 12, where the authors present the comparison of Pt/Ti and Nb/BDD electrodes, to treat real wastewater,

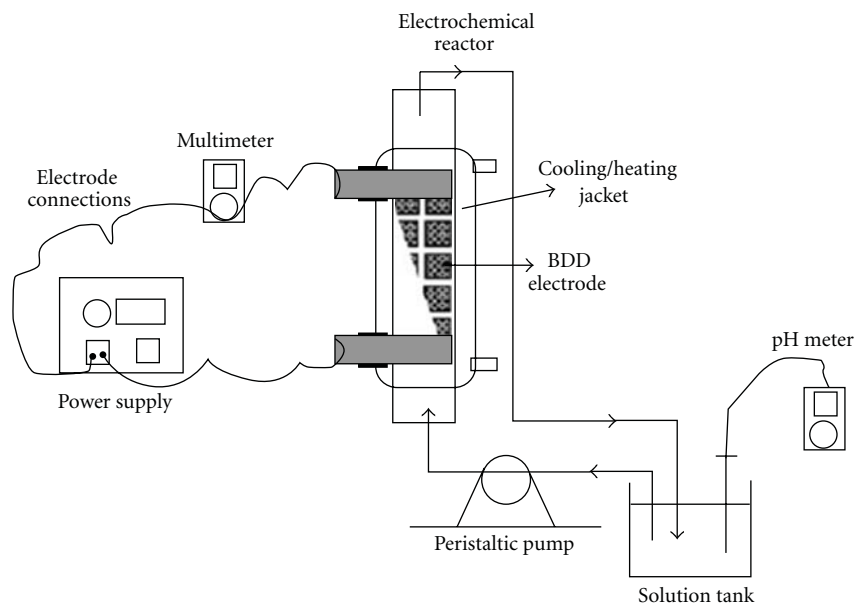


FIGURE 13: Experimental setup used in the studies for the degradation of Basic Red 29 (BR29) [26].

without any further addition of electrolytes. These results clearly indicated that after 30 min treatment, the rate of decoloration for the two anodes was very similar. However, the Nb/BDD achieved a higher decoloration removal (85–90%), resulting in practically colorless final wastewater.

Koparal et al. [26] has demonstrated that the electrochemical incineration of Basic Red 29 (BR29) treatment in a bipolar trickle tower (BTT) reactor by using Raschig's ring-shaped BDD electrodes is an originally setup to this goal. The experimental electrochemical reactor is illustrated in Figure 13. The effects of some important parameters such as initial dye concentration, Na_2SO_4 concentration as supporting electrolyte, current density, flow rate, and initial pH on the removal efficiency were studied. From the results by Koparal et al. [26], the initial COD of real effluent was 566.45 mg/L and decreased gradually to a final value of 52.38 mg/L after 8 h of treatment. A decrease in COD of nearly 91% was achieved with an energy consumption of 1.4 kWh/g COD removed. Usually, the toxicity assays for electrochemistry treatments are not performed, However, microtox bioassay tests were performed in this study to assess the textile wastewater treated in the electrochemical reactor in a given time intervals including the time zero. A toxicity result was given as relative toxicity index (RTI), Figure 14. Initial toxicity values showed that wastewater was highly toxic. According to the result, this method was found to be successful for dye and COD removal, indicating that it is also successful for toxicity reduction. As can be seen toxicity reduction was also achieved by using electrochemical oxidation, however, the toxicity was decreased to a lesser extent for textile wastewater.

Interesting research about the electrochemical oxidation of the biotic degradation products of the textile dye C.I. Acid Orange 7 (AO7) was achieved using a BDD electrode by Carvalho and collaborators [27]. They have proposed the use of real effluent obtained from anaerobic sludge

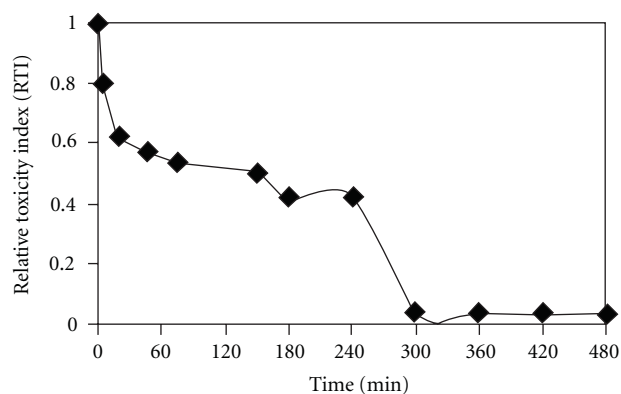


FIGURE 14: Variation of toxicity with time in the textile wastewater ($i = 1 \text{ mA/cm}^2$, $Q = 36.3 \text{ mL/min}$) [26].

blanket (UASB) reactors operating under mesophilic or thermophilic conditions. The electrolysis was studied using two supporting electrolytes: NaCl and Na_2SO_4 . The influences of some important variables such as initial metabolite concentration and current density on the electrodegradation rates of the biotic products were analyzed. Table 3 summarizes the results of the removal of COD, TOC, absorbance at 486 nm (AO7) and 250 nm (Arom) and relative current efficiency obtained after the electrochemical degradation of the effluents from the UASB reactors. Results have shown that under thermophilic conditions and 20 mA cm^{-2} of applied current density, it is possible to obtain higher removal efficiency of COD (90%) and TOC (30%) and diminished absorbance: Abs_{286} (100%) and Abs_{250} (90%). These data have demonstrated that BDD anodes could be an important tool for treating real effluents without the use of other chemical reagents or long time periods.

TABLE 3: Removals of COD and TOC, Absorbance at 468 nm (AO7) and 250 nm (Arom), and relative current efficiency obtained after the electrochemical degradation of the effluents from the UASB reactors [27].

Current density/mA cm ⁻² Electrolyte	10			20		
	N	S	C	N	S	C
<i>Mesophilic</i>						
% Removal						
COD	45	52	67	72	84	72
TOC	41	21	19	31	31	24
Abs ₄₈₆	66	77	90	89	100	100
Abs ₂₅₀	73	70	75	85	86	81
EC/EC _{N20}	0.31	0.19	0.19	1	0.57	0.52
<i>Thermophilic</i>						
% Removal						
COD	54	52	63	83	67	90
TOC	30	29	24	31	31	30
Abs ₄₈₆	72	43	100	81	81	100
Abs ₂₅₀	69	65	77	81	78	91
EC/EC _{N20}	0.32	0.24	0.20	1	0.58	0.51

N: no added electrolyte, S: sulphate, C: chloride, 10, 20: current densities of 10 and 20 mA cm⁻², EC: energy consumption, EC/EC_{N20}: relative efficiencies values are calculated with respect to the assay with no added electrolyte at 20 mA cm⁻².

On the other hand, Malpass et al. [49] report that about 90% decolorization was attained only when NaCl (5.85 g L⁻¹) was added to the real textile effluent (0.25 L), independently of the composition of the DSA anode used; from their data, one may infer that about 16 kCl L⁻¹ was used. From all these results, it becomes clear that decolorization by electrooxidation is facilitated by the addition of Cl⁻ ions to the real textile effluent. In other researches, degradation of dye chromophores is more easily attained in the presence of active chlorine. In fact, Malpass et al. [50] showed that complete real textile effluent decolorization could be attained by the direct addition of OCl⁻ ions at a concentration of ~0.50 g L⁻¹.

Most relevant applications of anodic oxidation for treating real effluents have been published [51–58]. The electrochemical treatment of acrylic fiber-manufacturing, biorefractory wastewater, simulated ground water containing MTBE and BTEX, tannery wastewater, olive pomace leachate, biologically pretreated dye wastewater, biologically pretreated coking wastewater, and ink effluents are some examples of the applicability of this technology using BDD anodes.

Diamadopoulou and coworkers [58] studied the effluent treatment from flexographic printing by precipitation/coagulation and electrochemical oxidation over BDD electrodes. Precipitation with 3 g/L of lime led to complete removal of effluent turbidity (initial value of about 410 NTU) but only about 20% decrease in chemical oxygen demand (COD) (initial value of about 1,900 mg/L). In addition, higher lime dosages (up to 15 g/L) had no

effect on separation. Preliminary electrochemical oxidation experiments in the presence of sulphuric acid as supporting electrolyte showed that treatment performance (in terms of COD removal and decrease in sample absorbance at 300 nm) increased with increasing applied current, being more efficient at shorter treatment times and lower currents with efficiency reaching 30%. Following lime precipitation, the effluent was electrochemically oxidized at alkaline conditions for 360 min yielding 64% absorbance reduction and 50% COD removal (this corresponds to 60% overall COD removal for the combined process). Finally, they attributed the slightly low electrochemical treatment performance to limestone deposition and fouling of electrodes and other electrochemical reactor components, as evidenced by the gradual drop in conductivity/current throughout the operation.

In another case, the electrochemical treatment of acrylic fiber-manufacturing wastewater (AFMW) with BDD electrode was investigated by Zhang et al. [51]. A factorial design methodology was employed to evaluate the statistically important operating variables of treatment time (1–2 h), flow rate (400–600 mL/min), current intensity (0.50–1.00 A), and initial COD load (362–723 mg/L) on the treatment efficiency. The latter was assessed in terms of COD and ammonia-nitrogen (NH₃-N) removal. The results clearly demonstrated the suitability of the BDD technology for COD removal, as well as the unique behavior in removing NH₃-N. However, they performed a comparison electrochemical treatment between DSA and BDD anodes in order to understand both behaviors. These results showed great potential of the BDD technology to be an effective option for treating AFMW, due to the efficient reduction of COD, energy consumption and treatment time in respect to the DSA anode, as shown in Figure 15. The excellent performance of the BDD technology might be attributed to the presence of free hydroxyl radicals generated on nonactive BDD electrode, as well as the chloride-free nature of AFMW.

A practical application of electrochemical oxidation in biorefractory wastewater treatment was performed by Zhu et al. [52]. In this study, the performance of a smaller BDD anode (24 cm²) system in a continuous mode of electrochemical oxidation of phenol-simulated wastewater was first investigated. The performance was described by the response surface methodology (RSM). Next, the RSM was extended to examine the scale-up feasibility of BDD anode systems with similar configurations. They demonstrated that both COD degradation efficiency and specific energy consumption could be expected at the same level even as the system was enlarged over 100 times, which implied that BDD anode system could be successfully scaled up through controlling the same retention time, current density, initial COD, and conductivity conditions. Based on this study, a larger BDD anode (2904 cm²) system was constructed, and systematic measurements were made on its performance in the electrochemical oxidation of phenol-simulated wastewater. Under optimum conditions, the larger BDD anode system easily reduced the COD of phenol simulated wastewater from 633 mg L⁻¹ to 145 mg L⁻¹ (<150 mg L⁻¹, National Discharge Standard of China) during 80 min with specific energy

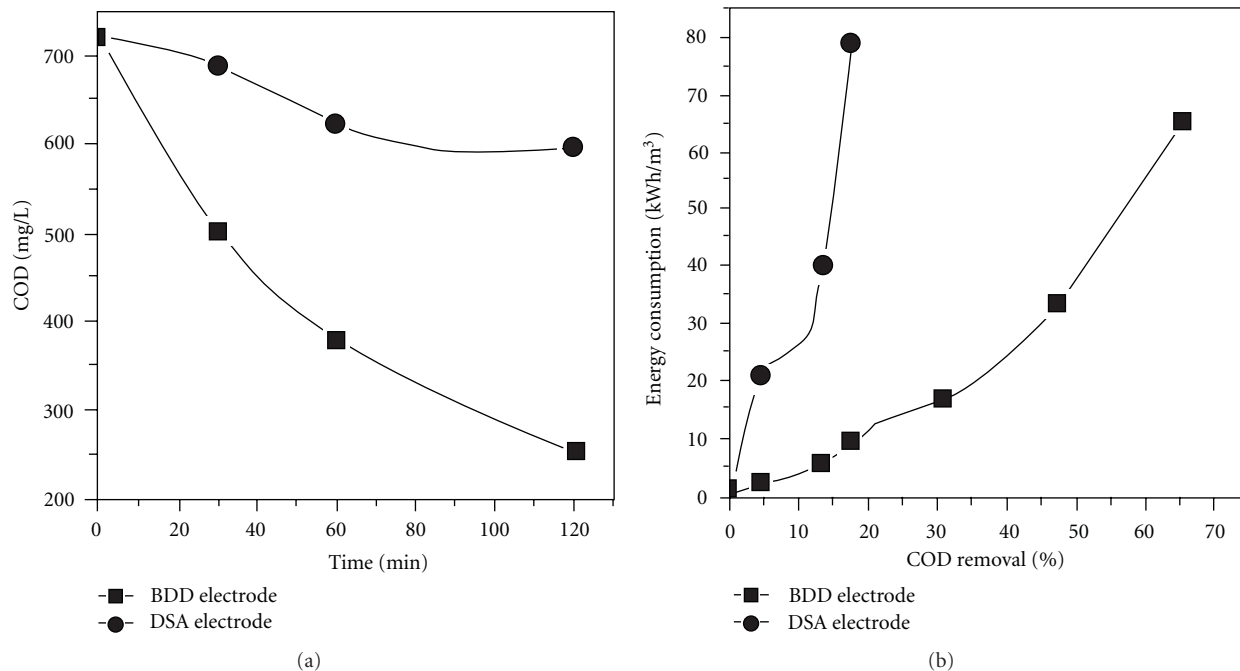


FIGURE 15: (a) Comparison of the evolution of COD during electrochemical treatment; (b) evolution of the specific energy consumption against COD removal during electrochemical treatment of acrylic fiber wastewater on DSA and BDD electrode. Conditions: applied current: 0.50 A, flow rate: 400 mL/min, $T = 45 \pm 1^\circ\text{C}$ [51].

consumption of only 31 kWh kg COD⁻¹. These engineering results can motivate other research groups to employ BDD anodes to scale up this electrochemical process.

Coking wastewater contains high concentrations of refractory and toxic compounds, and the water quality usually cannot meet the discharge standards after conventional biological treatment processes. For this reason, the electrochemical oxidation using BDD anode for advanced treatment of coking wastewater was investigated by Zhu et al. [59]. Under the experimental conditions (current density 20–60 mA cm⁻², pH 3–11, and temperature 20–60°C) using a BDD anode, complete mineralization of organic pollutants was almost achieved. Surplus ammonia-nitrogen (NH₃-N) was further removed thoroughly when pH was not adjusted at alkaline value. Moreover, the TOC and NH₃-N removal rates in the BDD anode cell were much greater than those in other common anode systems such as SnO₂ and PbO₂ anode cells. Also, the energy consumption of 64 kWh kg COD⁻¹ observed in the BDD anode system was only about 60% as much as those observed in SnO₂ and PbO₂ anode systems. Other results reported by these authors revealed that, in the BDD anode cell, organic pollutants were mainly degraded by reaction with free hydroxyl radicals, and electrogenerated oxidants (S₂O₈²⁻, H₂O₂, and other oxidants) played a less important role. Direct electrochemical oxidation and indirect electrochemical oxidation mediated by active chlorine can be negligible. These results showed great potential of BDD anode systems in engineering applications as a final treatment of coking wastewater.

A synthetic tannery wastewater, prepared with several compounds used by finishing tanneries, was studied in

chloride-free media [54] comparing the efficiency removal at different anode materials: Si/BDD, Ti/SnO₂-Sb, and Ti/SnO₂-Sb-Ir. The influence of pH and current density on the treatment was assessed by measuring total phenols, COD, TOC, and absorbance. Results showed that faster decrease in these parameters occurred when the Si/BDD anode was used (see Figure 16). Good results were obtained with the Ti/SnO₂-Sb anode, but its complete deactivation was reached after 4 h of electrolysis at 25 mA cm⁻², indicating that the service life of this electrode was short. The Ti/SnO₂-Sb-Ir anode is chemically and electrochemically more stable than the Ti/SnO₂-Sb anode, but it was not suitable for the electrochemical treatment under the studied conditions in this research. According to the authors, no significant changes were observed for electrolysis performed at different pH conditions with Si/BDD, and this electrode led to almost complete mineralization after 4 h of electrolysis at 100 mA cm⁻². The increase in current density resulted in faster wastewater oxidation, with lower current efficiency and higher energy consumption. Si/BDD proved to be the best electrochemical material for the direct electrooxidation of tannery wastewaters.

Moreover, the results published by these authors are evidence that electrooxidation in chloride-free media is more advantageous than that carried out in chloride-containing media because it avoids formation of toxic organochloride compounds.

3. Concluding Remarks

This paper summarizes the most relevant investigations carried out on electrochemical treatment processes for

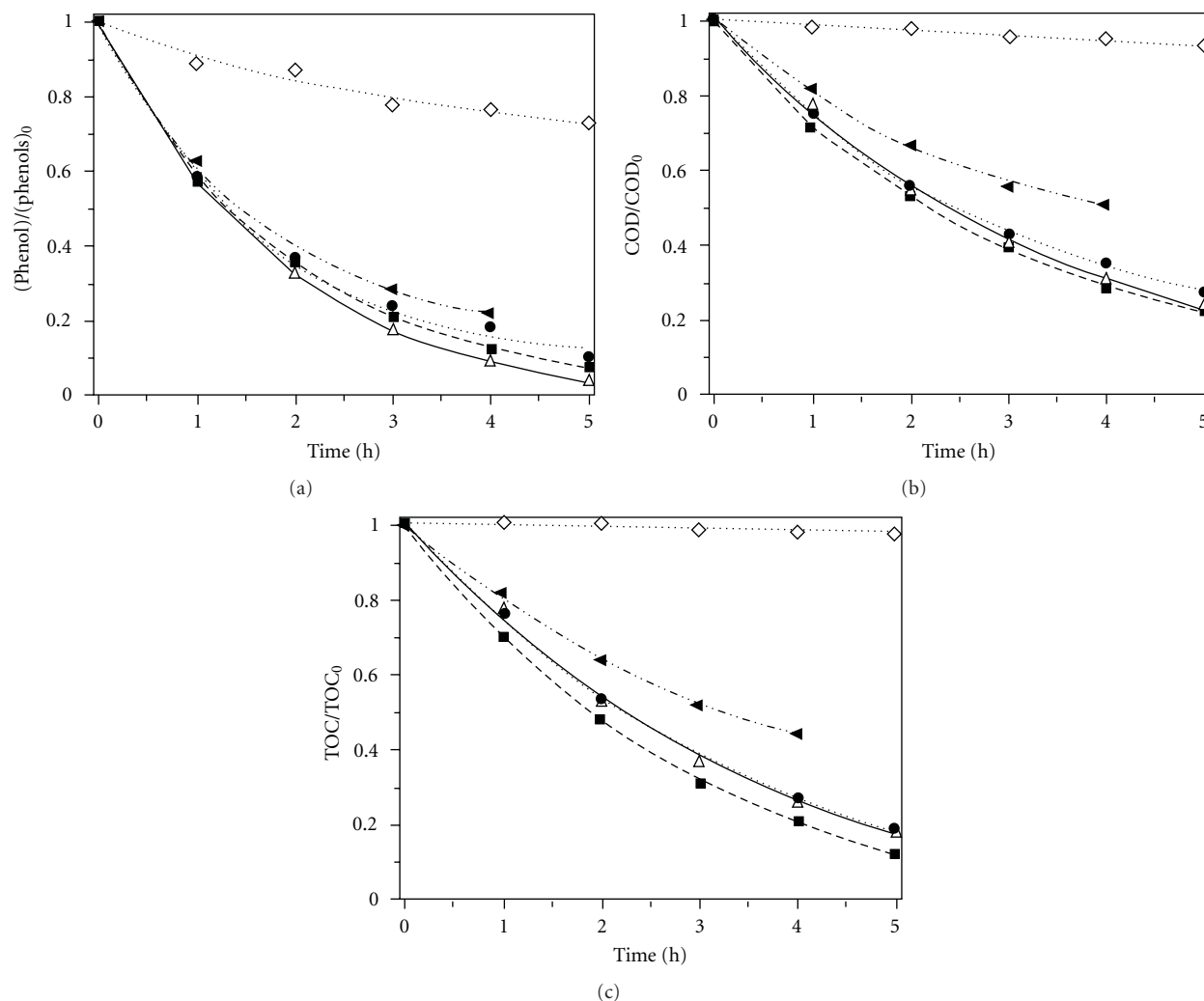


FIGURE 16: Effect of the electrodic material and pH on the electrooxidation of the synthetic tannery wastewater in $0.10 \text{ mol L}^{-1} \text{ Na}_2\text{SO}_4$ at 25 mA cm^{-2} : (a) $(\text{phenols})/(\text{phenols})_0$, (b) COD/COD_0 , and (c) TOC/TOC_0 as a function of electrolysis time. Electrolysis conditions: (\diamond) Ti/SnO₂-Sb-Ir and pH 2.4, (\blacktriangleleft) Ti/SnO₂-Sb and pH 2.4, (\blacksquare) Si/BDD and pH 2.4, (\bullet) Si/BDD and pH 7.3, and (\triangle) Si/BDD and pH 12.0 [54].

oxidation of synthetic dye compounds with the use of BDD anodes. The efficiency of these electrochemical processes seems to be strongly dependent on parameters such as synthetic dye concentration, pH, applied current intensity, and supporting electrolyte, but the most important parameter is the kind of electrode material. As was mentioned, several authors tested different surfaces, such as Ti/BDD, Ti/Sb₂O₅-SnO₂, Pt/Ti, TiRuO₂, and PbO₂ in order to evaluate an anode material with the best conditions with respect to high stability, high activity towards organic oxidation and low cost. However, BDD anodes always offer the most advantages regarding removal efficiency and decontamination of wastewaters. The cost of BDD application could be limited due to the price of BDD anode preparation and fragility of the required electrocatalytic materials. Additionally, electrical potentials exhibited by electrochemical oxidation processes using BDD anodes increase energy consumption, limiting the use in industrial application.

Perhaps, the key will be to use integrated methods or BDD electrochemical technologies coupled with other advanced oxidation processes.

Moreover, according to the results reported by other authors and in view of a concern for environmental protection, the advantages of BDD, high oxygen evolution potential, and low chlorine evolution potential will make it take precedence over other electrodes in the degradation of chloride-free dye wastewater. Therefore, in practical applications, the degradation of chloride-free wastewaters, especially the degradation of those in water supply and drainage system, should be performed on BDD electrodes rather than DSA for the sake of environmental protection in spite of high energy and time consumption. However, for effluents from industries and domestic sewage that contain Cl⁻ ions, electrochemical degradation should be carried out on DSA anodes, due to the higher energy requirements and lower removal efficiencies when using BDD anodes.

Acknowledgments

The authors thank Eng. N. Claudia Calderón Rosas and Eng. Leslie Knapp (cooperante sponsored by the US Peace Corps under agreement with CONACYT) for their help in the manuscript revision. The authors thank the CIATEC Ref.003/CEP/2011 for financial support.

References

- [1] C. Fernández, M. S. Larrechi, and M. P. Callao, "An analytical overview of processes for removing organic dyes from wastewater effluents," *Trends in Analytical Chemistry*, vol. 29, no. 10, pp. 1202–1211, 2010.
- [2] A. B. Dos Santos, F. J. Cervantes, and J. B. Van Lier, "Review paper on current technologies for decolourisation of textile wastewaters: perspectives for anaerobic biotechnology," *Bioresource Technology*, vol. 98, no. 12, pp. 2369–2385, 2007.
- [3] A. Srinivasan and T. Viraraghavan, "Decolorization of dye wastewaters by biosorbents: a review," *Journal of Environmental Management*, vol. 91, no. 10, pp. 1915–1929, 2010.
- [4] C. Baiocchi, M. C. Brussino, E. Pramauro, A. B. Prevot, L. Palmisano, and G. Marci, "Characterization of methyl orange and its photocatalytic degradation products by HPLC/UV-VIS diode array and atmospheric pressure ionization quadrupole ion trap mass spectrometry," *International Journal of Mass Spectrometry*, vol. 214, no. 2, pp. 247–256, 2002.
- [5] V. Augugliaro, C. Baiocchi, A. B. Prevot et al., "Azo-dyes photocatalytic degradation in aqueous suspension of TiO₂ under solar irradiation," *Chemosphere*, vol. 49, no. 10, pp. 1223–1230, 2002.
- [6] J. M. Peralta-Hernández, C. A. Martínez-Huitle, J. L. Guzmán-Mar, and A. Hernández-Ramírez, "Recent advances in the application of electro-Fenton and photoelectro-Fenton process for removal of synthetic dyes in wastewater treatment," *Journal of Environmental Engineering Management*, vol. 19, no. 5, pp. 257–265, 2009.
- [7] C. A. Martínez-Huitle and S. Ferro, "Electrochemical oxidation of organic pollutants for the wastewater treatment: direct and indirect processes," *Chemical Society Reviews*, vol. 35, no. 12, pp. 1324–1340, 2006.
- [8] J. M. Peralta-Hernández, S. Mejía, L. A. Godínez, and Y. Meas-Vong, "Fenton and electrochemical approaches for water purification technologies," in *Applications of Analytical Chemistry in Environmental Research*, M. Palomar, Ed., Research Signpost, Kerala, India, 2005.
- [9] K. Jüttner, U. Galla, and H. Schmieder, "Electrochemical approaches to environmental problems in the process industry," *Electrochimica Acta*, vol. 45, no. 15-16, pp. 2575–2594, 2000.
- [10] Ch. Comninellis, "Electrocatalysis in the electrochemical conversion/combustion of organic pollutants for waste water treatment," *Electrochimica Acta*, vol. 39, no. 11-12, pp. 1857–1862, 1994.
- [11] M. Panizza, E. Brillas, and Ch. Comninellis, "Application of boron-doped diamond electrodes for wastewater treatment," *Journal of Environmental Engineering Management*, vol. 18, no. 3, pp. 139–153, 2008.
- [12] F. Montilla, P. A. Michaud, E. Morallón, J. L. Vázquez, and Ch. Comninellis, "Electrochemical oxidation of benzoic acid at boron-doped diamond electrodes," *Electrochimica Acta*, vol. 47, no. 21, pp. 3509–3513, 2002.
- [13] S. Songa, L. Zhan, Z. Hea et al., "Mechanism of the anodic oxidation of 4-chloro-3-methyl phenol in aqueous solution using Ti/SnO₂-Sb/PbO₂ electrodes," *Journal of Hazardous Materials*, vol. 175, no. 1–3, pp. 614–621, 2010.
- [14] Ch. Tan, B. Xiang, Y. Li, J. Fang, and M. Huang, "Preparation and characteristics of a nano-PbO₂ anode for organic wastewater treatment," *Chemical Engineering Journal*, vol. 166, no. 1, pp. 15–21, 2011.
- [15] G. B. Raju, M. T. Karuppiah, S. S. Latha, D. Latha Priya, S. Parvathy, and S. Prabhakar, "Electrochemical pretreatment of textile effluents and effect of electrode materials on the removal of organics," *Desalination*, vol. 249, no. 1, pp. 167–174, 2009.
- [16] C. A. Martínez-Huitle and E. Brillas, "Decontamination of wastewaters containing synthetic organic dyes by electrochemical methods: a general review," *Applied Catalysis B*, vol. 87, no. 3-4, pp. 105–145, 2009.
- [17] O. Simond, V. Schaller, and Ch. Comninellis, "Theoretical model for the anodic oxidation of organics on metal oxide electrodes," *Electrochimica Acta*, vol. 42, no. 13-14, pp. 2009–2012, 1997.
- [18] M. Panizza and G. Cerisola, "Application of diamond electrodes to electrochemical processes," *Electrochimica Acta*, vol. 51, no. 2, pp. 191–199, 2005.
- [19] X. Chen, G. Chen, and P.-L. Yue, "Anodic oxidation of dyes at novel Ti/B-diamond electrodes," *Chemical Engineering Science*, vol. 58, no. 3–6, pp. 995–1001, 2003.
- [20] P. Cañizares, A. Gadri, J. Lobato et al., "Electrochemical oxidation of azoic dyes with conductive-diamond anodes," *Industrial and Engineering Chemistry Research*, vol. 45, no. 10, pp. 3468–3473, 2006.
- [21] A. Sakalis, K. Fytianos, U. Nickel, and A. Voulgaropoulos, "A comparative study of platinised titanium and niobe/synthetic diamond as anodes in the electrochemical treatment of textile wastewater," *Chemical Engineering Journal*, vol. 119, no. 2-3, pp. 127–133, 2006.
- [22] M. Panizza, A. Barbucci, R. Ricotti, and G. Cerisola, "Electrochemical degradation of methylene blue," *Separation and Purification Technology*, vol. 54, no. 3, pp. 382–387, 2007.
- [23] M. Panizza and G. Cerisola, "Electrochemical degradation of methyl red using BDD and PbO₂ anodes," *Industrial and Engineering Chemistry Research*, vol. 47, no. 18, pp. 6816–6820, 2008.
- [24] M. Panizza and G. Cerisola, "Removal of colour and COD from wastewater containing acid blue 22 by electrochemical oxidation," *Journal of Hazardous Materials*, vol. 153, no. 1-2, pp. 83–88, 2008.
- [25] N. Bensalah, M. A. Q. Alfaro, and C. A. Martínez-Huitle, "Electrochemical treatment of synthetic wastewaters containing Alphazurine A dye," *Chemical Engineering Journal*, vol. 149, no. 1–3, pp. 348–352, 2009.
- [26] A. S. Kopalal, Y. Yavuz, C. Gürel, and Ü. B. Ögütveren, "Electrochemical degradation and toxicity reduction of C.I. Basic Red 29 solution and textile wastewater by using diamond anode," *Journal of Hazardous Materials*, vol. 145, no. 1-2, pp. 100–108, 2007.
- [27] C. Carvalho, A. Fernandes, A. Lopes, H. Pinheiro, and I. Goncalves, "Electrochemical degradation applied to the metabolites of Acid Orange 7 anaerobic biotreatment," *Chemosphere*, vol. 67, no. 7, pp. 1316–1324, 2007.
- [28] C. Saez, M. Panizza, M. A. Rodrigo, and G. Cerisola, "Electrochemical incineration of dyes using a boron-doped diamond anode," *Journal of Chemical Technology and Biotechnology*, vol. 82, no. 6, pp. 575–581, 2007.

- [29] D. Montanaro and E. Petrucci, "Electrochemical treatment of Remazol Brilliant Blue on a boron-doped diamond electrode," *Chemical Engineering Journal*, vol. 153, no. 1–3, pp. 138–144, 2009.
- [30] J. Rodriguez, M. A. Rodrigo, M. Panizza, and G. Cerisola, "Electrochemical oxidation of Acid Yellow 1 using diamond anode," *Journal of Applied Electrochemistry*, vol. 39, no. 11, pp. 2285–2289, 2009.
- [31] Ch. Zhang and J. Wang, "Influence of cations during Orange-II degradation on boron-doped diamond electrode," *Journal of Electroanalytical Chemistry*, vol. 638, no. 1, pp. 91–99, 2010.
- [32] L. S. Andrade and T. T. Tasso, "On the performances of lead dioxide and boron-doped diamond electrodes in the anodic oxidation of simulated wastewater containing the Reactive Orange 16 dye," *Electrochimica Acta*, vol. 54, no. 7, pp. 2024–2030, 2009.
- [33] E. Hmani, S. Chaabane Elaoud, and Y. Samet, "Electrochemical degradation of waters containing O-Toluidine on PbO₂ and BDD anodes," *Journal of Hazardous Materials*, vol. 170, no. 2–3, pp. 928–933, 2009.
- [34] Y. Yavuz, A. Savaş Kopal, and Ü. B. Ögütveren, "Electrochemical oxidation of Basic Blue 3 dye using a diamond anode: evaluation of colour, COD and toxicity removal," *Journal of Chemical Technology and Biotechnology*, vol. 86, no. 2, pp. 261–265, 2011.
- [35] C. R. Costa, F. Montilla, and E. Morallón, "Electrochemical oxidation of acid black 210 dye on the boron-doped diamond electrode in the presence of phosphate ions: effect of current density, pH, and chloride ions," *Electrochimica Acta*, vol. 54, no. 27, pp. 7048–7055, 2009.
- [36] K. E. Carter and J. Farrell, "Electrochemical oxidation of trichloroethylene using boron-doped diamond film electrodes," *Environmental Science and Technology*, vol. 43, no. 21, pp. 8350–8354, 2009.
- [37] M. Wu, G. Zhao, M. Li, L. Liu, and D. Li, "Applicability of boron-doped diamond electrode to the degradation of chloride-mediated and chloride-free wastewaters," *Journal of Hazardous Materials*, vol. 163, no. 1, pp. 26–31, 2009.
- [38] M. J. Pacheco, V. Santos, L. Ciriaco, and A. Lopes, "Electrochemical degradation of aromatic amines on BDD electrodes," *Journal of Hazardous Materials*, vol. 186, no. 2–3, pp. 1033–1041, 2011.
- [39] M. Zhou, H. Särkkä, and M. Sillanpää, "A comparative experimental study on methyl orange degradation by electrochemical oxidation on BDD and MMO electrodes," *Separation and Purification Technology*, vol. 78, no. 3, pp. 290–297, 2011.
- [40] Ch. Zhang, L. Gu, and Y. Lin, "Degradation of X-3B dye by immobilized TiO₂ photocatalysis coupling anodic oxidation on BDD electrode," *Journal of Photochemistry and Photobiology A*, vol. 207, no. 1, pp. 66–72, 2009.
- [41] J. Sun, H. Lu, L. Du, and H. Lin, "Anodic oxidation of anthraquinone dye Alizarin Red S at Ti/BDD electrodes," *Applied Surface Science*, vol. 257, no. 15, pp. 6667–6671, 2011.
- [42] V. Santos, J. Diogo, M. J. A. Pacheco, L. Ciriaco, A. Morao, and A. Lopes, "Electrochemical degradation of sulfonated amines on SI/BDD electrodes," *Chemosphere*, vol. 79, no. 6, pp. 637–645, 2010.
- [43] M. Panizza and G. Cerisola, "Electrochemical degradation of gallic acid on a BDD anode," *Chemosphere*, vol. 77, no. 8, pp. 1060–1064, 2009.
- [44] R. E. Palma-Goyes, F. L. Guzmán-Duque, G. Peñuela, I. González, J. L. Nava, and R. A. Torres-Palma, "Electrochemical degradation of crystal violet with BDD electrodes: effect of electrochemical parameters and identification of organic by-products," *Chemosphere*, vol. 81, no. 1, pp. 26–32, 2010.
- [45] G. R. P. Malpass, D. W. Miwa, D. A. Mortari, S. A. S. Machado, and A. J. Motheo, "Decolorisation of real textile waste using electrochemical techniques: effect of the chloride concentration," *Water Research*, vol. 41, no. 13, pp. 2969–2977, 2007.
- [46] L. S. Andrade and T. T. Tasso, "On the performances of lead dioxide and boron-doped diamond electrodes in the anodic oxidation of simulated wastewater containing the Reactive Orange 16 dye," *Electrochimica Acta*, vol. 54, no. 7, pp. 2024–2030, 2009.
- [47] E. Chatzisyneon, N. P. Xekoukoulotakis, A. Coz, N. Kalogerakis, and D. Mantzavinis, "Electrochemical treatment of textile dyes and dyehouse effluents," *Journal of Hazardous Materials*, vol. 137, no. 2, pp. 998–1007, 2006.
- [48] S. K. Fytianos, U. Nickel, and A. Voulgaropoulos, "A comparative study of platinised titanium and niobe/synthetic diamond as anodes in the electrochemical treatment of textile wastewater," *Chemical Engineering Journal*, vol. 119, no. 2–3, pp. 127–133, 2006.
- [49] G. R. P. Malpass, D. W. Miwa, S. A. S. Machado, and A. J. Motheo, "Decolourisation of real textile waste using electrochemical techniques: effect of electrode composition," *Journal of Hazardous Materials*, vol. 156, no. 1–3, pp. 170–177, 2008.
- [50] G. R. P. Malpass, D. W. Miwa, D. A. Mortari, S. A. S. Machado, and A. J. Motheo, "Decolorisation of real textile waste using electrochemical techniques: effect of the chloride concentration," *Water Research*, vol. 41, no. 13, pp. 2969–2977, 2007.
- [51] C. Y. Zhanga, J. L. Wang, H. F. Zhou, D. Fua, and Z. Gu, "Anodic treatment of acrylic fiber manufacturing wastewater with boron-doped diamond electrode: a statistical approach," *Chemical Engineering Journal*, vol. 161, no. 1–2, pp. 93–98, 2010.
- [52] X. Zhu, J. Ni, and J. Wei, "Scale-up of BDD anode system for electrochemical oxidation of phenol simulated wastewater in continuous mode," *Journal of Hazardous Materials*, vol. 184, no. 1–3, pp. 493–498, 2010.
- [53] M. Mascia, A. Vacca, and A. M. Polcaro, "Electrochemical treatment of simulated ground water containing MTBE and BTEX with BDD anodes," *Journal of Chemical Technology & Biotechnology*, vol. 86, no. 1, pp. 128–137, 2010.
- [54] C. R. Costa, F. Montilla, and E. Morallón, "Electrochemical oxidation of synthetic tannery wastewater in chloride-free aqueous media," *Journal of Hazardous Materials*, vol. 180, no. 1–3, pp. 429–435, 2010.
- [55] P. Grafias and N. P. Xekoukoulotakis, "Pilot treatment of olive pomace leachate by vertical-flow constructed wetland and electrochemical oxidation: an efficient hybrid process," *Water Research*, vol. 44, no. 9, pp. 2773–2780, 2010.
- [56] X. Zhu, J. Ni, and J. Wei, "Destination of organic pollutants during electrochemical oxidation of biologically-pretreated dye wastewater using boron-doped diamond anode," *Journal of Hazardous Materials*, vol. 189, no. 1–2, pp. 127–133, 2011.
- [57] X. Zhu and J. Ni, "Advanced treatment of biologically pretreated coking wastewater by electrochemical oxidation using boron-doped diamond electrodes," *Water Research*, vol. 43, no. 17, pp. 4347–4355, 2009.

- [58] E. Diamadopoulos, H. Barndök, N. P. Xekoukoulotakis, and D. Mantzavinos, "Treatment of ink effluents from flexographic printing by lime precipitation and boron-doped diamond (BDD) electrochemical oxidation," *Water Science and Technology*, vol. 60, no. 10, pp. 2477–2483, 2009.
- [59] X. Zhu, J. Ni, and P. Lai, "Advanced treatment of biologically pretreated coking wastewater by electrochemical oxidation using boron-doped diamond electrodes," *Water Research*, vol. 43, no. 17, pp. 4347–4355, 2009.

Research Article

Anodic Stripping Voltammetry of Se^{4+} on Gold-Modified Boron-Doped Diamond Electrodes

**Stéphane Fierro,¹ Takeshi Watanabe,¹ Kazumi Akai,¹
Mikito Yamanuki,² and Yasuaki Einaga^{1,3}**

¹Department of Chemistry, Faculty of Science and Technology, Keio University, 3-14-1 Hiyoshi, Yokohama 223-8522, Japan

²Advanced R&D Center, HORIBA Ltd., Minami-ku, Kyoto 601-8510, Japan

³JST, CREST, 3-14-1 Hiyoshi, Yokohama 223-8522, Japan

Correspondence should be addressed to Yasuaki Einaga, einaga@chem.keio.ac.jp

Received 6 April 2011; Accepted 22 May 2011

Academic Editor: Giancarlo R. Salazar-Banda

Copyright © 2012 Stéphane Fierro et al. This is an open access article distributed under the Creative Commons Attribution License, which permits unrestricted use, distribution, and reproduction in any medium, provided the original work is properly cited.

Electrochemical detection of Se^{4+} has been performed by anodic stripping voltammetry on a boron-doped diamond (BDD) electrode modified with gold nanoparticles deposited through chronocoulometry. This method is based on the affinity between the gold nanoparticles and Se^0 , while the BDD electrode is presented as an ideal material for metal modification due to its unique properties. The resulting anodic stripping voltammograms exhibited a clear peak at 0.9 V versus AgCl related to Se^{4+} , and highly accurate ($r^2 = 0.99$) calibration curves could be obtained for a selenium concentration range between 10 and 100 $\mu\text{g/L}$. The influence of Se deposition time and other metals dissolved in solution (Cu, Cd, Pb, Cr, and B) has been investigated as well, and it was found that the Se^{4+} calibration curves remained unaltered. For all the experiments performed, a detection limit around 10 $\mu\text{g/L}$ was achieved. The high accuracy and reproducibility of the results as well as the excellent stability of the electrode material proves the excellent capabilities of this system for selenium detection.

1. Introduction

Selenium is an essential micronutrient for animals and humans but can be extremely toxic if absorbed in large doses (over 400 μg per day) [1]. Exceeding the tolerable upper intake level of 400 micrograms per day (15 μg per kg bodyweight) can lead to selenosis, which affects the respiratory, digestive, and neurological systems [2]. The maximum contaminant level of selenium in water allowed by the US Environmental Protection Agency is 50 $\mu\text{g/L}$ [3].

Selenium exists in many forms in the environment, but the most abundant are H_2SeO_3 (Se^{4+}), H_2SeO_4 (Se^{6+}), and their derivatives [4]. The quantification of both forms is important because Se species vary in their toxicity potential to animals and humans. However, if one sample contains both Se^{4+} and Se^{6+} species, it is possible to reduce the Se^{6+} to Se^{4+} by heating the sample at 85°C in concentrated HCl [4]. The concentration of Se in this solution is then considered as the sum of Se^{4+} and Se^{6+} . The difference between

the concentration of Se in digested and undigested samples is the concentration of Se^{6+} . Many techniques have been developed in order to analyze Se^{4+} concentrations at the $\mu\text{g/L}$ level but the most common method is stripping voltammetry due to its simplicity, rapidity, and excellent sensitivity. Both cathodic stripping voltammetry using a hanging mercury drop electrode [5–11] and anodic stripping voltammetry (ASV) using gold (rotating disk or film) electrodes [12–14] have been extensively studied for Se^{4+} determination in acidic solutions. These methods have been shown to be quite efficient for selenium determination. However, the anodic stripping on gold electrodes usually requires time-consuming pretreatments of the gold electrode in order to get reproducible results. Moreover, the main problem of these methods is the splitting of the stripping peaks [5, 6]. Several methods have been proposed to solve this problem like increasing the temperature of the support electrolyte [6, 8] or adding small amounts of copper or rhodium to the solutions [7–9, 11, 15]. Nevertheless, these steps tend

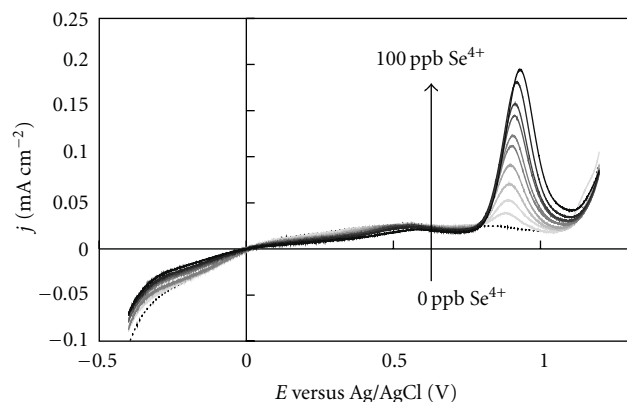


FIGURE 1: Stripping voltammograms of Se^{4+} in 0.1 M HClO_4 in the concentration range of 0–100 $\mu\text{g/L}$ recorded on a BDD electrode, which was previously modified by gold nanoparticles deposited by chronocoulometry (-35 mC cm^{-2} was applied for 1 minute in a solution of HAuCl_4 100 ppm in 0.1 M HCl). The deposition potential (-0.4 V versus Ag/AgCl) was applied during 2 minutes before the stripping, which was performed at a scan rate of 200 mV/s . The upper potential limit was fixed at 1.2 V versus Ag/AgCl . $T = 23^\circ\text{C}$.

to complicate the experimental procedure, and added to the delicate handling of mercury electrodes, these methods become less suited for real analytical applications.

In this work, the detection of Se^{4+} by anodic stripping voltammetry on gold-modified boron-doped diamond electrode is presented for the first time. BDD has been selected for gold deposition due to its outstanding properties compared to other conventional electrode materials such as a wide electrochemical potential window, low background current, and weak adsorption of polar molecules [16, 17]. These properties offer a significant advantage for metal modification as it was already shown for the detection of As^{3+} and As^{5+} mixtures [18]. Moreover, the high stability of these gold-modified BDD electrodes has been shown [18]. Therefore, the same method has been used for selenium detection in this study. Concentration of Se^{4+} was measured by a stripping method based on the simple electrochemical reduction of Se^{4+} to Se^0 followed by oxidation of the latter. The influence of Se deposition time is discussed. Moreover, the selective detection of Se^{4+} in the presence of interference metal ions was also studied.

2. Experimental

2.1. Chemicals and Materials. Selenious acid (H_2SeO_3), hydrogen tetrachloroaurate(III) trihydrate (HAuCl_4), hydrogen chloride (HCl), perchloric acid (HClO_4), copper chloride (CuCl_2), lead chloride (PbCl_2), boric acid (H_3BO_3), cadmium chloride (CdCl_2), and potassium dichromate ($\text{K}_2\text{Cr}_2\text{O}_7$) were purchased from Wako. All chemicals were used without further purification.

2.2. Preparation of BDD Electrodes. BDD thin films were deposited using a microwave plasma-assisted chemical vapor deposition (MPCVD) setup (ASTeX Corp.). Acetone was

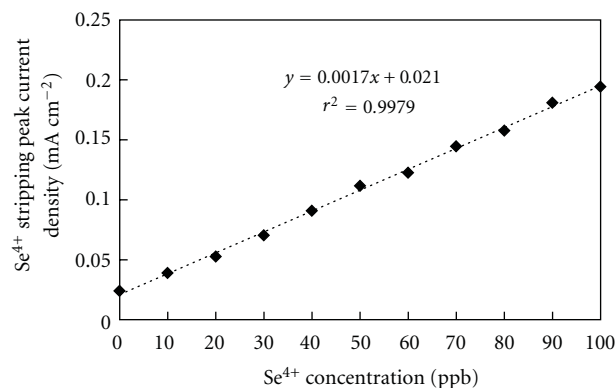


FIGURE 2: Calibration curve from the anodic stripping voltammograms presented in Figure 1. The peak current was plotted as a function of Se^{4+} concentration.

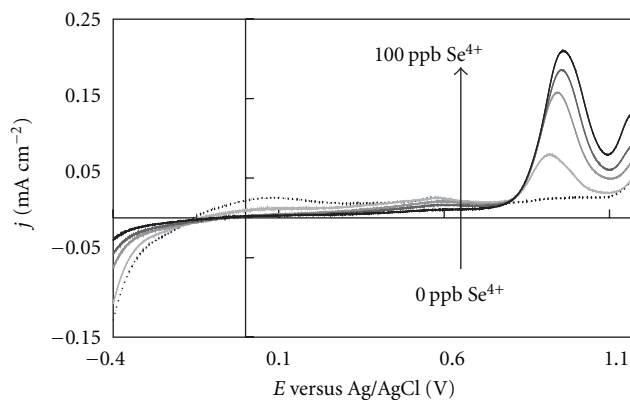


FIGURE 3: Stripping voltammograms of Se^{4+} in 0.1 M HClO_4 in the concentration range of 0–100 $\mu\text{g/L}$ recorded on a BDD electrode, which was previously modified by gold nanoparticles deposited by chronocoulometry (-70 mC cm^{-2} was applied for 1 minute in a solution of HAuCl_4 100 ppm in 0.1 M HCl). The deposition potential (-0.4 V versus Ag/AgCl) was applied during 2 minutes before the stripping, which was performed at a scan rate of 200 mV/s . The upper potential limit was fixed at 1.2 V versus Ag/AgCl . $T = 23^\circ\text{C}$.

used as carbon source and $\text{B}(\text{OCH}_3)_3$ as boron source. The concentration of the latter was 0.1% w/w in source. The surface morphology and crystalline structures were characterized using scanning electron microscopy (not shown in this work). The typical size of the diamond crystals was about $5 \mu\text{m}$. BDD films were deposited on Si (1 0 0) wafers in the MPCVD chamber at 5 kW using high-purity hydrogen as carrier gas. The BDD film thickness was about $40 \mu\text{m}$ after 10 hours of deposition. The Raman spectrum of this film exhibited a sharp peak at 1334 cm^{-1} , which is characteristic of crystalline diamond. The BDD electrodes were pretreated by ultrasonication in 2-propanol for about 10 minutes followed by rinsing with high-purity water in order to remove any organic impurities that may have remained within the BDD film after deposition in the MPCVD chamber.

Gold-modified BDD electrodes were prepared through the same procedure reported in [19]. The BDD electrode

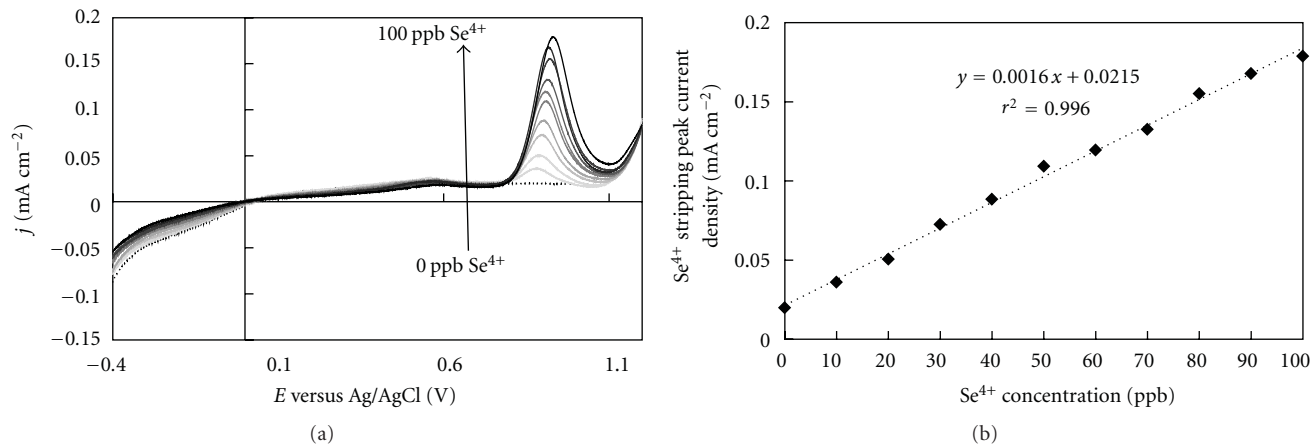


FIGURE 4: (a) Stripping voltammograms of Se^{4+} in 0.1 M HClO_4 in the concentration range of 0–100 $\mu\text{g/L}$ recorded on a BDD electrode, which was previously modified by gold nanoparticles deposited by chronocoulometry (-35 mC cm^{-2} was applied for 1 minute in a solution of HAuCl_4 100 ppm in 0.1 M HCl). The deposition potential (-0.4 V versus Ag/AgCl) was applied for 1 minute before the stripping, which was performed at a scan rate of 200 mV/s . The upper potential limit was fixed at 1.2 V versus Ag/AgCl . (b) Calibration curve extracted from these stripping voltammograms. $T = 23^\circ\text{C}$.

was immersed in 0.1 M HCl solution containing 100 ppm of HAuCl_4 , and gold nanoparticles deposition was performed through chronocoulometry.

2.3. Electrochemical Measurements. Electrochemical measurements were carried out in a single-compartment cell using a Hokuto Denko Hz-5000 potentiostat at room temperature (23°C). The reference electrode was Ag/AgCl , the counter electrode was a platinum wire, and the working electrode was BDD. The working geometric area was 0.283 cm^2 . The anodic stripping of Se was performed in 0.1 M HClO_4 , whereas the posttreatment was carried out in 0.1 M HCl . In this work, all potentials given are with respect to the Ag/AgCl reference electrode (0.2 V versus SHE).

3. Results and Discussion

3.1. Anodic Stripping Voltammetry of Se^{4+} . The anodic stripping voltammetry of Se^{4+} has been performed based on its reduction to Se^0 followed by oxidation of the latter. For the first measurements, gold particles were deposited through chronocoulometry at -35 mC cm^{-2} for 1 minute. A deposition potential of -0.4 V has been applied during 2 minutes for Se deposition because the Se^{4+} reduction peak was observed around that potential on gold-modified BDD electrodes (result not shown). For the stripping of selenium, the voltammetric scan was performed between the deposition potential (-0.4 V) and different upper limit potentials. The resulting voltammograms related to solutions containing different concentrations of Se^{4+} (from 10 to $100 \mu\text{g/L}$ dissolved in 0.1 M HClO_4) are displayed in Figure 1 for upper limit potential of 1.2 V . When the upper limit potential was fixed at 1.4 V , almost the same voltammogram as Figure 1 was observed (not shown). Both figures show the presence of a clear stripping peak situated at 0.9 V approximately, which is related to selenium. Therefore, an upper potential limit

of 1.2 V was selected for the anodic stripping voltammetry measurements. The peak currents obtained from Figure 1 were therefore plotted as a function of Se^{4+} concentration, and the resulting graph (presented in Figure 2) shows that a linear and highly accurate calibration curve ($r^2 = 0.99$) could be obtained under these conditions for a Se^{4+} concentration range between 10 and $100 \mu\text{g/L}$.

One set of measurements was performed on a gold-modified electrode where the chronocoulometry was performed at -70 mC cm^{-2} for 1 minute, and the resulting anodic stripping voltammograms presented on Figure 3 exhibit a similar profile; therefore, the charge applied during the modification of the BDD electrode was fixed at -35 mC cm^{-2} .

The influence of selenium deposition time was also studied. In fact, it was reduced from 2 to 1 minute. The resulting voltammograms together with the corresponding calibration curve are displayed on Figures 4(a) and 4(b), respectively. These results show that the time during which the deposition potential is applied has no influence neither on the profile of the stripping voltammograms nor on the accuracy of the corresponding calibration curve.

3.2. Influence of Other Metal Ions. In order to evaluate the influence of other metal ions present in the media, a mixture containing cadmium, copper, boron, chromium, and lead (all at a concentration of $100 \mu\text{g/L}$) was prepared. Anodic stripping voltammetry measurements were carried out using the aforementioned mixture and under the same conditions as those presented on Figure 1, that is, the BDD electrode was modified through chronocoulometry at -35 mC cm^{-2} for 1 min in a solution of HAuCl_4 100 mg/L in 0.1 M HCl . The deposition potential (-0.4 V) was applied during 2 minutes before performing the stripping voltammetry at 200 mV s^{-1} between -0.4 and 1.2 V . The corresponding anodic stripping voltammograms are presented in Figure 5(a). This figure

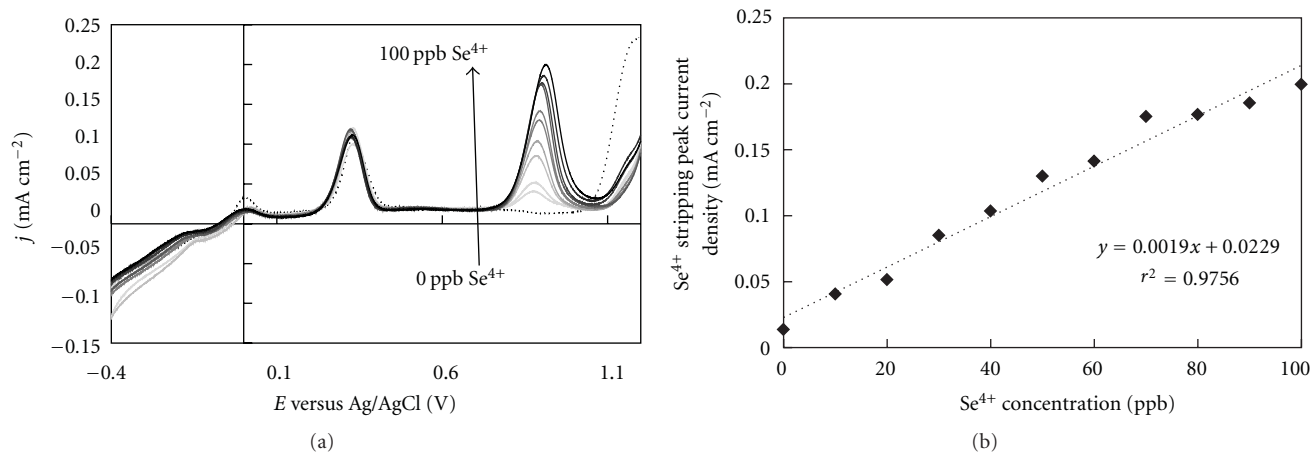


FIGURE 5: (a) Stripping voltammograms of Se^{4+} (concentration range 0–100 $\mu\text{g/L}$) in CuCl_2 , PbCl_2 , H_3BO_3 , CdCl_2 , and $\text{K}_2\text{Cr}_2\text{O}_7$, all 100 $\mu\text{g/L}$ in 0.1 M HClO_4 recorded on a BDD electrode, which was previously modified by gold nanoparticles deposited by chronocoulometry (-35 mC cm^{-2} was applied for 1 minute in a solution of HAuCl_4 100 ppm in 0.1 M HCl). The deposition potential (-0.4 V versus Ag/AgCl) was applied for 2 minutes before the stripping, which was performed at a scan rate of 200 mV/s . The upper potential limit was fixed at 1.2 V versus Ag/AgCl . (b) Calibration curve extracted from these stripping voltammograms. $T = 23^\circ\text{C}$.

shows a clear peak at 0.9 V corresponding to selenium stripping and another peak at 0.3 V which was attributed to the stripping of copper based on measurements performed with each of the interfering metals individually (results not shown). The peaks corresponding to the stripping of the other metals (Cr, Cd, B, and Pb) have a low intensity and are located between 0.2 and 0 V. Nevertheless, Figure 5(a) shows clearly that selenium has the highest affinity with the gold-modified BDD electrode because the intensity of the corresponding stripping peak is the highest when concentration of the interfering metals (100 $\mu\text{g/L}$) is equal to the concentration of selenium.

The intensity of the anodic stripping peak of selenium was then plotted as a function of its concentration. The result, presented in Figure 5(b), shows clearly that the selenium calibration curve is still linear and accurate ($r^2 = 0.97$) despite the presence of many other interfering metals in solution.

4. Conclusions

In this study, the determination of Se^{4+} has been performed through anodic stripping voltammetry on boron-doped diamond electrode modified by gold particles deposited by chronocoulometry. The results have shown that a clear peak related to selenium stripping can be observed at 0.9 V and that highly accurate concentration curve could be constructed for a selenium concentration range between 10 and 100 $\mu\text{g/L}$. The influences of selenium deposition time and gold particles deposition conditions were investigated, and it was found that the accuracy of the calibration curve remained unaltered. The influence of other metal ions in solution was also studied, and the results have shown that selenium has the highest affinity with the type of electrode used herein, and accurate calibration curves for Se^{4+} detection could still be constructed under these conditions.

These results prove that the BDD electrode modified by gold particles is an efficient material for Se^{4+} determination.

Acknowledgments

S. Fierro gratefully thanks the Fond National Suisse pour la Recherche Scientifique (FNSRS) for the financial support. This work was supported by New Energy and Industrial Technology Development Organization (NEDO).

References

- [1] Institute of medicine of the national academies (IOM), *Dietary Reference Intake for Vitamin C, Vitamin E, Selenium, and Carotenoids*, National Academy Press, Washington, DC, USA, 2000.
- [2] U. Tinggi, "Selenium toxicity and its adverse health effects," *Reviews in Food and Nutrition Toxicity*, vol. 4, pp. 29–55, 2005.
- [3] US Environmental Protection Agency, <http://water.epa.gov/drink/contaminants/basicinformation/selenium.cfm>.
- [4] K. J. Reddy, Z. Zhang, M. J. Blaylock, and G. F. Vance, "Method for detecting selenium speciation in groundwater," *Environmental Science and Technology*, vol. 29, no. 7, pp. 1754–1759, 1995.
- [5] G. Jarzabek and Z. Kublik, "Cyclic and stripping voltammetry of $\text{Se}^{(4)}$ and $\text{Se}^{(-2)}$ at the HMDE in acidic media," *Journal of Electroanalytical Chemistry*, vol. 137, no. 2, pp. 247–259, 1982.
- [6] G. Jarzabek and Z. Kublik, "Determination of traces of selenium(IV) by cathodic stripping voltammetry at the hanging mercury drop electrode," *Analytica Chimica Acta*, vol. 143, pp. 121–130, 1982.
- [7] S. B. Adeloju, A. M. Bond, and H. C. Hughes, "Determination of selenium, copper, lead and cadmium in biological materials by differential pulse stripping voltammetry," *Analytica Chimica Acta*, vol. 148, pp. 59–69, 1983.
- [8] L. Campanella and T. Ferri, "Voltammetric behaviour of selenium(IV) at hanging mercury drop electrodes in acetate

- buffer," *Journal of Electroanalytical Chemistry*, vol. 165, no. 1-2, pp. 241–249, 1984.
- [9] U. Baltensperger and J. Hertz, "Parameter evaluation for the determination of selenium by cathodic stripping voltammetry at the hanging mercury drop electrode," *Analytica Chimica Acta*, vol. 172, pp. 49–56, 1985.
- [10] G. Mattsson, L. Nyholm, and Å. Olin, "Cathodic stripping voltammetry of Cu₂Se at mercury electrodes," *Journal of Electroanalytical Chemistry*, vol. 379, no. 1-2, pp. 49–61, 1994.
- [11] W. Holak and J. J. Specchio, "Determination of selenium in food supplements by differential-pulse cathodic stripping voltammetry in the presence of added copper," *Analyst*, vol. 119, no. 10, pp. 2179–2182, 1994.
- [12] R. W. Andrews and D. C. Johnson, "Voltammetric deposition and stripping of selenium(IV) at a rotating gold-disk electrode in 0.1 M perchloric acid," *Analytical Chemistry*, vol. 47, no. 2, pp. 294–299, 1975.
- [13] T. W. Hamilton, J. Ellis, and T. M. Florence, "Determination of selenium and tellurium in electrolytic copper by anodic stripping voltammetry at a gold film electrode," *Analytica Chimica Acta*, vol. 110, no. 1, pp. 87–94, 1979.
- [14] R. S. Posey and R. W. Andrews, "Determination of selenium(IV) by anodic stripping voltammetry with an in situ gold-plated rotating glassy carbon disk electrode," *Analytica Chimica Acta*, vol. 124, no. 1, pp. 107–112, 1981.
- [15] J. Wang and J. Lu, "Ultratrace measurements of selenium by cathodic stripping voltammetry in the presence of rhodium," *Analytica Chimica Acta*, vol. 274, no. 2, pp. 219–224, 1993.
- [16] T. Yano, D. A. Tryk, K. Hashimoto, and A. Fujishima, "Electrochemical behavior of highly conductive boron-doped diamond electrodes for oxygen reduction in alkaline solution," *Journal of the Electrochemical Society*, vol. 145, no. 6, pp. 1870–1876, 1998.
- [17] A. Fujishima, Y. Einaga, T. N. Rao, and D. A. Tryk, Eds., *Diamond Electrochemistry*, Elsevier-BKC, Tokyo, Japan, 2005.
- [18] D. Yamada, T. A. Ivandini, M. Komatsu, A. Fujishima, and Y. Einaga, "Anodic stripping voltammetry of inorganic species of As³⁺ and As⁵⁺ at gold-modified boron doped diamond electrodes," *Journal of Electroanalytical Chemistry*, vol. 615, no. 2, pp. 145–153, 2008.
- [19] S. Hrapovic, Y. Liu, and J. H. T. Luong, "Reusable platinum nanoparticle modified boron doped diamond microelectrodes for oxidative determination of arsenite," *Analytical Chemistry*, vol. 79, no. 2, pp. 500–507, 2007.

Review Article

A Brief Review on the *In Situ* Synthesis of Boron-Doped Diamond Thin Films

Vadali V. S. S. Srikanth, P. Sampath Kumar, and Vijay Bhooshan Kumar

School of Engineering Sciences and Technology, University of Hyderabad, Hyderabad 500046, India

Correspondence should be addressed to Vadali V. S. S. Srikanth, vvssts@uohyd.ernet.in

Received 10 April 2011; Accepted 21 May 2011

Academic Editor: Carlos Alberto Martinez-Huitle

Copyright © 2012 Vadali V. S. S. Srikanth et al. This is an open access article distributed under the Creative Commons Attribution License, which permits unrestricted use, distribution, and reproduction in any medium, provided the original work is properly cited.

Diamond thin films are well known for their unsurpassed physical and chemical properties. In the recent past, research interests in the synthesis of conductive diamond thin films, especially the boron-doped diamond (BDD) thin films, have risen up to cater to the requirements of electronic, biosensoric, and electrochemical applications. BDD thin films are obtained by substituting some of the sp^3 hybridized carbon atoms in the diamond lattice with boron atoms. Depending on diamond thin film synthesis conditions, boron doping routes, and further processing steps (if any), different types of BDD diamond thin films with application-specific properties can be obtained. This paper will review several important advances in the synthesis of boron-doped diamond thin films, especially those synthesized via gas phase manipulation.

1. Introduction

Diamond thin films, which are *nowadays* routinely synthesized by employing chemical vapor deposition (CVD) technique, possess unique properties like high thermal conductivity, high carrier mobilities, high break-down field characteristics, chemical inertness, biocompatibility, bio-sensing ability and so forth [1–11]. In the recent past, researchers worldwide have been exploring diamond thin films especially for electronics, biosensing, and electrochemical applications [9–11]. However, to realize these applications, it is necessary that the diamond thin films are electrically conductive in nature (in addition to possessing a combination of the above-mentioned properties) which are otherwise insulating. The conductivity of diamond thin films can be attuned to an application requirement typically by carrying out suitable doping events. Amongst the available conductive (doped, p- and n-type [9–16]) diamond thin films, the p-type semiconducting boron-doped diamond (BDD) thin films [17–35] are the most popular ones and are being studied extensively. BDD thin films are synthesized by substituting some of the sp^3 hybridized carbon atoms in the diamond lattice with boron atoms. BDD thin films are mainly obtained by (i) *in situ* (during diamond thin film synthesis) and (ii)

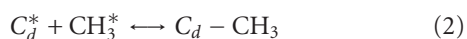
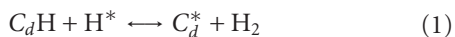
ex situ (after diamond thin film synthesis) doping routes. *In situ* doping involves gas phase manipulation, that is, addition of certain amount of boron containing gas species to the diamond forming gas mixtures during the diamond thin film synthesis. *Ex situ* doping involves boron doping into the already synthesized diamond thin films mainly via ion implantation. Depending on the diamond thin film synthesis conditions and the above-mentioned boron doping routes, and further processing steps (if any), different types of BDD thin films with application-specific properties can be obtained. BDD thin films-based electrochemical sensors, biosensors, water purification electrodes, unipolar devices, ultraviolet light generators, and so forth have already been developed [9–11].

This article will review several advances in the synthesis of BDD thin films (especially those synthesized via gas phase doping) that brought about unique variations in physical and chemical characteristics of the films making them as suitable electrode materials. In the next section, a brief discussion on the typical CVD technique used to synthesize diamond thin films will be made. In the subsequent section, several aspects of BDD thin films including concept of doping, *in situ* boron doping, and electrode applications will be discussed. This

paper will be concluded with several remarks on BDD thin films.

2. CVD of Diamond Thin Films

In CVD of diamond thin films, one carbon atom at a time is added from a carbon containing activated gas phase (maintained at a lower pressure) to an initial template (a pretreated substrate) resulting in a thin film that constitutes sp^3 carbon atom network (the diamond). Typical CVD diamond thin film synthesis protocol involves gas mixture activation, gas-phase reactions, and the subsequent transfer of diamond forming gas species onto the substrate surface; subsequent surface reactions lead to the formation of a diamond thin film. Hydrocarbon (typically methane)/hydrogen gas mixtures are employed and their activation leads to a harsh environment dominated by reactions involving atomic hydrogen. Activation can be done via surface-mediated thermal process (as in hot filament CVD) or via energy transfer from gas-phase collisions with excited free electrons (as in microwave plasma enhanced CVD). Due to the activation, molecular hydrogen (H_2) dissociates into atomic hydrogen. Diamond growth takes place via site-activation by a surface hydrogen abstraction reaction (1), followed by addition reaction (2) of a hydrocarbon radical like CH_3 . C_d represents a surface radical. The competition between surface activation reaction (1) and H-atom recombination reaction with the surface radical site (3) determines the number of active nucleation sites available for a particular set of synthesis conditions.



The stable nanosized crystallites formed during the nucleation stage typically exhibit spherical shapes. With time, nucleation density increases up to a certain value upon which it terminates or ceases to occur at a measurable rate. The isolated crystallites now grow and develop facets due to the relatively high rate of surface carbon diffusion from the surrounding surface sites. Once the crystals grow large enough to coalesce with each another, they form grain boundaries and then continue growing as a continuous diamond film. The morphology of a growing diamond surface depends on the rates at which different diamond planes grow. Under typical growth conditions, the morphology assessment of a diamond film can be made by the growth parameter $\alpha = \sqrt{3}(\nu_{100}/\nu_{111})$ where ν_{100} and ν_{111} are the normal growth velocities of (100) and (111) diamond planes, respectively. The grains exhibiting the fastest growth in the direction perpendicular to the substrate overshadow other slower-growing grains to form a continuous film with a columnar structure. This mode of film growth is known as evolutionary selection principle. Diamond grain growth dependent on facet reactivity and selectivity which is on the contrary to evolutionary selection principle is also possible under certain CVD experimental conditions. Depending on the synthesis conditions like substrate surface pretreatment,

reaction temperature and pressure, and gas composition, epitaxial, oriented, and polycrystalline (with micron- and nano-sized grains) diamond thin films (Figure 1) can be synthesized. Please refer to chapter 2 in reference [11] for more details on aspects of diamond thin film nucleation and growth.

After the advent of low pressure gas phase synthesis (CVD) of diamond thin films [38–40], numerous noteworthy and path breaking advances have successively taken place [1–11, 41–49]; these advances have made the following possible: (i) tremendous increase in diamond thin film growth rates, (ii) substrate selectivity and large area deposition, (iii) low temperature deposition, (iv) single crystalline thin film synthesis, (v) phase mixture diamond nanocomposite thin film deposition, (vi) doped diamond thin film synthesis, and so forth. At present various CVD methods such as hot filament, direct current (DC) plasma, radio frequency (RF) plasma, microwave plasma, electron cyclotron resonance (ECR) microwave plasma CVD, and so forth, and their hybrids are being used to synthesize diamond thin films with highly consistent and desired properties.

3. BDD Films

3.1. Concept of Doping Diamond Thin Films. Diamond is electrically semiconducting (almost insulating) in nature as a consequence of the tetrahedral closed/tight arrangement of carbon atoms that form the diamond lattice; the band structure of diamond constitutes a completely filled valence band and an empty conduction band separated by a wide band gap of 5.5 eV [50–53]. The energy band diagram of boron-doped diamond is shown in Figure 2. Diamond thin films synthesized via the previously mentioned CVD routes (Section 2) are also insulating in nature unless and otherwise they are synthesized in some special and specific conditions. As discussed previously, for many applications the diamond thin films need to be electrically conductive in nature to a desired extent (semiconducting through metallic to even superconducting). There are several ways of achieving this via controlled experiments.

Several nanometers depth of a hydrogen terminated diamond thin film surface can be made p-type semiconductive typically by exposing (via physisorption) it to appropriate adsorbates. These surface adsorbates can be solvated ionic species or neutral species with high electron affinity; in the former case, the species apparently extract electrons from the valence band and react electrochemically and in the later case, the species reduce the ionization potential of the diamond surface and makes its electron affinity apparently negative which in turn leads to an exchange of electrons between the valence band and the species. These processes leave behind holes as the charge carriers. This hole-mediated conduction is explained in terms of a doping famously known as surface transfer doping [54–56]. Diamond thin films can also be made conducting by annealing them under vacuum at high temperatures [57]. Due to annealing, the nondiamond conductive carbon phase formed along the

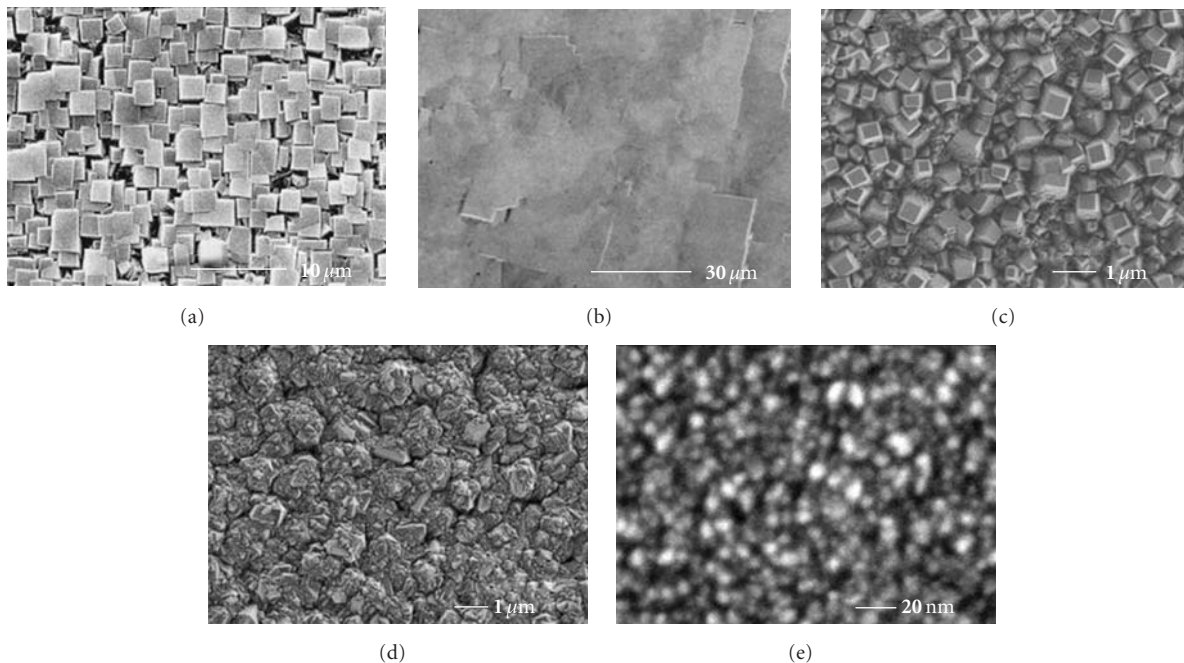


FIGURE 1: Plane view scanning electron micrographs of (a) epitaxial [36], (b) highly oriented (001) [37], (c) (001) oriented, (d) polycrystalline, and (e) nanocrystalline diamond thin films.

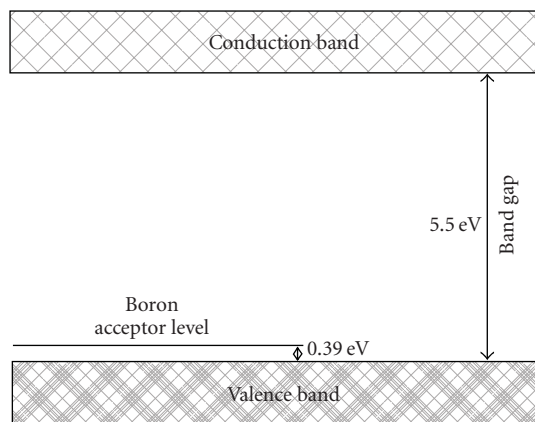


FIGURE 2: Boron acceptor level in the band gap of diamond.

diamond grain boundaries and structural defects formed in the film bulk will result in p-type semiconduction.

As mentioned previously, diamond thin films can also be made conductive by substitutional doping. Here, hetero-atoms (like B, Al, N, P, S, Si, Ni, As, Sb, Cr, Ni, Fe, W, Mo, etc.) with slightly different electronic configurations are made substitutes for some of the sp^3 carbon atoms in the diamond lattice leading to the formation of new energy levels in the band structure that facilitate both p- and n-type conduction depending on the type of dopant. The introduction of a p-type dopant (B, Al, etc.) causes the formation of discrete acceptor levels (Figure 2) above the valence band of diamond. These energy levels are accessible to valence band electrons. When electrons are promoted into

these levels, delocalized holes form in the valence band which facilitates the conductance. A hetero-atom inclusion causes n-type doping (N, P, etc.) by forming a donor level whose electrons can be easily excited into the conduction band.

The closely packed diamond lattice makes substitutional doping, a challenging task. Some of the above-mentioned dopants can be incorporated into the lattice during the synthesis of diamond thin films whilst some can be incorporated via ion implantation [58–60]. Doping via ion-implantation involves forcing the dopant ions into the subsurface regions of diamond thin films rendering them semiconductive. During ion-implantation, since the dopant ion energy is greater than the binding energy of the sp^3 carbon atoms, not only severe damage takes place in the diamond thin films but there is also a possibility of disturbing the stability of the metastable sp^3 bonds leading to the formation of stable sp^2 graphitic bonds upon subsequent high temperature annealing that is carried out to annihilate the damages. However, doping and damage levels can be evaluated prior to the ion-implantation experiments via computer simulations [61], and proper experiments can then be carried out. It has also been pointed out that doping via ion-implantation leads to the formation of resistive diamond thin films, probably due to the compensation (of the desired electrical activity of the dopants) arising from damage-related centers forming in between acceptor and donor energy levels [62]. Other substitutional doping issues that are still difficult to experimentally overcome are (i) high solubility of certain dopants like nitrogen leading to the formation of valueless very deep donor energy levels and (ii) the development of shallow n-type dopants [62].

Amongst the above-mentioned substitutional dopants, the most exploited and successful one is undoubtedly boron. Both geometrically (covalent radius of boron atom is 0.088 nm whilst that of carbon atom is 0.077 nm) and energetically [62] boron atoms are probably the only dopants that can be substitutes for carbon atoms in the diamond lattice. Boron doping into diamond thin films can be done by using any of the following: (i) gas phase manipulations while synthesizing diamond thin films via CVD routes, (ii) ion-implantation, and (iii) high temperature diffusion [25]. In the next section, various aspects of gas phase synthesis (*in situ*) of BDD thin films will be discussed.

3.2. BDD Thin Films via In Situ Doping. Boron containing precursors like diborane, trimethylboron, triethylboron, boron oxide dissolved in acetone/ethanol/methanol, trimethyl borate dissolved in the acetone [35], borane trimethylamine, boron trichloride, boric acid, and other boron-containing unconventional sources (obtained via etching boron, boron oxide, boron nitride, and boron rod) have been introduced into the gas phase during the CVD of diamond thin films to finally obtain BDD thin films [59, 60]. Theoretical thermodynamic studies suggested that the concentrations of BH_3 , BH_2 , and BH radicals in the activated B-C-H gas mixture modify the concentrations of diamond forming radicals (like CH_3 , C_2H_2 , etc.) and atomic hydrogen [63]. The relative efficiencies of boron and carbon incorporation into a growing film from a given B-C-H gas mixture are dependent upon gas phase activation route and other diamond synthesis conditions [64]. During the synthesis of BDD films, the boron species formed in the gas phase give assistance to the surface diffusion of diamond forming species on the already formed diamond surfaces [65]. This leads to the incorporation of boron atoms into both the growing {100} and {111} diamond thin film surfaces. It was found that there is preference (almost 10 times) in the incorporation of boron in {111} growth sectors [28–30]. Boron substitution, diamond crystallinity, and diamond surface morphology are closely related and greatly influence each other during the *in situ* synthesis of BDD thin films [66, 67]. Boron concentration relative to carbon in the gas phase (B/C) has also a strong effect on the growing diamond crystals structure and stability. Low level (<500 ppm B/C) boron addition into the gas-phase not only increases the sizes of growing diamond crystals that will finally constitute the diamond thin film but also enhances the diamond film growth rates. Intermediate level (1000–5000 ppm B/C) boron addition results in p-type BDD thin films with other characteristics similar to the diamond thin films that will be obtained without boron in the gas phase at the same experimental conditions. High level (>4000 ppm B/C) boron addition results in the loss of crystallinity [31, 32]. Still higher level (8000–10000 ppm B/C) disturbs the diamond phase stability. At this level of boron concentration, the much needed (to selectively etch graphite over diamond) atomic hydrogen content in the gas phase gets depleted due to the increase in reactions

between boron species and hydrogen. This in turn results in tremendous decrease in rate at which graphite is etched. Thereby more graphitic content can be found along with diamond in the final BDD thin films [33]. Synthesis of diamond thin films via CVD routes generally takes place in a highly diluted hydrogen gas environment. Thereby hydrogen develops as an impurity within the diamond lattice; but in the case of *in situ* boron doping, hydrogen can form a complex with substituted boron within the lattice and pacify it, which is undesired [68]. It has also been shown that deuterated BDD thin films can be n-type electrical conductors [69]. It has also been shown that single substitutional boron atoms are more stable than boron pairs [62, 70]. If carefully observed, irrespective of the CVD and doping methodologies, an approximately equal ratio of boron to carbon as used in the gas phase constitutes the BDD thin film composition [71].

Substrate selection is very important to synthesize BDD thin films as electrode materials. BDD thin films are often deposited on conductive and self-passivating substrates [72–77]. Natural diamond single crystals, Silicon, graphite, glassy carbon, carbon fiber, titanium, tantalum, tungsten, molybdenum, and niobium are the commonly used substrate materials. Uniform and defect-free BDD thin films can be deposited on silicon substrates. But the brittleness of silicon limits its usage in applications. Also, large area depositions are not possible on silicon. Large area BDD thin film depositions are possible on metal substrates. But to protect the metal substrates from hydrogen embrittlement during CVD process and to improve the adhesion of BDD thin film, an interlayer deposition prior to the BDD deposition is often needed. Thick free-standing BDD thin films can also be obtained. Firstly the thick film is deposited onto typically silicon substrates and in a subsequent step the silicon is removed by chemical etching. Single-crystalline BDD thin films can be obtained by using natural diamond single crystals as the substrates. BDD thin film-based conducting diamond electrodes are the most used ones [73]. In practice, it is required that the substitutional boron in BDD thin films stays in its position during any electrode operation in which the BDD film participates. Theoretically it was shown that the substitutional boron stays in the diamond lattice with a low dynamic distortion [62, 78], and its ionization energy has been predicted as 0.39 eV [62, 79] which matches very closely with the experimental value of 0.37 eV [80]. As the number of doped boron atoms in diamond lattice increases from high to very high values, the acceptor level starts to broaden into a band, and above 3.9×10^{21} boron atoms cm^{-3} in diamond lattice, the broadened band starts to overlap with the valence band resulting in a metal to insulator transition [60, 81]. BDD thin films with typically 10^{19} – 10^{21} boron atoms cm^{-3} in diamond lattice are useful, especially for electrode applications. BDD electrodes have been used to (a) detect very low concentrations of toxic metal ions like lead [82], (b) treat wastewater [83], (c) monitor industrial wastewater by determining chemical oxygen demand [84, 85], (d) synthesize organic and inorganic substances [86], (e) record neurochemical and electrical information in neural prosthesis [87], (f) sense several biomolecules [88], and so forth.

4. Conclusions and Future Perspectives

The research field of synthesis of BDD thin films has matured enough and is now delivering thin films with desired and reproducible properties. BDD thin films can now be synthesized routinely on a variety of substrates. However, the elementary general mechanisms of boron substitution into diamond lattice are not completely characterized, understood, and explained. This hinders the control on boron doping and thereby realization of applications that need to be yet explored. With the advent of powerful multiscale modeling and simulation (including quantum level) methodologies, it is now possible to (i) interpret complex experimental data and to establish predictive doping models, (ii) obtain clear-cut ideas on new dopants, and (iii) design and execute novel doping schemes. Compared to the p-type conduction in diamond thin films, n-type conduction has not that matured and demands a greater attention both experimentally and theoretically.

Acknowledgments

The first author thanks Professor Banda for inviting him to prepare this paper. He also thanks his wife Sailaja for proofreading this paper.

References

- [1] P. K. Bachmann and R. Messier, "Emerging technology of diamond thin films," *Chemical and Engineering News*, vol. 67, no. 20, pp. 24–39, 1989.
- [2] J. T. Field, "Electrical properties," *Properties of Natural and Synthetic Diamond*, Academic Press, London, UK, 1992.
- [3] R. F. Davis, *Diamond Films and Coatings: Development, Properties, and Applications*, Noyes Publications, Park Ridge, NJ, USA, 1993.
- [4] H. Lin and D. Dandy, *Diamond Chemical Vapor Deposition, Nucleation and Early Growth*, Noyes Publications, Park Ridge, NJ, USA, 1995.
- [5] B. Dishchler and C. Wild, *Low-Pressure Synthetic Diamond Manufacturing and Applications*, Springer, Heidelberg, Germany, 1998.
- [6] M. H. Nazaré and J. Neves, *Properties, Growth and Applications of Diamond*, INSPEC, London, UK, 2001.
- [7] K. Kobashi, *Diamond Films*, Elsevier, Oxford, UK, 2005.
- [8] O. A. Shenderova and D. M. Gruen, *Ultrananocrystalline Diamond: Synthesis, Properties, and Applications*, William Andrew, New York, NY, USA, 2006.
- [9] S. Koizumi, C. Nebel, and M. Nešladek, *Physics and Applications of CVD Diamond*, Wiley-VCH Verlag GmbH & Co. KGaA, Weinheim, Germany, 2008.
- [10] R. S. Sussmann, *CVD Diamond for Electronic Devices and Sensors*, John Wiley & Sons, West Sussex, UK, 2009.
- [11] E. Brillas and C. A. Martínez Huitle, *Synthetic Diamond Films: Preparation, Electrochemistry, Characterization and Applications*, John Wiley & Sons, Hoboken, NJ, USA, 2011.
- [12] K. Larsson, "Substitutional n-type doping of diamond," *Computational Materials Science*, vol. 27, no. 1-2, pp. 23–29, 2003.
- [13] M. Nešladek, "Conventional n-type doping in diamond: state of the art and recent progress," *Semiconductor Science and Technology*, vol. 20, no. 2, pp. R19–R27, 2005.
- [14] M. A. Pinault, J. Barjon, T. Kociniewski, F. Jomard, and J. Chevallier, "The n-type doping of diamond: present status and pending questions," *Physica B*, vol. 401-402, pp. 51–56, 2007.
- [15] P. W. May, M. Davey, K. N. Rosser, and P. J. Heard, "Arsenic and antimony doping: an attempt to deposit n-type CVD diamond," *Materials Research Society Symposium Proceedings*, vol. 1039, 2008, paper no. 1039-P15-01.
- [16] M. A. Pinault-Thaurya, T. Tillochera, N. Habkaa et al., "n-Type CVD diamond: epitaxy and doping," *Materials Science and Engineering B*. In press.
- [17] D. J. Poferl, N. C. Gardner, and J. C. Angus, "Growth of boron-doped diamond seed crystals by vapor deposition," *Journal of Applied Physics*, vol. 44, no. 4, pp. 1428–1434, 1973.
- [18] V. S. Vavilov, "Semiconducting diamond," *Physica Status Solidi (A)*, vol. 31, no. 1, pp. 11–26, 1975.
- [19] A. T. Collins and E. C. Lightowers, in *The Properties of Diamond*, J. E. Field, Ed., chapter 3, Academic Press, London, UK, 1979.
- [20] B. V. Spitsyn, L. L. Bouilov, and B. V. Derjaguin, "Vapor growth of diamond on diamond and other surfaces," *Journal of Crystal Growth*, vol. 52, no. 1, pp. 219–226, 1981.
- [21] N. Fujimori, T. Imai, and A. Doi, "Characterization of conducting diamond films," *Vacuum*, vol. 36, no. 1–3, pp. 99–102, 1986.
- [22] K. Okano, H. Naruki, Y. Akiba, T. Kurosu, M. Iida, and Y. Hirose, "Synthesis of diamond thin films having semiconductive properties," *Japanese Journal of Applied Physics, Part 2*, vol. 27, no. 2, pp. 173–175, 1988.
- [23] J. Mort, D. Kuhman, M. Machonkin et al., "Boron doping of diamond thin films," *Applied Physics Letters*, vol. 55, no. 11, pp. 1121–1123, 1989.
- [24] K. Okano, H. Naruki, Y. Akiba et al., "Characterization of boron-doped diamond film," *Japanese Journal of Applied Physics, Part 1*, vol. 28, no. 6, pp. 1066–1071, 1989.
- [25] W. Tsai, M. Delfino, D. Hodul et al., "Diamond MESFET using ultrashallow RTP boron doping," *Electron Device Letters*, vol. 12, no. 4, pp. 157–159, 1991.
- [26] A. E. Alexenko and B. V. Spitsyn, "Semiconducting diamonds made in the USSR," *Diamond and Related Materials*, vol. 1, no. 5-6, pp. 705–709, 1992.
- [27] C. Uzan-Saguy, A. Reznik, C. Cytermann et al., "Hydrogen diffusion in B-ion-implanted and B-doped homo-epitaxial diamond: passivation of defects vs. passivation of B acceptors," *Diamond and Related Materials*, vol. 10, no. 3–7, pp. 453–458, 2001.
- [28] R. Samslenki, C. Haug, R. Brenn, C. Wild, R. Locher, and P. Koidl, "Characterisation and lattice location of nitrogen and boron in homoepitaxial CVD diamond," *Diamond and Related Materials*, vol. 5, no. 9, pp. 947–951, 1996.
- [29] J. C. Angus, Y. V. Pleskov, and S. C. Eaton, "Chapter 3 Electrochemistry of diamond," *Semiconductors and Semimetals*, vol. 77, pp. 97–119, 2004.
- [30] P. Wurzinger, P. Pongratz, P. Hartmann, R. Haubner, and B. Lux, "Investigation of the boron incorporation in polycrystalline CVD diamond films by TEM, EELS and Raman spectroscopy," *Diamond and Related Materials*, vol. 6, no. 5–7, pp. 763–768, 1997.
- [31] P. Hartmann, S. Bohr, R. Haubner et al., "Diamond growth with boron addition," *International Journal of Refractory Metals and Hard Materials*, vol. 16, no. 3, pp. 223–232, 1998.
- [32] X. H. Wang, G. H. M. Ma, W. Zhu et al., "Effects of boron doping on the surface morphology and structural imperfections of diamond films," *Diamond and Related Materials*, vol. 1, no. 7, pp. 828–835, 1992.

- [33] E. Gheeraert, A. Deneuve, and J. Mambou, "Influence of diborane on the growth rate and phase stability of diamond films," *Carbon*, vol. 37, no. 1, pp. 107–111, 1999.
- [34] R. Ramamurti, M. Becker, T. Schuelke, T. A. Grotjohn, D. K. Reinhard, and J. Asmussen, "Deposition of thick boron-doped homoepitaxial single crystal diamond by microwave plasma chemical vapor deposition," *Diamond and Related Materials*, vol. 18, no. 5–8, pp. 704–706, 2009.
- [35] J. Zhao, J. Wang, J. Zhi, and Z. Zhang, "Preparation of grain size controlled boron-doped diamond thin films and their applications in selective detection of glucose in basic solutions," *Science China Chemistry*, vol. 53, no. 6, pp. 1378–1384, 2010.
- [36] X. Jiang, C. P. Klages, R. Zachai, M. Hartweg, and H. J. Füsser, "Epitaxial diamond thin films on (001) silicon substrates," *Applied Physics Letters*, vol. 62, no. 26, pp. 3438–3440, 1993.
- [37] X. Jiang, M. Fryda, and C. L. Jia, "High quality heteroepitaxial diamond films on silicon: recent progresses," *Diamond and Related Materials*, vol. 9, no. 9, pp. 1640–1645, 2000.
- [38] W. G. Eversole and N. Y. Kenmore, US Patents 3030187 and 3030188, 1962.
- [39] J. C. Angus, H. A. Will, and W. S. Stanko, "Growth of diamond seed crystals by vapor deposition," *Journal of Applied Physics*, vol. 39, no. 6, pp. 2915–2922, 1968.
- [40] B. V. Derjaguin, D. V. Fedoseev, V. M. Lukyanovich, B. V. Spitzin, V. A. Ryabov, and A. V. Lavrentyev, "Filamentary diamond crystals," *Journal of Crystal Growth*, vol. 2, no. 6, pp. 380–384, 1968.
- [41] S. Matsumoto, Y. Sato, M. Tsutsumi, and N. Setaka, "Growth of diamond particles from methane-hydrogen gas," *Journal of Materials Science*, vol. 17, no. 11, pp. 3106–3112, 1982.
- [42] R. A. Rudder, J. B. Posthill, and R. J. Markunas, "Thermal CVD of homoepitaxial diamond using CF_4 and F_2 ," *Electronics Letters*, vol. 25, no. 18, pp. 1220–1221, 1989.
- [43] D. M. Gruen, S. Liu, A. R. Krauss, J. Luo, and X. Pan, "Fullerenes as precursors for diamond film growth without hydrogen or oxygen additions," *Applied Physics Letters*, vol. 64, no. 12, pp. 1502–1504, 1994.
- [44] P. H. Gaskell, A. Saeed, P. Chieux, and D. R. McKenzie, "Neutron-scattering studies of the structure of highly tetrahedral amorphous diamondlike carbon," *Physical Review Letters*, vol. 67, no. 10, pp. 1286–1289, 1991.
- [45] J. F. Prins, "Ion-implanted structures and doped layers in diamond," *Materials Science Reports*, vol. 7, no. 7–8, pp. 275–364, 1992.
- [46] Q. Chen, J. Yang, and Z. Lin, "Synthesis of oriented textured diamond films on silicon via hot filament chemical vapor deposition," *Applied Physics Letters*, vol. 67, no. 13, article 1853, 3 pages, 1995.
- [47] X. S. Sun, N. Wang, H. K. Woo et al., "The effect of ion bombardment on the nucleation of CVD diamond," *Diamond and Related Materials*, vol. 8, no. 8–9, pp. 1414–1417, 1999.
- [48] P. Aublanc, V. P. Novikov, L. V. Kuznetsova, and M. Mermoux, "Diamond synthesis by electrolysis of acetates," *Diamond and Related Materials*, vol. 10, no. 3–7, pp. 942–946, 2001.
- [49] V. V. S. S. Srikanth, *Deposition and Characterization of Nanocrystalline Diamond/ β -SiC Composite Film System*, Shaker, Aachen, Germany, 2008.
- [50] C. D. Clark, R. W. Ditchburn, and H. B. Dyer, "The absorption spectra of natural and irradiated diamonds," *Proceedings of the Royal Society A*, vol. 234, no. 1198, pp. 363–381, 1956.
- [51] C. D. Clark, P. J. Dean, and P. V. Harris, "Intrinsic Edge Absorption in Diamond," *Proceedings of the Royal Society A*, vol. 277, no. 1370, pp. 312–329, 1964.
- [52] P. J. Dean and I. H. Jones, "Recombination radiation from diamond," *Physical Review A*, vol. 133, no. 6, pp. A1698–A1705, 1964.
- [53] J. Singh, *Physics of Semiconductors and Their Heterostructures*, McGraw-Hill, New York, NY, USA, 1993.
- [54] M. I. Landstrass and K. V. Ravi, "Resistivity of chemical vapor deposited diamond films," *Applied Physics Letters*, vol. 55, no. 10, pp. 975–977, 1989.
- [55] J. Ristein, "Surface transfer doping of diamond," *Journal of Physics D*, vol. 39, no. 4, pp. R71–R81, 2006.
- [56] R. Kalish, "Nano-scale modification and doping of diamond: Interesting science and promising technology," *International Journal of Nanotechnology*, vol. 6, no. 7–8, pp. 691–703, 2009.
- [57] Y. V. Pleskov, M. D. Krotova, V. V. Elkin, V. G. Ralchenko, A. V. Khomich, and R. A. Khmelnskiy, "The vacuum-annealed undoped polycrystalline CVD diamond electrodes: the impedance-spectroscopy and photoelectrochemical studies," *Electrochimica Acta*, vol. 50, no. 5, pp. 1149–1156, 2005.
- [58] S. Praver and R. Kalish, "Ion-beam-induced transformation of diamond," *Physical Review B*, vol. 51, no. 22, pp. 15711–15722, 1995.
- [59] R. Kalish, "Doping of diamond by ion implantation," in *Thin-Film Diamond I*, C. E. Nebel and J. Ristein, Eds., chapter 3, Elsevier, Menlo Park, Calif, USA, 2003.
- [60] A. Deneuve, "Boron doping of diamond films from the gas phase," in *Thin-Film Diamond I*, C. E. Nebel and J. Ristein, Eds., chapter 4, Elsevier, Menlo Park, Calif, USA, 2003.
- [61] J. P. Biersack and L. G. Haggmark, "A Monte Carlo computer program for the transport of energetic ions in amorphous targets," *Nuclear Instruments and Methods in Physics Research*, vol. 174, no. 1–2, pp. 257–269, 1980.
- [62] J. P. Goss, R. J. Eyre, and P. R. Briddon, "Theoretical models for doping diamond for semiconductor applications," in *Physics and Applications of CVD Diamond*, S. Koizumi, C. Nebel, and M. Nesladek, Eds., chapter 8, John Wiley & Sons, Weinheim, Germany, 2008.
- [63] R. Haubner, S. Bohr, and B. Lux, "Comparison of P, N and B additions during CVD diamond deposition," *Diamond and Related Materials*, vol. 8, no. 2–5, pp. 171–178, 1999.
- [64] P. Gonon, A. Deneuve, F. Fontaine et al., "Chemical vapor deposition of B-doped polycrystalline diamond films: growth rate and incorporation efficiency of dopants," *Journal of Applied Physics*, vol. 78, no. 12, pp. 7404–7406, 1995.
- [65] M. Hata, M. Tsuda, N. Fujii, and S. Oikawa, "Surface migration enhancement of adatoms in the photoexcited process on reconstructed diamond (001) surfaces," *Applied Surface Science*, vol. 79–80, pp. 255–263, 1994.
- [66] R. Locher, J. Wagner, F. Fuchs, M. Maier, P. Gonon, and P. Koidl, "Optical and electrical characterization of boron-doped diamond films," *Diamond and Related Materials*, vol. 4, no. 5–6, pp. 678–683, 1995.
- [67] J. H. Edgar, Z. Y. Xie, and D. N. Braski, "The effects of the simultaneous addition of diborane and ammonia on the hot-filament assisted chemical vapor deposition of diamond," *Diamond and Related Materials*, vol. 7, no. 1, pp. 35–42, 1998.
- [68] E. B. Lombardi, A. Mainwood, and K. Osuch, "Interaction of hydrogen with boron, phosphorus, and sulfur in diamond," *Physical Review B*, vol. 70, no. 20, Article ID 205201, pp. 205201–12, 2004.
- [69] Z. Teukam, J. Chevallier, C. Saguy et al., "Shallow donors with high n-type electrical conductivity in homoepitaxial deuterated boron-doped diamond layers," *Nature Materials*, vol. 2, no. 7, pp. 482–486, 2003.

- [70] J. P. Goss and P. R. Briddon, "Theory of boron aggregates in diamond: first-principles calculations," *Physical Review B*, vol. 73, no. 8, Article ID 085204, 8 pages, 2006.
- [71] M. Suzuki, H. Yoshida, N. Sakuma et al., "Electrical properties of B-related acceptor in B-doped homoepitaxial diamond layers grown by microwave plasma CVD," *Diamond and Related Materials*, vol. 13, no. 1, pp. 198–202, 2004.
- [72] M. Fryda, L. Schäfer, and I. Tröster, "Doped diamond—a new material for industrial electrochemistry," *Recent Research Developments in Electrochemistry*, vol. 4, pp. 85–97, 2000.
- [73] W. Haenni, P. Rychen, M. Fryda, and C. Comminellis, "Industrial application of diamond electrode," in *Thin-Film Diamond II*, C. E. Nebel and J. Ristein, Eds., chapter 5, Elsevier, Menlo Park, Calif, USA, 2004.
- [74] M. Fryda, T. Matthée, S. Mulcahy, A. Hampel, L. Schäfer, and I. Tröster, "Fabrication and application of Diachem® electrodes," *Diamond and Related Materials*, vol. 12, no. 10-11, pp. 1950–1956, 2003.
- [75] C. H. Goeting, F. Jones, J. S. Foord et al., "Electrochemistry at boron-doped diamond films grown on graphite substrates: redox-, adsorption and deposition processes," *Journal of Electroanalytical Chemistry*, vol. 442, no. 1-2, pp. 207–216, 1998.
- [76] H. B. Martin, A. Argoitia, J. C. Angus, and U. Landau, "Voltammetry studies of single-crystal and polycrystalline diamond electrodes," *Journal of the Electrochemical Society*, vol. 146, no. 8, pp. 2959–2964, 1999.
- [77] J. van de Lagemaat, D. Vanmaekelbergh, and J. J. Kelly, "Electrochemistry of homoepitaxial CVD diamond: energetics and electrode kinetics in aqueous electrolytes," *Journal of Electroanalytical Chemistry*, vol. 475, no. 2, pp. 139–151, 1999.
- [78] J. P. Goss, P. R. Briddon, R. Jones et al., "Deep hydrogen traps in heavily B-doped diamond," *Physical Review B*, vol. 68, no. 23, pp. 2352091–23520910, 2003.
- [79] L. G. Wang and A. Zunger, "Phosphorus and sulphur doping of diamond," *Physical Review B*, vol. 66, no. 16, Article ID 161202, pp. 1612021–1612024, 2002.
- [80] P. A. Crowther, P. J. Dean, and W. F. Sherman, "Excitation spectrum of aluminum acceptors in diamond under uniaxial stress," *Physical Review*, vol. 154, no. 3, pp. 772–785, 1967.
- [81] T. Tshepe, C. Kasl, J. F. Prins, and M. J. R. Hoch, "Metal-insulator transition in boron-ion-implanted diamond," *Physical Review B*, vol. 70, no. 24, Article ID 245107, 7 pages, 2004.
- [82] O. E. Tall, N. J. Renault, M. Sigaud, and O. Vittori, "Anodic stripping voltammetry of heavy metals at nanocrystalline boron-doped diamond electrode," *Electroanalysis*, vol. 19, no. 11, pp. 1152–1159, 2007.
- [83] M. A. Q. Alfaro, S. Ferro, C. A. Martínez-Huitle, and Y. M. Vong, "Boron doped diamond electrode for the wastewater treatment," *Journal of the Brazilian Chemical Society*, vol. 17, no. 2, pp. 227–236, 2006.
- [84] H. Yu, H. Wang, X. Quan, S. Chen, and Y. Zhang, "Amperometric determination of chemical oxygen demand using boron-doped diamond (BDD) sensor," *Electrochemistry Communications*, vol. 9, no. 9, pp. 2280–2285, 2007.
- [85] H. Yu, C. Ma, X. Quan, S. Chen, and H. Zhao, "Flow injection analysis of chemical oxygen demand (COD) by using a boron-doped diamond (BDD) electrode," *Environmental Science and Technology*, vol. 43, no. 6, pp. 1935–1939, 2009.
- [86] M. Panizza and G. Cerisola, "Application of diamond electrodes to electrochemical processes," *Electrochimica Acta*, vol. 51, no. 2, pp. 191–199, 2005.
- [87] H. Y. Chan, D. M. Aslam, J. A. Wiler, and B. Casey, "A novel diamond microprobe for neuro-chemical and -electrical recording in neural prosthesis," *Journal of Microelectromechanical Systems*, vol. 18, no. 3, pp. 511–521, 2009.
- [88] Y. Zhou and J. Zhi, "The application of boron-doped diamond electrodes in amperometric biosensors," *Talanta*, vol. 79, no. 5, pp. 1189–1196, 2009.

Review Article

Electrochemical Biosensor Based on Boron-Doped Diamond Electrodes with Modified Surfaces

Yuan Yu,¹ Yanli Zhou,² Liangzhan Wu,¹ and Jinfang Zhi¹

¹Key Laboratory of Photochemical Conversion and Optoelectronic Materials, Technical Institute of Physics and Chemistry, No. 2 Beiyitiao, Zhongguancun, Haidian District, Beijing 100190, China

²Department of Chemistry, Shangqiu Normal University, No. 298 Wenhua Road, Shangqiu 476000, China

Correspondence should be addressed to Jinfang Zhi, zhi-mail@mail.ipc.ac.cn

Received 19 June 2011; Revised 8 September 2011; Accepted 13 September 2011

Academic Editor: Giancarlo R. Salazar-Banda

Copyright © 2012 Yuan Yu et al. This is an open access article distributed under the Creative Commons Attribution License, which permits unrestricted use, distribution, and reproduction in any medium, provided the original work is properly cited.

Boron-doped diamond (BDD) thin films, as one kind of electrode materials, are superior to conventional carbon-based materials including carbon paste, porous carbon, glassy carbon (GC), carbon nanotubes in terms of high stability, wide potential window, low background current, and good biocompatibility. Electrochemical biosensor based on BDD electrodes have attracted extensive interests due to the superior properties of BDD electrodes and the merits of biosensors, such as specificity, sensitivity, and fast response. Electrochemical reactions perform at the interface between electrolyte solutions and the electrodes surfaces, so the surface structures and properties of the BDD electrodes are important for electrochemical detection. In this paper, the recent advances of BDD electrodes with different surfaces including nanostructured surface and chemically modified surface, for the construction of various electrochemical biosensors, were described.

1. Introduction

Combining the advantages of the electrochemical techniques, electrochemical biosensors have been increasingly developed for many applications in environmental monitoring, food analysis, detection of biological metabolites, and clinical chemistry, and so forth, due to their specificity, sensitivity, accuracy, and portability [1–3]. The performance of electrochemical biosensors mainly depend on the physical and chemical characteristics of the materials, including shape and structure, employed for the construction of the transducer and the methods used for the immobilization of biomolecules. Conventional carbon-based materials including, carbon paste, porous carbon, glassy carbon, and carbon nanotubes have been widely employed as electrochemical transducers in the field of biosensors due to simple preparation methods, large positive potential ranges, and suitability for chemical modification [4–7]. However, traditional carbon-based electrodes still suffer some drawbacks, such as electrode fouling, which limits their long-term stability and leads to frequent polishing or disposal of the electrode.

Boron-doped diamond (BDD) thin films, as one new kind of electrode materials, are gaining big researching interests. Nowadays, the development of diamond growth by chemical vapor deposition has enabled the preparation of the BDD electrodes with different surface structures on various substrates. The electrochemical properties of the BDD electrodes have also been intensively studied [8–12]. The results showed that the BDD electrodes possess many outstanding properties, including wide electrochemical potential window, low and stable capacitive background current, high response reproducibility and long-term response stability, and good biocompatibility. Therefore, BDD electrodes have been widely employed for the construction of various electrochemical biosensors. It was well known that electrochemical reactions proceed at the interface between electrolyte solutions and electrodes surfaces, so the surface structures and properties of BDD electrodes are important for electrochemical biosensors. The present paper summarizes the biosensors based on BDD electrodes materials with different surfaces, including nanostructured surfaces and chemically modified surface.

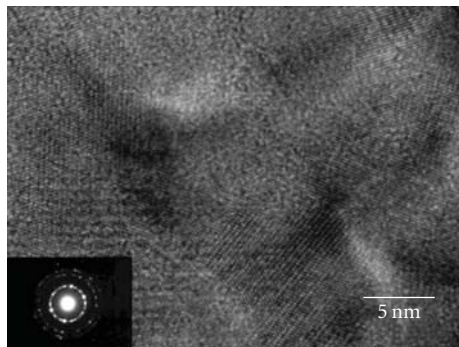


FIGURE 1: TEM image and ED pattern for a boron-doped nanocrystalline diamond thin film.

2. Biosensors Based on BDD Electrodes with Nanostructured Surfaces

Nanostructured materials are considered to be much more efficient and selective than traditional bulk materials for their high surface areas and high surface energy [13, 14]. For example, many carbon-based nanostructured materials have been shown to be ideal for biosensing applications since they are conductive, biocompatible, and easily functionalized and possess very large surface areas [15, 16]. However, the main disadvantage of these carbon-based materials is nonstability of potential, which remains a limiting factor. Therefore, it is of interest to inquire if BDD electrodes with much smaller lateral dimensions can be fabricated, and what properties such electrodes might possess. The methods for fabrication of nanostructured diamond films, such as diamond nanowhiskers and nanorods by microfabrication methods involving RIE (reactive ion etching) or plasma etching on diamond films [17–20], and homoepitaxially grown diamond nanorods by CVD technique using template [21, 22] have been reported. However, conductive nanostructured diamond films used in electro- or biochemistry applications have seldom been reported. Surface modification of the BDD electrodes is necessary to improve their detection performance; however, the ideal characteristics of the BDD electrodes could be lost. Hence, it is critical to create functional BDD films without the loss of favorable properties. This can be realized by creating nanostructured BDD electrodes. Show et al. deposited boron-doped nanocrystalline diamond thin films using CVD method from a $\text{CH}_4/\text{H}_2/\text{Ar}$ source gas mixture [23]. Figure 1 is a TEM image of the BDD film showing that the BDD film consists of 10–15 nm randomly oriented but atomically ordered diamond grains. The films exhibited a wide working potential window, a low voltammetric background current, and good responsiveness for $\text{Fe}(\text{CN})_6^{3-/4-}$, $\text{Ru}(\text{NH}_3)_6^{2+/3+}$, $\text{IrCl}_6^{2-/3-}$, and methyl viologen without any pretreatment. It was found to be useful for the detection of trace metal ions, such as Ag(I), Cu(II), Cd(II), Pb(II), and Zn(II).

Luo et al. combined the electroless metal deposition (EMD) and hot filament chemical vapour deposition (HFCVD) technique preparing a BDD nanorod forest

(BDDNF) electrode on silicon nanowires arrays, that is, transforming a planar BDD electrode to a three-dimensional nanostructured BDD electrode (Figures 2(a) and 2(b)) [24]. The BDD nanorod forest was demonstrated as a nonenzymatic glucose biosensor by simply putting it into the glucose solution. The BDD nanorod forest electrode exhibits very attractive electrochemical performance compared to conventional planar BDD electrodes, notably improved sensitivity and selectivity for glucose detection. The limit of detection was estimated at a signal-to-noise ratio of 3 to $0.2 \pm 0.01 \mu\text{M}$. Selective determination of glucose in the presence of AA and UA and high stability were also obtained.

Recently, a novel boron-doped diamond micronetwork (BDDMN) film shown in Figures 2(c) and 2(d) has been successfully prepared by the authors via a photomask microfabrication process coupled with synthesis of silicon nanowires and BDD films [25]. Uric acid (UA) was used to estimate the electrochemical biosensing properties of the BDDMN electrode. Studies of the amperometric response of the BDDMN electrode and the planar BDD electrode were carried out through successive addition of UA in 0.1 M PBS solution under continuously stirring conditions. As shown in Figure 3. The current response of the BDDMN electrode was higher than that of the BDD electrode for the same concentration of UA. Sensitivity for UA was obtained with $21.35 \mu\text{A}\text{mM}^{-1}$ on the BDDMN electrode and $6.28 \mu\text{A}\text{mM}^{-1}$ on the planar electrode by linearization of the response current on the concentration. This result is ascribed to the network structure that could change the reactive sites, resulting in different adsorption sites and catalytic effect toward the analyte.

A simple method to prepare a BDD nanoglass array on a BDD film by reactive ion etching has been reported [26, 27]. The nanoglass array with $\sim 20 \text{ nm}$ diameter and $\sim 200 \text{ nm}$ length has been formed on the BDD surface after oxygen plasma etching treatment. The effect of the nanoglass array structure on the enhancement of electrocatalytic activity of electrodes was demonstrated by detecting DA and UA. On the BDD nanoglass array electrode, there are two well-defined peaks at 0.38 V and 0.78 V in neutral buffer solution, corresponding to the oxidation of DA and UA. This result is ascribed to the nanoglass array on the BDD surface that could change the reactive sites, resulting in a different adsorption affinity and catalytic effect toward the different substances, thus enhancing the selectivity for some coexisting compounds [26]. The electrochemical behavior of different redox systems and detection of catechol were performed on the as-grown boron-doped diamond (BDD) electrodes and the nanoglass array BDD. Compared with as-grown BDD, the electron transfer on the nanoglass array BDD surface became slower toward the negatively charged $\text{Fe}(\text{CN})_6^{3-}$ whereas changed little toward the positively charged $\text{Ru}(\text{NH}_3)_6^{3+}$. The nanoglass array BDD showed higher electrocatalytic activity toward the catechol detection than did the as-grown BDD. Good linearity was observed for a concentration range from 5 to 100 mM with a sensitivity of $719.71 \text{ mA M}^{-1} \text{ cm}^{-2}$ and a detection limit of 1.3 mM on the nanoglass array BDD [27].

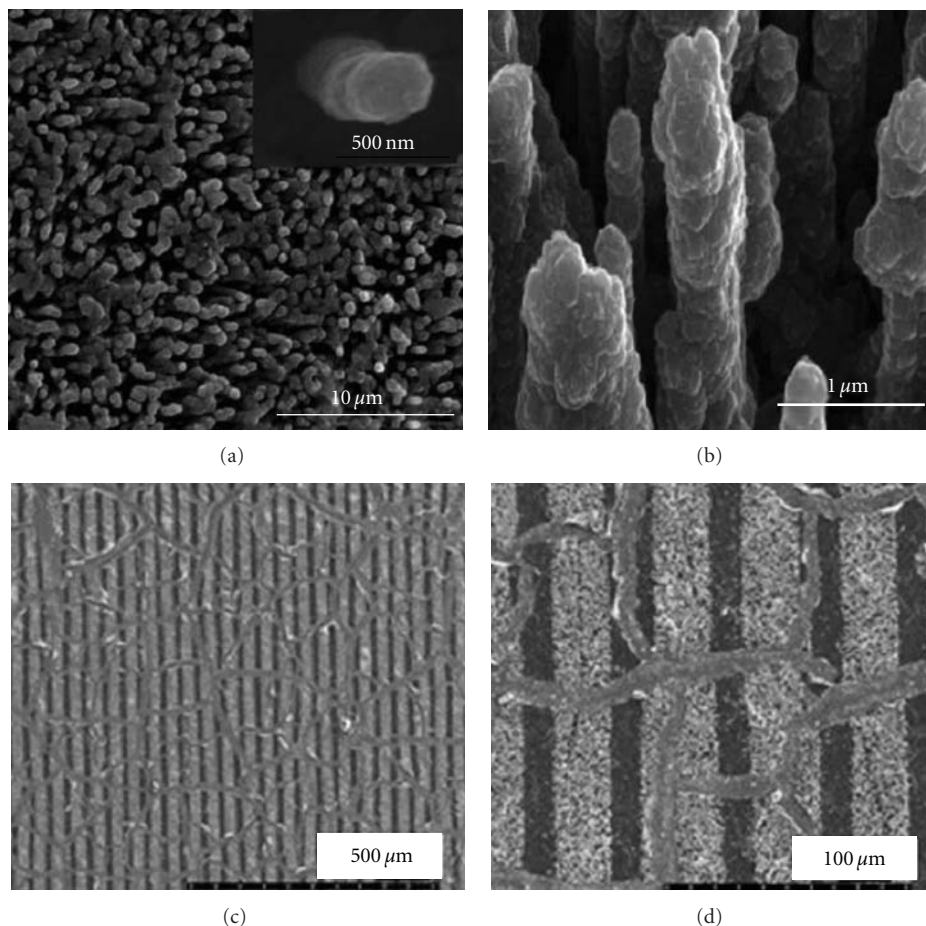


FIGURE 2: Images of BDD films with nanostructured surfaces: (a) and (b) BDD nanorod forest electrode image taken from different magnifications; (c) and (d) 2D micronetwork of boron-doped diamond film taken from different magnifications.

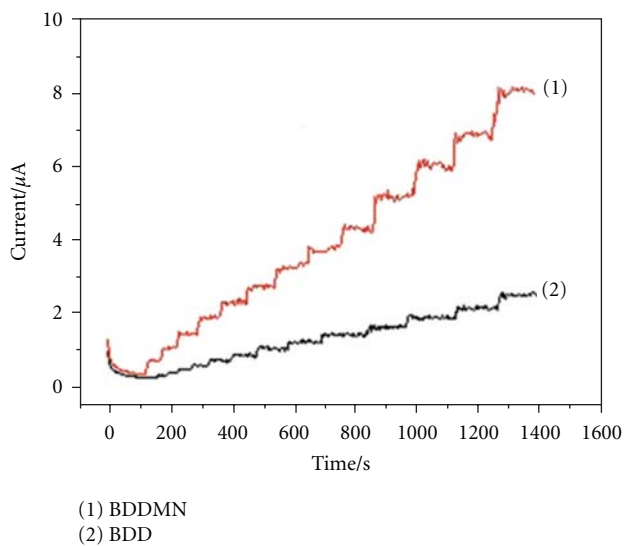


FIGURE 3: Current-time responses of the BDD electrode (1) and the BDDMN electrode (2) through successive addition of UA (each step of the curves indicates 0.013, 0.026, 0.04, 0.052, 0.064, 0.076, 0.088, 0.1, 0.15, 0.2, 0.25, 0.3, 0.35, and 0.4 mM from low to high) in 0.1 M PBS solution at an applied potential of 0.4 V (versus SCE, for both electrodes, the oxidation current response occurs at 0.4 V).

The nanostructured BDD electrodes can improve the reactive site, accelerate the electron transfer, promote the electrocatalytic activity, and enhance the selectivity [28]. They not only overcome the disadvantages of the as-grown BDD film electrodes but also avoid the disadvantages associated with surface modification of the electrode. The above excellent properties of these nanostructured BDD electrodes indicate the promise for real biochemical applications.

3. Electrochemical Biosensors Based on Planar BDD Electrodes with Chemically Modified Surface

Electrochemical reactions perform at the interface between electrolyte solutions and the electrodes surfaces, so the surface properties of the BDD electrodes are important for electrochemical detection. The recent advances of BDD electrodes with different surfaces including hydrogen-terminated, oxygen-terminated, metal nanoparticles modified, amine-terminated, and carboxyl-terminated thin films, for the construction of various biosensors or the direct detection of biomolecules were described.

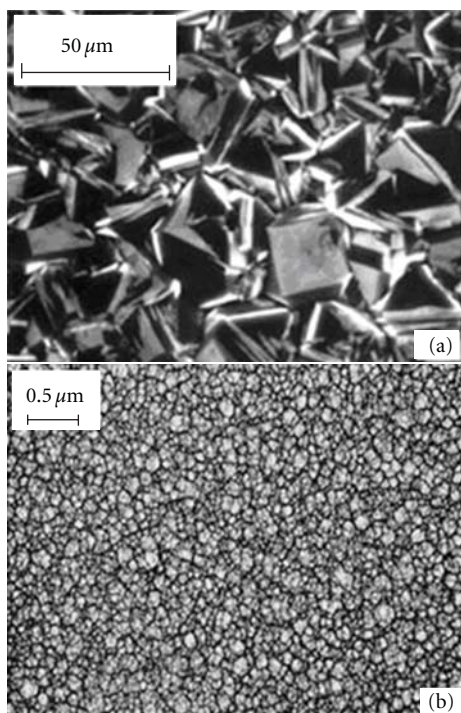


FIGURE 4: SEM images of (a) a polycrystalline BDD thin film and (b) a nanocrystalline BDD thin film.

3.1. Electrochemical Biosensors Based on Hydrogen-Terminated BDD Electrode. The surface of an as-deposited polycrystalline BDD electrode (Figure 4(a)) and nanocrystalline BDD electrode (Figure 4(b)) prepared by chemical vapor deposition using hydrogen gas as carrier gas is recognized to be hydrogen-terminated, and its scanning electron microscopy images is shown in Figure 4(a) [10]. A clean and homogeneous hydrogen-terminated BDD surface could be obtained by treatment of oxygen-terminated BDD surfaces with hydrogen plasma or heating at high temperatures (800–1000°C) under hydrogen atmosphere. The hydrogen-terminated BDD electrodes have high stability and sensitivity for analysis of a number of biological species, and the performances for the detection of several selected biomolecules are summarized.

Ivandini et al. reported that oxalic acid could be electrochemically detected at as-deposited BDD electrodes [29]. The BDD electrodes exhibited well-defined peaks of oxalic acid oxidation, as shown in Figure 5, with a linear response range of 0.05–10 μM and a detection limit of ~0.5 nM (S/N = 3). For comparison, at a glassy carbon electrode, an ill-defined peak and a high background signal were observed. Clearly, the as-deposited BDD electrode showed higher sensitivity than the bare glassy carbon electrode for the detection of oxalic acid because of its low and stable background current. Moreover, at an oxygen-terminated BDD electrode, no peak was observed within the cycling potential from 0 to 2.2 V (versus Ag/AgCl), which could be ascribed to the repulsion between the negative electrode surface and the negatively charged molecules due to its two

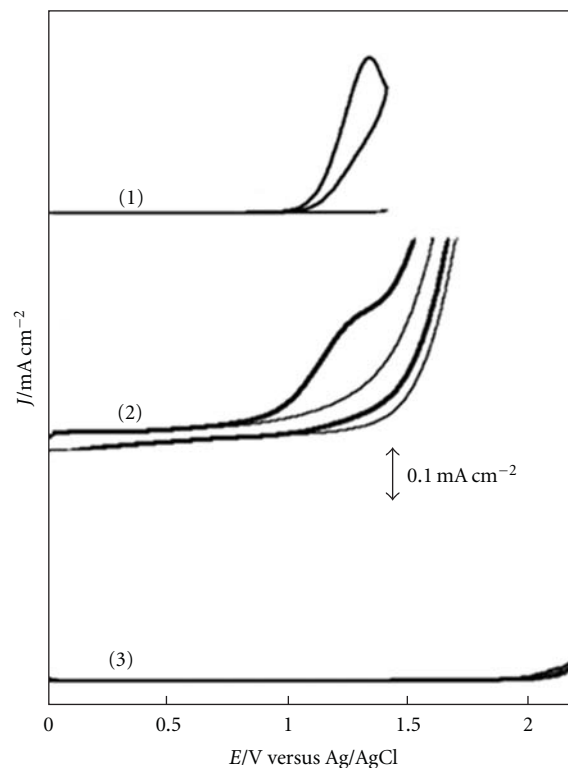


FIGURE 5: Cyclic voltammograms of 0.1 M PBS (pH 2.1) at the as-deposited (hydrogen-terminated) BDD (1), glassy carbon (2), and oxygen-terminated BDD (3) electrodes with (bold line) and without (thin line) the presence of 100 μM oxalic acid. The scan rate was 100 mV s⁻¹.

carboxyl functional groups, suggesting that surface termination contributed highly to the control of the electrochemical reaction.

L-cysteine (CySH), a sulfur-containing amino acid, plays crucial roles in biological systems, and its deficiency is associated with a number of clinical situations, for example, liver damage, skin lesions, slowed growth, and AIDS. Therefore, it is very important to investigate the electrochemical behavior and sensitive detection of CySH. Noble metal and bare carbon electrodes have been used for the study of CySH oxidation reaction, but, in this case, the detection selectivity and sensitivity was low due to the high potential. Although high electrocatalytic activity was observed at chemically modified electrodes, the activity inevitably decreased with time.

Spătaru et al. reported the studies of the electrochemical oxidation of CySH at as-deposited BDD electrodes [30]. Voltammetric and polarization studies showed that the CySH oxidation mechanism at BDD electrodes involved the dissociation of the proton from the thiol group, followed by the electrochemical oxidation of the CyS⁻ species, while, at glassy carbon electrodes, the electrochemical oxidation reaction was controlled by the desorption of the reaction products. For this reason, CySH oxidation had higher stability and sensitivity at BDD electrodes compared to glassy

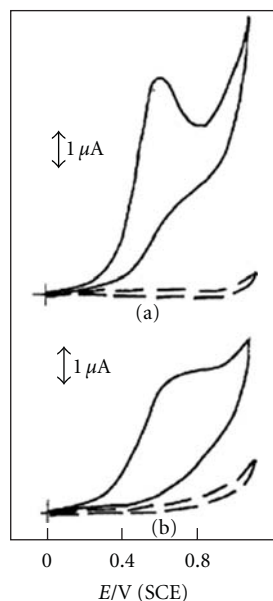


FIGURE 6: Cyclic voltammograms recorded in 0.5 M KHCO_3 containing 1 mM CySH: initial potential, 0.0 V (SCE); sweep rate, 5 mV s^{-1} . (a) BDD electrode; (b) GC electrode. (Dashed lines represent background current.)

carbon electrodes. Micromolar concentration range of 0.1–100 μM and low detection limit of 21 nM ($S/N = 3$) were obtained for CySH detection at the BDD electrodes. The deactivation of the electrode with time, which was common at the chemically modified electrodes, was also avoided due to the extreme electrochemical stability of the BDD electrode (as shown in Figure 6). That is to say, the use of BDD electrodes results in a simple and useful analytical procedure for the detection of CySH.

In addition, hydrogen-terminated BDD shows advantages for electrochemical oxidation of other biological compounds, especially negative charged molecules, such as nicotinamide adenine dinucleotide (NADH) [31, 32], biogenic amines [33], glucose [34–36], Tyr [37], Trp [38], Hb [39], and DNA [40–42] in the given buffer solutions, based on their wide potential window and low background current. In most of these studies, BDD electrode was found to outperform glassy carbon in terms of stability and sensitivity. Fundamental studies on BDD films have revealed that the lack of oxygen functional groups on the as-deposited BDD surface and the very low tendency for adsorption of most chemical species on the inert surface of diamond are mainly responsible for the superior performance of the BDD electrodes. Additionally, the oxidation reaction of the above biomolecules is very less at an oxygen-terminated BDD electrode because of the electrostatic repulsion between its carbon-oxygen dipoles and the negative charged compounds. However, at the hydrogen-terminated surface, the positive dipolar field created attracts the above biomolecules, facilitating the electrochemical reaction. Therefore, the control of surface termination is important for the electrochemical detection of some negative charged molecules by the use of BDD electrodes.

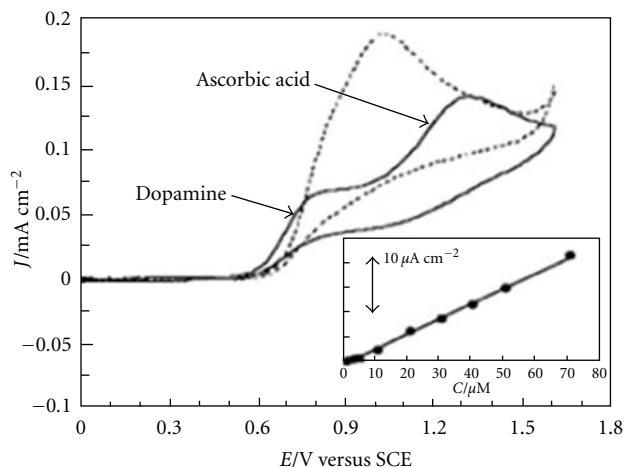


FIGURE 7: Cyclic voltammogram for a 0.1 M HClO_4 solution containing 0.1 mM DA and 1 mM AA at as-deposited and oxidized BDD electrodes. The scan rate was 100 mV s^{-1} . Inset shows a cyclic voltammogram calibration curve for DA in 0.1 M HClO_4 solution in the presence of 1 mM AA.

3.2. Electrochemical Biosensors Based on Oxygen-Terminated BDD Electrode. Dopamine (DA) is an important neurotransmitter in mammalian central nervous system. A loss of DA-containing neurons may result in serious disease such as Parkinson's disease. Recently, some nanomaterials, for example, carbon nanotubes [43], gold nanoparticles [44], and polymer thinfilm [45] modified glassy carbon electrodes, were used to carry out the simultaneous detection of DA and AA. However, there are difficulties remaining to be solved, such as complicated preparation methods and long-term stability.

Fujishima's group researched the electrochemical detection of DA in the presence of AA at BDD electrodes [46, 47]. As shown in Figure 7, at as-deposited BDD (hydrogen-terminated) electrode, the anodic peak potential ($E_{p,a}$) of DA and AA was 0.76 and 0.80 V (versus saturated calomel electrode, SCE) in 0.1 M HClO_4 , respectively. After electrochemical treatment of BDD (oxygen-terminated) electrode, the $E_{p,a}$ of DA and AA was 0.80 and 1.3 V (versus SCE), respectively. Cyclic voltammogram for a solution containing both DA and AA in 0.1 M HClO_4 at the oxygen-terminated BDD electrode exhibited two well-defined anodic peaks. Therefore, DA can be selectively determined in the presence of AA using the oxygen-terminated BDD electrode, and, as a result, a low detection limit of 50 nM ($S/N = 3$) was obtained. Possible explanation of the selective detection for DA is that the oxidized BDD surface acquires surface dipoles as a result of introducing C=O functional groups, which then electrostatically repel the oxygen-containing group on AA with strong dipoles. That is to say, the AA oxidation is impeded owing to the high potential required and the spatial locations separates from oxidized BDD surface. For the protonated DA, the interaction between the ammonium group of DA is relatively strong with both hydrogen- and oxygen-terminated BDD electrode, so that the equilibrium

distances and the electron transfer rates are not greatly different.

Popa et al. reported the selective detection of UA in the presence of AA at anodized BDD electrodes [48]. The C=O groups of BDD electrodes were expected to form a surface dipolar field, which repelled AA molecules that have oxygen-containing functional groups surrounding a central core, as noted in Section 3.1. In differential pulse voltammograms, the oxidation peak potential of AA was ~ 450 mV more positive than that of UA at oxidized BDD electrodes. Thus, the detection of UA could obtain excellent selectivity and sensitivity with a detection limit of 1.5×10^{-8} M ($S/N = 3$) in the presence of high concentrations of AA by use of chronoamperometry. Meanwhile, the oxidized BDD electrode exhibited high reproducibility and long-term stability (repeatedly used for more than 3 months), and the practical analytical utility was demonstrated in human urine and serum.

Moreover, Terashima et al. studied the amperometric detection of GSSG and GSH at anodically oxidized BDD electrodes [49]. Ivandini et al. described the simultaneous detection of purine and pyrimidine bases at BDD electrodes [50]. At anodized BDD electrode, well-defined anodic peaks were observed for the oxidation of purine and pyrimidine bases in acid medium due to its high overpotential of oxygen evolution reaction. In brief, the oxygen-terminated BDD electrodes have outstanding features in a much wider potentials window and higher surface stability from fouling compared to hydrogen-terminated BDD electrodes. Importantly, the oxygen-terminated BDD electrodes are able to achieve selective detection of certain compounds under certain conditions. The significant advantages including very ease of preparation, very high stability, high sensitivity, and good selectivity make oxygen-terminated BDD electrodes an interesting candidate for the study of the direct detection of biological molecules.

3.3. Biosensors Based on Amine-Terminated BDD Electrodes. Generally, amine-terminated BDD electrodes could be achieved by modification of several methods, such as etching a hydrogen-terminated BDD surface by NH_3 plasma, chemical modification of an oxidized BDD surface with (3-aminopropyl) triethoxysilane [51], photochemical reaction of amino molecules by free radical mechanism [52], and diazonium functionalization of 4-nitrobenzenediazonium tetrafluoroborate with combined chemical and electrochemical processes [53]. Thus, a layer of amine groups introduced on the BDD surface could serve as binding sites for attachment of biomolecules.

Notsu et al. reported the immobilization of tyrosinase on a BDD electrode. Firstly, (3-aminopropyl) triethoxysilane was used to modify BDD electrode treated by electrochemical oxidation and then a tyrosinase film cross-linked with glutaraldehyde. The low limit with 10^{-6} M for bisphenol-A was achieved at the enzyme electrodes by using a flow injection system. However, the tyrosinase-modified BDD electrode retained its initial activity only for a few days in storage under dry conditions, due to weak bonding of (3-aminopropyl) triethoxysilane with BDD surface.

To improve the stability of tyrosinase-based BDD electrodes, Zhi's group studied the covalent immobilization of tyrosinase onto the amine-terminated BDD electrode [54, 55]. The amine active BDD surfaces were obtained by two methods. One was that the hydrogen-terminated BDD surface was treated with allylamine by photochemical reaction. Another was that the hydrogen-terminated BDD surface was treated with 4-nitrobenzenediazonium tetrafluoroborate. Both of the two tyrosinase-modified BDD electrodes by the above methods exhibited fast response, high sensitivity, and wide linear range for the detection of phenolic compounds, as shown in Figure 8 (taking diazonium method as an example). The sensitivity of the enzyme electrode by diazonium method was also higher than those of the tyrosinase biosensors reported [56–58], which could be attributed to the high and reliable loading of enzyme by present method. The two developed enzyme electrodes could retain about 90% of its initial activity for the response of phenols after 1 month. The high stability could be ascribed to the strongly covalent bonding of tyrosinase to the BDD electrodes and the high chemical and electrochemical stability of the BDD substrates. To sum up, the amine-functionalized BDD electrodes is an interesting alternative for application in biosensing technology.

3.4. Biosensors Based on Carboxyl-Terminated BDD Electrodes. The sp^2 -bonded carbon phase on grain boundaries of nanocrystalline BDD films can provide charge carriers and high carrier mobility pathways, which may lead to better reversible properties of electrodes for redox systems [59]. Thus, BDD electrode is expected to be a more suitable candidate to provide a high activity for biosensors. Zhi's group reported the functionalization of nanocrystalline BDD films via photochemical reaction with undecylenic acid methyl ester and subsequent removal of the protection ester groups to produce a carboxyl-terminated surface [60]. Then cytochrome *c* was successfully immobilized on nanocrystalline BDD electrode by the bonding of negatively charged carboxylic groups and positively charged lysine residue of Cyt *c* (pI 10). The cytochrome *c*-modified nanocrystalline BDD electrode showed a pair of quasi-reversible redox peaks with a formal potential (E^0) of 0.061 V (versus Ag/AgCl) in 0.1 M PBS (pH 7.0) and a high electron transfer constant (k_s) of $5.2 \pm 0.6 \text{ s}^{-1}$.

Photochemical surface reaction between hydrogen-terminated BDD and 4-pentenoic acid was used to modify the BDD electrode surface, producing carboxyl-terminated surface [61]. The differential pulse voltammogram for the solution containing DA and AA at the above carboxyl-terminated surface showed well-separated oxidation peaks for DA and AA at 0.4 and 0.6 V, respectively, and the sensitivity enhanced distinctly than the oxygen-terminated BDD electrodes. The good selectivity and sensitivity were partly due to simple electrostatic effects and partly due to suppression of the polymerization of DA oxidation products by the terminal carboxyl groups.

3.5. Biosensors Based on Metal (Oxide)-Modified BDD Electrodes. Assembly of ordered metal (oxide) nanoparticles, in

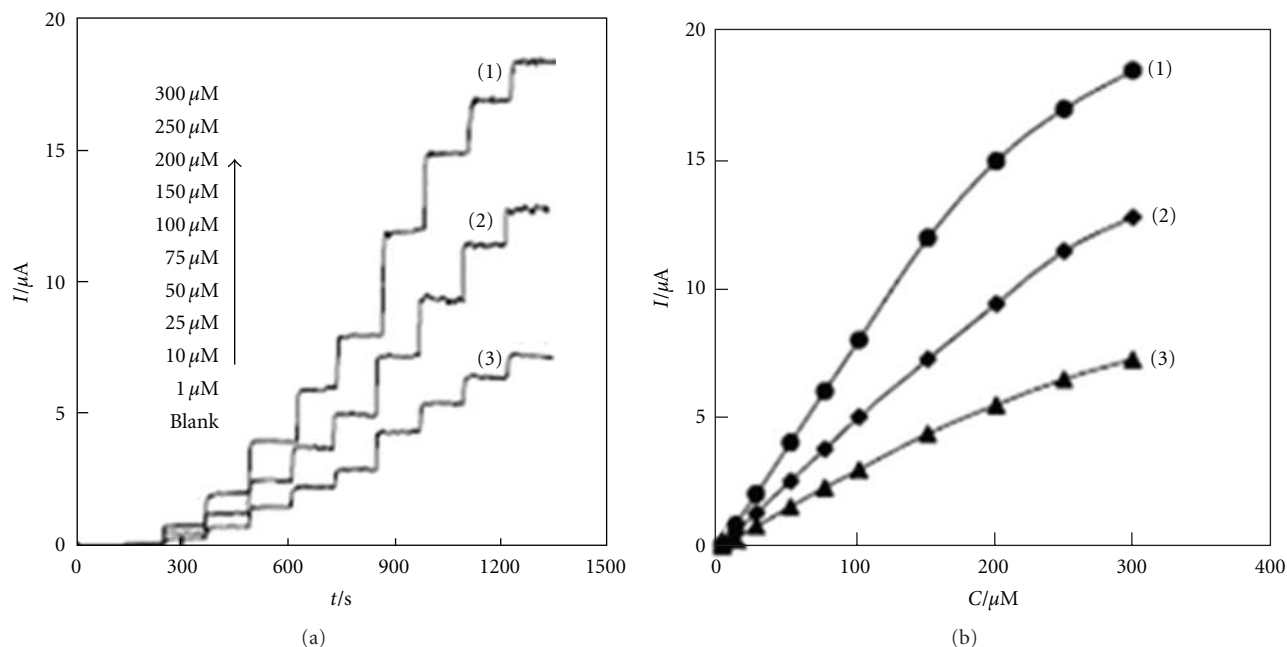


FIGURE 8: (a) Current-time recording and (b) calibration curve of the tyrosinase-modified BDD electrode to *p*-cresol (1), 4-chlorophenol (2), and phenol (3). Supporting electrolyte was 0.1 M PBS (pH 6.5). Applied potential was -0.15 V versus SCE.

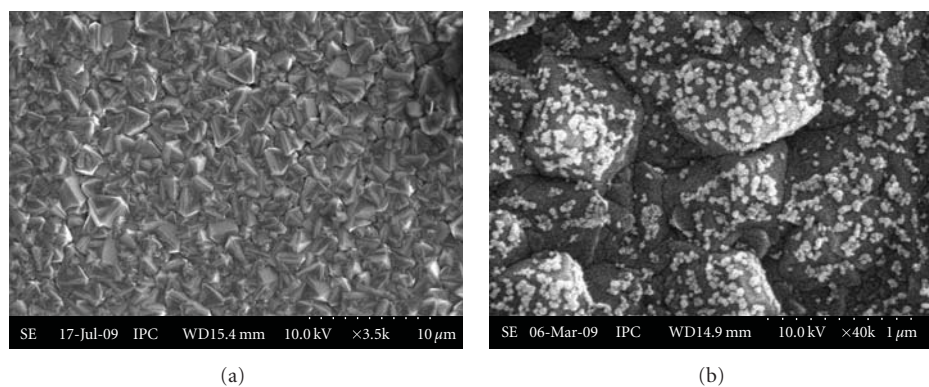


FIGURE 9: SEM images obtained from the BDD (a) and OT-Au-BDD (b) surfaces.

particular gold nanoparticles, has a wide range of applications in electronics, catalysis, and analysis. Metal (oxide) nanoparticles could be immobilized on diamond surface by vacuum vapor deposition, electrochemical deposition, sputtering, or layer-by-layer self-assembly.

Wang et al. designed an octanethiolate gold particles modified boron-doped diamond (OT-Au-BDD) electrode for CPB analysis (Figure 9) [62]. The alkane chains come from octanethiol used as an adsorbent of CPB on the surface of electrode, and the length of alkane chain was chosen in a suitable range which made the adsorbent not deteriorate the electron transfer too much. The obtained OT-Au-BDD electrode displayed a detection limit of $0.2 \mu\text{M}$ and good reproducibility in CPB analysis. Weng et al. reported that BDD electrode was modified with gold clusters by electrodeposition and the electrochemical performance of DA and AA was investigated on the Au/BDD electrode

[63]. The electrochemical oxidation of purine bases, adenine or guanine, and DNA have been investigated at a nickel nanoparticle modified boron-doped diamond electrode by Harfield et al. [64]. An oxidative response was observed at the Ni-BDDE for each analyte, particularly notable of the adenine as the oxidation overpotential was reduced to below 0.5 V versus SCE and was otherwise unobserved at the unmodified electrode. Other metal nanoparticles modified BDD electrode, such as antimony [65], bismuth [66], cobalt [67], copper [68–70], and platinum [71–73], have been widely investigated. The benefits and use of nanoparticles in electroanalysis are discussed in more detail in the extensive review by Welch and Compton [74] in 2006 that was recently updated by Campbell and Compton [75].

Terashima et al. demonstrated the electrocatalytic activity of hydrous iridium oxide (IrO_x) modified on BDD electrodes by electrodeposition [76]. Highly dispersed and stable IrO_x

nanoparticles could be obtained by the control of the deposition conditions, and the deposition of a low amount of IrO_x (ca. 2 nmol cm⁻²) on the BDD electrode exhibited an excellent analytical performance for H₂O₂ detection with a wide dynamic range (0.1–100 μM). The sensitivity for H₂O₂ was ca. 10 times higher than that of the usual Pt-bulk electrodes. Furthermore, the IrO_x modified BDD electrodes enabled H₂O₂ detection in neutral media, which was an advantage compared to sensors obtained by IrO_x deposition on other substrates.

In brief, the modification of metal (oxide) nanoparticles on the BDD electrode makes it a candidate to prepare highly active electrode for the catalytic oxidation (or reduction) of biomolecules. Especially, the immobilization of charged nanoparticles on BDD electrode could determinate special biomolecules in biological system with high selectivity and high sensitivity. The metal nanoparticle modification of BDD offers a simple yet effective approach to enhancing the electroanalytical ability of the electrode material.

4. Conclusions

In conclusion, several functional BDD electrodes, including nanostructured BDD surface electrodes, and chemically modified BDD surface electrodes, such as hydrogen-terminated, oxygen-terminated, amine-terminated, and carboxyl-terminated and metal-modified BDD films, have been used for determining various bioanalytes over the past decade or so. Because of the excellent properties of BDD substrates, these BDD-based biosensors exhibited good performances in terms of high sensitivity, selectivity, reproducibility, and long-term stability. That is to say, BDD electrodes are interesting candidates for the construction of electrochemical biosensors or the direct electrochemical detection of biomolecules.

Acknowledgment

The authors are grateful for the support of the National Science Foundation of China (Grant no. 21175144 and 20903111).

References

- [1] F. Febbraio, L. Merone, G. P. Cetrangolo, M. Rossi, R. Nucci, and G. Manco, "Thermostable esterase 2 from *Alicyclobacillus acidocaldarius* as biosensor for the detection of organophosphate pesticides," *Analytical Chemistry*, vol. 83, no. 5, pp. 1530–1536, 2011.
- [2] J. Wang, "Electrochemical glucose biosensors," *Chemical Reviews*, vol. 108, no. 2, pp. 814–825, 2008.
- [3] G. S. Wilson and Y. Hu, "Enzyme-based biosensors for in vivo measurements," *Chemical Reviews*, vol. 100, no. 7, pp. 2693–2704, 2000.
- [4] N. J. Forrow and S. W. Bayliff, "Electroanalysis of dopamine and NADH at conductive diamond electrodes," *Biosensors and Bioelectronics*, vol. 21, pp. 581–587, 2005.
- [5] R. Maalouf, A. Soldatkin, O. Vittori et al., "Study of different carbon materials for amperometric enzyme biosensor development," *Materials Science and Engineering C*, vol. 26, no. 2-3, pp. 564–567, 2006.
- [6] A. Kowalczyk, A. Nowicka, R. Jurczakowski, M. Fau, A. Krolikowska, and Z. Stojek, "Construction of DNA biosensor at glassy carbon surface modified with 4-aminoethylbenzediazonium salt," *Biosensors and Bioelectronics*, vol. 26, no. 5, pp. 2506–2512, 2011.
- [7] J. Wang and Y. Lin, "Functionalized carbon nanotubes and nanofibers for biosensing applications," *Trends in Analytical Chemistry*, vol. 27, no. 7, pp. 619–626, 2008.
- [8] F. Bouamrane, A. Tadjeddine, J. E. Butler, R. Tenne, and C. Lévy-Clément, "Electrochemical study of diamond thin films in neutral and basic solutions of nitrate," *Journal of Electroanalytical Chemistry*, vol. 405, no. 1-2, pp. 95–99, 1996.
- [9] A. E. Fischer, Y. Show, and G. M. Swain, "Electrochemical performance of diamond thin-film electrodes from different commercial sources," *Analytical Chemistry*, vol. 76, no. 9, pp. 2553–2560, 2004.
- [10] R. G. Compton, J. S. Foord, and F. Marken, "Electrochemical detection of tyrosine derivatives and protein tyrosine kinase activity using boron-doped diamond electrodes," *Electroanalysis*, vol. 15, pp. 1349–1363, 2003.
- [11] M. C. Granger, M. Witek, J. Xu et al., "Standard electrochemical behavior of high-quality, boron-doped polycrystalline diamond thin-film electrodes," *Analytical Chemistry*, vol. 72, no. 16, pp. 3793–3804, 2000.
- [12] T. A. Ivandini, R. Sato, Y. Makide, A. Fujishima, and Y. Einaga, "Electroanalytical application of modified diamond electrodes," *Diamond and Related Materials*, vol. 13, no. 11-12, pp. 2003–2008, 2004.
- [13] H. Zheng, C. Ma, W. Wang, and J. Huang, "Nanorod tungsten carbide thin film and its electrocatalytic activity for nitromethane electroreduction," *Electrochemistry Communications*, vol. 8, no. 6, pp. 977–981, 2006.
- [14] H. Lee, S. W. Yoon, E. J. Kim, and J. Park, "In-situ growth of copper sulfide nanocrystals on multiwalled carbon nanotubes and their application as novel solar cell and amperometric glucose sensor materials," *Nano Letters*, vol. 7, no. 3, pp. 778–784, 2007.
- [15] V. Vamvakaki, K. Tsagaraki, and N. Chaniotakis, "Carbon nanofiber-based glucose biosensor," *Analytical Chemistry*, vol. 78, no. 15, pp. 5538–5542, 2006.
- [16] S. E. Baker, P. E. Colavita, K. Y. Tse, and R. J. Hamers, "Functionalized vertically aligned carbon nanofibers as scaffolds for immobilization and electrochemical detection of redox-active proteins," *Chemistry of Materials*, vol. 18, no. 18, pp. 4415–4422, 2006.
- [17] E. S. Baik, Y. J. Baik, S. W. Lee, and D. Jeon, "Fabrication of diamond nano-whiskers," *Thin Solid Films*, vol. 377-378, pp. 295–298, 2000.
- [18] E. S. Baik, Y. J. Baik, and D. Jeon, "Aligned diamond nanowhiskers," *Journal of Materials Research*, vol. 15, no. 4, pp. 923–926, 2000.
- [19] N. Yang, H. Uetsuka, E. Osawa, and C. E. Nebel, "Vertically aligned nanowires from boron-doped diamond," *Nano Letters*, vol. 8, no. 11, pp. 3573–3576, 2008.
- [20] S. Okuyama, S. I. Matsushita, and A. Fujishima, "Periodic submicrocylinder diamond surfaces using two-dimensional fine particle arrays," *Langmuir*, vol. 18, no. 22, pp. 8282–8287, 2002.

- [21] H. Masuda, T. Yanagishita, K. Yasui et al., "Synthesis of well-aligned diamond nanocylinders," *Advanced Materials*, vol. 13, no. 4, pp. 247–249, 2001.
- [22] A. S. Barnard, M. L. Terranova, and M. Rossi, "Density functional study of H-induced defects as nucleation sites in hybrid carbon nanomaterials," *Chemistry of Materials*, vol. 17, no. 3, pp. 527–535, 2005.
- [23] Y. Show, M. A. Witek, P. Sonthalia, and G. M. Swain, "Characterization and electrochemical responsiveness of boron-doped nanocrystalline diamond thin-film electrodes," *Chemistry of Materials*, vol. 15, no. 4, pp. 879–888, 2003.
- [24] D. Luo, L. Wu, and J. Zhi, "Fabrication of boron-doped diamond nanorod forest electrodes and their application in nonenzymatic amperometric glucose biosensing," *ACS Nano*, vol. 3, no. 8, pp. 2121–2128, 2009.
- [25] D. Luo, L. Wu, and J. Zhi, "2-Dimensional micro-network of boron-doped diamond film: fabrication and electrochemical sensing application," *Chemical Communications*, vol. 46, no. 35, pp. 6488–6490, 2010.
- [26] M. Wei, C. Terashima, M. Lv, A. Fujishima, and Z. Z. Gu, "Boron-doped diamond nanoglass array for electrochemical sensors," *Chemical Communications*, no. 24, pp. 3624–3626, 2009.
- [27] M. Lv, M. Wei, F. Rong, C. Terashima, A. Fujishima, and Z. Z. Gu, "Electrochemical detection of catechol based on as-grown and nanoglass array boron-doped diamond electrodes," *Electroanalysis*, vol. 22, no. 2, pp. 199–203, 2010.
- [28] N. Yang, R. Hoffmann, W. Smirnov, A. Kriele, and C. E. Nebel, "Direct electrochemistry of cytochrome c on nanotextured diamond surface," *Electrochemistry Communications*, vol. 12, no. 9, pp. 1218–1221, 2010.
- [29] T. A. Ivandini, T. N. Rao, A. Fujishima, and Y. Einaga, "Electrochemical oxidation of oxalic acid at highly boron-doped diamond electrodes," *Analytical Chemistry*, vol. 78, no. 10, pp. 3467–3471, 2006.
- [30] N. Spătaru, B. V. Sarada, E. Popa, D. A. Tryk, and A. Fujishima, "Voltammetric determination of L-cysteine at conductive diamond electrodes," *Analytical Chemistry*, vol. 73, no. 3, pp. 514–519, 2001.
- [31] A. Fujishima, T. N. Rao, E. Popa, B. V. Sarada, I. Yagi, and D. A. Tryk, "Electroanalysis of dopamine and NADH at conductive diamond electrodes," *Journal of Electroanalytical Chemistry*, vol. 473, no. 1, pp. 179–185, 1999.
- [32] T. N. Rao, I. Yagi, T. Miwa, D. A. Tryk, and A. Fujishima, "Electrochemical oxidation of NADH at highly boron-doped diamond electrodes," *Analytical Chemistry*, vol. 71, no. 13, pp. 2506–2511, 1999.
- [33] B. V. Sarada, T. N. Rao, D. A. Tryk, and A. Fujishima, "Electrochemical oxidation of histamine and serotonin at highly boron-doped diamond electrodes," *Analytical Chemistry*, vol. 72, no. 7, pp. 1632–1638, 2000.
- [34] J. Lee and S. M. Park, "Direct electrochemical assay of glucose using boron-doped diamond electrodes," *Analytica Chimica Acta*, vol. 545, no. 1, pp. 27–32, 2005.
- [35] J. Zhao, D. Wu, and J. Zhi, "A direct electrochemical method for diabetes diagnosis based on as-prepared boron-doped nanocrystalline diamond thin film electrodes," *Journal of Electroanalytical Chemistry*, vol. 626, no. 1–2, pp. 98–102, 2009.
- [36] J. Zhao, L. Wu, and J. Zhi, "Non-enzymatic glucose detection using as-prepared boron-doped diamond thin-film electrodes," *Analyst*, vol. 134, no. 4, pp. 794–799, 2009.
- [37] M. Chiku, K. Horisawa, N. Doi, H. Yanagawa, and Y. Einaga, "Electrochemical detection of tyrosine derivatives and protein tyrosine kinase activity using boron-doped diamond electrodes," *Biosensors and Bioelectronics*, vol. 26, no. 1, pp. 235–240, 2010.
- [38] G. Zhao, Y. Qi, and Y. Tian, "Simultaneous and direct determination of tryptophan and tyrosine at boron-doped diamond electrode," *Electroanalysis*, vol. 18, no. 8, pp. 830–834, 2006.
- [39] O. Nekrassova, N. S. Lawrence, and R. G. Compton, "Direct oxidation of haemoglobin at bare boron-doped diamond electrodes," *Analyst*, vol. 129, no. 9, pp. 804–805, 2004.
- [40] C. Prado, G. U. Flechsig, P. Grüdler, J. S. Foord, F. Marken, and R. G. Compton, "Electrochemical analysis of nucleic acids at boron-doped diamond electrodes," *Analyst*, vol. 127, no. 3, pp. 329–332, 2002.
- [41] J. Wang, G. Chen, A. Muck Jr., D. Shin, and A. Fujishima, "Microchip capillary electrophoresis with a boron-doped diamond electrode for rapid separation and detection of purines," *Journal of Chromatography A*, vol. 1022, no. 1–2, pp. 207–212, 2004.
- [42] T. A. Ivandini, B. V. Sarada, T. N. Rao, and A. Fujishima, "Electrochemical oxidation of underivatized-nucleic acids at highly boron-doped diamond electrodes," *Analyst*, vol. 128, no. 7, pp. 924–929, 2003.
- [43] M. Zhang, K. Gong, H. Zhang, and L. Mao, "Layer-by-layer assembled carbon nanotubes for selective determination of dopamine in the presence of ascorbic acid," *Biosensors and Bioelectronics*, vol. 20, no. 7, pp. 1270–1276, 2005.
- [44] L. Zhang and X. Jiang, "Attachment of gold nanoparticles to glassy carbon electrode and its application for the voltammetric resolution of ascorbic acid and dopamine," *Journal of Electroanalytical Chemistry*, vol. 583, no. 2, pp. 292–299, 2005.
- [45] X. Lin, Y. Zhang, W. Chen, and P. Wu, "Electrocatalytic oxidation and determination of dopamine in the presence of ascorbic acid and uric acid at a poly (p-nitrobenzenazo resorcinol) modified glassy carbon electrode," *Sensors and Actuators, B: Chemical*, vol. 122, no. 1, pp. 309–314, 2007.
- [46] E. Popa, H. Notsu, T. Miwa, D. A. Tryk, and A. Fujishima, "Selective electrochemical detection of dopamine in the presence of ascorbic acid at anodized diamond thin film electrodes," *Electrochemical and Solid-State Letters*, vol. 2, no. 1, pp. 49–51, 1999.
- [47] D. A. Tryk, H. Tachibana, H. Inoue, and A. Fujishima, "Boron-doped diamond electrodes: the role of surface termination in the oxidation of dopamine and ascorbic acid," *Diamond and Related Materials*, vol. 16, no. 4–7, pp. 881–887, 2007.
- [48] E. Popa, Y. Kubota, D. A. Tryk, and A. Fujishima, "Selective voltammetric and amperometric detection of uric acid with oxidized diamond film electrodes," *Analytical Chemistry*, vol. 72, no. 7, pp. 1724–1727, 2000.
- [49] C. Terashima, T. N. Rao, B. V. Sarada, and A. Fujishima, "Amperometric detection of oxidized and reduced glutathione at anodically pretreated diamond electrodes," *Chemistry Letters*, vol. 32, no. 2, pp. 136–137, 2003.
- [50] T. A. Ivandini, K. Honda, T. N. Rao, A. Fujishima, and Y. Einaga, "Simultaneous detection of purine and pyrimidine at highly boron-doped diamond electrodes by using liquid chromatography," *Talanta*, vol. 71, no. 2, pp. 648–655, 2007.
- [51] H. Notsu, T. Tsuma, and A. Fujishima, "Tyrosinase-modified boron-doped diamond electrodes for the determination of phenol derivatives," *Journal of Electroanalytical Chemistry*, vol. 523, no. 1–2, pp. 86–92, 2002.

- [52] W. Yang, O. Auciello, J. E. Butler et al., "DNA-modified nanocrystalline diamond thin-films as stable, biologically active substrates," *Nature Materials*, vol. 1, no. 4, pp. 253–257, 2002.
- [53] W. Yang, S. E. Baker, J. E. Butler et al., "Electrically addressable biomolecular functionalization of conductive nanocrystalline diamond thin films," *Chemistry of Materials*, vol. 17, no. 5, pp. 938–940, 2005.
- [54] Y. Zhou and J. Zhi, "Development of an amperometric biosensor based on covalent immobilization of tyrosinase on a boron-doped diamond electrode," *Electrochemistry Communications*, vol. 8, no. 12, pp. 1811–1816, 2006.
- [55] Y. L. Zhou, R. H. Tian, and J. F. Zhi, "Amperometric biosensor based on tyrosinase immobilized on a boron-doped diamond electrode," *Biosensors and Bioelectronics*, vol. 22, no. 6, pp. 822–828, 2007.
- [56] B. Wang, J. Zhang, and S. Dong, "Silica sol-gel composite film as an encapsulation matrix for the construction of an amperometric tyrosinase-based biosensor," *Biosensors and Bioelectronics*, vol. 15, no. 7-8, pp. 397–402, 2000.
- [57] V. Carralero Sanz, M. L. Mena, A. González-Cortés, P. Yáñez-Sedeño, and J. M. Pingarrón, "Development of a tyrosinase biosensor based on gold nanoparticles-modified glassy carbon electrodes: application to the measurement of a bioelectrochemical polyphenols index in wines," *Analytica Chimica Acta*, vol. 528, no. 1, pp. 1–8, 2005.
- [58] Rajesh, W. Takashima, and K. Kaneto, "Amperometric phenol biosensor based on covalent immobilization of tyrosinase onto an electrochemically prepared novel copolymer poly (N-3-aminopropyl pyrrole-co-pyrrole) film," *Sensors and Actuators, B*, vol. 102, no. 2, pp. 271–277, 2004.
- [59] J. A. Bennett, J. Wang, Y. Show, and G. M. Swain, "Effect of sp²-bonded nondiamond carbon impurity on the response of boron-doped polycrystalline diamond thin-film electrodes," *Journal of the Electrochemical Society*, vol. 151, no. 9, pp. E306–E313, 2004.
- [60] Y. Zhou, J. Zhi, Y. Zou, W. Zhang, and S. T. Lee, "Direct electrochemistry and electrocatalytic activity of cytochrome c covalently immobilized on a boron-doped nanocrystalline diamond electrode," *Analytical Chemistry*, vol. 80, no. 11, pp. 4141–4146, 2008.
- [61] T. Kondo, Y. Niwano, A. Tamura et al., "Enhanced electrochemical response in oxidative differential pulse voltammetry of dopamine in the presence of ascorbic acid at carboxyl-terminated boron-doped diamond electrodes," *Electrochimica Acta*, vol. 54, no. 8, pp. 2312–2319, 2009.
- [62] Y. Wang, J. Zhi, Y. Liu, and J. Zhang, "Electrochemical detection of surfactant cetylpyridinium bromide using boron-doped diamond as electrode," *Electrochemistry Communications*, vol. 13, no. 1, pp. 82–85, 2011.
- [63] J. Weng, J. Xue, J. Wang et al., "Gold-cluster sensors formed electrochemically at boron-doped-diamond electrodes: detection of dopamine in the presence of ascorbic acid and thiols," *Advanced Functional Materials*, vol. 15, no. 4, pp. 639–647, 2005.
- [64] J. C. Harfield, K. E. Toghil, C. Batchelor-Mcauley, C. Downing, and R. G. Compton, "Nickel nanoparticle modified BDD electrode shows an electrocatalytic response to adenine and DNA in aqueous alkaline media," *Electroanalysis*, vol. 23, no. 4, pp. 931–938, 2011.
- [65] K. E. Toghil, L. Xiao, G. G. Wildgoose, and R. G. Compton, "Electroanalytical determination of cadmium(II) and lead(II) using an antimony nanoparticle modified boron-doped diamond electrode," *Electroanalysis*, vol. 21, no. 10, pp. 1113–1118, 2009.
- [66] K. E. Toghil, G. G. Wildgoose, A. Moshar, C. Mulcahy, and R. G. Compton, "Fabrication and characterization of a bismuth nanoparticle modified boron doped diamond electrode and its application to the simultaneous determination of cadmium(II) and lead(II)," *Electroanalysis*, vol. 20, no. 16, pp. 1731–1737, 2008.
- [67] A. O. Simm, X. Ji, C. E. Banks, M. E. Hyde, and R. G. Compton, "AFM studies of metal deposition: instantaneous nucleation and the growth of cobalt nanoparticles on boron-doped diamond electrodes," *ChemPhysChem*, vol. 7, no. 3, pp. 704–709, 2006.
- [68] A. O. Simm, C. E. Banks, S. Ward-Jones et al., "Boron-doped diamond microdisc arrays: electrochemical characterisation and their use as a substrate for the production of microelectrode arrays of diverse metals (Ag, Au, Cu) via electrodeposition," *Analyst*, vol. 130, no. 9, pp. 1303–1311, 2005.
- [69] C. M. Welch, M. E. Hyde, C. E. Banks, and R. G. Compton, "The detection of nitrate using in-situ copper nanoparticle deposition at a boron doped diamond electrode," *Analytical Sciences*, vol. 21, no. 12, pp. 1421–1430, 2005.
- [70] C. M. Welch, A. O. Simm, and R. G. Compton, "Oxidation of electrodeposited copper on boron doped diamond in acidic solution: manipulating the size of copper nanoparticles using voltammetry," *Electroanalysis*, vol. 18, no. 10, pp. 965–970, 2006.
- [71] T. A. Ivandini, R. Sato, Y. Makide, A. Fujishima, and Y. Einaga, "Pt-implanted boron-doped diamond electrodes and the application for electrochemical detection of hydrogen peroxide," *Diamond and Related Materials*, vol. 14, no. 11-12, pp. 2133–2138, 2005.
- [72] S. Hrapovic, Y. Liu, and J. H. T. Luong, "Reusable platinum nanoparticle modified boron doped diamond microelectrodes for oxidative determination of arsenite," *Analytical Chemistry*, vol. 79, no. 2, pp. 500–507, 2007.
- [73] L. Hutton, M. E. Newton, P. R. Unwin, and J. V. Macpherson, "Amperometric oxygen sensor based on a platinum nanoparticle-modified polycrystalline boron doped diamond disk electrode," *Analytical Chemistry*, vol. 81, no. 3, pp. 1023–1032, 2009.
- [74] C. M. Welch and R. G. Compton, "The use of nanoparticles in electroanalysis: a review," *Analytical and Bioanalytical Chemistry*, vol. 384, no. 3, pp. 601–619, 2006.
- [75] F. W. Campbell and R. G. Compton, "The use of nanoparticles in electroanalysis: an updated review," *Analytical and Bioanalytical Chemistry*, vol. 396, no. 1, pp. 241–259, 2010.
- [76] C. Terashima, T. N. Rao, B. V. Sarada, N. Spataru, and A. Fujishima, "Electrodeposition of hydrous iridium oxide on conductive diamond electrodes for catalytic sensor applications," *Journal of Electroanalytical Chemistry*, vol. 544, pp. 65–74, 2003.